



# **Aeroacoustic Analogies based on Compressible Flow Data**

**Dissertation**

**Dipl.-Ing. Stefan SCHODER**

Die approbierte Originalversion dieser  
Dissertation ist in der Hauptbibliothek der  
Technischen Universität Wien aufgestellt und  
zugänglich.  
<http://www.ub.tuwien.ac.at>



The approved original version of this thesis is  
available at the main library of the Vienna  
University of Technology.

<http://www.ub.tuwien.ac.at/eng>

*Ohne Musik wäre das Leben ein Irrtum.*

Friedrich Nietzsche



TECHNISCHE  
UNIVERSITÄT  
WIEN



Dissertation

# **Aeroacoustic Analogies based on Compressible Flow Data**

ausgeführt zum Zwecke der Erlangung des akademischen Grades eines

**Doktor der technischen Wissenschaften**

unter der Leitung von

Univ.-Prof. Dipl.-Ing. Dr.techn. Manfred KALTENBACHER

Institut für Mechanik und Mechatronik, E325 A4

eingereicht an der Technischen Universität Wien, Fakultät für Maschinen-  
wesen und Betriebswissenschaften, von

Dipl.-Ing. Stefan J. SCHODER

00925762

Schubertplatz 4

3361 Aschbach

und begutachtet von

Prof. Christophe Schram

Department of

Aeronautics and Aerospace

Waterloosesteenweg 72

B-1640 Sint-Genesius-Rode

Belgium

Prof. Claus-Dieter Munz

Institut für

Aerodynamik und Gasdynamik

Pfaffenwaldring 21

70569 Stuttgart

Deutschland

## Eidesstattliche Erklärung

Ich erkläre an Eides statt, dass ich meine Dissertation mit dem Titel *Aeroacoustic Analogies based on Compressible Flow Data* selbständig und ohne Benutzung anderer als der angegebenen Hilfsmittel angefertigt habe und dass ich alle Stellen, die ich wörtlich oder sinngemäß aus Veröffentlichungen entnommen habe, als solche kenntlich gemacht habe. Die Arbeit hat bisher in gleicher oder ähnlicher Form oder auszugsweise noch keiner Prüfungsbehörde vorgelegen.

Wien, am December 4, 2018

---

Dipl.-Ing. Stefan J. SCHODER



# Acknowledgement

Ein großes Dankeschön gilt meiner Freundin Barbara, meinen Eltern Michaela und Johann und meinen Geschwistern Liesa Maria, Maria-Sophie, Joahannes Michael und Gregor Benedikt SCHODER, die mich während des Studiums hervorragend unterstützten. Ich danke den Partnern meiner Geschwister Mathias, Markus, Johannes und Gregors Freundin, den Eltern und Geschwistern meiner Freundin, Maria und Alois, Harald, Bettina, Karin, Andrea und deren Partner Verena, Hannes, Rula, Thomas.

Mein Dank gilt Univ. Prof. Dipl.-Ing. Dr.-Ing. Manfred KALTENBACHER an dessen Institut ich diese Arbeit anfertigte. Besonderer Dank gebührt den Kollegen für die fachlich kompetente Resonanz und die rege Diskussion.

Ein besonderes Dankeschön möchte ich meinen Freunden Andreas RUTHMEIER und Susanne WILD, David HALBMAYER, Ivo STEINBRECHER, Jakob STIEBLEHNER, Hannes BÜHRINGER, Frank NIESSEN und allen die ich hier nicht angeführt habe aussprechen, welche immer mit Rat und Tat beiseite standen und für jede Diskussion ein offenes Ohr hatten.

Hiermit bedanke ich mich bei meinen Studenten, späteren Kollegen und Freunden, Klaus ROPPERT, Ivan LAZAROV und Michael WEITZ.



# Abstract

The thesis in hand focuses on a novel numerical simulation method to compute aeroacoustic analogies based on compressible flow data by a hybrid technique. Industrial applicability of aeroacoustic simulation technologies is computational demanding. The computational workload is reduced with the hybrid approach to an efficient minimum. With the proposed workflow we are capable of combining the properties of a fully resolved compressible flow simulation (including feedback from acoustics to flow structures) and the desirable advantage of a separated acoustic simulation. A separation of the physical fields during the simulation yields in a computationally efficient algorithm, which is capable of including relevant physical effects due to the flow and acoustically specific boundaries, like impedance, can be applied.

In this sense, we extend the hybrid approach from underlying incompressible flow simulations to compressible flow simulations using Helmholtz projection to obtain a vortical base flow and apply the known hybrid methodologies. The application of this hybrid methodology seems to be unconventional and fluid dynamically not rigorous, but with the correct wave operator the equation obeys the fluid dynamic conservation equations. We apply the method to aeroacoustic examples involving aeroacoustic feedback mechanisms, which require a compressible flow simulation. However, practical applications show that sometimes even for incompressible flow simulations "typical feedback mechanism", as described by Rossiter, are captured. A short mathematical explanation, why feedback is even possible for incompressible flow structures, is given based on compact acoustics.

Hybrid aeroacoustic analogies rely on energy conserving and accurate transformation schemes that convert the known physical quantities, like pressure, and velocity, from one grid to another. Simple Nearest Neighbor mappings are not accurate enough for source term computation. Therefore, a combination of a local Radial Basis Function framework and conservative integration procedure relying on cell intersections is applied to transform the physical quantities and construct accurate derivatives on them for a robust simulation workflow.

# Kurzfassung

In dieser Dissertation wird eine neuartige hybride Simulationsmethode zur Berechnung strömungsakustischer Effekte entwickelt. Industrielle Anwendung mit Akustik als Qualitätsmerkmal treiben die Nachfrage nach effizienten Berechnungsmethoden. Durch den hybriden Ansatz wird der Effizienz Rechnung getragen und der Simulationsaufwand, im Vergleich zu einer direkten Simulation von Strömung und Akustik, wesentlich reduziert. Zusätzlich kann durch die Trennung eine detailliertere Akustiksimulation samt spezieller Randbedingungen und Materialverteilungen durchgeführt werden.

Eine wesentliche Herausforderung stellt die Erweiterung von hybriden Ansätzen auf kompressible Strömungsdaten dar. Aus der Sicht eines Strömungsmechanikers wirft dieser unkonventionelle Workflow Fragen auf (besonders im höheren Machzahl-Bereich). Bei speziellen Problemstellungen mit strömungsakustischen Feedback erfordert die Physik eine kompressible Strömungsmodellierung und daher eine Erweiterung der hybriden Methode. In diesem Sinne wird die Rahmenbedingung (inkompressible Strömungssimulation) der hybriden Methoden auf eine kompressible Strömungsrechnung erweitert. Die Helmholtz Zerlegung projiziert anschließend die kompressible Lösung auf einen inkompressiblen Lösungsraum. Diese Projektion wird dann in der aeroakustischen Analogie verwendet. Interessanterweise wird in der Praxis oft auch bei inkompressiblen Strömungssimulationen ein Rossiter-Feedback Mechanismus festgestellt, welcher physikalisch nicht möglich ist.

Die hybride Methode verlangt eine exakte und energieerhaltende Gittertransformation der physikalischen Größen. Ein einfacher Nächster-Nachbar-Algorithmus ist nicht ausreichend. Darum wird eine Interpolation mit radialen Basisfunktionen in Kombination mit einer konservativen Integration verwendet.

# Used Symbols

## Symbols

$\mathbf{A}$	Vector potential
$D$	Cavity depth
$D_c$	Cavity neck correction length
$D_M$	Cavity neck length
$E$	Total energy
$\mathbf{F}$	Force
$F_{\text{int}}$	Mechanical energy due to an internal force density
$H$	Specific enthalpy, Heaviside distribution
$\text{He}$	Helmholtz number
$\mathbf{I}$	Momentum
$L$	Characteristic length scale, Cavity length
$\mathbf{L}$	Lamb vector
$M$	Mach number
$M_{\text{bound}}$	Work due to shear force on the control volume surface
$P_{\text{bound}}$	Work due to pressured control volume surface
$Q_{\text{int}}$	Internal heat production
$Q_{\text{bound}}$	Heat exchange over the control volume surface
$R_s$	Specific gas constant (Air: $287.12 \text{ J/kgK}$ ), can be derived from the universal gas constant $R$
$\text{Re}$	Reynolds number
$\text{St}$	Strouhal number
$S$	Cavity neck surface
$T$	Temperature
$T_p$	Time period
$U$	Characteristic flow velocity
$V$	Volume
$W$	Filter function, Cavity width
$\mathbf{X}$	Eigenvectors
$b$	Particle distribution function LBM
$c$	Isentropic speed of sound (Air: $c_0 = 343.4 \text{ m/s}$ at $p = 101325 \text{ Pa}$ and $T = 20^\circ\text{C}$ )
$c_g$	Group velocity
$c_{\text{ph}}$	Phase velocity
$c_p$	Specific heat at constant pressure (Air: $1006 \text{ J/kgK}$ at $p = 101325 \text{ Pa}$ and $p = 20^\circ\text{C}$ )
$c_{\text{ph}}$	Phase velocity
$c_v$	Specific heat at constant volume (Air: $717.8 \text{ J/kgK}$ at $p = 101325 \text{ Pa}$ and $p = 20^\circ\text{C}$ )
$d$	Length
$e$	Specific total energy
$\mathbf{e}_i$	Microscopic velocities of the Lattice Boltzmann method (LBM)
$f$	Frequency, Surface function that describes solid surfaces
$\mathbf{f}$	Volume force density
$h$	Specific enthalpy, Smooth transition
$k$	Conductivity of Fourier's law

$\mathbf{k}$	Wavenumber vector
$l_v$	Characteristic vortex length
$m$	Mass
$n_{\text{mesh}}$	Number of mesh points
$\mathbf{n}$	Normal vector on surface
$p$	Fluid pressure
$q$	Specific heat production
$q_{\text{mass}}$	Mass source of the acoustic wave equation
$q_{\text{mom}}$	Momentum source of the acoustic wave equation
$q_T$	Specific surface heat flux vector
$r$	Radial coordinate
$s$	Specific entropy, Surface area
$t$	Time
$u$	Specific internal energy
$\mathbf{u}$	Fluid velocity
$v$	Specific volume
$w$	Specific work, Cavity neck width
$\mathbf{x}$	Principal Cartesian coordinate directions (Eulerian), observer coordinate
$\mathbf{x}'$	Source coordinate
$\mathbf{z}$	Principal Cartesian coordinate directions
$\Gamma$	Boundary
$\Phi$	Scalar potential APE
$\Omega$	Control volume
$\partial\Omega$	Boundary of the control volume
$\alpha$	Flatness scaling parameter
$\delta$	Boundary layer thickness, Delta distribution
$\delta_2$	Momentum thickness
$\epsilon$	Mass regularization parameter
$\lambda$	Wavelength, Eigenvalues
$\lambda_\mu$	Bulk viscosity
$\phi$	Scalar potential, Thermal viscous dissipation
$\psi$	Scalar potential
$\theta$	Scalar potential
$\kappa$	Ratio of the specific heats $\frac{c_p}{c_v}$ , isentropic exponent
$\mu$	Dynamic viscosity (Air: $18.21 \mu\text{Pas}$ at $p = 101325 \text{ Pa}$ and $p = 20^\circ\text{C}$ )
$\nu$	Kinematic viscosity (Air: $15.32 \mu\text{m}^2/\text{s}$ at $p = 101325 \text{ Pa}$ and $p = 20^\circ\text{C}$ )
$\rho$	Mass density
$\rho_1$	Hardin and Pope's density correction
$\theta$	General potential
$\omega$	Angular frequency
$\boldsymbol{\omega}$	Vorticity
$\boldsymbol{\xi}$	Principal Cartesian coordinate directions (Lagrangian)
$\mathbb{C}$	Cauchy stress tensor

$\mathbf{E}$	Strain tensor
$\mathbf{F}$	General tensor
$\mathbf{I}$	Identity tensor
$\mathbf{J}$	Jacobi-transformation matrix, Deformation gradient tensor
$\mathbf{S}$	Deviatoric stress tensor
$\mathbf{T}$	Lighthill tensor

$\mathcal{B}$	Homogeneous fluid body, Control volume
$\mathcal{F}$	Collision operator of the Boltzmann transport equation

### *Operators*

$\overline{(\star)}$	Temporal mean operator
$(\star)'$	Fluctuation or perturbation operator
$\tilde{\star}$	Base component
$\Delta$	Laplace operator with respect to the Cartesian coordinate system $\mathbf{x}$
$\nabla$	Nabla operator with respect to the Cartesian coordinate system $\mathbf{x}$
$\frac{d\star}{dt}$	Substantial, convective, total or material derivative with respect to parameter $t$
$\frac{\partial\star}{\partial t}$	Partial derivative with respect to parameter $t$
$\square$	d'Alembert operator or generic wave operator
$:$	Scalar product : $a : a = a_{ij}a_{ji}$
$\mathbf{tr}$	Extracts the sum of diagonal elements, trace
$\mathbf{E}$	Operator matrix of the linearized Euler equation

### *Superscripts*

0	Incompressible component
(0)	Thermodynamic component
a	Acoustic part
c	Compressible part
h	Harmonic part
ic	Incompressible part
no	Non radiating part
v	Vortical part
*	Joint function, Modified state

### *Subscripts*

0	Reference state
$\infty$	Far-field state
a	Acoustic part
c	Convective, advective component, correction
n	Numerical
v	Vortical part

## Used Acronyms

APE	Acoustic perturbation equations
BEM	Boundary element method
CFD	Computational Fluid Dynamics
CFL	Courant–Friedrichs–Lewy condition
CAA	Computational Aeroacoustic
D	Dimensions
DNS	Direct simulation of turbulent flows
DSC	Direct sound computation
DX	Direct simulation of flows and acoustics
EIF	Expansion about the incompressible flow
FE	Finite Element
FEM	Finite Element Method
FW-H	Ffowcs Williams and Hawking
IML	Infinite mapping layer
LBM	Lattice Boltzmann method
LEE	Linearized Euler equations
LES	Large eddy simulation
LPCE	Linearized perturbed compressible equations
PCE	Perturbed compressible equations
PCWE	Perturbed convective wave equation
PDE	Partial differential equations
RANS	Reynolds averaged Navier-Stokes equations
RBF	Radial basis function
PML	Perfectly Matched Layer
RHS	Right hand side of a PDE
URANS	Unsteady RANS
SBES	Stress blended eddy simulation
SNGR	Synthetic noise generation
SPL	Sound Pressure Level
SST	Shear stress transport
STM	Synthetic turbulence model







# Contents

<b>1</b>	<b>Introduction</b>	<b>1</b>
1.1	Daily experience – Noise and Sound . . . . .	1
1.2	History of aeroacoustic models . . . . .	3
1.3	Aim of the thesis . . . . .	5
<b>2</b>	<b>Computational Aeroacoustics</b>	<b>7</b>
2.1	Fluid dynamics – Conservation equations . . . . .	7
2.1.1	Continuum approximation . . . . .	7
2.1.2	Reynolds transport theorem . . . . .	8
2.1.3	Conservation of mass . . . . .	9
2.1.4	Conservation of momentum . . . . .	9
2.1.5	Conservation of energy . . . . .	10
2.2	Constitutive laws . . . . .	11
2.2.1	Equation of state – Perfect gas . . . . .	12
2.2.2	Newtonian fluid . . . . .	13
2.3	Dimensionless numbers in fluid dynamics . . . . .	14
2.3.1	Reynolds number . . . . .	14
2.3.2	Strouhal number . . . . .	14
2.3.3	Helmholtz number . . . . .	15
2.3.4	Mach number . . . . .	15
2.4	Acoustics . . . . .	15
2.4.1	Compact acoustics . . . . .	16
2.4.2	Acoustics and Fluid dynamics . . . . .	17
2.5	Helmholtz decomposition . . . . .	17
2.5.1	Sequence of temporal images . . . . .	19
2.5.2	Decompose the fluctuating component . . . . .	19
2.5.3	Helmholtz decomposition and conservation laws . . . . .	20
2.6	Aeroacoustic models . . . . .	21
2.6.1	General acoustic analogies . . . . .	21
2.6.2	Direct simulation of flow and acoustic . . . . .	23
2.6.3	Perturbation equations . . . . .	26
2.7	Cavity tones . . . . .	32
2.7.1	Historical perspective and classification . . . . .	33
2.7.2	Aeroacoustic feedback – Shear layer mode . . . . .	35
2.7.3	Fluid dynamic feedback – Wake mode . . . . .	37
2.7.4	Acoustic resonances or fluid resonant . . . . .	37

2.7.5	Fluid elastic resonant - fluid structure interaction . . . . .	39
2.7.6	Factors of influence - shear layer mode . . . . .	40
<b>3</b>	<b>Flow-Acoustic Coupling and Aeroacoustic splitting</b>	<b>45</b>
3.1	Direct numerical simulation . . . . .	45
3.2	Direct sound computation . . . . .	46
3.3	Hybrid methodology – Incompressible flow . . . . .	48
3.3.1	Feedback . . . . .	49
3.4	Hybrid methodology – Compressible flow . . . . .	50
3.5	Source term modeling in aeroacoustic analogies . . . . .	50
3.5.1	Implicit formulation . . . . .	51
3.5.2	Explicit reformulation . . . . .	51
3.6	Taylor expansion . . . . .	53
3.6.1	Alternative derivation of Lighthill’s Analogy . . . . .	53
3.6.2	RHS linearization of Lighthill’s Analogy . . . . .	54
3.6.3	Modified Lighthill’s Analogy . . . . .	55
3.6.4	Linearization of vortex sound . . . . .	55
<b>4</b>	<b>Helmholtz decomposition and acoustic analogies</b>	<b>58</b>
4.1	Simply connected domain . . . . .	58
4.2	Helmholtz decomposition . . . . .	59
4.3	Scalar potential . . . . .	61
4.3.1	Weak formulation . . . . .	61
4.3.2	Boundary conditions . . . . .	63
4.3.3	Poisson problem – Shortcomings . . . . .	64
4.4	Singularity at reentrant corners . . . . .	64
4.4.1	Poisson problem . . . . .	64
4.4.2	Curl-curl equation . . . . .	65
4.5	Vector potential . . . . .	67
4.5.1	Weak formulation . . . . .	67
4.5.2	Boundary conditions . . . . .	70
4.5.3	Boundary term – Transformation . . . . .	71
4.6	Helmholtz-Hodge decomposition . . . . .	71
<b>5</b>	<b>Aeroacoustic source interpolation</b>	<b>73</b>
5.1	Interpolation Schemes . . . . .	74
5.1.1	Radial basis function interpolation . . . . .	75
5.1.2	Proof of convergence of the interpolation . . . . .	77
5.1.3	On the optimal choice of neighbors . . . . .	77
5.1.4	Convergence of interpolation . . . . .	79
5.2	Derivatives based on RBFs . . . . .	82
5.2.1	Convergence of derivatives . . . . .	85
5.3	Application of RBF algorithm . . . . .	86
5.4	Conservative Interpolation . . . . .	86

<b>6</b>	<b>Validation and Applications</b>	<b>90</b>
6.1	Cylinder in a crossflow – 2D . . . . .	91
6.1.1	Fluid dynamics . . . . .	92
6.1.2	Helmholtz decomposition . . . . .	92
6.1.3	Conclusions . . . . .	92
6.2	Cavity with a lip – 2D . . . . .	93
6.2.1	Simulation workflow . . . . .	94
6.2.2	Fluid dynamics . . . . .	94
6.2.3	Helmholtz decomposition . . . . .	97
6.2.4	Acoustic propagation . . . . .	98
6.2.5	Conclusions . . . . .	100
6.3	Cavity with a lip – 3D . . . . .	102
6.3.1	Fluid dynamics . . . . .	102
6.3.2	Helmholtz decomposition . . . . .	107
6.3.3	Mapping 3D to 2D . . . . .	110
6.3.4	Acoustics . . . . .	111
6.3.5	Discussion of the deviation . . . . .	113
6.4	Cavity 2M4 and 2M8 . . . . .	114
6.4.1	Helmholtz decomposition . . . . .	115
6.4.2	Aeroacoustic simulation . . . . .	117
6.4.3	Conclusions . . . . .	121
<b>7</b>	<b>Summary and Conclusions</b>	<b>122</b>
7.1	Application . . . . .	123
7.2	Properties of the extended hybrid workflow . . . . .	125
7.3	Further investigations . . . . .	126
<b>A</b>	<b>Infinite mapping layer</b>	<b>127</b>
A.1	Mapping Layer Formulation . . . . .	127
A.2	Finite Element Implementation . . . . .	130
A.3	Laplace Operator . . . . .	130
	<b>Bibliography</b>	<b>131</b>



# 1 Introduction

Humans experience nature and culture in a flourishing enthusiastic way with their incredible senses. Singing birds, pounding waves and means of harmony are associated with typical sounds. Music even connects opposing cultures and expresses emotions. Hearing assists all kinds of species with an audible 360 degree picture of their surrounding, saving them in case of danger. The magnificent human sense of hearing has a lower limit of audible pressure at  $p_0^a = 20 \mu\text{Pa}$  (reference sound pressure for the sound pressure level 0 dB) and reaches out to the threshold of pain at around 20 Pa/120 dB. The sound pressure level (SPL) is commonly used in acoustics, since it describes the wide audible range of the human ear relatively to the hearing threshold.

In contrast to the passive acoustic organ, the speech organ is the active part transmitting sound. Humans express and exchange feelings and communicate with it actively. Both organs are valuable for participative communication and save humans from unexpected hazards. These essential safety and life quality aspects increase the value of hearing and speaking. The quality of humans' lives puts special emphasis on protecting humans by reducing the daily sound and noise level.

Besides the reduction of other types of pollution, modern cities aim to decrease the sound level and noise exposure of housing and living areas. Therefore, highly sophisticated transportation concepts are developed in the context of zero emissions. This zero emission target for noise leads to the questions:

"What are sound sources? Where are these sources located?"

Empirical and simulative studies derive aeroacoustic source mechanisms from flow data. This thesis intends to develop computational models for predicting aeroacoustic sound sources arising from engineering applications. People typically label acoustic radiation due to engineering applications and manufacturing machinery as distracting noise. In most applications noise develops as a parasitic byproduct, which can even effect labor productivity [1]. To conclude, parasitic noise effects humans' health, causes an economic impact and avoiding noise is an important goal of science.

## 1.1 Daily experience – Noise and Sound

Noisy environment decreases the effectiveness of means of communication, increases organ disorders, and reduces social participation. Intensive noise exposure and all changes in noise levels, shape and quality distract humans' life. Humans are especially sensitive to a changing environment and they are alarmed, when the environment changes. A highly noisy environment causes a lack of concentration and defocuses people from their intention. Additionally, cognitive performance is highly influenced by a noisy environment. Modern applications (e.g. smartphones) are exploiting this evidence to get humans attraction, a special ring-tone or other sounds trigger that something amazing is happening right now. Even the regeneration phase is destructed and elongated by noise. In conclusion humans' lives and especially work, studying, and sports are influenced by noise and sound. Sounds to one's desire will encourage, whereas noise generally defocuses people.

Transportation business, industry and urban environments expose humans to an increasing number (qualitatively and quantitatively) of sound sources at different levels. The engineering discipline "sound design" boosts the quality of sound to the passenger's desire. Noise sources are minimized to prevent individuals from distortion. Even a medium SPL range in conjunction with a sufficiently long exposure duration causes hearing disorder. The defect increases with increasing SPL one is exposed to. Luckily, as other organs, the ear regenerates itself within several days and gains hearing capabilities back. However, a severe damage is only recovered insufficiently.

In the context of acoustic engineering a tremendous number of acoustic applications are of public interest. What they all have in common is that an increasing sound quality serves mankind with a lower audible stress state. This includes medical treatment, industry, transportation and construction businesses.

- Health care - applications assisting people with hearing and speaking disorders [2].
- Prophylaxis - applications to reduce the noise exposure of people in an active or passive way.
- Transportation business, industry and machinery - due to the highly dynamic, taylorized, and globalized the need of transportation, industry and machinery is enormous. Thus, the commercially induced noise shall be minimized to a favorable background noise.
- Building and comfort - applications to increase the comfort of people in their personal housing or at the office.

In modern transport systems, passengers' comfort is greatly influenced by noise. The main noise source can be roughly separated into three main acoustic source generation effects.

- Structural vibrations cause noise emissions from vibrating surfaces of all kind of dynamic structures (e.g. machinery). A famous representative is hammering of iron or a ringing bell of an old church tower. This field of scientific research is named *vibroacoustic* and combines structural dynamics and acoustics.
- Thermal or combustion noise arises from thermal gradients in a given fluid and fluid expansion. For example, jet engines radiate combustion noise. *Combustion acoustics* relates acoustics and thermodynamics.
- Vorticity and turbulence are generating flow born noise inside the medium. The acoustic waves are generated by a wide range of flow phenomena including cavities, gaps and compression shocks. The research field is called *aeroacoustics* and is physically described by fluid dynamics.

Figure 1.1 shows typical noise sources of a car with a combustion engine. With increasing transportation speed, the flow induced noise component and its interaction with the other noise generation mechanisms becomes the most important acoustic source. Vortical, turbulent flow structures radiate acoustic waves and modify acoustic structures by scattering. If the acoustic wave length coincides with a geometric mechanical dimension of a car, this lock-on state causes severe acoustic transmission to the driver's ear and should be avoided during design.

In the automotive industry, aiming for the age of electrification and lightweight constructions [4], flow induced noise sources are no longer masked by other noise sources and influence passengers' comfort, as well as their safety. These two comfort factors have become a distinctive capability in the premium automotive segment [5]. The sound design of air-conditioning systems in cars is a special comfort feature for premium class products. To be specific, a major part of noise level in public transportation is airborne; imagine a train rushing through the station or flying jets. Often, special mechanisms produce sound at



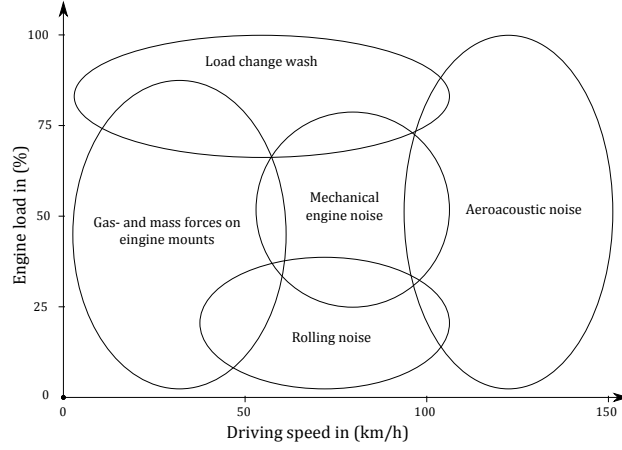


Figure 1.1: Noise sources of a vehicle with a combustion engine. Extracted from [3].

discrete frequencies, like a whistle or cavities. Physicists and engineers are interested in a causal relation of the source and the reaction of these mechanisms. In the last 70 years, numerous acoustic effects have been studied by different physical models.

## 1.2 History of aeroacoustic models

The first proposed acoustic analogy by Lighthill [6, 7] transforms the compressible Navier-Stokes equation into an exact inhomogeneous wave equation. Lighthill's equation describes a general wave equation in terms of the fluctuating density. In its local form no assumptions are given with respect to the boundaries. However, Lighthill proposed the solution of the wave equation by using Green's function of the wave equation for free field radiation. In doing so, resonators and bodies in the neighborhood of the sources as well as diffraction, scattering, absorption and reflection by solid boundaries are neglected. Curle [8] investigated the effects of stationary surfaces in the context of the integral solution of Lighthill's theory. Stationary surfaces are equivalent to a surface dipole distribution. Ffowcs Williams and Hawking [9] extended Kirchhoff's formula [10] and generalized the integral solution towards accounting for arbitrary moving bodies in the source domain.

Ribner [11] and Powell [12] based their theories on comparing a slightly compressible flow with an incompressible flow, where vorticity  $\omega$  sources dominate. Further investigations on vortex sound were carried out by Howe [13], Möhring [14], and Doak [15]. Recently, Goldstein [16] proposed his generalized acoustic analogy, which shows that the Navier-Stokes equations can be rewritten as a set of linearized Euler equations.

Aeroacoustic analogies compute noise radiation efficiently. However, basic assumptions restrict the application of these methods, e.g. acoustic compact sources. Acoustic compact sources imply that the characteristic size of the sources contributing to the acoustics are small compared to the generated wavelength. Additionally, ambiguity of the acoustic analogies arises since the sources depend on the solution of the equations.

The direct computation of flow and acoustic solves the compressible Navier-Stokes equations and gains the united field of flow and acoustics. Compared to acoustic analogies this method is more general since fewer model assumptions are made, when computing flow and acoustics with a single simulation. However, the required resources are comparably high in the range of low Mach numbers. In this regime small vortices develop large acoustic waves, extending the required computational domain. At low Mach numbers acoustic waves propagate over long distances, requiring a conservative, non-dissipative scheme.

In general, the acoustic quantities are of orders of magnitude weaker than the fluid dynamic ones. This method is preferably used in the mid to high Mach number regime. Over the years this method was extensively used to validate acoustic analogies and calculate applications in jet noise [17]. Today, these methods are even used in the low Mach number regime. Recently, the Lattice Boltzmann approach gains popularity in solving the flow and acoustic field directly. The applications of this method in acoustics reach from airframe noise [18], to acoustic simulations of landing gears [19], and industrial applications [20].

Freund [21] used a wave number decomposition to separate the united field of flow and acoustics. Goldstein [22] states the desired properties of a filtered flow variable, such that no radiating components (acoustic) are present. The condition is the dispersion relation of acoustic waves in a quiescent medium. Two main possibilities are given to realize the filtering. The first one is a local approach applying the corresponding d'Alembert operator to the filtered variable. The second technique is based on a convolution that cuts out the acoustic components.

An unresolved issue are exact transparent free field boundary conditions for the Navier-Stokes equation. The available conditions are categorized in linear characteristic boundary conditions [23–26], and absorbing layers [24, 27]. Furthermore, typical flow boundary conditions mistreat the acoustic reality and design engineers have to evaluate the significance of the modeling assumptions on the acoustics during aeroacoustic design. Ideally both common modeling errors are avoided: an inaccurate resolution of the source mechanism, and an improper boundary treatment.

The third approach for computing aeroacoustics, aims towards a systematic decomposition of the field properties. The general flow field is decomposed into a fluid dynamic part and an acoustic part. To derive the linearized Euler equations, the field variables  $(\rho, \mathbf{u}, p)$  are decomposed in a temporal mean component  $(\overline{\star})$  and a fluctuating component  $(\star)'$ . Bailly *et al.* [28, 29] indicate the significant aeroacoustic source terms on the momentum equation of the linearized Euler equations (LEE). Over the years, the linearized Euler equation was modified to guarantee that only acoustic is propagated [30]. Ewert and Schröder [31] proposed a different filtering technique for a uniform flow field. Instead of filtering the flow field, the source terms of the wave equations are filtered according to the properties of the acoustic modes, obtained from the LEE.

Ribner [11] formulated his dilatation equation such that the primary fluctuating pressure variable of Lighthill's analogy is decomposed in a pseudo pressure and an acoustic pressure part  $p' = p^0 + p^a$ . Hardin and Pope [32] formulated their viscous/acoustic splitting technique expansion about the incompressible flow (EIF), where they introduced a density correction  $\rho_1$ . The method relies on an incompressible flow simulation to extract the sources. The perturbed variables converge to the acoustic perturbations in the far field. In the near field Hardin and Pope stated that the perturbed variables are the difference between the compressible and the incompressible solution of the flow field. EIF is validated by the pulsating sphere and the flow over a rectangular cavity. Inconsistency critics arose on the original EIF formulation [33]. Shen and Sørensen [33, 34] modified this method to account for non-isentropic flows. Their extension is validated against the pulsating sphere and the circular cylinder. Slimon *et al.* [35] proposed an aerodynamic/acoustic splitting method, which is cost-effective and is validated for a non-compact source regions. This further development of the EIF method is derived systematically via a Mach number expansion.

As noticed by Seo and Moon [36] the viscous/acoustic formulation neglects near field coupling effects. Thus, they proposed a different version of perturbation equations named perturbed compressible equations (PCE) for handling near field coupling effects. This method was applied to human phonation simulations [37]. At low Mach numbers the sound field is grid dependent. As a consequence, Seo and Moon [38] reformulated their nonlinear PCE to a grid independent, perturbed vorticity suppressing linear formulation. At low Mach numbers, the total derivative of the incompressible fluid dynamic pressure

acts as the dominant source. The dominant source is consistent with the source term in Goldstein’s generalized acoustic analogy [16] and the acoustic perturbation equations for incompressible flow [31].

Ewert and Schröder [31] utilized a slightly different approach to derive the acoustic perturbation equations (APE), in several versions and complexity. APE-1 is the general formulation describing the total system via the pressure perturbation and the velocity perturbation. The APE-2 formulation is used in conjunction with an incompressible unsteady flow simulation. At low Mach numbers, the source term is approximated by the time derivative of the pressure perturbation of the incompressible flow simulation. The introduced APE-3 system coincides with the APE-1 system, where the system is based on the perturbed total enthalpy. This formulation has one advantage over the APE-1, since no Poisson’s equation (source term filtering) has to be solved to determine the source terms. The APE-4 variant of the formulation is based on the APE-1 system such that the sources are easily computed by a compressible flow simulation. Hüppe and Kaltenbacher [39] derived a computational efficient reformulation of the APE-2 system and named it perturbed convective wave equation (PCWE).

Munz and coworkers [40–42] proposed an alternative derivation of perturbed equations for acoustic by a Mach number scaling. This ansatz is inserted into the compressible Euler equations and constitutes the linearized Euler equations with the total derivative of the incompressible pressure perturbation as significant source term.

De Roeck and Desmet [43] thought about the necessity of a aerodynamic/acoustic splitting technique based on Helmholtz decomposition. First, the field is decomposed in a mean flow field and a fluctuating part, as introduced during the derivation of the LEE, and subsequently the fluctuations are further decomposed in an aerodynamic and an acoustic component. The acoustic field is irrotational and the aerodynamic part rotational.

### 1.3 Aim of the thesis

Knowing the computational limitations of *direct simulation of acoustic and flow* when applying it to an industrial applications, we aim for a hybrid methodology that is based on a compressible flow simulation. This means that acoustics is already partly resolved during the flow computation and we have to adapt the wave propagation model and filter the source terms to reduce the already resolved acoustics within them. The thesis in hand is focusing on the Helmholtz decomposition of the compressible velocity field. Based on the decomposed field, we construct a consistent wave propagation formulation that can be derived from existing aeroacoustic analogies. The method will be validated through four applications.

Practical applications (e.g. cavity with a lip) often seek for compressible simulation, since acoustic feedback mechanisms excite flow structures [44]. However, compressible source term simulations in conjunction with the arising computational effort demand huge computational resources. The method derived in this thesis claims to combine the computational efficiency of aeroacoustic analogies and a compressible source term computation. Computational efficiency is introduced by the hybrid procedure. Hybrid methods separate the flow simulation and the acoustic simulation; each simulation model is well suited to the physical phenomenon. The vorticity dominates the acoustic source of several aeroacoustic applications. Helmholtz decomposition extracts the vorticity components fast and elegant. The aim of this thesis is to filter the flow field, based on the divergence free property of vortical structures. In this sense the compressible flow is split into vortical mode and compressible mode (remaining part).

Additionally, the procedure aims to correct an inaccurate boundary treatment, during the flow simulation, e.g. non-exact radiation condition. In general, the hybrid workflow focuses on the proper acoustic model with a sufficient resolution of the main aeroacoustic sources. The current model does not incorporate nonlinear interaction of different aeroacoustic source mechanisms and the acoustic quantity.

The rest of the thesis is structured as follows: Chapter 2 presents the fundamental equations, a historical evolution of computational techniques of aeroacoustics, and the theoretical background on cavity noise, since the application examples include mostly cavities with a Rossiter feedback loop. Chapter 3 introduces the physical relevancy of splitting the flow field into a vortical and a compressible part for aeroacoustic and Chap. 4 formulates the Helmholtz decomposition. The computation of the aeroacoustic sources is illustrated in Chap. 5. Chapter 6 validates the developed method by several benchmark examples including a direct simulation of flow and acoustics and its decomposition into acoustic and vortical components. From the direct simulation of flow and acoustics, the reader will be convinced that Helmholtz decomposition is an excellent way of visualizing acoustics. Finally, Chap. 7 concludes the main findings.

# 2 Computational Aeroacoustics

The theoretical part introduces the basic concepts and the common footprint of fluid dynamics and acoustics. In its general form, flow and acoustics are described by the same set of equations including conservation of mass, momentum, and energy [45, 46]. The continuum theory and model specific assumptions specify different simplifications of these equations for acoustics and flow. In conjunction with the constitutive laws, primarily using a Newtonian fluid and the perfect gas law, we have a closed system of equations. Acoustics and its inherent propagating nature relies on a compressible, inviscid fluid. These fluid properties excite wave modes. In contrast, general fluid dynamics is modeled with a viscous fluid. Below Mach 0.3 the incompressibility assumption of the fluid neglects acoustic modes in the simulation.

## 2.1 Fluid dynamics – Conservation equations

Conservation of mass, momentum and energy describe the properties of a fluid based on the assumptions of continuum theory. In conjunction with the constitutive equation (e.g.: Newtonian fluid) and equation of state (e.g.: ideal gas law), a closed set of partial differential equations describes the dynamic fluid properties.

### 2.1.1 Continuum approximation

In the context of continuum theory, a homogeneous fluid body  $\mathcal{B}$  consists of a volumetric conglomerate of homogenized mass particles. The size of these particles is assumed to be large enough such that molecular effects are negligible. Each particle must represent the physical field accurately, which limits the size on the upper scale. To apply the continuum theory successfully a compromise between the upper and lower limit must be found.

Continuum theory allows to write physical quantities of the flow field as a function of the coordinate  $\mathbf{x}$  and the time  $t$  (density  $\rho(\mathbf{x}, t)$ , pressure  $p(\mathbf{x}, t)$ , velocity  $\mathbf{u}(\mathbf{x}, t)$ , ...). Physically speaking, the total change of a field quantity (e.g. density  $\rho(\mathbf{x}, t)$ ) is defined as

$$d\rho = \frac{\partial \rho}{\partial t} dt + \nabla_{\mathbf{x}} \rho d\mathbf{x} . \quad (2.1)$$

The total derivative of the density, in fluid dynamics often called substantial derivative of the density, is given by

$$\frac{d\rho}{dt} = \frac{\partial \rho}{\partial t} + (\mathbf{u} \cdot \nabla_{\mathbf{x}}) \rho \quad (2.2)$$

A generalization for arbitrary tensor fields is simple. The substantial derivative of a tensor field in an Eulerian reference frame writes as

$$\frac{d\star}{dt} = \frac{\partial \star}{\partial t} + (\mathbf{u} \cdot \nabla_{\mathbf{x}}) \star . \quad (2.3)$$

### 2.1.2 Reynolds transport theorem

The Reynolds transport theorem is a general rule to treat balance equations [47] and formalize the treatment of conserved quantities. Important applications of the Reynolds transport theorem are the conservation of mass, momentum, and energy. In the next section, we apply this theorem to derive the Navier-Stokes equation.

**Theorem 2.1.1** *For a given tensor field  $\mathbb{F}(\mathbf{x}, t)$  with index  $i \geq 0$  uniquely defined on  $\Omega$ ,  $C^1$ , and a flow field  $\mathbf{u}(\mathbf{x}, t)$  the relation*

$$\frac{d}{dt} \int_{\Omega(t)} \mathbb{F}(\mathbf{x}, t) d\mathbf{x} = \int_{\Omega(t)} \frac{\partial \mathbb{F}(\mathbf{x}, t)}{\partial t} d\mathbf{x} + \int_{\partial\Omega(t)} \mathbb{F}(\mathbf{x}, t) \mathbf{u}(\mathbf{x}, t) \cdot \mathbf{n} ds \quad (2.4)$$

holds.

First, we rewrite the material derivative over the volume integral from the Eulerian configuration  $\mathbf{x}$  to the Lagrangian configuration  $\boldsymbol{\xi}$ . The time independent integral is transformed using the determinant of the deformation gradient tensor (determinant of the Jacobi-transformation matrix)  $\mathbb{J} := \nabla_{\boldsymbol{\xi}} \mathbf{x}$ . Now, the time derivative and integral can be changed (Leibnitz integral rule) and due to time independent domain the material derivative is equal to the partial derivative

$$\frac{d[\star(\boldsymbol{\xi}, t)]}{dt} = \frac{\partial[\star(\boldsymbol{\xi}, t)]}{\partial t} + \left( \frac{\partial \boldsymbol{\xi}}{\partial t} \cdot \nabla_{\boldsymbol{\xi}} \right) [\star(\boldsymbol{\xi}, t)] = \frac{\partial[\star(\boldsymbol{\xi}, t)]}{\partial t}. \quad (2.5)$$

This leads to

$$\frac{d}{dt} \int_{\Omega(t)} \mathbb{F}(\mathbf{x}, t) d\mathbf{x} = \int_{\Omega} \frac{\partial \mathbb{F}(\boldsymbol{\xi}, t) \mathbb{J}}{\partial t} d\boldsymbol{\xi} \quad (2.6)$$

for the time dependent integral. Using product rule and the identity for the time derivative of the Jacobian  $\frac{\partial \mathbb{J}}{\partial t} = (\nabla_{\boldsymbol{\xi}} \cdot \mathbf{u}) \mathbb{J}$ , we obtain

$$\int_{\Omega} \frac{\partial \mathbb{F}(\boldsymbol{\xi}, t) \mathbb{J}}{\partial t} d\boldsymbol{\xi} = \int_{\Omega} \left( \frac{\partial \mathbb{F}(\boldsymbol{\xi}, t)}{\partial t} \mathbb{J} + \mathbb{F}(\boldsymbol{\xi}, t) (\nabla_{\boldsymbol{\xi}} \cdot \mathbf{u}) \mathbb{J} \right) d\boldsymbol{\xi}. \quad (2.7)$$

Transforming the integral back to the moving configuration, we find

$$\begin{aligned} & \int_{\Omega} \left( \frac{\partial \mathbb{F}(\boldsymbol{\xi}, t)}{\partial t} \mathbb{J} + \mathbb{F}(\boldsymbol{\xi}, t) (\nabla_{\boldsymbol{\xi}} \cdot \mathbf{u}) \mathbb{J} \right) d\boldsymbol{\xi} = \\ & = \int_{\Omega(t)} \left( \frac{\partial \mathbb{F}(\mathbf{x}, t)}{\partial t} + [\mathbb{F}(\mathbf{x}, t) \nabla_{\mathbf{x}} \cdot \mathbf{u} + \mathbf{u} \nabla_{\mathbf{x}} \cdot \mathbb{F}(\mathbf{x}, t)] \right) d\mathbf{x}. \end{aligned} \quad (2.8)$$

Additionally, the tensor identity  $\mathbb{F} \nabla_{\mathbf{x}} \cdot \mathbf{u} + \mathbf{u} \nabla_{\mathbf{x}} \cdot \mathbb{F} = \nabla_{\mathbf{x}} \cdot (\mathbf{u} \mathbb{F})$  is utilized. Finally applying the divergence theorem, we derive Theorem 2.1.1.

$$\begin{aligned} & \int_{\Omega(t)} \left( \frac{\partial \mathbb{F}(\mathbf{x}, t)}{\partial t} + \nabla_{\mathbf{x}} \cdot (\mathbf{u} \mathbb{F}) \right) d\mathbf{x} = \\ & = \int_{\Omega(t)} \frac{\partial \mathbb{F}(\mathbf{x}, t)}{\partial t} d\mathbf{x} + \int_{\partial\Omega(t)} \mathbb{F}(\mathbf{x}, t) \mathbf{u}(\mathbf{x}, t) \cdot \mathbf{n} ds \end{aligned} \quad (2.9)$$

The first term formulates the temporal change of the tensor field inside the control volume, whereas the second term is the boundary exchange of the control volume. From that point on the Eulerian description is used and all operators are based on the coordinate  $\mathbf{x}$ ,  $\nabla := \nabla_{\mathbf{x}}$ .

### 2.1.3 Conservation of mass

The mass  $m$  of a body  $\mathcal{B}$  is defined by the volume integral of the body's mass density distribution  $\rho(\mathbf{x}, t)$

$$m := \int_{\Omega} \rho dx. \quad (2.10)$$

Mass conservation describes the well known effect that the mass of a body is conserved over time in a control volume, as long as there is no source or drain

$$\frac{d}{dt}m = 0. \quad (2.11)$$

The mass conservation holds for any control volume. Applying Reynolds' transport theorem (2.1.1) and assuming a continuous mass density field, the mass conservation results in the local differential representation for a compressible fluid

$$\frac{\partial \rho}{\partial t} + \nabla \cdot (\rho \mathbf{u}) = 0. \quad (2.12)$$

Equation (2.12) is called equation of continuity and with respect to the equation, the mass density  $\rho$  and the velocity  $\mathbf{u}$  must be at least continuously differentiable. In the case of incompressibility, the density is constant over a streamline and if it is initially uniform it stays uniform. This fact simplifies the continuity equation (2.12) to

$$\nabla \cdot \mathbf{u} = 0, \quad (2.13)$$

and restrict the incompressible flow field to be divergence free. This property of the flow field is used in Chap. 3 to derive a vorticity dominated aeroacoustic analogy based on compressible flow quantities.

### 2.1.4 Conservation of momentum

The momentum  $\mathbf{I}$  of a body  $\mathcal{B}$  is defined by the volume integral of the body's local momentum density distribution  $\rho \mathbf{u}$

$$\mathbf{I} := \int_{\Omega} \rho \mathbf{u} dx. \quad (2.14)$$

Conservation of momentum generalizes Newton's second law, one fundamental axiom of classical mechanics. Any change of momentum is driven by the acting force  $\mathbf{F}$

$$\frac{d}{dt}\mathbf{I} = \mathbf{F}. \quad (2.15)$$

To derive the Navier-Stokes equation, the conservation of momentum is applied to a physical domain, the control volume. The Reynolds' transport theorem (2.1.1) quantifies the change of momentum on the left hand side. According to Newton's second law, this change is due to a volume force density  $\mathbf{f}$  and surface forces  $\mathbb{C} \cdot \mathbf{n}$ .

$$\int_{\Omega} \frac{\partial}{\partial t}(\rho \mathbf{u}) dx + \int_{\partial \Omega} \rho \mathbf{u} \mathbf{u} \cdot d\mathbf{s} = \int_{\partial \Omega} \mathbb{C} \cdot d\mathbf{s} + \int_{\Omega} \mathbf{f} dx \quad (2.16)$$

The Cauchy stress tensor  $\mathbb{C}$  is split into a hydrostatic stress tensor  $-p\mathbb{I}$  (all eigenvalues of the characteristic equation are  $-p$ ) and a deviatoric stress tensor  $\mathbb{S}$

$$\mathbb{C} = -p\mathbb{I} + \mathbb{S}. \quad (2.17)$$

Applying the divergence theorem to the surface integrals of the conservation of momentum (2.16), the boundary (surface) integrals are transformed into a volume integral. Furthermore, we assume the consti-

tutive relation of a Newtonian fluid (see Sec. 2.2.2), which yields to the Navier Stokes equations in their conservative form

$$\int_{\Omega} \left( \frac{\partial}{\partial t}(\rho \mathbf{u}) + \nabla \cdot (\rho \mathbf{u} \mathbf{u}) + \nabla p - \mu(\Delta \mathbf{u} - \frac{1}{3} \nabla \nabla \cdot \mathbf{u}) - \mathbf{f} \right) dx = 0. \quad (2.18)$$

Since the equation holds for arbitrary control volumes, the continuous integrand vanishes, which leads to the Navier-Stokes equations in the local, conservative, strong formulation.

$$\frac{\partial}{\partial t}(\rho \mathbf{u}) + \nabla \cdot (\rho \mathbf{u} \mathbf{u}) = -\nabla p + \mu(\Delta \mathbf{u} + \frac{1}{3} \nabla \nabla \cdot \mathbf{u}) + \mathbf{f} \quad (2.19)$$

The Navier-Stokes equation describes two structurally different vortical flow states, laminar and turbulent flow. A limited range of length and energy scales occur during a laminar flow, which makes it relatively simply to compute. With increasing Reynolds number  $Re$ , the viscous forces are unable to keep the laminar layers together and as a result turbulent mixing forms turbulent eddies in the flow. These turbulent flow structures have a wide range of different length and energy scales. Kolmogorov spectrum [48] describes these scales and the conversion of scales up to viscous dissipation. A direct simulation of turbulent structures demands excessive computational resources. Thus, the turbulent eddy spectrum is modeled by specific turbulence models. This type of modeling is known as closure problem in fluid mechanics.

### 2.1.5 Conservation of energy

The total energy  $E$  of a body  $\mathcal{B}$  is defined by the volume integral of the local energy density distribution  $\rho(e + \frac{\mathbf{u} \cdot \mathbf{u}}{2})$

$$E := \int_{\Omega} \rho \left( e + \frac{\mathbf{u} \cdot \mathbf{u}}{2} \right) dx. \quad (2.20)$$

Both, the change of the inner energy  $e$  and the kinetic energy  $\frac{\mathbf{u} \cdot \mathbf{u}}{2}$  are described by conservation of energy,

$$\frac{d}{dt} E = Q_{\text{int}} + Q_{\text{bound}} + P_{\text{bound}} + M_{\text{bound}} + F_{\text{int}}, \quad (2.21)$$

that associates any change of energy [49] to an internal heat production  $Q_{\text{int}}$

$$Q_{\text{int}} := \int_{\Omega} q dx, \quad (2.22)$$

a heat exchange on the surface  $Q_{\text{bound}}$

$$Q_{\text{bound}} := \int_{\partial \Omega} \mathbf{q}_T \cdot \mathbf{n} ds, \quad (2.23)$$

the work done by a surface pressure  $P_{\text{bound}}$

$$P_{\text{bound}} := \int_{\partial \Omega} p \mathbf{u} \cdot \mathbf{n} ds, \quad (2.24)$$

the work done by a shear force on the surface (traction)  $M_{\text{bound}}$

$$M_{\text{bound}} := \int_{\partial \Omega} (\mathbb{S} \cdot \mathbf{u}) \cdot \mathbf{n} ds, \quad (2.25)$$

and the mechanical energy of an internal force density  $\mathbf{f}$

$$F_{\text{int}} := \int_{\Omega} \mathbf{f} \cdot \mathbf{u} dx. \quad (2.26)$$



The divergence theorem transforms the surface integrals to volume integrals and afterwards Reynolds' transport theorem (2.1.1) and mass conservation is used for further manipulation. Since the obtained equation holds for arbitrary control volumes, the continuous integrand vanishes and we obtain the local form of the energy conservation

$$\rho \frac{d}{dt} \left( e + \frac{\mathbf{u} \cdot \mathbf{u}}{2} \right) = q - \nabla \cdot (\mathbf{q}_T + p\mathbf{u} - \mathbb{S} \cdot \mathbf{u}) + \mathbf{f} \cdot \mathbf{u}. \quad (2.27)$$

By exploiting the properties of the specific entropy  $s(\mathbf{x}, t)$  in thermodynamics, Howe [50] writes the conservation of energy as

$$\rho T \frac{ds}{dt} = q - \nabla \cdot \mathbf{q}_T + \mathbb{S} : \nabla \mathbf{u}. \quad (2.28)$$

Adiabatic flows characterize no heat exchange over the control volume boundary. A further tightening restriction is an isentropic flow that is adiabatic and reversible. The term reversible indicates a conservative system; no dissipation is present; thus viscous dissipation is neglected. If no internal heat source is present, isentropic flow fulfills the relation

$$\rho T \frac{ds}{dt} = 0. \quad (2.29)$$

The most restrictive thermodynamic flow state is a homentropic fluid that is homogeneous and with uniform entropy in the control volume ( $ds = 0$ ).

**Pressure equation:** In computational fluid dynamics it is partly convenient to use a pressure equation instead of the tedious energy equation. The thermodynamic definition of the specific enthalpy  $h$ ,

$$dh = Tds + vdp \quad (2.30)$$

with the specific volume  $v = 1/\rho$ , allows to rewrite the energy equation in the entropy form (2.28). The left hand side of the equation is further simplified by conservation of mass and yields

$$\rho \frac{d}{dt} h - \frac{d}{dt} p = q - \nabla \cdot \mathbf{q}_T + \mathbb{S} : \nabla \mathbf{u}. \quad (2.31)$$

Exploiting the fact that an ideal gas is inert, the ideal gas law (2.41) holds and the change of specific enthalpy  $dh = c_p dT$ . Expressing  $R_s/c_p = (\kappa - 1)/\kappa$ , the relation between the pressure  $p$ , the density  $\rho$ , and the specific enthalpy  $h$  is obviously

$$p = \frac{\kappa - 1}{\kappa} \rho h. \quad (2.32)$$

These relations are inserted into the derivatives on the left hand side. The relation between the pressure  $p$ , the density  $\rho$ , and the specific enthalpy  $h$  in conjunction with the conservation of mass again, we obtain the final result of the pressure equation

$$\frac{d}{dt} p + \kappa p \nabla \cdot \mathbf{u} = (\kappa - 1)(q - \nabla \cdot \mathbf{q}_T + \mathbb{S} : \nabla \mathbf{u}). \quad (2.33)$$

## 2.2 Constitutive laws

The three principal conservation equations, conservation of mass, momentum, and energy, introduce unknown field variables. In fact, more unknowns are part of the equations than the number of equations the conservation laws accounts for. This leads to an undetermined problem. To close the system, additional empirical models connect certain unknowns and form constitutive relations of fluid dynamics.

In aeroacoustic, the relevant constitutive laws are the ideal gas law and the concept of the Newtonian fluid. The ideal or perfect gas (state equation) relation is used to derive the pressure equation; the Newtonian fluid links the velocity and the stress tensor during the derivation of Navier-Stokes equation.

### 2.2.1 Equation of state – Perfect gas

In this case, the fluid is considered to be in thermodynamic equilibrium and to be homogeneous. Thus, the thermodynamic state is universally represented by two intrinsic state variables. The first law of thermodynamics states that a change in the specific internal energy  $e$  is caused by heat exchange or work

$$de = dq + dw. \quad (2.34)$$

Thermodynamic equilibrium requires a sufficiently slow (quasi-static) compression of the fluid. The intrinsic state variables are the specific entropy  $s$  and the specific volume  $v$ . In this sense, we can express the heat change by the change of the specific entropy  $s$

$$dq = Tds. \quad (2.35)$$

The representation of the internal energy as  $u = u(s, v)$  restricts the mechanical work to isobaric work. A volumetric compression of the fluid element is defined by

$$dw = -p dv. \quad (2.36)$$

In the field of acoustics, the density  $\rho$  is a more convenient second intrinsic state variable than the specific volume  $v$ . Therefore, the differential of the specific volume in terms of the density is rewritten as

$$dv = d\frac{1}{\rho} = -\frac{1}{\rho^2}d\rho. \quad (2.37)$$

If the previous definitions are inserted, we obtain the relation of the internal energy (fundamental thermodynamic relation) based on two intrinsic state variables  $s$  and  $\rho$

$$de = Tds + \frac{1}{\rho^2}d\rho. \quad (2.38)$$

Furthermore, the pressure  $p$  is an acoustically relevant state variable. Considering thermodynamic state description, the same intrinsic variables  $s$  and  $\rho$  are used to express the change of the pressure by the definition of its differential change

$$dp = \left(\frac{\partial p}{\partial s}\right)_{\rho=const} ds + \left(\frac{\partial p}{\partial \rho}\right)_{s=const} d\rho. \quad (2.39)$$

Per definition, the isentropic ( $ds = 0$ ) speed of sound relates the density and pressure perturbation  $dp = c^2 d\rho$ . Comparing the coefficients leads to

$$c^2 = \left(\frac{\partial p}{\partial \rho}\right)_{s=const}. \quad (2.40)$$

At a sufficiently high temperature above the boiling point of the medium and at a sufficiently low pressure as well as supposing that the kinetic energy of the particle is large, the interaction of gas particles is low.

Neglecting the attraction between particles, the gas is modeled by the perfect gas law

$$p = \rho R_s T, \quad (2.41)$$

with the specific gas constant  $R_s$ . Acoustics in air at ambient pressure and temperature satisfies the assumptions of an ideal gas. For an ideal inert gas we can express the internal energy  $u$  by

$$de = c_v dT. \quad (2.42)$$

Replacing the left hand side in equation (2.38), using the ideal gas law (2.41), and an isentropic state  $ds = 0$  we derive

$$\frac{dT}{T} = \frac{R_s}{c_v} \frac{d\rho}{\rho}. \quad (2.43)$$

The differential of the ideal gas law divided by the ideal gas law results in

$$\frac{dp}{p} = \frac{dT}{T} + \frac{d\rho}{\rho}. \quad (2.44)$$

Now (2.43) is inserted into (2.44). Additionally, the definition of the isentropic exponent  $\kappa := \frac{c_p}{c_v}$ , the relation between the specific heats, and the specific gas constant  $R_s = c_p - c_v$  simplifies the result to

$$\frac{dp}{p} = \kappa \frac{d\rho}{\rho}. \quad (2.45)$$

To conclude, we obtain the isentropic speed of sound  $c$  from the relation,

$$dp = \kappa R_s T d\rho = c^2 d\rho. \quad (2.46)$$

The isentropic speed of sound depends on the media through the constants  $R_s$  and  $\kappa$  as well as on the thermodynamic state via the temperature  $T$  [51]. For ambient conditions in air, the isentropic speed of sound is approximately 340 m/s.

## 2.2.2 Newtonian fluid

Newtonian fluid or Stokes relation constitutes a viscous fluid. Stokes relation connects the velocity  $\mathbf{u}$ , respectively the strain rate tensor  $\mathbb{E}$ , and the deviatoric stress tensor  $\mathbb{S}$  linearly with the dynamic viscosity  $\mu$  and the bulk viscosity  $\lambda_\mu$ . Both constants are positive  $\mu > 0$  and  $\lambda_\mu \geq 0$

$$\mathbb{S} = 2\mu\mathbb{E} + \lambda_\mu \text{tr}(\mathbb{E})\mathbb{I}. \quad (2.47)$$

The strain rate tensor is defined by velocity gradients

$$\mathbb{E} = \frac{1}{2}(\nabla\mathbf{u} + (\nabla\mathbf{u})^T). \quad (2.48)$$

In thermodynamic equilibrium, according to Stokes hypotheses the bulk viscosity and the dynamic viscosity is related by  $\lambda_\mu = -(2/3)\mu$ . As a consequence, the divergence of the stress tensor can be written as

$$\nabla \cdot \mathbb{S} = \mu(\Delta\mathbf{u} + \frac{1}{3}\nabla\nabla \cdot \mathbf{u}). \quad (2.49)$$

Often, computational fluid dynamics treats the bulk part of the stress tensor as an additional isentropic term, like pressure.

## 2.3 Dimensionless numbers in fluid dynamics

Fluid dynamics develops different flow phenomena with respect to the flow configuration and the geometry. Dimensionless numbers relate flow phenomena to characteristic flow quantities. Based on these numbers a general similarity between different flow states is observed.

Perhaps the most popular one is known as Reynolds number, which is widely utilized to separate laminar flow and turbulent flow characteristics. Two configurations with identical Reynolds number

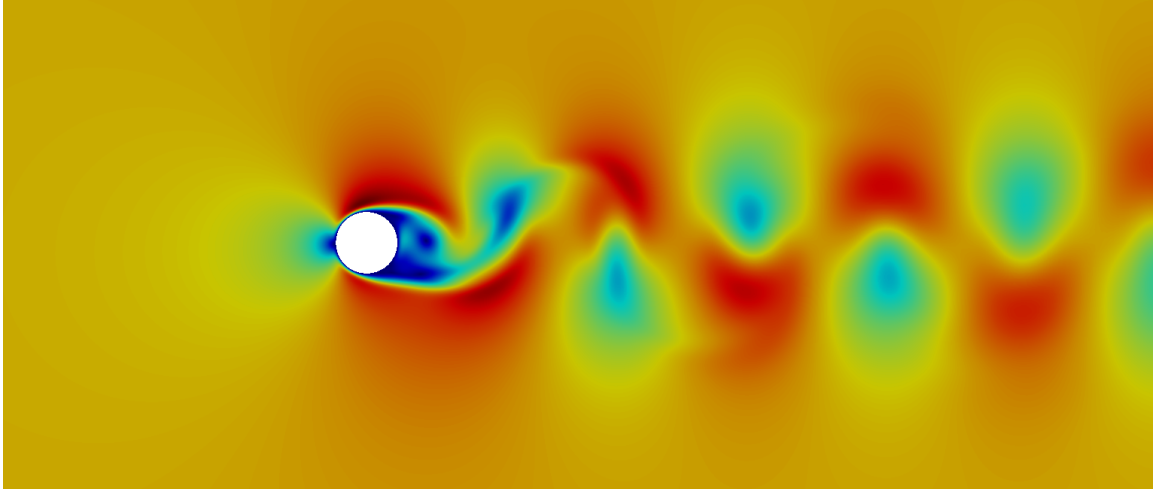


Figure 2.1: Kármán's vortex street behind a cylinder in a crossflow,  $Re = 200$ .

behave in a similar way, with respect to viscous effects. Typically aeroacousticians work with four similarities: Reynolds number  $Re$ , Strouhal number  $St$ , Helmholtz number  $He$ , and the Mach number  $Ma$ . To enhance the reader's understanding, the dimensionless numbers are applied to the flow around a cylinder, which forms a von Kármán's vortex street (see Fig. 2.1).

### 2.3.1 Reynolds number

Reynolds investigated the similarity of stream lines for different flow configurations in pipes. He explored Reynolds similarity. A flow configuration is Reynolds similar if the Reynolds number  $Re$  coincides. With this in mind, Reynolds equivalent down sizing of flow configurations is possible.  $Re$  is defined as

$$Re = \frac{\rho UL}{\mu} = \frac{UL}{\nu}, \quad (2.50)$$

with a characteristic length  $L$  (diameter of the cylinder), the mass density  $\rho$ , the dynamic viscosity  $\mu$ , the kinematic viscosity  $\nu$ , and the characteristic flow velocity  $U$  (free stream velocity). Reynolds number relates the inertia forces and the viscous forces acting on a fluid particle.

$$\frac{\text{inertia}}{\text{viscous}} = \frac{\| \rho(\mathbf{v} \cdot \nabla) \mathbf{v} \|}{\| \mu \Delta \mathbf{v} \|} \quad (2.51)$$

This ratio indicates the transition between laminar and turbulent fluid dynamics; above a critical Reynolds number the flow is most likely turbulent.

### 2.3.2 Strouhal number

An additional similarity parameter of a flow configuration is the Strouhal number  $St$ . Strouhal number specifies oscillatory flow unsteadiness and cyclic variations in the flow. Obviously, the wake of the cylinder,

the von Kármán's vortex street, is oscillating and at medium Reynolds numbers periodic vortex shedding occurs. The Strouhal number describes these unsteady phenomena

$$\text{St}_n = \frac{f_n L}{U} \approx |_{n=1} \mathcal{O}(1), \quad (2.52)$$

and relates the vortex shedding frequency  $f_n$  to a characteristic flow time scale. Typical values for the flow unsteadiness are in the range of 0.1 - 0.2 for the first order cycles. Two flow configurations are dynamically similar, if both the Reynolds number and the Strouhal number are identical.

### 2.3.3 Helmholtz number

As Strouhal number describes the periodic structures of unsteady flow, the Helmholtz number  $\text{He}$  qualifies periodic structures based on the speed of sound  $c$ . Acoustic phenomena are characterized by the Helmholtz number.

$$\text{He}_n = \frac{L}{\lambda_n} = \frac{f_n L}{c} = \text{St Ma} \quad (2.53)$$

The vortical structures of the von Kármán's vortex street radiate acoustic waves at the same frequency  $f_n$ , but the acoustic wavelength  $\lambda$  is  $1/\text{Ma}$  larger than the characteristic length of vortical structures, where  $\text{Ma}$  denotes the Mach number.

A special case for  $\text{He} \ll 1$  is compact acoustics that approximates the wave equation by a Poisson equation. Acoustic compact bodies do not scatter sound, they are "transparent" to the acoustic wave and neglecting these bodies in an acoustic propagation simulation leads to an insignificant error.

### 2.3.4 Mach number

The Mach number interprets the significance of a density variation due to a velocity variation in the flow field. The ratio of the characteristic velocity  $U$  and the isentropic speed of sound  $c$  yields the Mach number

$$\text{Ma} = \frac{U}{c}. \quad (2.54)$$

In one dimension and for steady isentropic flows, the conservation of momentum describes that a density change is proportional to a velocity change scaled by the square of the Mach number

$$-\text{Ma}^2 \frac{dU}{U} = \frac{d\rho}{\rho}. \quad (2.55)$$

This fact divides fluid dynamics into an incompressible ( $\text{Ma} < 0.3$ ) and a compressible ( $\text{Ma} \geq 0.3$ ) regime. If we are interested in vortical flow structures at low Mach numbers, the flow is typically modeled as incompressible. However, direct simulation of acoustics requires a compressible fluid.

## 2.4 Acoustics

Conservation of mass, momentum and energy and the constitutive relations provide the equations of fluid dynamics and acoustics. We start the derivation of the linear acoustic wave equation from the linearized Euler equations. The acoustic perturbations are assumed to be sufficiently small [49] and are defined

around a mean field by

$$\rho = \bar{\rho} + \rho^a, \quad (2.56)$$

$$p = \bar{p} + p^a, \quad (2.57)$$

$$\mathbf{u} = \bar{\mathbf{u}} + \mathbf{u}^a. \quad (2.58)$$

Furthermore, the derivation assumes a zero mean velocity ( $\bar{\mathbf{u}} = \mathbf{0}$ ) flow field and an isentropic thermodynamic state  $ds = 0$

$$\frac{\partial \rho^a}{\partial t} + \bar{\rho} \nabla \cdot \mathbf{u}^a = q_{\text{mass}} \quad (2.59)$$

$$\bar{\rho} \frac{\partial \mathbf{u}^a}{\partial t} + \nabla p^a = \mathbf{q}_{\text{mom}} \quad (2.60)$$

$$p^a = c^2 \rho^a, \quad (2.61)$$

where we introduced a mass source  $q_{\text{mass}}$  and a momentum force term  $q_{\text{mom}}$ . The manipulation of (2.59) to (2.61) results in the well known formula of linear isentropic acoustics

$$\frac{1}{c^2} \frac{\partial^2 p^a}{\partial t^2} - \nabla \cdot \nabla p^a = \frac{\partial q_{\text{mass}}}{\partial t} - \nabla \cdot \mathbf{q}_{\text{mom}}. \quad (2.62)$$

A Fourier transformation of the acoustic wave equation yields in Helmholtz's equation of acoustics,

$$k^2 \hat{p}^a + \nabla \cdot \nabla \hat{p}^a = j\omega \hat{q}_{\text{mass}} - \nabla \cdot \hat{\mathbf{q}}_{\text{mom}}, \quad (2.63)$$

with the Fourier transformed pressure  $\hat{p}^a$ , the imaginary unit  $j$ , and the Fourier transformed source terms  $\hat{q}_{\text{mass}}$ ,  $\hat{\mathbf{q}}_{\text{mom}}$ , and the wave number  $k = \omega/c$ . The wave number is connected to the spatial periodicity, the wavelength  $\lambda$ , by

$$k = 2\pi/\lambda. \quad (2.64)$$

The dispersion relation connects the wavelength and the wave frequency by the speed of sound  $c$  as

$$\lambda = \frac{c}{f}. \quad (2.65)$$

For a non-disperse wave, the group velocity  $c_g$  of the wave

$$c_g = \frac{d\omega}{dk} = c \quad (2.66)$$

and the phase velocity  $c_{\text{ph}}$  of the wave

$$c_{\text{ph}} = \frac{\omega}{k} = c \quad (2.67)$$

are the same as it results from the dispersion relation.

### 2.4.1 Compact acoustics

As mentioned above, the Helmholtz number characterizes compact acoustics. In the case of compact acoustics [51] with  $He \ll 1$ , the linear isentropic acoustic wave equation (2.62) is approximated by the Poisson problem,

$$-\nabla \cdot \nabla p^a = \frac{\partial q_{\text{mass}}}{\partial t} - \nabla \cdot \mathbf{q}_{\text{mom}}. \quad (2.68)$$

In comparison to the wave equation the information speed is infinite,  $c \rightarrow \infty$ . As a consequence, the infinite simulation domains must be modeled by a special boundary condition [52].

### 2.4.2 Acoustics and Fluid dynamics

According to the governing equations of fluid dynamics, acoustics is an integral part of fluid dynamics. The acoustic field requires a compressible media to be propagated. Acoustic quantities fluctuate and as a consequence the stationary component of an acoustic quantity is zero

$$\overline{\mathbf{u}^a} = \mathbf{0}. \quad (2.69)$$

The acoustic part of the velocity field  $\mathbf{u}^a$  is an irrotational field

$$\nabla \times \mathbf{u}^a = \mathbf{0}. \quad (2.70)$$

In terms of Helmholtz decomposition the velocity field  $\mathbf{u} \in L^2(\Omega)$  can be separated into a vortical part  $\mathbf{u}^v$  and a compressible part  $\mathbf{u}^a$

$$\mathbf{u} = \mathbf{u}^v + \mathbf{u}^a, \quad (2.71)$$

where the properties of the acoustic component are ( $\nabla \times \mathbf{u}^a = \mathbf{0}$ ,  $\overline{\mathbf{u}^a} = \mathbf{0}$ , and  $|\mathbf{u}^v| \gg |\mathbf{u}^a|$ ). This decomposition can be accomplished for arbitrary fields. A separation into a vortical part, being a synonym to mathematically incompressible flow, and a compressible acoustic part works for low Mach numbers, since all compressible effects are due to the acoustic mode. Naturally, an irrotational acoustic field gives rise to a Helmholtz decomposition of the compressible flow field into a scalar  $\phi^a$  and vector potential  $\mathbf{A}^v$

$$\mathbf{u} = \mathbf{u}^v + \mathbf{u}^a = \nabla \times \mathbf{A}^v + \nabla \phi^a. \quad (2.72)$$

By applying the (inverse) Helmholtz decomposition the irrotational and the solenoidal part of the flow field are determined.

## 2.5 Helmholtz decomposition

A fundamental theorem in fluid dynamics is the Helmholtz decomposition. Both, the Helmholtz decomposition and the inverse problem, are often denoted by the term Helmholtz decomposition, without making a difference. This work focuses on the inverse Helmholtz decomposition [53–57], obtaining the split from a given flow field into distinct parts. The decomposition isolates the irrotational (longitudinal process) and the solenoidal part (transverse process) of the flow field  $\mathbf{u}$  and allows to study the specific properties of incompressible flow and vortex dynamics on the relevant flow components, using potential representation and stream functions.

**Theorem 2.5.1** *Every vector field  $\mathbf{u}$ ,  $\mathcal{C}^1$  smooth, on a simply connected domain  $\Omega \subseteq \mathbb{R}^3$  (unbounded  $\Omega_+ = \mathbb{R}^3$ ) with the property  $\lim_{r \rightarrow \infty} \mathbf{u}(r)r = \mathbf{0}$  of a radial coordinate  $r = \|\mathbf{x}\|_2$  with  $\mathbf{x} \in \mathbb{R}^3$ , can be decomposed in  $L^2$ -orthogonal velocity field components*

$$\mathbf{u} = \mathbf{u}^v + \mathbf{u}^c = \nabla \times \mathbf{A}^v + \nabla \phi^c, \quad (2.73)$$

*with the vector potential  $\mathbf{A}^v$  satisfying  $\nabla \cdot \mathbf{A}^v = 0$  (toroidal component of the vector potential) and the scalar potential  $\phi^c$ .*

The proof of the Helmholtz theorem involves several steps. Starting from the vector identity

$$\mathbf{u} = \nabla \cdot \nabla \boldsymbol{\theta} = \nabla(\nabla \cdot \boldsymbol{\theta}) - \nabla \times \nabla \times \boldsymbol{\theta} = \nabla \phi^c + \nabla \times \mathbf{A}^v, \quad (2.74)$$

we use Green's function of the Laplace equation

$$-\nabla \cdot \nabla \frac{1}{4\pi \|\mathbf{x} - \mathbf{x}'\|_2} = \delta(\mathbf{x} - \mathbf{x}') \quad (2.75)$$

to solve the vector identity for  $\boldsymbol{\theta}$

$$\boldsymbol{\theta}(\mathbf{x}) = \int_{\Omega} \boldsymbol{\theta}(\mathbf{x}') \delta(\mathbf{x} - \mathbf{x}') d\mathbf{x}' = - \int_{\Omega} \frac{\mathbf{u}}{4\pi \|\mathbf{x} - \mathbf{x}'\|_2} d\mathbf{x}'. \quad (2.76)$$

The divergence of  $\boldsymbol{\theta}$  computes the inverse Helmholtz decomposition for  $\phi^c(\mathbf{x})$  on a bounded domain

$$\phi^c(\mathbf{x}) = \nabla \cdot \boldsymbol{\theta} = -\nabla \cdot \int_{\Omega} \frac{\mathbf{u}(\mathbf{x}')}{4\pi \|\mathbf{x} - \mathbf{x}'\|_2} d\mathbf{x}' \quad (2.77)$$

$$= - \int_{\Omega} \mathbf{u} \cdot \nabla \frac{1}{4\pi \|\mathbf{x} - \mathbf{x}'\|_2} d\mathbf{x}' \quad (2.78)$$

$$= \int_{\Omega} \mathbf{u} \cdot \nabla' \frac{1}{4\pi \|\mathbf{x} - \mathbf{x}'\|_2} d\mathbf{x}' \quad (2.79)$$

$$= - \int_{\Omega} \frac{\nabla' \cdot \mathbf{u}}{4\pi \|\mathbf{x} - \mathbf{x}'\|_2} d\mathbf{x}' + \int_{\Omega} \nabla' \cdot \frac{\mathbf{u}}{4\pi \|\mathbf{x} - \mathbf{x}'\|_2} d\mathbf{x}' \quad (2.80)$$

$$= - \int_{\Omega} \frac{\nabla' \cdot \mathbf{u}}{4\pi \|\mathbf{x} - \mathbf{x}'\|_2} d\mathbf{x}' + \int_{\partial\Omega} \mathbf{n} \cdot \frac{\mathbf{u}}{4\pi \|\mathbf{x} - \mathbf{x}'\|_2} ds'. \quad (2.81)$$

Analog to the scalar potential the vector potential is solved

$$\mathbf{A}^v(\mathbf{x}) = \int_{\Omega} \frac{\nabla \times \mathbf{u}}{4\pi \|\mathbf{x} - \mathbf{x}'\|_2} d\mathbf{x}' - \int_{\partial\Omega} \frac{\mathbf{n} \times \mathbf{u}}{4\pi \|\mathbf{x} - \mathbf{x}'\|_2} ds'. \quad (2.82)$$

The calculation of the vector potential implies the gauge condition  $\nabla \cdot \mathbf{A}^v = \nabla \cdot \nabla \times \boldsymbol{\theta} = 0$ . For an unbounded domain the surface integral vanishes as long as the field decays towards zero at infinity. Alternatively, the scalar potential can be obtained by directly applying Green's function

$$\phi^c(\mathbf{x}) = \int_{\Omega} \phi^c(\mathbf{x}') \delta(\mathbf{x} - \mathbf{x}') d\mathbf{x}' = -\nabla \cdot \int_{\Omega} \frac{\mathbf{u}(\mathbf{x}')}{4\pi \|\mathbf{x} - \mathbf{x}'\|_2} d\mathbf{x}' \quad (2.83)$$

$$= - \int_{\Omega} \frac{\nabla' \cdot \mathbf{u}}{4\pi \|\mathbf{x} - \mathbf{x}'\|_2} d\mathbf{x}' + \int_{\partial\Omega} \mathbf{n} \cdot \frac{\mathbf{u}}{4\pi \|\mathbf{x} - \mathbf{x}'\|_2} ds' \quad (2.84)$$

and the vector potential (using the gauge condition)

$$\mathbf{A}^v(\mathbf{x}) = \int_{\Omega} \mathbf{A}^v(\mathbf{x}') \delta(\mathbf{x} - \mathbf{x}') d\mathbf{x}' = -\nabla \times \int_{\Omega} \frac{\mathbf{u}(\mathbf{x}')}{4\pi \|\mathbf{x} - \mathbf{x}'\|_2} d\mathbf{x}' \quad (2.85)$$

$$= \int_{\Omega} \frac{\nabla \times \mathbf{u}}{4\pi \|\mathbf{x} - \mathbf{x}'\|_2} d\mathbf{x}' - \int_{\partial\Omega} \frac{\mathbf{n} \times \mathbf{u}}{4\pi \|\mathbf{x} - \mathbf{x}'\|_2} ds'. \quad (2.86)$$

The decomposition considers both bounded and unbounded domains. For bounded domains, the boundary integral represents the interface condition to the exterior and ensures uniqueness.

The origin of Helmholtz's decomposition reaches far into the history of science [58] and is utilized by many disciplines such as electrodynamics [59], fluid dynamics [46] and computer visualization. Based on fluid dynamics, the motion of a continuum point has been proven to be a combination of three exclusive shapes [46] (see Fig. 2.2).



- (a) An isotropic expansion proportional to the volumetric rate of expansion  $\nabla \cdot \mathbf{u}$ . This field component can be described by a scalar potential associated with the compressibility of the fluid.
- (b) Irrotational deformation without volume change. The classical theory of potential flow equations describes this velocity field and is well known in fluid dynamics. This flow component is both, divergence-free and curl-free.
- (c) A rigid-body rotation at an angular velocity of  $\frac{1}{2}\nabla \times \mathbf{u}$ . Vortical or incompressible flow structures are described by the vorticity and its dynamics.

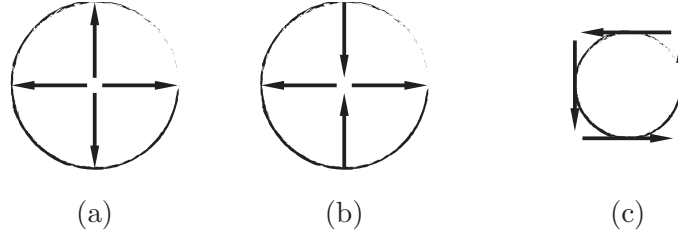


Figure 2.2: Illustration of the deformation shapes of a continuum point. (a) isotropic expansion, (b) irrotational deformation without volume change, and (c) rigid-body rotation.

A curl-free representation of a flow field includes mode (a) and (b). Respectively a divergence free field includes both modes (c) and (b). This effect seems to be difficult to understand, thus a different explanation of (b) is that this deformation is the homogeneous solution of both partial differential equations, solving mode (a) or (c). The extension of the Helmholtz decomposition on homologically trivial domains (domains with holes) is served by a generalization, with suited boundary treatment (see Chap. 4). A further generalization to manifold is the Helmholtz-Hodge decomposition.

### 2.5.1 Sequence of temporal images

Helmholtz decomposition transforms only the spatial representation of the velocity field; the connection between the time steps is guided by the compressible velocity data. The velocity field  $\mathbf{u}(\mathbf{x}, t_i)$  is a sorted sequence of flow snapshots, with an intrinsic transformation from one time index  $t_i$  to another  $t_{i+1}$ . Time  $t_i$  is a parameter associated with the state of the velocity field that represents the physical evolution. Therefore, the time invariant Helmholtz decomposition is interpreted as a filter at a frozen time  $t_i$ .

### 2.5.2 Decompose the fluctuating component

A separation of the overall flow field into a mean and a fluctuating field

$$\mathbf{u} = \bar{\mathbf{u}} + \mathbf{u}' \quad (2.87)$$

can be beneficial with respect to the decomposition and the boundary treatment. For fields that do not vanish at the boundaries, the assumptions and requirements enhance the computation with further difficulties to ensure an orthogonal decomposition pair. Therefore, it might be promising to assume that the compressible field is a fluctuating field, at least at the boundaries

$$\mathbf{u}^c|_{\partial\Omega} = \mathbf{u}'|_{\partial\Omega}. \quad (2.88)$$

This implies that all vortical perturbations are fully decayed towards the boundaries. Assuming this, a promising substitution for the vortical solution at the boundary can be formulated

$$\mathbf{u}^v|_{\partial\Omega} = \bar{\mathbf{u}}|_{\partial\Omega}. \quad (2.89)$$

With this boundary conditions we have a well defined Helmholtz decomposition. De Roeck [43] proposed a decomposition of the fluctuating velocity field. If the flow disturbances are bounded within the domain  $\Omega_F$ , we may prolongate the domain virtually towards infinity and use a well defined Helmholtz decomposition of the fluctuating field  $\mathbf{u}'$ .

### 2.5.3 Helmholtz decomposition and conservation laws

A frequently asked question on the validity of Helmholtz decomposition is, if the decomposition obeys the conservation laws. Statements like the colorful nature of fluid dynamics are not subject to such a trivial decomposition and one is misled to think that all vortical structures like grained turbulence can be captured. This physical and emotional myth ignores the mathematical capability of the Helmholtz decomposition and mixes facts. Helmholtz decomposition is not capable of computing fluid dynamics, but it is capable of separating it into distinct vortical and compressible subparts.

The terminology related to Helmholtz decomposition confuses physicists and mathematicians and corrupts their dialog. Stating the commons and the differences, mathematically incompressible means the vortical part of a compressible flow in physics. Mathematically incompressible does not necessarily mean physically an incompressible flow that obeys the equations of a physically incompressible flow and is consequently a result of an incompressible flow simulation. Although a terminological difference could imply ambiguity, the Helmholtz decomposition derives indeed a possible incompressible flow system based upon a compressible flow simulation.

The vortical part satisfies per definition the divergence free condition of an incompressible flow. By inserting this vortical flow into the continuity equation one obtains a condition for the vortical density, which is not necessarily constant (as assumed for a physical incompressible flow). The substantial derivative of the density being zero

$$\frac{\partial \rho^v}{\partial t} + \mathbf{u}^v \cdot \nabla(\rho^v) = 0 \quad (2.90)$$

means that the density of a particle remains constant over time. That density requirement is exactly physically incompressible. A decomposed vortical flow is directly connected to a vortical density field that acts like an incompressible one. Computational algorithms solving incompressible flow rely on Helmholtz decomposition to construct the divergence free flow field.

So far, the vortical flow field and the vortical density field are incompressible-like fields. The third state of an incompressible flow configuration is the incompressible pressure, which is extracted by the momentum equation for the reverse conclusion drawn here. Navier-Stokes equation (2.19) provides the missing link to the vortical pressure distribution  $p^v$  for the decomposed vortical field

$$\nabla p^v = -\rho^v \frac{\partial}{\partial t}(\mathbf{u}^v) - \rho^v \nabla \cdot (\mathbf{u}^v \mathbf{u}^v) + \mu \Delta \mathbf{u}^v + \mathbf{f}. \quad (2.91)$$

Summing up, the vortical flow part, computed by Helmholtz decomposition, is incompressible-like in both mathematical and physical terms; the components are therefore labeled by a superscript (v).

## 2.6 Aeroacoustic models

This section gives a comprehensive overview of research in the field of aeroacoustic at low Mach numbers. Zheng *et al.* [60] categorize aeroacoustic methods in three groups: general acoustic analogies, direct numerical simulation and acoustic equations based on splitting/filtering techniques. Motivated by this categorization, we start historically from acoustic analogies, go over to direct simulation of flow and acoustic, and finally discuss perturbation equations.

### 2.6.1 General acoustic analogies

The first proposed acoustic analogy by Lighthill [6, 7] transforms the compressible flow equations into an exact inhomogeneous wave equation, without any assumptions to boundaries and the equations. Lighthill's equation describes a general wave equation in terms of the fluctuating density  $\rho'$ , which reads as follows

$$\frac{\partial^2}{\partial t^2} \rho' - c^2 \nabla \cdot \nabla \rho' = \nabla \cdot \nabla \cdot \mathbb{T} . \quad (2.92)$$

Lighthill's tensor  $\mathbb{T}$  represents all remaining nonlinear terms when rearranging the mass and momentum equation:

$$\mathbb{T} = \rho \mathbf{u} \mathbf{u} + \mathbb{S} + p' \mathbb{I} - c^2 \rho' \mathbb{I} . \quad (2.93)$$

This source term incorporates sound generation, refraction, convection with the flow, and dissipation by the viscosity. The underlying fluid is stated to be a uniform acoustic medium at rest. During the derivation the variables are reduced and to be computational efficient and meaningful this implicit formulation requires further manipulation. In computational aeroacoustics, Lighthill's wave equation in combination with a hybrid computational procedure is widely used for subsonic flows and an approximate Lighthill source term<sup>1</sup>

$$\mathbb{T} \approx \rho \mathbf{u} \mathbf{u} . \quad (2.94)$$

The approximation error is proportional to  $M^2$ . As prominent at this time, Lighthill utilizes Green's function of the free field radiation to solve the wave equation. In doing so, Lighthill implicitly neglected resonators and other bodies near sources, hence diffraction, scattering, absorption and reflection by solid boundaries. Curle [8] investigated the effects of static surfaces on the integral solution in terms of Green's function on Lighthill's theory. Static surfaces are equivalent to a surface dipole distribution in the resulting radiated field. Difficulties in the acoustic prediction arise if the flow is incompressible and the surface not acoustically compact [61]. Ffowcs Williams and Hawking [9] generalized Curle's integral representation towards accounting for the effects of arbitrary moving bodies in the source domain, extending Kirchhoff's formula derived in [10]. The extension uses the known facts of distribution theory. Finally, the wave equation is extended to

$$\begin{aligned} & \frac{1}{c^2} \frac{\partial^2}{\partial t^2} p' - \nabla \cdot \nabla p' = \\ & \nabla \cdot \nabla \cdot \mathbb{T} + \nabla \cdot ((\mathbb{S} + p) \cdot \delta(f) \nabla f) + \frac{\partial}{\partial t} (\rho \mathbf{u} \delta(f) \nabla f) . \end{aligned} \quad (2.95)$$

<sup>1</sup> The approximation involves three assumptions

- For high Reynolds numbers we can neglect the stress tensor  $\mathbb{S}$ , since  $\rho \mathbf{u} \mathbf{u} \gg \mathbb{S}$ .
- An isentropic state relates the pressure perturbation to the density perturbation,  $p' = c^2 \rho'$ . Simulating combustion noise the pressure and the density are related by the enthalpy of the heat source,  $p' = c^2 \rho' + \rho_0 (\kappa - 1) h'$ .
- Assuming low Mach numbers the density is close to the density of the resting media,  $\rho(\mathbf{x}) = \rho_0$ .

These approximations reduce the analogy to self-noise and shear-noise, but neglect refraction interactions of the acoustic components with the mean flow. In particular, these refraction interactions should be considered by the wave operator and not the source terms (see Chap. 3).

Here,  $\delta$  denotes the delta distribution and  $f$  is a distribution describing the surface of bodies. In the integral formulation, the first additional term results in Curle's dipole radiation and the second additional one is Ffowcs Williams and Hawking's monopole radiation due to the motion of the surfaces. The application of distribution theory in aeroacoustic is intensively discussed by Farassat [62], and its application to Kirchhoff's and Ffowcs Williams and Hawkings formula is revisited in [63]. Ffowcs Williams and Hawking's integral formulation relies on a compressible flow simulation. Only if the sources are compact an incompressible flow solution can be utilized to solve the integral sufficiently well. Further simplifications are possible, if the integration surface of the integral contains all volume sources, the volume integral vanishes. However, the acoustic waves must be propagated at least to the integration surface.

Ribner [11] and Powell [12] based their theory on comparing a slightly compressible flow with an incompressible flow, where the vorticity  $\boldsymbol{\omega}$  plays a major role in the derivation of the acoustic propagation. After applying vector calculus theorems the nonlinear term of the Lighthill tensor is formulated by

$$\rho \nabla \cdot (\mathbf{u}\mathbf{u}) = \rho (\boldsymbol{\omega} \times \mathbf{u}) + \rho \nabla \left( \frac{\mathbf{u} \cdot \mathbf{u}}{2} \right), \quad (2.96)$$

where  $\boldsymbol{\omega} = \nabla \times \mathbf{u}$  describes the vorticity of the fluid. Howe [13] derived that the main sources for  $\text{Ma} \ll 1$  and  $\text{Re} \gg 1$  are almost entirely formed by the Lamb vector  $\mathbf{L} = \boldsymbol{\omega} \times \mathbf{u}$ . Thus, vortical structures generate the major acoustic far-field at low Mach numbers. The first term of (2.96) is known as the Lamb vector, where the acoustic far field of this component  $p_1$  scales as

$$p_1 \sim \frac{L}{|x|} \rho_0 U^2 \text{Ma}^2, \quad (2.97)$$

and the second term radiates  $p_2$  into the far field

$$p_2 \sim \frac{L}{|x|} \rho_0 U^2 \text{Ma}^4 + \frac{L}{|x|} \rho_0 u^2 \text{Ma}^2 \frac{1}{\text{Re}}. \quad (2.98)$$

Here,  $L$  denotes a spatial length scale and  $U$  a characteristic flow velocity. For uniform flow in the far field, Lighthill's wave equations and the integral derivatives compute the directivity pattern of the noise efficiently. This assumes acoustic compact sources or a bounded source region. Acoustically compact means that the size of the flow sources contributing to the acoustic are small compared to the generated wavelength. This requirement is inherently fulfilled for low Mach number applications. A dimensional analysis shows that vorticities generate acoustic waves with an order of magnitude  $\text{Ma}^{-1}$  larger length scale [31]. Mathematically speaking, the Helmholtz number  $\text{He} = kL = \text{StMa} \ll 1$  is small. However, a specific source distribution may exceed this limit. A main problem of the acoustic analogies arises since the sources originally depend on the solution of the wave equation and hence back coupling must be modeled somehow or the waves are already incorporated in the aeroacoustic sources. The application of aeroacoustic analogies in a hybrid strategy with compressible sources is not free from ambiguity, which is discussed later.

Howe [13], Möhring [14], and Doak [15] carried out further investigations on vortex sound. Theory of vortex sound focus on vorticity and entropy inhomogeneities as dominant sources of sound. The theory assumes an irrotational mean flow specified by a velocity potential. Howe started his derivation from Crocco's form of the momentum equation, which includes the total stagnating enthalpy  $H = h + \mathbf{u}^2/2$ ,

$$H = \int \frac{dp}{\rho} + \frac{1}{2} \mathbf{u}^2, \quad (2.99)$$

as primary variable of the wave equation. After applying reformulations, Howe arrived at the well known

vortex sound equation for homentropic flow (for simplicity excluding entropy and thermal effects),

$$\frac{d}{dt} \frac{1}{c^2} \frac{d}{dt} H + \frac{1}{c^2} \frac{d\mathbf{u}}{dt} \cdot \nabla H - \Delta H = \nabla \cdot (\boldsymbol{\omega} \times \mathbf{u}) - \frac{1}{c^2} \frac{d\mathbf{u}}{dt} \cdot (\boldsymbol{\omega} \times \mathbf{u}) \quad \text{with} \quad \frac{d}{dt} = \frac{\partial}{\partial t} + \mathbf{u} \cdot \nabla. \quad (2.100)$$

Möhring [14, 64] derived a similar acoustic analogy that claims to be more general<sup>2</sup>. Finally, the nonlinear wave equation is denoted as Möhring's acoustic analogy (for simplicity excluding entropy and thermal effects),

$$\frac{d}{dt} \frac{1}{c^2} \frac{d}{dt} H - \frac{1}{\rho} \nabla \cdot \rho \nabla H = \frac{1}{\rho} \nabla \cdot (\rho \boldsymbol{\omega} \times \mathbf{u}) \quad \text{with} \quad \frac{d}{dt} = \frac{\partial}{\partial t} + \mathbf{u} \cdot \nabla. \quad (2.101)$$

For high Reynolds numbers, low Mach numbers and homentropic flows Howe's, Möhring's and Doak's convective wave equations converge to each other. Linearization yields a convenient convective wave equation for low Mach numbers

$$\frac{1}{c^2} \frac{d^2}{dt^2} H - \nabla \cdot \nabla H = \nabla \cdot (\boldsymbol{\omega} \times \mathbf{u}) \quad \text{with} \quad \frac{d}{dt^2} = \frac{\partial}{\partial t} + \mathbf{u}^{\text{ic}} \cdot \nabla. \quad (2.102)$$

This vortex sound sources are more localized than Lighthill's sources and reduce the relevant computation source domain [57].

Recently, Goldstein [16] proposed his generalized acoustic analogy, which shows that the equations of fluid dynamics can be rewritten as a set of linearized equations around a base flow. He derived several variants of analogies, considering a non-radiating as well as a radiating base flow. In the case of non-radiating unsteady base flow (e.g. incompressible flow), the total derivative of the pressure is the main source of this acoustic analogy.

## 2.6.2 Direct simulation of flow and acoustic

The direct computation of flows and acoustics (DNX) solves the compressible Navier-Stokes equations and gains the united field of flow and acoustics. Compared to acoustic analogies this method gains generality since model restriction such as a low Mach number, a high Reynolds number, and compactness of the source are no longer necessary conditions for valid results. Fewer empirical modeling uncertainties are made when computing flows and acoustics with a single simulation. However, the required resources are comparably high in the range of low Mach numbers. In this regime small vortices excite acoustic waves with large wave length, demanding the extension of the computational flow domain compared to an incompressible flow simulation. A major drawback of this method is to separate the acoustic and the fluid dynamic pressure components accurately. In general, the acoustic quantities are orders of magnitude lower than the fluid dynamic ones. At low Mach numbers acoustic waves propagate over long distances and require a conservative, non-dissipative numerical scheme. Thus, this method is preferably used in the mid to high Mach number regime.

Freund *et al.* [17] simulated a turbulent jet and its acoustic near field by means of the compressible fluid dynamic equations. The simulation was carried out at Mach 1.92, with a special boundary layer to minimize acoustic reflections [27]. Outside the source domain a linear wave equation extrapolates the acoustic into the far field. Gloerfelt [66] compared two different numerical methods to compute the noise of a 2D cavity at Mach 0.7. Both Ffowcs Williams and Hawkings method and the direct computation of noise by the compressible fluid dynamic equations show good results. They stated that the main drawback of the direct computation is that the extrapolation to the far field is computationally expensive. Tam

<sup>2</sup> "Howe's calculations are restricted to the lowest order in Mach number. The same is true for many other applications of Eq. (11). One of the reasons for this restriction is the lack of a reciprocity relation for Eq. (11) for higher Mach numbers. Equation (11) admits such a relation only to first order in Mach number or, what amounts to the same thing, it is not self-adjoint. Recently Möhring (1979) found a modification of Eq. (11) that is self-adjoint for  $B$  for arbitrary functions  $c$ ,  $\mathbf{u}$ , and  $p$ , and therefore admits a reciprocity relation for all Mach numbers." [65]

and Dong's [23] radiation boundary condition is implemented to account for the open domain. To reduce computational burden Schwartzkopff and Munz [40, 41] propose a domain decomposition method for direct simulation of flow and acoustics. In regions where nonlinear effects are negligible, the linearized Euler equations are applied to propagate waves. They put special emphasis on making the transition from the Euler equation to the linearized Euler equation non reflective. Sandberg *et al.* [67] performed a direct simulation of the trailing edge noise in the mid Mach number range.

In the recent years, direct simulations of flow and acoustics treat feedback mechanisms in the low Mach number range. Frank and Munz [68] simulated the acoustic feedback mechanism of a car side mirror utilizing a higher order discontinuous Galerkin method to solve the fluid dynamic equations.

### Lattice Boltzmann Approach

In the recent years, the Lattice Boltzmann approach [69, 70] has gained popularity in solving the flow and acoustic field directly. Applications of this method in acoustics reach from airframe noise [18], to acoustic simulations of landing gears [19], and industrial applications [20]. The method is capable of describing unsteady, compressible, turbulent low Mach number flows in an efficient way and the algorithm is intrinsically parallelizable. Every Lattice Boltzmann method [71] is based on the Boltzmann transport equation

$$\frac{\partial b}{\partial t} + \mathbf{u} \cdot \nabla b = \mathcal{F} , \quad (2.103)$$

where  $b$  is the particle distribution function,  $\mathbf{u}$  is the particle velocity, and  $\mathcal{F}$  is the collision operator. The Navier Stokes equation can be recovered by this method using a proper choice of the collision operators. In 2D a fluid particle, one node of the lattice, has 9 degrees of freedom. Based on the Maxwell-Boltzmann particle distribution and the moments of this distribution, the macroscopic density, velocity, and energy of the fluid are computed. The (macroscopic) fluid density  $\rho$  is obtained by summing up the particle distribution functions

$$\rho = \sum_{i=1}^9 b_i \quad (2.104)$$

and the overall (macroscopic) velocity  $\mathbf{u}$  is computed by the sum of the particle distribution weighted by the microscopic velocities  $\mathbf{e}_i$

$$\mathbf{u} = \frac{1}{\rho} \sum_{i=1}^9 c b_i \mathbf{e}_i . \quad (2.105)$$

### Boundary conditions

A general drawback of DNX is the lack of acoustic boundary treatment that starts simply with the following uncertainty: "What is acoustics in a DNX?"

In the case of linear partial differential equations, far field, radiation or absorbing boundary conditions were developed (see [72]). Colonius [73] reviews different open boundary techniques for compressible flow simulations. The methods are categorized in linearized boundary conditions (far-field approximations), nonlinear characteristic boundaries and absorbing layers. A general technique is to linearize the equations and treat the boundaries of the nonlinear system with the characteristic boundary of the linearized system [23, 24]. Thompson [25, 26] derived open boundary conditions for the linear hyperbolic equations based on a 1D open domain boundary

$$\left( \frac{\partial}{\partial t} \pm c \frac{\partial}{\partial x} \right) p = 0 . \quad (2.106)$$

However, the boundaries have to be improved to find suitable boundary conditions for the nonlinear equations. Freund [27] developed a boundary layer technique for the compressible fluid dynamic equations

that drives the solution to a quiescent target state. Freund's conclusion states that the reflections are significantly reduced compared to the local boundary condition of Thompson. Tam *et al.* [24] developed a perfectly matching layer (PML) formulation for the linearized Euler equations. The stabilized PML performs well as absorbing boundary condition. However, in a confined flow the group and the phase velocity of the wave may have opposite sign, where the PML will not work well.

Impedance boundaries are available for linearized Euler equation [74] in the frequency domain or discrete time domain, where the convolution integral is z-transformed [75]. For the full nonlinear Navier-Stokes equations impedance boundaries are challenging. Furthermore, the impedance boundary of a material is known to be incident angle depending. In the context of DNX, the modeling of acoustic surfaces is limited to acoustically hard walls or full resolution of the absorbing material [76], e.g. micro perforated plates or fibrous absorbers. Typically, acoustic simulations capture these damping effects, by relatively simple and accurate models, e.g. complex fluid model. These models are validated by standard measurement procedures and are tuned towards the experimental data. DNX focus on the details of modeling nonlinear fluid dynamic effects on the sound propagation with reduced capabilities in modeling the enclosed body surfaces. In this case a design engineer has to judge the importance of the distinct effects with respect to the design objectives during product development.

After a valid DNX simulation, filtering methods are applied to determine the acoustic part of the simulation. A basic approach filters the acoustic with respect to the wavenumber. Freund [21] applied the wavenumber decomposition to a turbulent jet at Mach 0.9. The analysis was performed in one spatial and the temporal coordinate, to extract the aerodynamic part.

Goldstein [22] states the desired properties of a filtered variable  $g$ , such that no radiating components are present. The Fourier transformation of the filtered variable is defined by

$$\hat{g} = \int \int g e^{-(\omega t - \mathbf{k} \cdot \mathbf{x})} d^3 \mathbf{x} dt . \quad (2.107)$$

For an unbounded domain, the relation for a non-radiating filter in the Fourier space is

$$\hat{g}^{\text{no}} = 0, \quad \text{if} \quad |\mathbf{k}| = \omega/c . \quad (2.108)$$

This condition is the dispersion relation of acoustic waves in a quiescent medium. In general, two possibilities are available to realize the filtering. The first filtering technique is a local approach applying the corresponding differential operator to the filtered variable. In the case of an unbounded quiescent medium, the d'Alembert operator is

$$\square := \frac{1}{c^2} \frac{\partial^2}{\partial t^2} - \Delta . \quad (2.109)$$

This property ensures that if  $g = (\frac{1}{c^2} \frac{\partial^2}{\partial t^2} - \Delta) g^{\text{no}}$ , the condition (2.108) is satisfied. This filter can be used directly in space-time to filter out radiating components. A second filtering technique is based on a convolution filter equivalent to a window function  $W$  in the Fourier space.

$$\hat{g}^{\text{no}} = W \hat{g} \quad (2.110)$$

The main challenge of this method is to define an accurate window for the investigated problem. A perfect window has the following characteristic

$$\begin{aligned} W(\omega, \mathbf{k}) &= 0 & \text{when} & \quad |\mathbf{k}| = \omega/c \\ W(\omega, \mathbf{k}) &= 1 & \text{otherwise} . \end{aligned} \quad (2.111)$$

The convolution targets the acoustic components. Practical realizations of such filters are problem dependent and challenging. A more convenient realization targets the main flow components instead of filtering the acoustic ones. Sinayoko *et al.* [77] applied this filtering techniques to a parallel shear layer flow with promising results.

### 2.6.3 Perturbation equations

The third main approach, computing aeroacoustics, are perturbation equations that follow a systematic separation of the fluid dynamic variables. A general flow field is decomposed into a fluid dynamic part and an acoustic part. Klainerman and Majda [78] showed in the limit of low Mach numbers that acoustics is the perturbation of the incompressible solution. The fundamental bases are mass, momentum and energy balance and the constitutive equations relating pressure-density and stress-velocity. As for aeroacoustic analogies, the computational workflow of perturbation equation follows the hybrid aeroacoustic method that separates flow and acoustic simulation.

This promising idea of deriving perturbation equations extends the field decomposition technique that is used to derive the linearized Euler equation (LEE). Before we discuss specific perturbation equations, the LEE are derived. Starting from the Euler equations

$$\frac{d\rho}{dt} + \rho \nabla \cdot \mathbf{u} = 0 \quad (2.112)$$

$$\rho \frac{d\mathbf{u}}{dt} + \nabla p = \mathbf{0} \quad (2.113)$$

$$\rho \frac{de}{dt} + p \nabla \cdot \mathbf{u} = \nabla \cdot (k \nabla T) \quad (2.114)$$

that are the high Reynolds number limit of the compressible fluid dynamic equations, where viscous effects are neglected,  $e$  denotes the total specific energy,  $k$  the conductivity of Fourier's law and  $T$  the temperature. The energy equation of the Euler equation (2.114) is written as

$$\frac{dp}{dt} + \kappa p \nabla \cdot \mathbf{u} = (\kappa - 1) \nabla \cdot (k \nabla T), \quad (2.115)$$

when dealing with acoustics and assuming an ideal gas. These equations describe an inviscid fluid, where no boundary effects are essential and may be used for nonlinear wave propagation at high Mach numbers with these underlying assumptions [79]. Based on the Euler equations the LEE are derived. The field variables  $(\rho, \mathbf{u}, p)$  are decomposed into a temporal mean component  $\overline{(\cdot)}$  and a fluctuating component  $(\cdot)'$  – perturbation. Finally, the LEE

$$\frac{\partial \rho'}{\partial t} + \bar{\mathbf{u}} \cdot \nabla \rho' + \mathbf{u}' \cdot \nabla \bar{\rho} + \bar{\rho} \nabla \cdot \mathbf{u}' + \rho' \nabla \cdot \bar{\mathbf{u}} = 0 \quad (2.116)$$

$$\frac{\partial \mathbf{u}'}{\partial t} + \bar{\mathbf{u}} \cdot \nabla \mathbf{u}' + \mathbf{u}' \cdot \nabla \bar{\mathbf{u}} + \frac{1}{\bar{\rho}} \nabla p' - \frac{1}{\bar{\rho}^2} \nabla (p' \bar{\rho}) = \mathbf{0} \quad (2.117)$$

$$\frac{\partial p'}{\partial t} + \bar{\mathbf{u}} \cdot \nabla p' + \mathbf{u}' \cdot \nabla \bar{p} + \kappa \bar{p} \nabla \cdot \mathbf{u}' + \kappa p' \nabla \cdot \bar{\mathbf{u}} = 0 \quad (2.118)$$

are obtained in their general form, neglecting conductivity. Bailly *et al.* [28, 29] developed special aeroacoustic LEE forced by aeroacoustic source terms on the momentum equation. The dominant source term is of second order

$$\nabla \cdot (\rho \mathbf{u}' \mathbf{u}') - \overline{\nabla \cdot (\rho \mathbf{u}' \mathbf{u}')} . \quad (2.119)$$

Since then, the LEE have been modified to guarantee pure acoustics propagation [30].

The first idea to introduce a pressure reformulation of Lighthill's dominant source term at low Mach



numbers for an incompressible flow was proposed by Meecham and Ford [80]. Ribner [11] formulated his dilatation equation that the primary pressure variable of Lighthill's analogy is decomposed in a pseudo and an acoustic part  $p' = p^0 + p^a$ . This decomposition leads to the following known formulations of Lighthill's analogy based on an incompressible estimation of Lighthill's tensor,

$$\frac{1}{c^2} \frac{\partial^2}{\partial t^2} p' - \nabla \cdot \nabla p' = \nabla \cdot \nabla p^{\text{ic}} . \quad (2.120)$$

Furthermore, the acoustic part can be obtained by

$$\frac{1}{c^2} \frac{\partial^2}{\partial t^2} p^a - \nabla \cdot \nabla p^a = \frac{1}{c^2} \frac{\partial^2}{\partial t^2} p^{\text{ic}} . \quad (2.121)$$

Additionally, Ribner extended the wave operator to uniform mean flow, without any physical justification. Perturbed convective wave equation (PCWE) [39], follows right after Ribner's extension to mean flow convection, by inserting the definition of the acoustic potential into the acoustic pressure. The derivation of PCWE is an exact reformulation of the APE 2 [31], in contrast to Ribner.

Hardin and Pope [32] formulated their viscous/acoustic splitting technique expansion about the incompressible flow (EIF), where they introduced a density correction  $\rho_1$

$$\begin{aligned} \mathbf{u} &= \mathbf{u}^{\text{ic}} + \mathbf{u}' \\ p &= p^{\text{ic}} + p' \\ \rho &= \rho^{\text{ic}} + \rho_1 + \rho' . \end{aligned} \quad (2.122)$$

The set of variables  $(\mathbf{u}, p, \rho)$  is the compressible solution,  $(\mathbf{u}^{\text{ic}}, p^{\text{ic}}, \rho^{\text{ic}})$  the incompressible solution and the primed values are labeled as perturbations of the system. Inserting this into the mass balance and momentum balance and utilizing the state equation  $p'(\rho')$  yields a closed system of equation. This density correction is not an acoustic variable, but needs to be taken into account such that the resulting field is isentropic [81].

All perturbations (compressible part of a low Mach number flow) are computed in a second separate acoustic simulation. In terms of Lighthill's approach, this density correction modifies the source term of Lighthill's equation and satisfies an isentropic perturbation density, by solving

$$\frac{\partial^2}{\partial t^2} \rho' - c^2 \nabla \cdot \nabla \rho' = \nabla \cdot \nabla \cdot \mathbb{T} - \frac{\partial^2}{\partial t^2} \rho_1 - c^2 \nabla \cdot \nabla \rho_1 . \quad (2.123)$$

The method relies on an incompressible flow simulation to extract the sources. Perturbation variables converge to the acoustic perturbations in the far field. In the near field Hardin and Pope stated that the primed variables are the difference between the compressible and the incompressible solution of the flow field. This is validated by the pulsating sphere and the flow over a rectangular cavity. Inconsistency critics arose on the EIF formulation of Hardin and Pope [33]. Shen and Sørensen [33, 34] modified this method to account for non-isentropic flows. Their method is validated against the pulsating sphere and the circular cylinder. Slimon *et al.* [35] proposed an aerodynamic/acoustic splitting method, which is cost-effective and is validated for non-compact source regions. This further development of the expansion about the incompressible limit method is derived systematically via a Mach number expansion.

As noticed by Seo and Moon [36] the viscous/acoustic formulation neglects coupling effects, which play a role in the near-field. Thus, they proposed their version of perturbation equations named perturbed compressible equations (PCE) for handling near-field coupling effects. They decompose the flow field into

an incompressible and a compressible part

$$\begin{aligned}\mathbf{u} &= \mathbf{u}^{\text{ic}} + \mathbf{u}' \\ p &= p^{\text{ic}} + p' \\ \rho &= \rho^{\text{ic}} + \rho' .\end{aligned}\tag{2.124}$$

The incompressible variables  $(\mathbf{u}^{\text{ic}}, p^{\text{ic}}, \rho^{\text{ic}})$  represent the unsteady viscous flow and the primed variables the difference between the compressible and incompressible field. In the far-field the compressible perturbed quantities coincide with the acoustic part (irrotational in the far-field  $\nabla \times \mathbf{u}' = \mathbf{0}$ ), whereas in the near-field more complicated phenomena are described. Near field coupling effects are investigated in terms of the perturbed vorticity  $\boldsymbol{\omega}'$  equation of the flow

$$\boldsymbol{\omega} = \boldsymbol{\omega}^{\text{ic}} + \boldsymbol{\omega}' .\tag{2.125}$$

They derived the PCE by subtracting the incompressible flow dynamics equations from their compressible counterpart and obtained their formulation in the nonconservative form

$$\frac{\partial \rho'}{\partial t} + \mathbf{u} \cdot \nabla \rho' + \rho \nabla \cdot \mathbf{u}' = 0\tag{2.126}$$

$$\frac{\partial \mathbf{u}'}{\partial t} + \mathbf{u} \cdot \nabla \mathbf{u}' + \frac{1}{\rho} \nabla p' + \mathbf{u}' \cdot \nabla \mathbf{u}^{\text{ic}} + \frac{\rho'}{\rho} \frac{d\mathbf{u}^{\text{ic}}}{dt} = \frac{1}{\rho} \nabla \cdot \mathbb{S}'\tag{2.127}$$

$$\begin{aligned}\frac{\partial p'}{\partial t} + \mathbf{u} \cdot \nabla p' + \kappa p \nabla \cdot \mathbf{u}' + \mathbf{u}' \cdot \nabla p^{\text{ic}} &= -\frac{dp^{\text{ic}}}{dt} \\ &+ (\kappa - 1) (\phi - \nabla \cdot \mathbf{q}_T) ,\end{aligned}\tag{2.128}$$

where  $\frac{d}{dt} := \frac{\partial}{\partial t} + \mathbf{u}^{\text{ic}} \cdot \nabla(\cdot)$  and the incompressible pressure must be rescaled such that  $p_{\infty}^{\text{ic}} = \rho^{\text{ic}} c^2 / \kappa$ .  $\phi$  is the thermal viscous dissipation term and  $\mathbf{q}_T$  the heat flux vector. This method was applied to human phonation simulations [37]. At low Mach numbers the influence of the perturbed vorticity on the sound field is negligible and causes a grid dependent solution. Thus, Seo and Moon [38] reformulated their nonlinear PCE to a grid independent, perturbed vorticity suppressing linear formulation. By neglecting nonlinear terms and using vector identities to reformulate vortical structures the linear PCE can be written as

$$\frac{\partial \rho'}{\partial t} + \mathbf{u}^{\text{ic}} \cdot \nabla \rho' + \rho^{\text{ic}} \nabla \cdot \mathbf{u}' = 0\tag{2.129}$$

$$\frac{\partial \mathbf{u}'}{\partial t} + \nabla(\mathbf{u}^{\text{ic}} \cdot \mathbf{u}') + \frac{1}{\rho^{\text{ic}}} \nabla p' = -(\boldsymbol{\omega}^{\text{ic}} \times \mathbf{u}') - (\boldsymbol{\omega}' \times \mathbf{u}^{\text{ic}})\tag{2.130}$$

$$- \frac{\rho'}{\rho^{\text{ic}}} \frac{d\mathbf{u}^{\text{ic}}}{dt} + \frac{1}{\rho^{\text{ic}}} \nabla \cdot \mathbb{S}'\tag{2.131}$$

$$\begin{aligned}\frac{\partial p'}{\partial t} + \mathbf{u}^{\text{ic}} \cdot \nabla p' + \kappa p^{\text{ic}} \nabla \cdot \mathbf{u}' + \mathbf{u}' \cdot \nabla p^{\text{ic}} &= -\frac{dp^{\text{ic}}}{dt} \\ &+ (\kappa - 1) (\phi - \nabla \cdot \mathbf{q}_T) .\end{aligned}\tag{2.132}$$

A Mach number scaling  $\mathbf{u} = \mathbf{u}^{\text{ic}} + \text{Ma} \mathbf{u}^{(1)} + \text{Ma}^2 \mathbf{u}^{(2)} + \dots$  is utilized to show the Mach number dependency of the terms. The perturbed velocity is proportional to the first expanded term  $\mathbf{u}' \sim \text{Ma} \mathbf{u}^{(1)}$ . Additionally, all fluid dynamic variables are scaled by their free stream values, and the perturbed variables are non dimensionalized by acoustic quantities. The dependency of the Mach number motivates further simplifications on the linear PCE such that the linearized perturbed compressible equations are

obtained.

$$\frac{\partial \rho'}{\partial t} + \mathbf{u}^{\text{ic}} \cdot \nabla \rho' + \rho^{\text{ic}} \nabla \cdot \mathbf{u}' = 0 \quad (2.133)$$

$$\frac{\partial \mathbf{u}'}{\partial t} + \nabla(\mathbf{u}^{\text{ic}} \cdot \mathbf{u}') + \frac{1}{\rho^{\text{ic}}} \nabla p' = \mathbf{0} \quad (2.134)$$

$$\frac{\partial p'}{\partial t} + \mathbf{u}^{\text{ic}} \cdot \nabla p' + \kappa p^{\text{ic}} \nabla \cdot \mathbf{u}' + \mathbf{u}' \cdot \nabla p^{\text{ic}} = -\frac{dp^{\text{ic}}}{dt} \quad (2.135)$$

At low Mach numbers the total derivative of the incompressible fluid dynamic pressure acts as the main source. Goldstein [16] as well as Ewert and Schröder [31] indicate this source term as the dominant source at low Mach numbers.

Ewert and Schröder [31] utilized a slightly different approach to derive the acoustic perturbation equations (APE) in several versions and levels of complexity. The perturbation quantities of the APE system are defined as the following decomposition of the flow field

$$\mathbf{u} = \bar{\mathbf{u}} + \mathbf{u}' = \bar{\mathbf{u}} + \mathbf{u}^{\text{v}} + \mathbf{u}^{\text{a}}. \quad (2.136)$$

In this equation  $\bar{\mathbf{u}}$  denotes the time averaged mean flow,  $\mathbf{u}^{\text{v}}$  the solenoidal (vortical) fluctuating velocity perturbation and  $\mathbf{u}^{\text{a}}$  an irrotational acoustic velocity perturbation. Based on this field decomposition four APE formulations are derived. The sources of the APE system are subject to Ewert and Schröder's source term filtering, which extracts the acoustic relevant source term projections on the modes. Instead of filtering the flow field, the source terms of the wave equations are filtered according to the mode properties. Chu and Kovasznay [82] showed that the linearized, viscous, compressible and heat-conducting flow equations excite three fluctuation modes. The vorticity mode (turbulence), the entropy mode (heat conduction), and the acoustic mode (compressibility) are activated by this equation and each mode corresponds to an eigenvalue and an eigenvector. Acoustically active source terms are filtered by the acoustic eigenmode projection. Therefore, the linearized Euler equations are transformed from space-time  $(\mathbf{x}, t)$  to the wavenumber-frequency domain  $(\mathbf{k}, \omega)$ . Now an algebraic system of equations is obtained

$$\mathbf{E}\mathbf{U} = i(\mathbf{S} + \mathbf{U}_{\text{init}}/2\pi), \quad (2.137)$$

where  $\mathbf{E}$  is the operator matrix of the linearized Euler equation in frequency domain,  $\mathbf{U}$  the vector of the primary variables with its initial conditions  $\mathbf{U}_{\text{init}}$ , and  $\mathbf{S}$  the source term. The eigenvalues  $\lambda_i$  and eigenvectors  $\mathbf{X}_i$  (vorticity, entropy and acoustic) of the system matrix  $\mathbf{A}$  are evaluated. By projecting the excitation to the acoustic subspace, the acoustic excitation is extracted. Finally, the system of equations of the filtering is transformed back to space-time  $(\mathbf{x}, t)$ . In the original space the filtering is equivalent to the solution of Poisson's equation of the original source term  $\mathbf{S} = (S_1, \dots, S_5)^T$  due to the compressible flow simulation. Thus, the acoustic source term reads as

$$\mathbf{S}^{\text{a}} = \begin{pmatrix} c^{-2} S_5 \\ \nabla \Phi \\ S_5 \end{pmatrix}, \quad (2.138)$$

where the condition for  $\Phi$  is  $\Delta \Phi = \frac{\partial S_2}{\partial x} + \frac{\partial S_3}{\partial y} + \frac{\partial S_4}{\partial z}$ . The extension to a nonuniform flow field provides a challenging task since the products of the mean flow and the perturbed quantities cannot be treated separately in the frequency domain.

To derive the APE equations the mass and momentum conservation are expressed by the enthalpy  $h$  and the velocity  $\mathbf{u}$  as primary variables. These equations are finally expressed in terms of the perturbed

pressure  $p'$  and the acoustic velocity perturbation  $\mathbf{u}^a$  as the APE-1 formulation

$$\frac{\partial p'}{\partial t} + c^2 \nabla \cdot \left( \bar{\rho} \mathbf{u}^a + \bar{\mathbf{u}} \frac{p'}{c^2} \right) = c^2 \left( -\nabla \rho \cdot \mathbf{u}^v + \frac{\bar{\rho}}{c_p} \frac{ds'}{dt} \right) \quad (2.139)$$

$$\frac{\partial \mathbf{u}^a}{\partial t} + \nabla(\bar{\mathbf{u}} \cdot \mathbf{u}^a) + \nabla \frac{p'}{\bar{\rho}} = \nabla \Phi_P + \nabla q_{\bar{\omega}} + T' \nabla \bar{s} - s' \nabla \bar{T}, \quad (2.140)$$

where  $\frac{d}{dt} := \frac{\partial}{\partial t} + \bar{\mathbf{u}} \cdot \nabla(\cdot)$ . Additionally,  $c_p$  is the specific heat capacity,  $s$  is the entropy and  $T$  the temperature.  $\Phi_P$  contains velocity source terms as products of  $(\bar{\mathbf{u}}, \mathbf{u}^v)$  and  $q_{\bar{\omega}}$  vortical source terms. For a low Mach number and incompressible applications only the term of  $\Phi_P$  matters, which further reduces to  $\Phi_P \approx (\nabla(p^{\text{ic}})')/\rho_\infty$ , with  $(p^{\text{ic}})'$  as the incompressible pressure perturbation.

The APE-2 formulation decomposes the pressure perturbation  $p'$  further to exclude the incompressible pressure perturbation  $(p^{\text{ic}})' \approx \bar{\rho} \Phi_P$

$$p' = \bar{\rho} \Phi_P + p^a \quad (2.141)$$

from the remaining acoustic pressure perturbation  $p^a$ . APE-2 is used in conjunction with an incompressible unsteady flow simulation. At low Mach numbers and when neglecting nonlinear coupling, the source term is approximated by the total time derivative of the pressure perturbation of the incompressible flow simulation.

The introduced APE-3 system coincides with the APE-1 system, where the system is based on the perturbed total enthalpy. This formulation has one advantage over the APE-1, since no Poisson's equation has to be solved to determine the source terms.

The APE-4 variant is based on the APE-1 system, with a focus on an efficient source term computation by a compressible flow simulation, without solving a Poisson problem. Considering vortex sound problems, the dominant source term of APE-4 is the Lamb vector.

An elegant wave equation with the total derivative of the incompressible fluid dynamic pressure as source term was proposed by Hüppe and Kaltenbacher [39]. PCWE, which is formulated as

$$\frac{1}{c^2} \frac{d^2 \phi^a}{dt^2} - \Delta \phi^a = \frac{1}{\rho_0 c^2} \frac{dp^{\text{ic}}}{dt}, \quad (2.142)$$

is an exact reformulation of APE-2. Compared to the APE only one scalar equation is solved; the computation is more efficient with respect to all computational resources. The acoustic velocity potential  $\phi^a$  is connected to the acoustic particle velocity and the acoustic pressure via

$$\mathbf{u}^a = \nabla \phi^a \quad (2.143)$$

$$p^a = -\rho_0 \frac{d\phi^a}{dt} = \rho_0 \left( \frac{\partial \phi^a}{\partial t} + \bar{\mathbf{u}} \cdot \nabla \phi^a \right). \quad (2.144)$$

By inserting the definition of the velocity potential into PCWE yields the formulation in the acoustic pressure and velocity formulation

$$\frac{1}{\rho_0 c^2} \frac{dp^a}{dt} + \nabla \cdot \mathbf{u}^a = -\frac{1}{\rho_0 c^2} \frac{dp^{\text{ic}}}{dt}. \quad (2.145)$$

The derivation of the PCWE assumes an incompressible averaged mean flow, with uniform mean density ( $\rho_0 = \bar{\rho}$ ) and state equation ( $p' = c^2 \rho'$ ). Starting from the APE-2 system, with incompressible

aeroacoustic sources

$$\frac{\partial \rho'}{\partial t} + \nabla \cdot (\bar{\rho} \mathbf{u}^a + \bar{\mathbf{u}} \rho') = 0 \quad (2.146)$$

$$\frac{\partial \mathbf{u}^a}{\partial t} + \nabla (\bar{\mathbf{u}} \cdot \mathbf{u}^a) + \nabla \frac{p'}{\bar{\rho}} = \nabla \Phi_P + \nabla q_{\bar{\omega}} + T' \nabla \bar{s} - s' \nabla \bar{T} \quad (2.147)$$

$$\frac{\partial p^a}{\partial t} - c^2 \frac{\partial \rho'}{\partial t} = -\frac{\partial p^{\text{ic}}}{\partial t}, \quad (2.148)$$

the first equation is inserted into the last and the properties of the assumptions are used to rewrite the variables

$$\frac{1}{c^2} \left( \frac{\partial p^a}{\partial t} + \bar{\mathbf{u}} \cdot \nabla p' \right) + \rho_0 \nabla \cdot \mathbf{u}^a = -\frac{1}{c^2} \frac{\partial p^{\text{ic}}}{\partial t}. \quad (2.149)$$

The definition of the pressure fluctuations in the APE-2 equation  $p' = p^{\text{ic}} + p^a$  is used to get the final version of the PCWE equation

$$\frac{1}{c^2} \left( \frac{\partial p^a}{\partial t} + \bar{\mathbf{u}} \cdot \nabla p^a \right) + \rho_0 \nabla \cdot \mathbf{u}^a = -\frac{1}{c^2} \left( \frac{\partial p^{\text{ic}}}{\partial t} + \bar{\mathbf{u}} \cdot \nabla p^{\text{ic}} \right). \quad (2.150)$$

Munz and coworkers [40–42] proposed an alternative derivation of perturbed equations for acoustic by a Mach number scaling. They decomposed the field variables in the following way

$$\begin{aligned} \mathbf{u} &= \mathbf{u}^{\text{ic}} + \text{Ma} \mathbf{u}' \\ p &= p^{(0)} + \text{Ma}^2 (p^{\text{ic}} + p') \\ \rho &= \rho^{(0)} + \text{Ma}^2 (\rho^{\text{ic}} + \rho'), \end{aligned} \quad (2.151)$$

where the incompressible density correction is related to the incompressible pressure  $p^{\text{ic}} = c^2 \rho^{\text{ic}}$ . Additionally,  $p^{(0)}$  and  $\rho^{(0)}$  are the thermodynamic parts of the pressure and density. The decomposition is inserted into the compressible Euler equations. After some manipulations, the linearized Euler equations with the total derivative of the incompressible pressure perturbation as source are constituted as

$$\frac{\partial \rho'}{\partial t} + \mathbf{u}^{\text{ic}} \cdot \nabla \rho' + \frac{\rho^{(0)}}{\text{Ma}} \nabla \cdot \mathbf{u}' = -\frac{\partial \rho^{\text{ic}}}{\partial t} - \mathbf{u}^{\text{ic}} \cdot \nabla \rho^{\text{ic}} \quad (2.152)$$

$$\frac{\partial \mathbf{u}'}{\partial t} + \nabla \cdot (\mathbf{u}^{\text{ic}} \mathbf{u}' + \mathbf{u}' \mathbf{u}^{\text{ic}}) + \frac{1}{\text{Ma} \rho^{(0)}} \nabla p' = \mathbf{0} \quad (2.153)$$

$$\frac{\partial p'}{\partial t} + \mathbf{u}^{\text{ic}} \cdot \nabla p' + \frac{\kappa p^{(0)}}{\text{Ma}} \nabla \cdot \mathbf{u}' = -\frac{\partial p^{\text{ic}}}{\partial t} - \mathbf{u}^{\text{ic}} \cdot \nabla p^{\text{ic}}. \quad (2.154)$$

The dominant source is the incompressible pressure perturbation, all other sources are at least by a factor  $\text{Ma}$  weaker. The equation models boundary compression and viscous effects. In the case of a vanishing incompressible background flow, the formulation constitutes the linear acoustic wave equation, with the second time derivative of the incompressible pressure as source term. The application of the method is valid for subsonic flows, especially in the low Mach number regime.

Recently, Henke [83] proposed that the flow can be decomposed by an uniform asymptotic expansion around the path-line averaged base flow. This decomposition shows that Lighthill's acoustic analogy with the approximated source term is the first order perturbation around the path-line averaged base flow.

In difference to the standard perturbation equations, De Roeck and Desmet [43] considered the properties of fluid dynamics at low Mach numbers. At low Mach numbers fluid dynamic effects are assumed to be incompressible, while compressible effects are of acoustic nature. This assumption gives rise to a Helmholtz decomposition of the compressible flow field and is the core concept of the aerodynamic/acoustic splitting technique. Therefore, the field is decomposed into a mean flow field and a fluctuating part,

as introduced for the LEE. Furthermore, the fluctuating part is decomposed into an aerodynamic and an acoustic component to split the field by its mathematical properties. The acoustic field is irrotational, the aerodynamic part rotational and the source field, a compressible flow simulation, is separated into these two parts. For both parts a Poisson's equation is solved. The acoustic part follows from

$$\Delta\phi = \nabla \cdot \mathbf{u}' \quad (2.155)$$

$$\mathbf{u}'_a = \nabla\phi, \quad (2.156)$$

and the aerodynamic part is obtained by solving a vector valued Poisson's equation

$$\nabla \times \nabla \times \mathbf{A} = \Delta\mathbf{A} = -\nabla \times \mathbf{u}' \quad (2.157)$$

$$\mathbf{u}'_v = \nabla \times \mathbf{A}. \quad (2.158)$$

With these equations the source domain is filtered to obtain the accurate acoustic and aerodynamic quantities. At the coupling interfaces the information is propagated to the far field with an irrotational formulation of the linearized Euler equations.

### Source truncation

The domain, computing the aeroacoustic sources, is typically smaller than the propagation domain. A smooth truncation of the source field is of special interest during hybrid methods [84], since otherwise spurious sound modes are generated by this interface [85, 86]. Ewert [87] proposed two ideas to correct this artificial interface error. The first correction is based on the fact that the source is truncated by a Heaviside distribution

$$\mathbf{L}^* = H(f(x))\mathbf{L}. \quad (2.159)$$

Hence, the source vector is modified to  $\mathbf{L}^*$  and excites nonphysical modes. These modes can be corrected by an additional source term. The modified source term is written as

$$\nabla \cdot \mathbf{L}^* = H(f(x))\nabla \cdot \mathbf{L} + \delta(f(x))(\mathbf{n} \cdot \mathbf{L}). \quad (2.160)$$

Now the modified source term can be corrected by a line source on the artificial boundary due to the truncation of the source field. The second approach suppresses spurious noise by a smooth window function on the source domain. This window function reduces the edge effects. For a smoothed growth  $h$  of the source terms with length  $d$ , waves of the size of  $\lambda \ll d$  are unaffected.

$$\delta(f(x))(\mathbf{n} \cdot \mathbf{L}) \longrightarrow \frac{\partial H}{\partial x}(\mathbf{n} \cdot \mathbf{L}) \quad (2.161)$$

For a special filter function one can estimate the wave-number dependency of the filter.

## 2.7 Cavity tones

The aeroacoustic method that is developed throughout this thesis is validated against specific cavity problems. These cavity simulations utilize Helmholtz's decomposition as a post processing tool as well as an underlying concept for aeroacoustic propagation simulations. In order to be familiar with the fundamental physical behavior, this chapter describes known effects of overflowed cavities.

Figure 2.3 shows a typical cavity, that is overflowed perpendicular to the cutout and parallel to the  $L$  cursor. Overflowed cavities, such as cutouts in overflowed plates, generate various flow configurations.

A turbulent boundary layer along the plate produces a free turbulent shear layer above the neck of the cavity, complex recirculation inside the cavity, acoustic waves, and multiple interactions. The conservation equations of viscous, heat-conducting, compressible fluid dynamics describe all effects of aeroacoustics, including nonlinear interactions. According to Chu and Kovasznay [82], the linearized equations excite

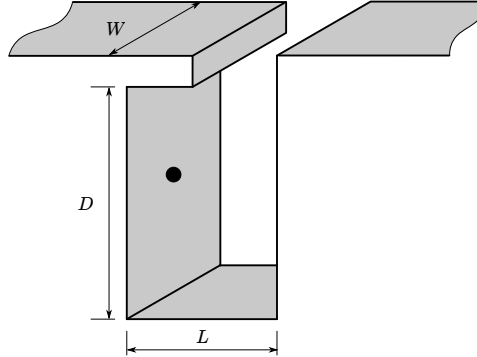


Figure 2.3: Example of a cavity with a lip [88].

three fluctuation modes, the vorticity mode (turbulence), the entropy mode (heat conduction) and the acoustic mode (compressibility). Fluid dynamic modes or vorticity modes are perturbations that describe viscous and turbulent fluid effects and are modeled by the incompressible fluid dynamic equations at low Mach numbers. The entropy mode represents thermal effects of the fluid. Sound, or acoustic mode, is linked to the compressible fluid and the wave can travel upstream and downstream below Mach one. This list of excitation mode is extended to a fourth mode, the boundary excitation mode, which includes vibrating surface and fluid structure interaction.

Multilateral interaction between these independently described modes is possible. A mode coupling may modify the flow configuration towards a totally different phenomenon. Therefore, an exclusive nonlinear interaction between the vorticity mode and the acoustic mode is assumed. Under this condition the vortical limit cycle dominates the acoustic radiation [89]. The complex interaction is illustrated by two simplified processes that transfer energy from flow to acoustic and vice versa. First, if streaming fluid is accelerated or decelerated, respectively by wall interaction, vortices are formed. The energy of these vortices is provided by the streaming fluid and the acoustic that triggers the instability. The second process simply shows that any vortical structure radiates sound, especially when it hits a solid surface (whistle). Acoustic waves have a large wave length at low Mach numbers and may interact with channels or geometrical configurations. During an experimental investigation one must consider these effects carefully. In most applications the net energy transfer supplies the acoustic mode, although the coupling phenomena are quite different; this sound is summarized as cavity tones.

### 2.7.1 Historical perspective and classification

Since 1950, many scientists have been studying cavities. Pioneers like Roshko [92] and Karamcheti [90,93] studied cavity noise considering aviation and aerospace applications. Roshko investigated the influence of cavities on the flow. The experience of flow-induced vibrations and the enormous increase in drag gave rise to intensive experimental investigations. He identified a primary recirculation inside the cavity and secondary in the cavity corners, as known from a lid driven cavity. Despite the prior reason of investigation, undesired structural vibrations lead to fatigue and generation of noise, reducing the capabilities and maintenance intervals of aircrafts. Karamcheti was the first who analyzed acoustic radiation in the sub and supersonic regime, including the influence of the boundary layer. Figure 2.4 shows the

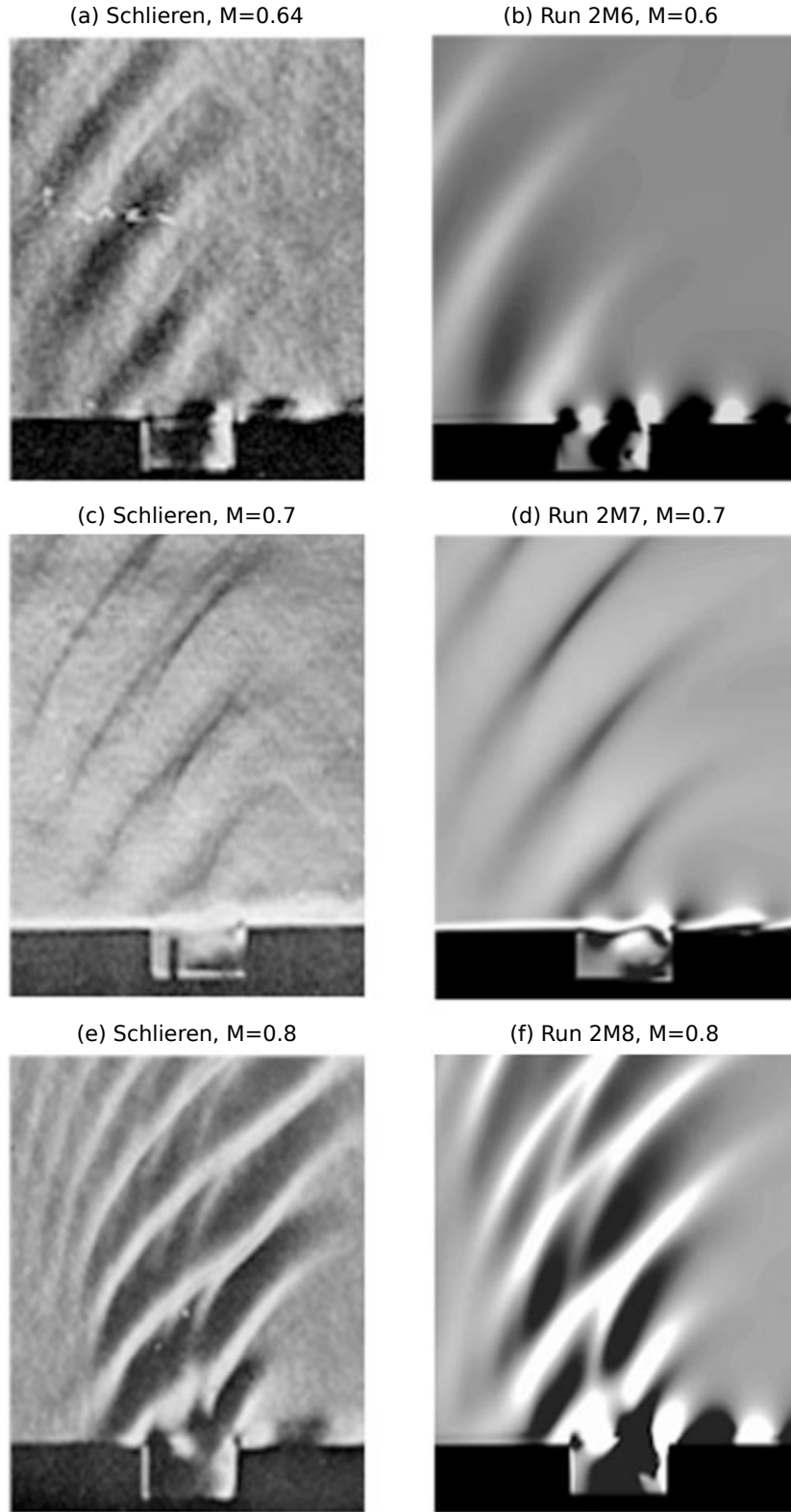


Figure 2.4: Comparison of schlieren photographs [90] with contours of density gradient from the DNS. In the schlieren photographs, the knife edge is horizontal in (c), vertical in the others; in the DNS figures,  $\partial\rho/\partial y$  is shown in (d),  $\partial\rho/\partial x$  in the others. Extracted from [91]



radiation pattern of overflowed cavities. A downstream amplification of the wave front was identified. In the 1960's, the next remarkable effects were explored by Plumblee *et al.* [94] for deep cavities, where the cavity resonance couples to the turbulent shear layer instabilities. Years later, Elder *et al.* [95] named the interaction between the Helmholtz resonator and the turbulent flow, turbulent rumble. Again, this mechanism was not the last being detected. After an extensive parameter study, Rossiter [96] reported severe resonances for laminar and turbulent flows, known as shear layer mode or Rossiter mode. His well known semi-empirical formula defines the aeroacoustic feedback loop of a self sustained oscillation. In the late 1970's, Rockwell and Naudasher [97,98] stated the importance of the vortex-edge interaction for self sustained interactions and published their popular classification of three typical cavity excitation groups, fluid dynamic (aeroacoustic feedback), fluid-resonant (acoustic resonances), and fluid-elastic (fluid-structure interaction) (see Fig. 2.5).

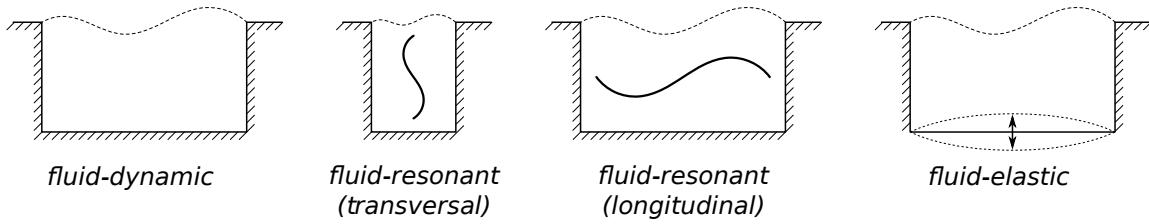


Figure 2.5: Rockwell and Naudasher's classification of cavity tones [99].

The experimental breakthrough from Gharib und Roshko [100] was the identification of the wake mode during an incompressible cavity study. A wake mode is present for thin boundary layers and produces a high flow resistance. Although the flow properties are very different, one can confuse shear layer and wake mode.

The number of experimental and numerical studies increased the last years tremendously, especially at low fluid speeds [101–105]. Low Mach number applications are motivated by the construction and automotive industry [106, 107]. As obvious consequence of a low Mach number application, the fluid is modeled incompressible [100, 108–111] and somehow aeroacoustic feedback is resolved. Section 3.3 explains "why an incompressible flow simulation might resolve aeroacoustic feedback".

## 2.7.2 Aeroacoustic feedback – Shear layer mode

Aerodynamic feedback (or fluid dynamic excitation) of cavities is one major noise mechanism. Under special flow and geometry conditions, typical Kelvin-Helmholtz instabilities of the shear layer in conjunction with acoustic instabilities form a feedback loop [89,97], called self sustained oscillations. This mechanism is not limited to cavities, it is also known as jet-edge tone interaction, where a free jet flow impinges on a solid wedge and involves feedback. Acoustic feedback inside cavities occurs for small ratios of the cavity length  $L$  to the acoustic wave length  $\lambda$ ,  $L/\lambda \ll 1$ .

Being geometry dependent, the boundary layer separates at the leading edge of the cavity and forms a shear layer. This initially stable or unstable shear layer reaches from the leading to the trailing edge. If the flow condition is suitable, the shear layer is unstable and Kelvin-Helmholtz instabilities convect towards the trailing edge. These instabilities interact with the edge, causing mass oscillations [101, 104]. The fluid motion drags fluid particles partly into the cavity and the remaining part is convected downstream. Different escape phenomena have been classified by Rockwell and Knisely [112] (see Fig. 2.6). Each interaction with the flow around the trailing edge originates an acoustic wave. Inside and outside the cavity waves travel towards the leading edge and ignite new instabilities (see Fig. 2.6). This ignition relies on the existing velocity gradient through the width of the shear layer. The newly generated instabilities convect downstream and interacts with the trailing edge to form a closed loop. Strong acoustic

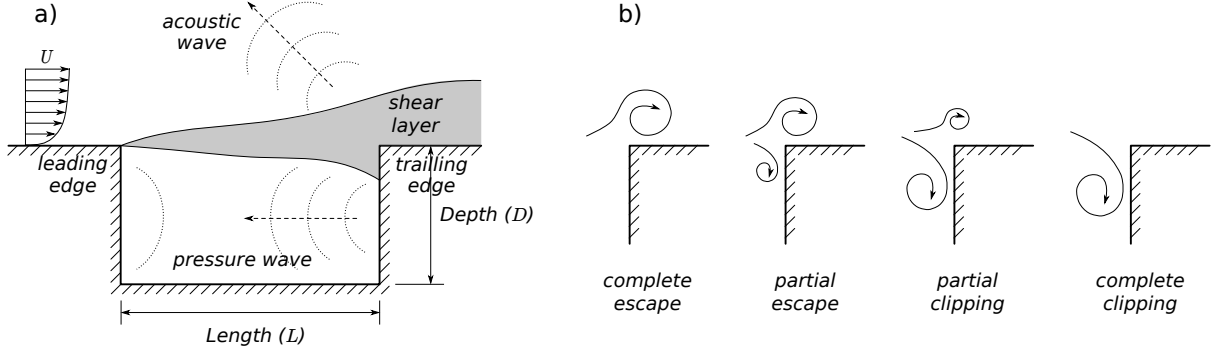


Figure 2.6: (a) Schematic of the shear layer mode [104]. (b) Rockwell and Knisely's [112] classification of the edge interaction.

amplification is a consequence of a distinctive and effective in-phase feedback [113]. If the acoustic wave is present but not effective in triggering a new oscillatory instability at the upstream location no self sustained oscillation is formed. Figure 2.7 shows a sequence of characteristic flow structures during one feedback loop.

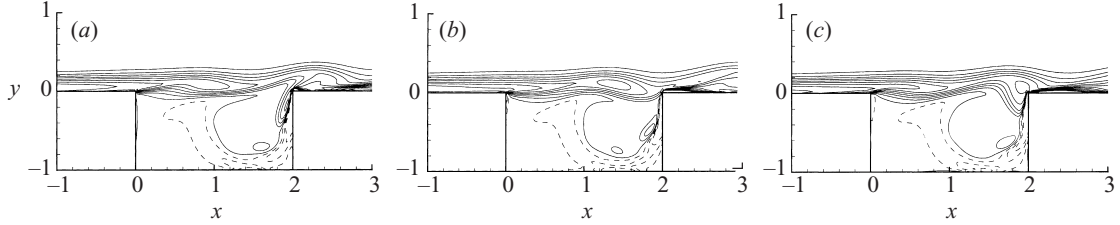


Figure 2.7: Instantaneous vorticity contours for run L2 (shear-layer mode) at three different times (a-c), corresponding to approximately one-third phase intervals of the dominant mode of oscillation (2nd Rossiter mode). 15 equi-spaced contours between  $\omega D/U = -5$  and  $1.67$  are shown; positive contours are dashed. Only a small portion of the computational domain near the cavity is shown. Extracted from [91].

Laufer and Monkewitz [114] derived the characteristic frequency based on matching traveling times of the vortex shading the pressure wave. Unknown parameters were estimated and the phase lag of the acoustic emission was introduced by Rossiter. Rossiter [96] fitted a semi-empirical model describing the characteristic frequency of the acoustic noise depending on the Mach number  $Ma$

$$St_n = \frac{n - \alpha}{\frac{U_\infty}{U_c} + Ma} \quad \forall n \in \mathbb{N}^+. \quad (2.162)$$

The model is limited to Mach numbers above 0.4, where  $\alpha$  is the phase lag that corresponds to the time delay from an impinging vortex at the trailing edge and the emission of the acoustic noise. The free stream velocity  $U_\infty$  and the convective velocity  $U_c$  of the vortex in the shear layer complete Rossiter's formula. Parameter estimates are given in literature [66, 96, 104, 115, 116]. Rossiter's formula computes the base frequency of the  $n^{\text{th}}$  shear layer mode. Each shear layer mode has further multiples  $k$  of this base mode at

$$f_{nk} = k \frac{St_n L}{U_\infty} \quad \forall n, k \in \mathbb{N}^+. \quad (2.163)$$

Elder [117] detected speed variations during the convection of the vortices. With increasing distance from the leading edge the growing structure accelerates since it is driven by a larger tangential velocity. In laminar boundary layers vortices are convected faster than in turbulent boundary layers, since laminar

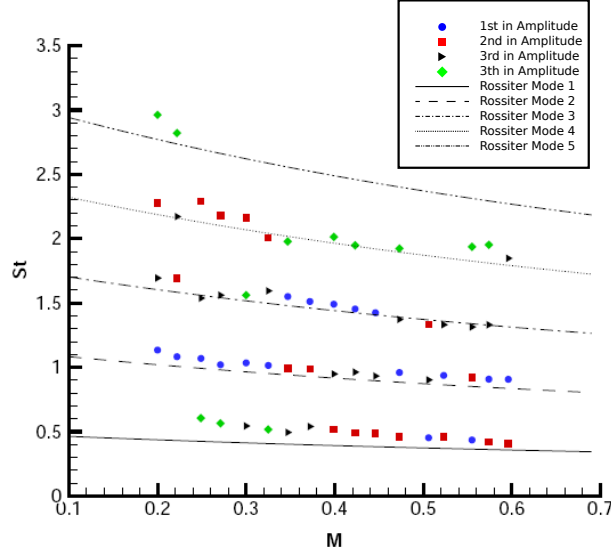


Figure 2.8: Rossiter modes. Variation of the peak frequencies as a function of the Mach number for the cavity experiments of Kegerise [115] for  $L/D = 2$ . Extracted from [89].

vortices are typically further away from the wall [89]. Figure 2.8 illustrates the remarkable prediction of the shear layer frequency. Although, various known influences on cavity noise are ignored or simplified, the location of the characteristic frequency is predicted well (as long as the fitted parameters are valid). Trailing edge interaction variations [97,98], the effects of the cavity depth [118], and complex recirculation inside the cavity are neglected by Rossiter's formula.

### 2.7.3 Fluid dynamic feedback – Wake mode

The wake mode is a fluid dynamic cavity mode causing high flow resistance. The shed vortex in the wake mode has nearly the dimensions of the cavity size, as depicted in Fig. 2.9. A transition from the shear layer mode to the wake mode is observed with increasing Mach number and increasing relative width and depth (based on the leading edge boundary layer thickness). Under these conditions the Kelvin-Helmholtz instabilities are so large and strong that they dominate the flow inside the cavity as well as the feedback. Figure 2.9 shows the evolution of the flow structures over one period. A strong vortex is formed at the leading edge that pushes out the vortex of the previous period, while it drags in fluid from the free stream. The squeezed vortex is roughly drawn over the trailing edge and separates the flow after the cavity. In the clean cavity the new vortex enlarges until it separates from the leading edge and the next leading edge pushes the vortex structure further downstream. The characteristic frequency of the wake mode coincides with the vortex shedding frequency and depends weakly on the Mach number that indicates a fluid dynamic feedback [91]. Compared to the shear layer much stronger pressure fluctuations occur in the mouth of the cavity. Although, the wake mode and shear layer mode are Kelvin-Helmholtz instabilities, the resonant behavior and origin is quite different and should not be mixed up.

### 2.7.4 Acoustic resonances or fluid resonant

If the box mode condition or Helmholtz condition is fulfilled, oscillatory effects in the fluid excite these cavities. Firstly, the cavities characteristic length has to be equal or larger than the acoustic wave length (box mode or duct mode). Secondly, the Helmholtz mode is a compressibility effect, since the cavity neck and the back volume form a single-mass spring system. The Helmholtz condition is fulfilled if an excitation frequency meets the natural frequency of the fluid mass oscillations. Interaction between the acoustic

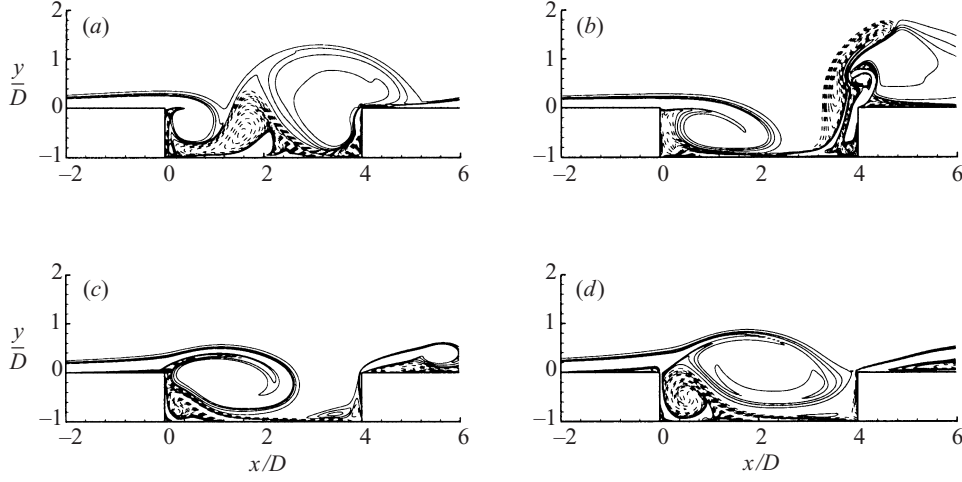


Figure 2.9: Instantaneous vorticity contours for run L4 (wake mode) at three different times (a-d), corresponding to approximately quarter-phase intervals of the periodic cycle. 15 equi-spaced contours between  $\omega D/U = -5$  and 1.67 are shown; positive contours are dashed. Only a small portion of the computational domain near the cavity is shown. Extracted from [91].

resonant effect and the fluid oscillatory effects are small and also the superelevation of the resonance is smaller than the amplification of aeroacoustic resonances. The excitation mechanisms, turbulent rumble (see Fig. 2.10) and damped fluid dynamic oscillations are not subject to any feedback mechanism. Inside the boundary layer turbulent pressure fluctuations trigger distinctive cavity modes. These pressure

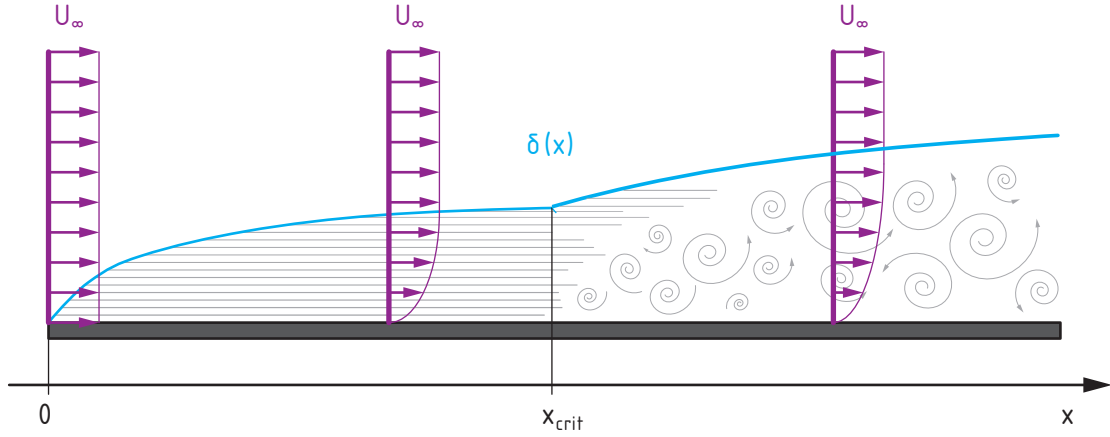


Figure 2.10: Schematic of boundary layer at an overflowed flat plate [119] that undergoes the transition from a laminar boundary layer to a turbulent boundary layer at the location  $x_{\text{crit}}$  at a boundary layer thickness of  $\delta$ . Extracted and modified from [120].

fluctuations above the neck of the cavity are called turbulent rumble [117, 121]. Cavities interact with broadband fluctuations and elaborate a selective amplification of the sound source. The resonator (cavity) filters the sound like a band-pass. CAA resolves turbulent rumble either by a highly resolved large eddy simulation (LES) or direct numerical simulation (DNS), or a hybrid synthetic turbulence model. In contrast to aeroacoustic feedback, damped oscillations are not in phase with the feedback mechanism and therefore not self-sustained. The acoustics generated by the mechanism is not coupling to the source oscillation (no energy is transferred back). If this flow oscillation extinguishes, the sound generation

and amplification diminishes rapidly. However, the co-existence of aeroacoustic feedback and acoustic feedback is possible and in the case of coinciding frequencies this lock-on state causes even higher sound levels. The lock-on state is characterized such that almost all energy of flow disturbances is trapped in this frequency and multiple harmonics.

### Duct modes

Acoustic modes of a cavity can be approximated by a simple box model. The cavity fluid box consists of five sound hard walls and one sound soft top. This model describes duct resonances and accounts for mode coupling (see Fig. 2.11). The main parameters of the box model are the cavities length  $L$ , depth  $D$ , and width or span  $W$  as well as the isentropic speed of sound  $c_0$ . Box resonance frequencies follow the equation

$$f_{n_x, n_y, n_z} = \frac{c_0}{2} \sqrt{\left(\frac{n_x}{L}\right)^2 + \left(\frac{n_y}{2D}\right)^2 + \left(\frac{n_z}{W}\right)^2} \quad \forall n_x, n_y, n_z \in \mathbb{N}. \quad (2.164)$$

In the case of shallow cavities  $L/D > 1$  the radiation loss is so dominant that these acoustic modes are highly damped and cause no effective noise amplification.

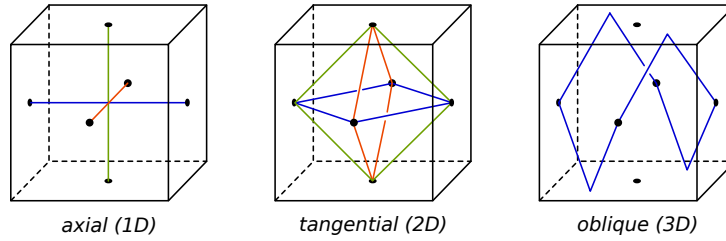


Figure 2.11: Duct modes and their radiation path [122].

### Helmholtz resonance

Named after the German physicist Hermann von Helmholtz, a Helmholtz resonator is an acoustic resonator that looks like a bottle (see Fig. 2.12). Today, room acousticians use Helmholtz resonators frequently as sound absorbers to improve the acoustic quality of rooms. Beside these positive associations, unintended Helmholtz resonators arise during vehicle design (e.g. sunroof [123], door gaps [124]). Cavities with a reduced neck and a relatively large back volume are Helmholtz resonators. Figure 2.12 describes this resonance type by an illustrative mechanical analogy to a single-mass oscillator [125]. The grazing flow through the orifice and the relative stiffness of the back volume allows the resonator to amplify one distinctive frequency

$$f = \frac{c_0}{2\pi} \sqrt{\frac{S}{V(D_{Ma} + D_c)}}. \quad (2.165)$$

The resonance depends on the cross section of the neck  $S$ , the total back volume of the cavity  $V$ , the length of the neck  $D_{Ma}$  and the correction length of the neck  $D_c$  (e.g.  $D_c = W\pi/2$ , neck width  $W$ ). Further, investigations on Helmholtz resonators aim to include dissipative effects and derive a more general lumped mass model [126].

### 2.7.5 Fluid elastic resonant - fluid structure interaction

Finally, fluid elastic resonant effects are discussed briefly, since all simulations within this thesis consider rigid walls. A starting point for further insight in fluid elastic cavity effects could be [99]. Elastic cavity wall vibrations are an important sound generation mechanism. Prominent examples of fluid elastic

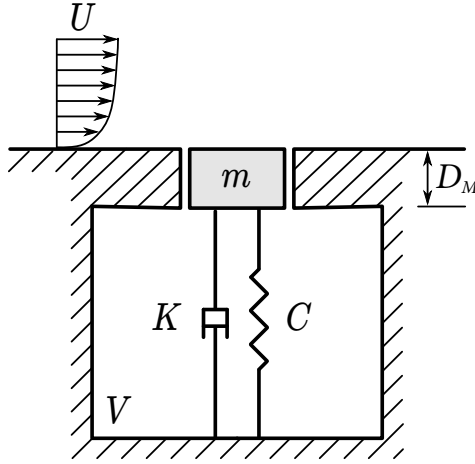


Figure 2.12: Schematic of the single-mass oscillator model analogy of the Helmholtz resonator. Extracted from [88].

resonances are musical instruments, like guitars and drums. If structural vibration and the acoustic resonant or aeroacoustic resonant effects are in phase and amplify each other (lock-on state) sound is generated efficiently.

### 2.7.6 Factors of influence - shear layer mode

Experimental studies characterized general influence factors on the different cavity modes and air towards a more fundamental perspective. A common classification based on the dimensionless depth  $L/D$  of the cavity misdirected pioneers work, since it was believed that the dimensionless depth adds value to the experimental cavity studies. East [127] analyzed deep cavities and concluded that aeroacoustic effects should be indicated by real flow parameters rather than geometrical parameters. Characteristic flow parameters are the dimensionality of the flow, the free stream velocity, the boundary layer thickness, effective viscosity, and recirculation. The following paragraphs discuss the most important influence factors on shear layer modes.

#### Mach number

Known from Rossiter's formula, the free stream velocity, respectively the Mach number, in combination with the cavity length  $L$  is a key parameter of cavity noise. Rossiter modes are proportional to the velocity; this dependency is known as ladder structure when the Rossiter mode frequencies are plotted over the Mach number. Two possible reasons cause Mach number independent Rossiter modes. Firstly, the Rossiter mode couples with an acoustic mode, usually with the depth mode. Secondly, the wake mode is wrongly identified as shear layer mode. According to Ahuja and Mendoza [104], higher Mach numbers cause higher sound pressures for the whole frequency range. This increase is explained by nonlinear interactions and higher harmonics.

#### Evolution of the shear layer

Gloerfelt *et al.* [128] describe the evolution of the shear layer throughout the cavity. When the boundary layer arrives at the leading edge, fluid exchange between the moving and resting fluid drives momentum thickness growth. Figure 2.13 separates the growth of the momentum thickness  $\delta_2$  into three subprocesses. Second order growth of Kelvin-Helmholtz instabilities is estimated by the first two linear growth

subprocesses (1) and (2). Initially, the acoustic disturbance in conjunction with vortex pairing promotes a strong increase of Kelvin-Helmholtz instabilities. In the second part, viscous energy transfer without vortex interaction reduces the initial growth rates. The third region near the trailing edge is dominated by the impact which widens the vortices laterally with high deviations between consecutive collisions.

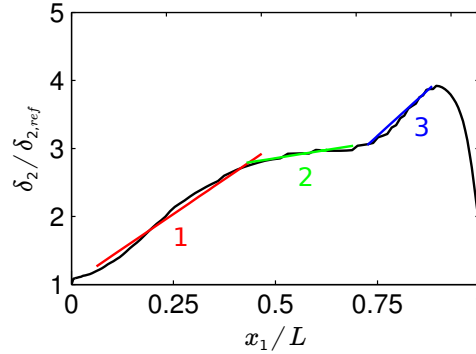


Figure 2.13: Non-dimensional momentum thickness  $\delta_2/\delta_{2,ref}$  between the two corners of the cavity: LES of  $L/D = 3$ ,  $Ma = 0.8$ , and  $Re_L = 1.23 \cdot 10^5$  cavity. Extracted from [128].

At increasing Reynolds numbers, the initial vortex pairing is believed to be superior to the acoustic trigger. In this state different metastable shear layer modes coexist, mode switching can occur through spontaneous reorganization of tiny turbulent vortices and additional low frequent components are produced by complex recirculation [89]. The overall dependency on the Reynolds number is emphasized in the next section.

### Reynolds number

Reynolds number describes the transition from laminar to turbulent flows, but is not specific for cavities. However, the flow state inside the laminar and turbulent regime is essential for the Kelvin-Helmholtz instabilities of the shear layer. For low Reynolds numbers, the shear layer may remain stable. Weak, three dimensional recirculations occur inside the cavity. Until reaching a critical Reynolds number, these recirculations are intensified (see Fig. 2.14). Above the critical Reynolds number the turbulent vortices are different from Kelvin-Helmholtz instabilities and excite broadband noise, turbulent rumble.

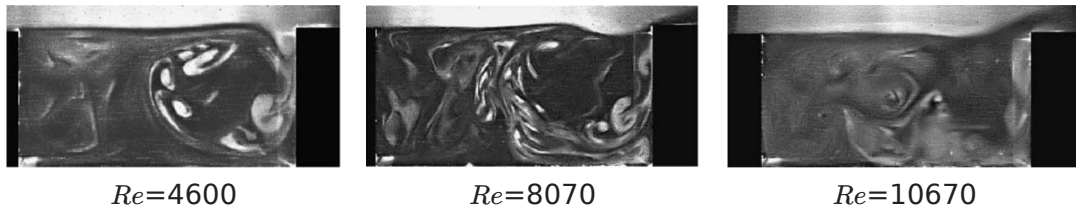


Figure 2.14: Increased unsteadiness of the recirculation zone as the Reynolds number is increased in the water tunnel experiments of Faure *et al.* [107] for a  $L/D = 2$  cavity.

### Boundary layer thickness

By applying stability theory to the shear layer, the boundary layer thickness was found to be a main influence factor [129]. Having the same shear layer mode, a decreasing boundary layer thickness increases the mode frequency, the pressure level inside the cavity, and the radiated sound pressure level [44, 88]. Gharib and Roshko [100] observed a minimum relative cavity length  $L/\delta_2$ ; beneath it, the laminar shear layer instability is stable. The DSC study [66] indicated that the third Rossiter mode is likely for thinner

boundary layers, whereas the second Rossiter mode is present for the thicker cavity mode (see Fig. 2.15). This interpretation lacks generality, since only two configurations are compared.

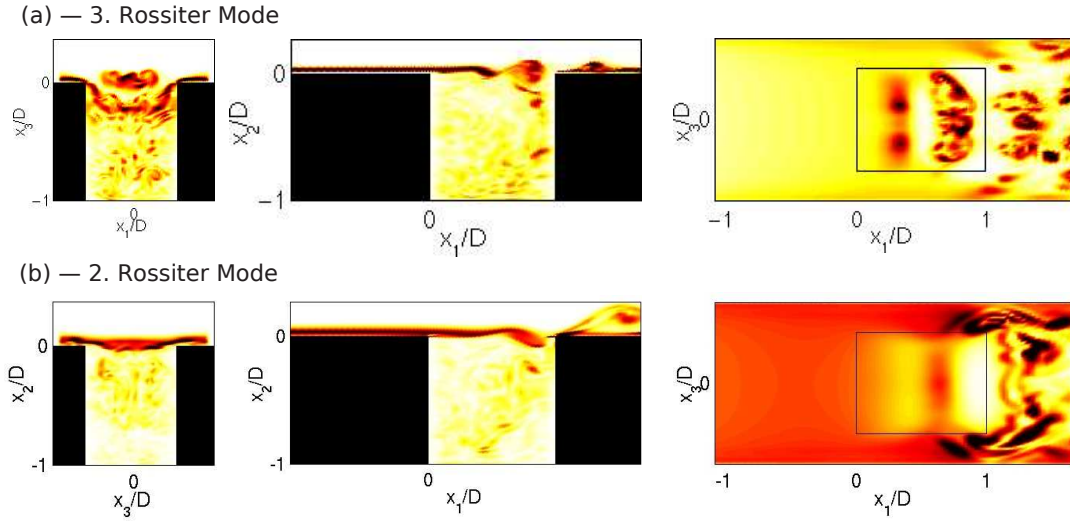


Figure 2.15: Influence of the boundary layer thickness on the selection of the mode of oscillations at low Reynolds numbers. Crossview, sideview and planview of the norm of the vorticity for the cases (a)  $L/\delta_2 = 105$ , (b)  $L/\delta_2 = 76$  [66].

For high Reynolds number  $Re_L > 10^6$ , the flow modes are independent of the boundary layer thickness [130]. Figure 2.16 depicts the flow disturbances for two boundary layers at  $Ma = 0.78$ . Beside turbulent rumble, the modes coincide qualitatively. Additionally, Gloerfelt [131] validated his LES by

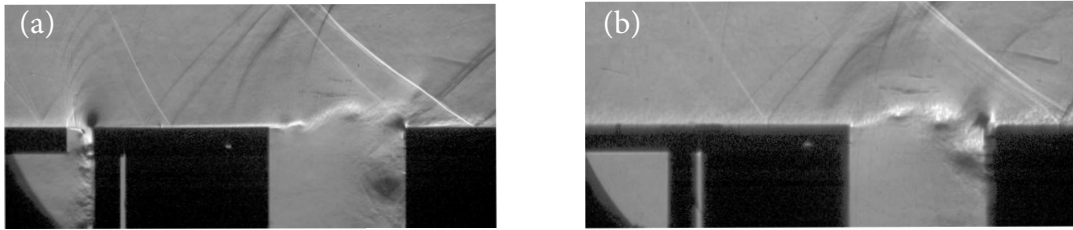


Figure 2.16: Influence of boundary layer thickness at a high Reynolds number. Schlieren pictures with knife edge horizontal for a cavity with  $L/D = 0.42$  and a Mach number  $Ma = 0.78$  with (a) or without (b) suction of the boundary layer ahead of the cavity. Extracted from Illy [130].

Kegerise's high Reynolds number experiments [115]. The profound LES study varied the boundary layer thickness ( $\delta = 3.5$  mm and  $\delta = 6.1$  mm) and the turbulent intensity of the boundary layer. Analog to previous discussions, the flow inside the cavity is independent of the boundary layer thickness and an increase in turbulence reduces the strength of the large vortices (see Fig. 2.17).

### Dimensionless width

Although downsizing of flow properties to geometrical ones is critical, the dimensionality of the flow is expressed by the dimensionless width  $L/W$ . In the case of wide cavities ( $L/W < 1$ ) the shear layer forms coherent structures transverse to the flow. These coherent structures can be seen as a two dimensional flow. All effects of the side walls are less important for the overall flow condition. For slender cavities ( $L/W > 1$ ) these side wall effects interact with the main shear layer and produce three dimensional and incoherent structures. The geometric limit is not absolute and additionally depends on the Mach number, the boundary layer thickness, and the recirculation inside the cavity. A two dimensional shear



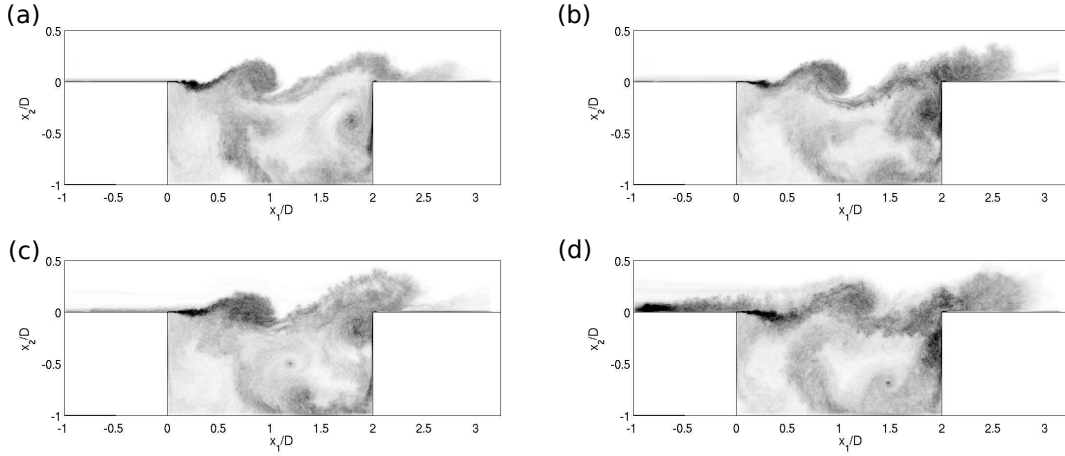


Figure 2.17: Influence of boundary layer thickness at high Reynolds numbers. Large-eddy simulation of a  $L/D = 2$  cavity at a Mach number of 0.4 [131]. Snapshots of instantaneous vorticity modulus averaged over the cavity span with: (a)  $\delta = 3.5$  mm and no perturbation; (b)  $\delta = 6.1$  mm and no perturbation; (c)  $\delta = 3.5$  mm with turbulent inflow; (d)  $\delta = 6.1$  mm with turbulent inflow. Extracted from [89].

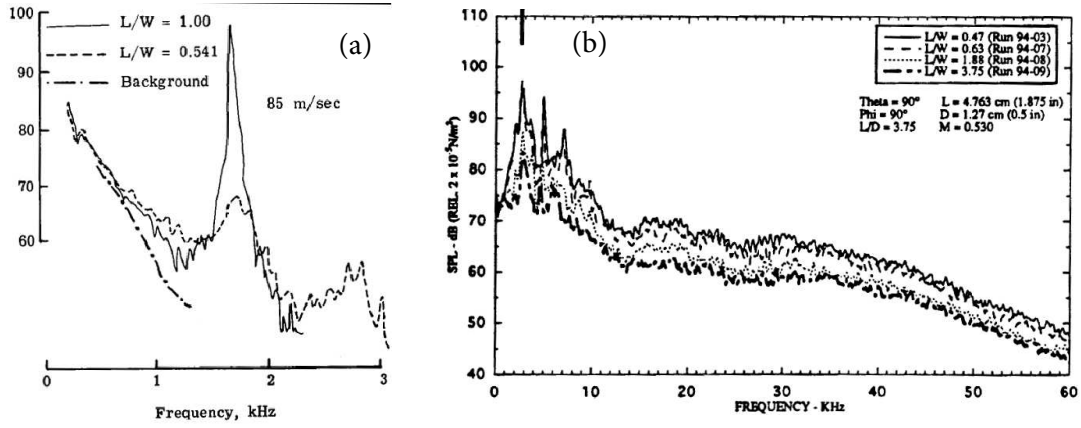


Figure 2.18: Effect of  $L/W$  on cavity flow narrow band noise spectra measured by Block [101] (a), and Ahuja and Mendoza [104] (b).

layer typically forms a three dimensional recirculation inside the cavity [89]. Rossiter [96], Block [101], as well as Ahuja and Mendoza [104] investigated the aeroacoustic relevancy of  $L/W$ . Figure 2.18 shows

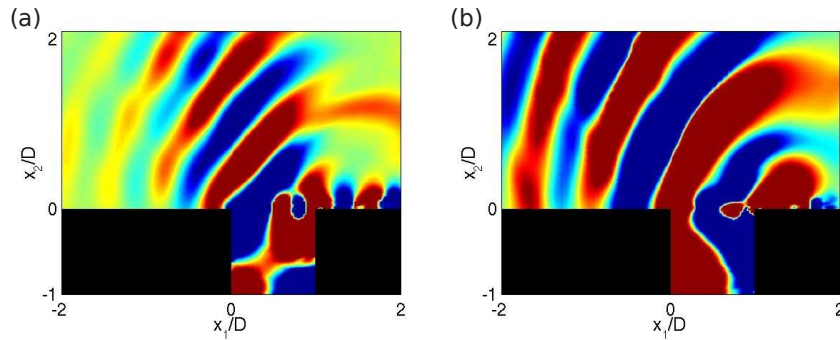


Figure 2.19: Pressure fields in the span-wise midplane for the two simulations at Mach 0.6:  $L/W = 1.28$  in (a),  $L/W = 0.5$  in (b). PL between -500 and 500 Pa. Extracted from [66].

both wide and slender cavities excite a common frequency. The studies are not clear whether the slender or the wider cavity is louder.

A DSC study of Gloerfelt *et al.* [66] analyzed the acoustic radiation pattern with respect to the cavity width at  $Ma = 0.6$ . The results of a slender cavity  $L/W = 1.28$  and wide cavity  $L/W = 0.5$  confirm differences in the radiation and the number of vortices (3 and 2.5) in the orifice of the cavity (see Fig. 2.19).

### Recirculation and 3D effects

Two dimensional recirculation inside the cavity may turn unstable and form three dimensional Taylor-Görtler vortex pairs (see Fig. 2.20). The extension of the Taylor-Görtler vortex pairs depends on the

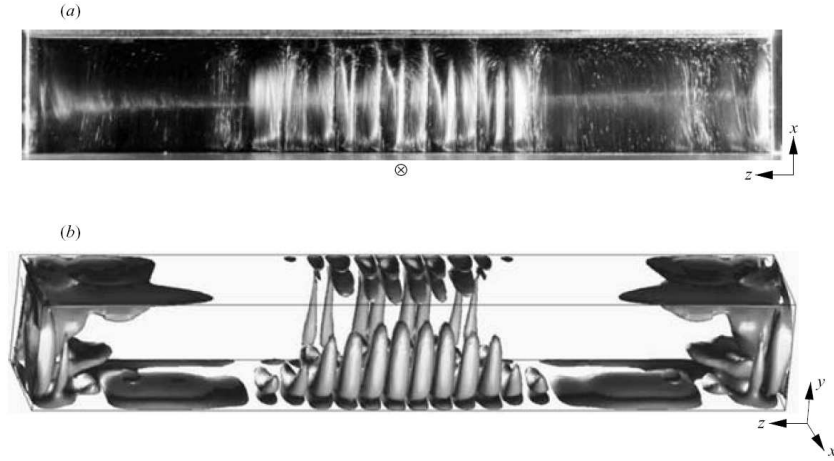


Figure 2.20: (a) Experimental stationary Taylor-Görtler vortices for  $Re = 850$  reproduced from Albensoeder and Kuhlmann [132]. The flow is from the top to the bottom, and was illuminated in the plane  $y \approx -1/2$  by a light sheet. (b) Numerical simulation of the flow for the same parameters as in (a). Vorticity iso-surfaces  $|\omega_x| = 210$  are shown. Extracted from [132].

intensity of the primary vortex and its side wall interaction. Side wall modified span-wise modulation of the shear layer transfers additional three dimensional momentum into the recirculation. The recirculation causes an upstream convection inside the front part of the cavity (see Fig. 2.21). The continuous upstream interacts with the shear layer and the transversal coherence of the flow structures vanish inside the neck. Each modulation shear layer by the upstream component triggers low frequent components in the pressure spectra. As already noted in the previous paragraph, low frequent velocity oscillations can also be a product of vortex pairing, or mixing layer and jet-edge interaction phenomena.

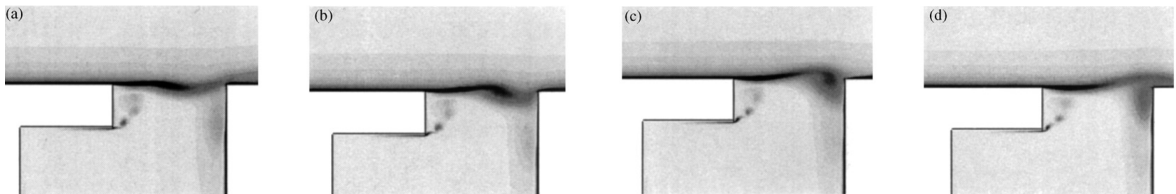


Figure 2.21: Instantaneous vorticity contour sequence (a-d); compressible 2D URANS study [133].

# 3 Flow-Acoustic Coupling and Aeroacoustic splitting

Preliminary, this chapter discusses the possible issues during DSC (direct sound computation). DSC describes the computation of flow and acoustic. Acoustics is one of multiple modes of fluid dynamics [134] and the special physical requirements on the algorithms are appraised. The DSC resolves acoustics directly and, in contrast to acoustics, turbulence is modeled or computed directly.

If acoustics is not resolved and all turbulence is computed directly, this simulation type is called a direct numerical simulation (DNS). What is DSC and what DNS? DSC simulates acoustics directly; DNS simulates turbulence directly. However, a DSC that computes turbulence directly is also a DNS and vice versa, called direct multi-scale simulation (DX) afterwards.

## 3.1 Direct numerical simulation

DNS solves the compressible fluid dynamic equations and the emerging unsteady turbulent fluctuations directly. Unsteady turbulent fluctuations contain turbulent kinetic energy and the essence of DNS is to resolve the whole turbulent kinetic energy spectrum. The turbulent spectrum (see Fig. 3.1) reaches from the large turbulent vortices, represented by the integral length, to the tiny turbulent structures, estimated by the Kolmogorov scale. Advantages and limitations of DNS lie close to each other, resolving all possible turbulence scales makes the DNS the superior turbulence treatment with the contradiction on the computational workload. The number of mesh points  $n_{\text{mesh}}$  is assessed by the ratio of the integral length and the Kolmogorov scale in three dimensions

$$n_{\text{mesh}} \sim \text{Re}^{9/4}. \quad (3.1)$$

*"Despite the considerable progress in computing resources [...], it is still only possible to reach moderate values of the Reynolds number in direct numerical simulation."* [135]

However, DNS drives the development and validates the applicability of turbulence models. In practical flow application, large eddy simulations (LES), unsteady Reynolds averaged Navier-Stokes models (URANS) or hybrid LES-URANS turbulent models are currently used.

Although these turbulence descriptions are applied in direct sound computation, hybrid aeroacoustics has found a different way to model turbulence. These synthetic turbulence models (e.r. SNGR [137]) mimic turbulent structures for aeroacoustic investigations and reduce the computational cost. The herein developed method can be extended towards separating distinctive aeroacoustic effects onto the modeled turbulent source terms [16]. In particular, the vortex sound approximation in combination with a synthetic turbulence model is computationally efficient for high Reynolds number aeroacoustics.

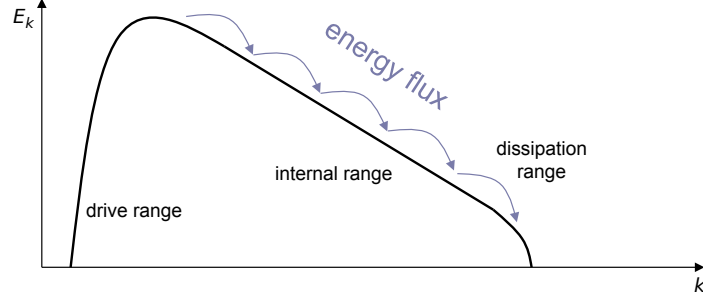


Figure 3.1: Energy cascade of turbulent kinetic energy spectrum. Extracted from [136].

### 3.2 Direct sound computation

For practical applications, DSC is infeasible, even though great advances have been made in direct computation of aerodynamic sound. Section 2.6.2 discussed already the open issues of DSC and for transonic and supersonic flow configurations simulations show satisfactory results with respect to the computational burden. In this range of Mach numbers, Helmholtz number and the Strouhal number are of the same magnitude. Physically speaking, the vortical and the acoustic length scale are of the same order. For subsonic flows, we determine the disparity of acoustic length scales (wavelength)  $\lambda$  and the vortical length scale  $l_v$  by the Mach number  $Ma$

$$\lambda = \frac{l_v}{Ma}. \quad (3.2)$$

At low Mach numbers, DSC suffers from this disparity of length scales and although the flow can be modeled as incompressible, the simulation has to solve the compressible flow equations. Possible challenges of DSC are summarized below.

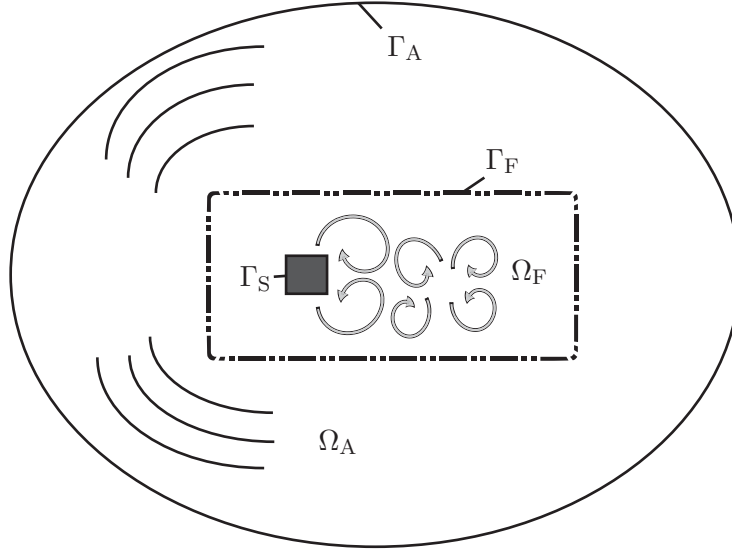


Figure 3.2: Typically, the domain  $\Omega$  of a hybrid aeroacoustic workflow consists of two subsets: The domain  $\Omega_F$ , where vortical structures are present and the subsequent acoustic propagation domain  $\Omega_A$ .

## Compressible fluid

The propagation of an acoustic field requires a compressible fluid. Compared to an incompressible flow simulation, wave propagation and feedback of the acoustic field onto the flow field is incorporated. Numerically and mathematically speaking, wave propagation is only possible if the computational scheme suits the compressible flow equations.

## Farfield decay

Based on Biot-Savart formula, an incompressible flow perturbation decays with  $O(1/||\mathbf{x}||_2^3)$ , whereas the acoustic field decays with  $O(1/||\mathbf{x}||_2)$  [13]. This decay discrepancy leads to a larger domain ( $\Omega = \Omega_F \cap \Omega_A$ ) for a DSC, as if hybrid aeroacoustic methods are used (only  $\Omega_F$ ). Additionally, the weak acoustic decay involves an accurate radiation boundary treatment at  $\Gamma_A$  that transmit waves without reflections.

## Disparity of scales

Small vortices, at low Mach numbers ( $\text{Ma} < 0.3$ ), produce waves with a much longer wavelength. In order to model these waves in the flow domain, the fluid domain and the discretization is adjusted in order to resolve acoustics. The number of mesh points is proportional to

$$n_{\text{mesh}} \sim \frac{1}{\text{Ma}^3} . \quad (3.3)$$

Analog to the length scale disparity, the difference in the energy scale of vortical structures and acoustics is enormously. For subsonic flows, the energy concentration in vortical structures leads to a higher amplitude of flow fluctuations compared to acoustic perturbations. The acoustic perturbations  $||\mathbf{u}^a||/||\mathbf{u}|| \cong 10^{-3}$  are potentially so small [138, 139] that they could be computational noise, and the aeroacoustic sources for subsonic flows are inefficient  $\sim \text{Ma}^5$ . As a consequence, a separate acoustic computation has been proposed – hybrid aeroacoustic.

## Discretization

The numerical resolution of partial differential equations approximates, discretizes, the continuous space and time derivatives by algebraic terms. For wave equations, a spatial discretization of about 20 computational points per wavelength with a second order scheme leads to an acceptable dispersion error for engineering applications<sup>1</sup>. In combination with a time derivative, numerical stability requires that the time step of an explicit time scheme must satisfy the Courant–Friedrichs–Lewy (CFL) condition

$$\text{CFL} = \Delta t \frac{U_i}{\Delta X_i} \leq \text{CFL}_{\text{crit}} . \quad (3.7)$$

---

<sup>1</sup> Classification of numerical errors of the wave equation:

- Phase velocity error, the numerical phase velocity  $c_{\text{ph}}$  is not the speed of sound

$$c_{\text{ph}} = \frac{\omega}{||\mathbf{k}||} \neq c , \quad (3.4)$$

and results in a phase shift over the propagation.

- Group velocity error, the numerical group velocity  $c_{\text{g}}$  is not the speed of sound

$$c_{\text{g}} = \frac{\partial \omega}{\partial ||\mathbf{k}||} \neq c , \quad (3.5)$$

and results in a energy transport delay during wave propagation.

- Amplitude error, the numerical angular frequency  $\omega_{\text{n}}$  is complex

$$\omega_{\text{n}} = \omega_{\text{rn}}(\mathbf{k}) + i\omega_{\text{in}}(\mathbf{k}) \quad (3.6)$$

and the wave loses or gains energy.

At low Mach number the critical CFL region is where tiny flow structures are resolved by the refined grid. To stabilize the flow simulation, the time step must be reduced accordingly.

The discussed difficulties arise with the structure of the partial differential equation and the physically correct boundary conditions. In particular for fluid dynamics, the structure of the partial differential equation changes from an elliptic-parabolic equation (incompressible) to a hyperbolic-parabolic equation in the compressible constitution. The hyperbolic part describes the wave propagation. Analog to the incompressible flow simulation, the compressible flow simulation has fluid dynamically speaking similar boundary conditions, but impinging waves of the acoustic component must be treated.

#### **Farfield radiation**

The DSC boundary conditions must transmit, absorb, and reflect waves physically. For the non-linear compressible fluid dynamic equations no exact acoustic free field boundary conditions are available yet. Today, the damping properties of the grid or/and additional artificial viscosity damp the waves in a sponge zone<sup>2</sup>. If this technique is not used, spurious reflections will corrupt the DSC. It is obvious that a profound DSC must consider these boundary effects. When just modeling fluid dynamic, even though acoustic scales are small, the compressible flow solution must be boundary-robust<sup>3</sup> against acoustic effects.

#### **Acoustic absorbing material**

If special acoustically relevant materials are investigated, such as absorbing material, the flow simulation must either model the boundary or resolve acoustic material. Typically, a full scale resolution of absorbers is beyond computational resources. Simplified CFD models mimic the flow resistance and the acoustic behavior. In most cases a hybrid aeroacoustic simulation can incorporate known acoustic effects during the acoustic simulation easily.

Finally, the currently available proprietary tools incorporate additional damping inside the computational method to increase robustness. Acoustically suboptimal first or second order approximation schemes are usually used.

### **3.3 Hybrid methodology – Incompressible flow**

Compared to DSC, hybrid methods increase the computational efficiency. Figure 3.3 illustrates the hybrid workflow. A highly specialized incompressible flow solver calculates the fluid dynamics and resolves necessary turbulent scales. In a second simulation the acoustic propagation is computed. This hybrid procedures ensures a fast and accurate computation of the flow on a reduced domain, as well as an efficient acoustic propagation on a larger domain. Both solvers are well-suited for their application. Typically, hybrid aeroacoustics is applied in conjunction with an incompressible flow simulation.

Known physical effects, like the Rossiter mode, involve acoustic feedback and the flow simulation must resolve acoustics. If an acoustic feedback mechanism triggers flow structures, physical theory suggests a compressible flow simulation and hence an incompressible simulation is inappropriate. However, in some applications even an incompressible flow simulation catches this feedback – somehow (e.g. Rossiter mode [44]).

<sup>2</sup> A sponge zone is usually utilized to damp acoustic and vortical perturbation. For large wave length, the zone extension might violate acoustic compactness and acoustic reflections can occur.

<sup>3</sup> Robust flow configuration are flow states that include no aeroacoustic feedback and therefore no aeroacoustic flow modulation. In this sense, a robust compressible flow configuration converges to the incompressible flow configuration for low Mach numbers. A boundary-robust configuration is unaffected by small spurious boundary reflections.

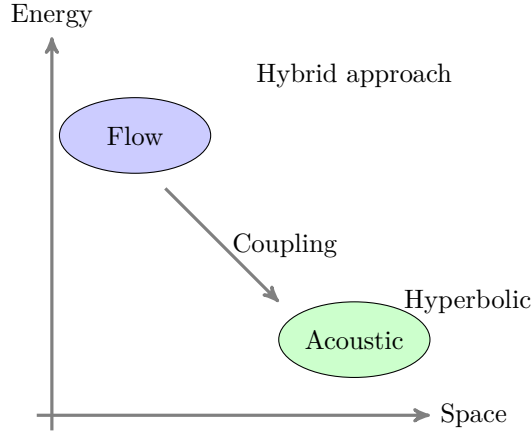


Figure 3.3: Schematic of a typical hybrid approach in aeroacoustic. One way coupling of the resolved flow to the acoustics.

### 3.3.1 Feedback

In this section, we investigate the role of coupling of flow and acoustics during an incompressible flow simulation (see Fig. 3.4). Prior to discussing incompressible feedback and consolidating the conclusion, the feedback situation during a compressible simulation is outlined. For a compressible flow simulation it is clear that the acoustic waves are part of the solution and trigger feedback. This feedback mechanism is a closed loop of simplified processes. At first, a vortex is triggered by an acoustic wave. Secondly, the vortex is convected and transformed while sound is emitted. The radiated sound travels "back" to the flow structure trigger point and causes new flow instability. This process description has been used by Rossiter to deduce his well-known feedback formula. This feedback occurs since phase relations inside the flow are considered by traveling effects and a limited speed of sound. In contrast to the compressible flow, an incompressible flow neglects these traveling effects and violates phase relations. However, in the low Mach number range of a compressible flow simulation these phase relations are nearly identical to the incompressible approximation, with unlimited speed of sound.

In the case of an incompressible simulation, this coupling phenomenon is studied by compact acoustics. Compact acoustics approximates the acoustic field by an elliptic equation for small Helmholtz numbers  $He \ll 1$ . Lighthill's compact acoustic version reads as

$$-\nabla \cdot \nabla p' = \nabla \cdot \nabla \cdot \mathbb{T}. \quad (3.8)$$

The feedback mechanism is similar to the feedback of compressible flows, with an instantaneous "back" traveling of compact acoustics (elliptic equation). We show that the compact form of Lighthill's aeroacoustic analogy coincides with the pressure correction equation of the incompressible CFD. We start the derivation from the incompressible Navier-Stokes equations without external forcing

$$\rho_0 \frac{d\mathbf{u}}{dt} = -\nabla p - \eta \Delta \mathbf{u}. \quad (3.9)$$

If we represent the velocity Laplacian by the vorticity  $\Delta \mathbf{u} = \nabla \times \boldsymbol{\omega}$ , the incompressible Navier-Stokes equations is

$$\rho_0 \frac{d\mathbf{u}}{dt} = -\nabla p - \eta \nabla \times \boldsymbol{\omega} \quad (3.10)$$

and taking the divergence afterwards yields the pressure correction equation

$$\rho_0 \nabla \cdot (\mathbf{u} \cdot \nabla) \mathbf{u} = -\nabla \cdot \nabla p. \quad (3.11)$$

After the velocity term is simplified  $\nabla \cdot (\mathbf{u} \cdot \nabla) \mathbf{u} = \nabla \cdot \nabla \cdot \mathbb{T} - \nabla \cdot \mathbf{u} \nabla \cdot \mathbf{u}$ , Lighthill's tensor  $\mathbb{T}$  is introduced and the consequence of incompressible flow  $\nabla \cdot \mathbf{u} = 0$  is used. In this sense, the pressure correction equation is reorganized to

$$-\nabla \cdot \nabla p = \nabla \cdot \nabla \cdot \mathbb{T}. \quad (3.12)$$

To conclude, compact acoustic propagation is part of the incompressible flow simulation and feedback might be possible.

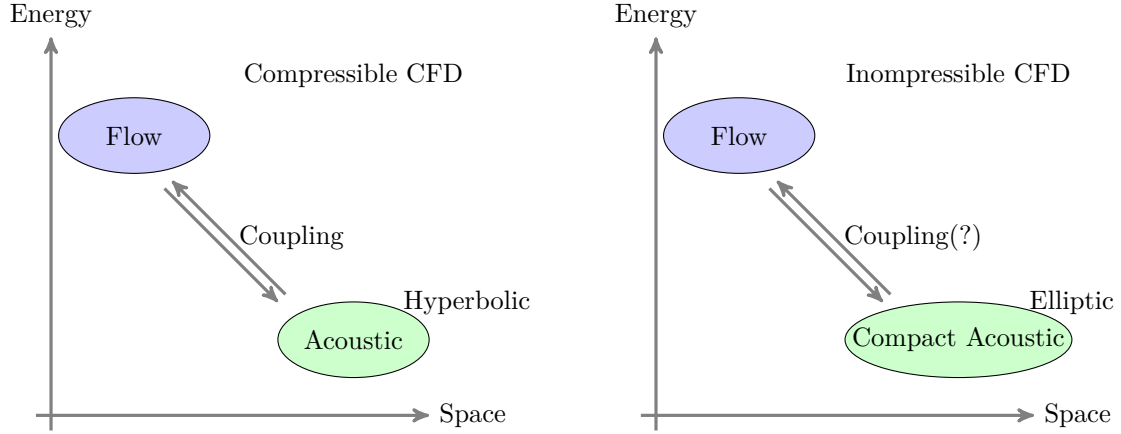


Figure 3.4: Comparison of compressible CFD and incompressible CFD and the feedback mechanisms of flow and acoustics.

### 3.4 Hybrid methodology – Compressible flow

Section 2.7.2 describes a well-known feedback mechanism of compressible fluids. Compressible fluid dynamics includes all wave phenomena as well as aeroacoustic feedback. In combination with a hybrid workflow, a compressible flow simulation must resolve the acoustic already perfectly (DSC) in order to satisfy the equation reassembly of acoustic analogies (see next paragraph). Implicitly, the aeroacoustic source terms include wave refraction and scattering. This means, for an accurate acoustic simulation, after the flow simulation, the engineers have to know the whole physics and gain no computational efficiency by the separate far-field propagation. Having this in mind, an aeroacoustic analogy that distinguishes between resolved and unresolved acoustics would be of great importance.

### 3.5 Source term modeling in aeroacoustic analogies

DSC resolves flow and acoustics at all Mach numbers. However, the open issues of proprietary CFD, which is discussed in Sec. 3.2, severely diminishes the applicability in product development. Acoustic analogies, used in current hybrid approaches (see Fig. 3.3), overcome these open issues, except the aeroacoustic feedback. To incorporate aeroacoustic feedback, the presented hybrid aeroacoustic method relies on a compressible flow simulation.

Before this method is outlined, the derivation of aeroacoustic analogies is generalized. Aeroacoustic analogies rearrange terms of the flow equations; just rearranging terms, does not change the mathematical



properties of the physical model. Often, this fact is neglected during term manipulation. Assumptions and simplifications empower the analogy and despite all criticism remarkable results have been obtained.

### 3.5.1 Implicit formulation

A general aeroacoustic analogy assumes a causal forward coupling of the forcing (obtained by an independent flow simulation) on fluctuating quantities, e.g. the fluctuating pressure  $p'$  that approaches the acoustic pressure  $p^a$  at large distances from the turbulent region. Thereby, a general acoustic analogy composes a hyperbolic left hand side defined by a wave operator and a generic right hand side **RHS**( $\star$ )

$$\square p' = \mathbf{RHS}(p, \mathbf{u}, \rho, \dots). \quad (3.13)$$

Lighthill's inhomogeneous wave equation perfectly fits to this class, which reads as [6, 7]

$$\frac{\partial^2 \rho'}{\partial t^2} - c_0^2 \nabla \cdot \nabla \rho' = \nabla \cdot \nabla \cdot \mathbb{T}. \quad (3.14)$$

In (3.14),  $\rho'$  denotes the density fluctuation,  $c_0$  the constant speed of sound and  $\mathbb{T}$  the Lighthill tensor. Lighthill's tensor is computed by

$$\mathbb{T} = \rho \mathbf{u} \mathbf{u} + \left( (p - p_0) - c_0^2 (\rho - \rho_0) \right) \mathbb{I} - \mathbb{S} \quad (3.15)$$

with the fluid velocity  $\mathbf{u}$ , the pressure and density fluctuations  $p' = p - p_0$ ,  $\rho' = \rho - \rho_0$  and the viscous stresses  $\mathbb{S}$ . It is obvious that the right hand side **RHS**( $\star$ ) of Lighthill's inhomogeneous wave equation contains not only source terms, but also interaction terms between the sound and flow field, which includes effects, such as convection and refraction of the sound by the flow. Therefore, the whole set of compressible flow dynamics equations has to be solved in order to calculate the right hand side of (3.14). If the right hand side **RHS**( $\star$ ) is computed, a DSC must already resolve the acoustics as implicit part of the right hand side **RHS**( $\star$ ), which is a challenge for any numerical scheme and the computational noisy errors itself may strongly disturb the physical radiating wave components [140]. Phillips and Lilley [141, 142] moved interaction effects, at least to some extent, to the wave operator  $\square$  and predicted certain aspects of jet-noise quite accurately. These effects are neglected by Lighthill's wave operator and are often not present in Lighthill's source term (3.15) due to the restricted numerical resolution of interactions during a preceding flow simulation [143]. For low Mach number flows, the source terms are based on an incompressible CFD, one possible non-radiating base flow, and Lighthill's tensor reduces to

$$\mathbb{T} = \rho_0 \mathbf{u}^{\text{ic}} \mathbf{u}^{\text{ic}} \quad (3.16)$$

with the incompressible flow velocity  $\mathbf{u}^{\text{ic}}$ . The incompressible flow simulation constrains hybrid methods to low Mach numbers and simulation cases, where aeroacoustic feedback is negligible.

### 3.5.2 Explicit reformulation

In year 2003, Goldstein [16] proposed a method to split flow variables  $(p, \mathbf{u}, \dots)$  into a base flow (non-radiating) and a remaining component (acoustic, radiating fluctuations)

$$\star = \tilde{\star} + \star'. \quad (3.17)$$

Although Goldstein's idea has a different perspective, a separation into a base flow and a remaining component shows distinctive features of sound in the source terms and treats the models physically and

mathematically accurate. What are the components, non-radiating or radiating?

### Base flow (preferable non-radiating)

Per definition, the base flow is the flow around the flow equations are linearized. A base flow could either be radiating (compressible CFD) or non-radiating. Due to several drawbacks of radiating base flows (accurate resolution of flow and acoustics, numerical schemes and boundaries adapted to wave phenomena) [16], we prefer the non-radiating base flow. A non-radiating base flow is a base flow that has no radiating components inside, but can possibly emit sound (like an incompressible flow solutions). Prominent realizations of non-radiating base flows are RANS solutions or incompressible flow solutions. RANS simulation base flow techniques yield synthetic noise generation models (SNGR) and reduce the computational workload with respect to a DNS. Incompressible CFD simulations form the basis of hybrid aeroacoustics at low Mach numbers. In the case of a compressible CFD, an incompressible solution is constructed via Helmholtz decomposition (see Chap. 4).

### Remaining component

The residual component deviates from the base flow and is usually small. Depending on the base flow selection, the remaining component describes parts of the radiation, or the complete radiating component, the sound field. Even in supersonic flows, the radiated sound is many orders of magnitude smaller than the non-radiating components. Consequently, numerical errors may hide the acoustic component and suggest to separate the acoustic simulation from the overwhelming base flow.

Applying the decomposition to the right hand side of the wave equation, the left hand side of the equation is already treated in this manner during the derivation of the acoustic analogy, which leads to

$$\square p' = \mathbf{RHS}(\tilde{p}, \tilde{\mathbf{u}}, \tilde{\rho}, p', \mathbf{u}', \rho', \dots). \quad (3.18)$$

Now interaction terms can be moved to the differential operator to take, e.g., convection and refraction effects or even nonlinear interactions<sup>4</sup> into account. Exactly this approach has been applied in the theories of Phillips and Lilley, and furthermore in the derivation of perturbation equations [31, 36, 42, 144].

Referring to Goldstein's concept, the Mach number constraint imposed by the incompressible flow simulation is relaxed. Naturally, this leads to a compressible flow simulation. Acoustics and other radiating components are already incorporated in the flow quantities, composing the right hand side of the wave equation. From a mathematical aspect, these quantities are modeled by the left hand side.

To account for the separation and to avoid the Mach number constraint imposed by the incompressible flow simulation, a three step Mach number extended workflow is proposed. At first, we perform a compressible flow simulation, which incorporates two-way coupling of the flow and acoustics and extends aeroacoustic analogies to physical phenomena, where feedback matters. Secondly, we assume that the main interaction terms between the flow and the acoustic field are modeled by the wave operator, e.g. convection and refraction effects as in the case of APE. Thirdly, the aeroacoustic sources are filtered, such that a non-radiating field is obtained which computes the sources and solves with an appropriate wave operator  $\tilde{\square}$  the radiating field

$$\tilde{\square} p' = \mathbf{RHS}(\tilde{p}, \tilde{\mathbf{u}}, \tilde{\rho}, \dots). \quad (3.19)$$

Thereby, Helmholtz decomposition provides the non-radiating base flow (see Chap. 4). This approach is of high practical relevance, since the decomposition into the base flow mitigates noisy artifacts<sup>5</sup> encountered

<sup>4</sup> The nonlinear interactions (3.30) are described in terms of the acoustic potential  $\phi^a$ .

<sup>5</sup> Acoustic modeling errors due to boundary treatment and numerical scheme dependent resolution of the acoustic waves.

by the use of flow solvers.

An additional note on DSC: the computational variables are the aggregated flow variables and contain both, radiating and non-radiating components. In this case, a decomposition into radiating and non-radiation components extracts sound.

## 3.6 Taylor expansion

Nonlinear partial differential equations can be expanded around an operating condition. In this case the operating condition is the base flow of the underlying flow field. Generally, flow equations<sup>6</sup> can be written in this form

$$\mathbf{F}(p, \mathbf{u}, \rho) = \mathbf{0}. \quad (3.20)$$

An additive decomposition separates the field quantities into a base component  $\tilde{\mathbf{g}} = [\tilde{p}, \tilde{\mathbf{u}}, \tilde{\rho}]^T$  and a perturbation component  $\mathbf{g}' = [p', \mathbf{u}', \rho']^T$

$$\mathbf{g} = \tilde{\mathbf{g}} + \mathbf{g}'. \quad (3.21)$$

The Taylor expansion of  $\mathbf{F}$  is defined as

$$\mathbf{F} = \mathbf{F}(\tilde{\mathbf{g}}) + \nabla_{\mathbf{g}} \mathbf{F}|_{\tilde{\mathbf{g}}} \cdot \mathbf{g}' + (\mathbf{g}')^T \cdot (\nabla_{\mathbf{g}} \nabla_{\mathbf{g}} \mathbf{F})|_{\tilde{\mathbf{g}}} \cdot \mathbf{g}' + \mathcal{O}(\mathbf{g}'^3). \quad (3.22)$$

### 3.6.1 Alternative derivation of Lighthill's Analogy

Taylor expansion of the continuity and the Navier-Stokes equation yields Lighthill's analogy. Assuming a linear acoustic medium at rest, Lighthill's base flow obeys four assumptions:

- The fluid is assumed to be at rest ( $\mathbf{u}_0 = 0$ ) and has a uniform background pressure  $p_0$ , and density  $\rho_0$ .
- The base flow satisfies the continuity equation that yields  $\frac{\partial \rho_0}{\partial t} = 0$ .
- Newtons constitutive equation calculates the baseflow stress tensor  $\mathbb{S}_0 = 0$ .
- By inserting the already defined base flow components into the momentum conservation, an additional pressure condition  $\nabla p_0 = 0$  is determined.

Consequently, the base flow solves the flow equations. The component vector  $\mathbf{g}$  defines the expansion variables

$$\mathbf{g} = [\frac{\partial \rho}{\partial t}, \nabla \cdot (\rho \mathbf{u}), \frac{\partial \rho \mathbf{u}}{\partial t}, \nabla \cdot (\rho \mathbf{u} \mathbf{u}), \nabla p, \nabla \cdot \mathbb{S}]^T. \quad (3.23)$$

Furthermore, the base flow is collected in  $\tilde{\mathbf{g}}$

$$\tilde{\mathbf{g}} = [\frac{\partial \rho_0}{\partial t}, 0, 0, 0, \nabla p_0, ]^T, \quad (3.24)$$

and respectively the nonlinear fluctuating components are

$$\mathbf{g}' = [\frac{\partial \rho - \rho_0}{\partial t}, \nabla \cdot (\rho \mathbf{u}), \frac{\partial \rho \mathbf{u}}{\partial t}, \nabla \cdot (\rho \mathbf{u} \mathbf{u}), \nabla (p - p_0), \nabla \cdot \mathbb{S}]^T. \quad (3.25)$$

The base flow reduces  $\mathbf{F}$  to

$$\mathbf{F}(\tilde{\mathbf{g}}) = \mathbf{0}, \quad (3.26)$$

---

<sup>6</sup> The generic flow equation (3.20) can be any known reformulation of conservation of mass, momentum and energy with flow specific constitutive laws.

and proves that the base flow fulfills the continuity and the momentum equation. A first order approximation desires the gradient of  $\mathbf{F}$  to be

$$\nabla_g \mathbf{F} = \begin{pmatrix} 1 & 1 & 0 & 0 & 0 & 0 \\ 0 & 0 & 1 & 1 & 1 & 1 \end{pmatrix} \quad (3.27)$$

in a standard form, since nonlinear terms are treated in their inherent structure. These ingredients are inserted into Taylor's expansion

$$\frac{\partial \rho - \rho_0}{\partial t} + \nabla \cdot (\rho \mathbf{u}) = 0 \quad (3.28)$$

$$\frac{\partial \rho \mathbf{u}}{\partial t} + \nabla \cdot (\rho \mathbf{u} \mathbf{u}) + \nabla (p - p_0) + \nabla \cdot \mathbb{S} = 0. \quad (3.29)$$

If  $\nabla c_0^2(\rho - \rho_0)$  is added on both sides of the momentum equation (3.29) and  $\nabla \cdot (3.29)$  is subtracted from  $\partial(3.28)/\partial t$ , Lighthill's analogy is derived.

### 3.6.2 RHS linearization of Lighthill's Analogy

The linearization of the source tensor around the vortical base flow leads to a separation of the vortical contribution and all interactions of compressibility and vorticity. This allows a detailed study of vortical sound sources. If there are artificial acoustic domain resonances in the flow solution, they are fully separated into the second nonlinear contribution and do not disturb the sound calculation.

$$\nabla \cdot (\rho \mathbf{u} \mathbf{u}) = \nabla \cdot (\rho^v \mathbf{u}^v \mathbf{u}^v) + (\nabla \cdot (\rho \mathbf{u} \mathbf{u}) - \nabla \cdot (\rho^v \mathbf{u}^v \mathbf{u}^v)) \quad (3.30)$$

Furthermore, the second part contains terms that depend on the solution variable, linearly and nonlinearly, and should be solved iteratively. If all compressible terms are modeled and only acoustics plays a role in (3.30), the additional contributions are functions of the velocity potential  $\phi^a$ . The vortical velocity deviation

$$\mathbf{u}^a = \mathbf{u} - \mathbf{u}^v \sim \nabla \phi^a \quad (3.31)$$

and the vortical density deviation<sup>7</sup>

$$\rho^a = \rho - \rho^v \sim \frac{1}{c^2} \left( \frac{\partial \phi^a}{\partial t} + \mathbf{u}^v \cdot \nabla \phi^a \right) \quad (3.32)$$

are functions of the acoustic particle velocity potential. By inserting these definitions into (3.30)

$$(\nabla \cdot (\rho \mathbf{u} \mathbf{u}) - \nabla \cdot (\rho^v \mathbf{u}^v \mathbf{u}^v)) = \mathcal{O}(\phi^a) + \mathcal{O}((\phi^a)^2) + \nabla \cdot \left( \frac{1}{c^2} \frac{\partial \phi^a}{\partial t} \nabla \phi^a \nabla \phi^a \right) \quad (3.33)$$

non-linear acoustic terms are derived. The additional refraction and scattering due to the base flow is then accounted by the base flow and the wave operator.<sup>8</sup>

<sup>7</sup> Using d'Alembert solution of the wave equation, the convective term of the acoustic density can be neglected for low Mach numbers.

<sup>8</sup> Side note: Interpreting the numerical solution as data bundle, proper orthogonal decomposition (POD) or dynamic mode decomposition (DMD) [145] can be utilized to investigate effects of different interaction modes and if necessary exclude artificial modes.

$$(\nabla \cdot (\rho \mathbf{u} \mathbf{u}) - \nabla \cdot (\rho^v \mathbf{u}^v \mathbf{u}^v)) = \sum_{\text{modes}} \nabla \cdot (\rho \mathbf{u} \mathbf{u}) \quad (3.34)$$

Further investigations of the source data modes determine the energy content and the contribution to the acoustics. Obviously, spurious modes should not contribute to acoustics. Furthermore, the radiation of specific modes can be investigated. If we decompose the deviation from the vortical sources, we clarify the radiation pattern given by refraction, convection and scattering and may explore additional interactions.

### 3.6.3 Modified Lighthill's Analogy

In this section, the base flow is considered to be a RANS simulation (non radiating). Since a RANS simulation is time independent representation of a turbulent flow field, no wave modes are part of the solution. Taylor expansion of the continuity equation and the Navier-Stokes equation yields a modified Lighthill's analogy. The component vector  $\mathbf{g}$  defines the expansion variables

$$\mathbf{g} = [\frac{\partial \rho}{\partial t}, \nabla \cdot (\rho \mathbf{u}), \frac{\partial \rho \mathbf{u}}{\partial t}, \nabla \cdot (\rho \mathbf{u} \mathbf{u}), \nabla p, \nabla \cdot \mathbb{S}]^T. \quad (3.35)$$

For the base flow, we obtain  $\tilde{\mathbf{g}}$

$$\tilde{\mathbf{g}} = \mathbf{g}^{\text{RANS}} = [\frac{\partial \rho^{\text{RANS}}}{\partial t}, \nabla \cdot (\rho \mathbf{u})^{\text{RANS}}, \frac{\partial (\rho \mathbf{u})^{\text{RANS}}}{\partial t}, \nabla \cdot (\rho \mathbf{u} \mathbf{u})^{\text{RANS}}, \nabla p^{\text{RANS}}, \nabla \cdot \mathbb{S}^{\text{RANS}}]^T \quad (3.36)$$

and respectively for the nonlinear fluctuating components

$$\mathbf{g}' = \mathbf{g} - \mathbf{g}^{\text{RANS}}. \quad (3.37)$$

The base flow reduces  $\mathbf{F}$  to

$$\mathbf{F}(\tilde{\mathbf{g}}) = \mathbf{0}, \quad (3.38)$$

and proves that the base flow fulfills the continuity equation and momentum equation. An exact first order approximation delivers the gradient of  $\mathbf{F}$

$$\nabla_{\mathbf{g}} \mathbf{F} = \begin{pmatrix} 1 & 1 & 0 & 0 & 0 & 0 \\ 0 & 0 & 1 & 1 & 1 & 1 \end{pmatrix} \quad (3.39)$$

in a standard form, since nonlinear terms are treated in their inherent structure. Finally, Taylor's expansion yields the modified equation is corrected by the RANS solution

$$\frac{\partial \rho - \rho^{\text{RANS}}}{\partial t} + \nabla \cdot (\rho \mathbf{u}) - \nabla \cdot (\rho \mathbf{u})^{\text{RANS}} = 0 \quad (3.40)$$

$$\begin{aligned} \frac{\partial \rho \mathbf{u}}{\partial t} - \frac{\partial (\rho \mathbf{u})^{\text{RANS}}}{\partial t} + \nabla \cdot (\rho \mathbf{u} \mathbf{u}) - \nabla \cdot (\rho \mathbf{u} \mathbf{u})^{\text{RANS}} \\ + \nabla (p - p^{\text{RANS}}) + \nabla \cdot \mathbb{S} - \nabla \cdot \mathbb{S}^{\text{RANS}} = 0. \end{aligned} \quad (3.41)$$

By supposing that the base flow is a RANS simulation, then the deviation to an URANS or LES is the aeroacoustic source term ( $\Delta \text{URANS/LES}$ ). All unresolved turbulent scales can be modeled by a synthetic turbulence model ( $\Delta \text{STM}$ ), but limitations on the statistical modeling must be solved.

$$\nabla \cdot (\rho^v \mathbf{u}^v \mathbf{u}^v) = (\nabla \cdot (\rho^v \mathbf{u}^v \mathbf{u}^v))^{\Delta \text{URANS/LES}} + (\nabla \cdot (\rho^v \mathbf{u}^v \mathbf{u}^v))^{\Delta \text{STM}} \quad (3.42)$$

### 3.6.4 Linearization of vortex sound

Howe [146] derives the equation of vortex sound and states the relevant assumptions

$$\frac{d}{dt} \frac{1}{c^2} \frac{d}{dt} H - \frac{1}{\rho} \nabla \cdot \rho \nabla H = \frac{1}{\rho} \nabla \cdot (\rho \boldsymbol{\omega} \times \mathbf{u}). \quad (3.43)$$

The substantial derivative is based on the total velocity  $\mathbf{u}$  and therefore the wave operator is nonlinear. Most important is that viscous stresses are negligible for high Reynolds number flows. In contrast to Howe, the total velocity is approximated by the incompressible velocity component and quadratic non-linear contributions to the wave operator are neglected. The linearized equation around the incompressible base

flow leads to a valid approximation, whenever compressible contributions  $u - u^v \ll u$  [138, 139] are small,

$$\frac{dH}{dt} := \frac{\partial H}{\partial t} + \mathbf{u} \cdot \nabla H = \frac{\partial H}{\partial t} + \mathbf{u}^v \cdot \nabla H + (\mathbf{u} - \mathbf{u}^v) \cdot \nabla H. \quad (3.44)$$

Additionally, the incompressible base flow confirms a constant speed of sound and density. As proposed previously, the RHS is linearized and for computational simplicity we neglect the interaction terms.

$$\frac{1}{c^2} \frac{d_v^2}{dt^2} H - \nabla \cdot \nabla H = \nabla \cdot (\boldsymbol{\omega} \times \mathbf{u}^v). \quad (3.45)$$

The linearized wave operator is defined by

$$\frac{d_v H}{dt} := \frac{\partial H}{\partial t} + \mathbf{u}^v \cdot \nabla H. \quad (3.46)$$

All material parameter interactions are neglected. The base flow speed of sound and the base flow density are constant in space and time. Second order effects of the wave operator are neglected

$$\rho^v \left[ \frac{\partial(\mathbf{u} - \mathbf{u}^v) \cdot \nabla H}{\partial t} + \mathbf{u}^v \cdot (\mathbf{u} - \mathbf{u}^v) \cdot \nabla H + (\mathbf{u} - \mathbf{u}^v) \cdot (\mathbf{u}^v) \cdot \nabla H \right] \quad (3.47)$$

$$+ (\rho - \rho^v) \left[ \frac{1}{c^2} \frac{d_v^2}{dt^2} H \right] \quad (3.48)$$

$$- \nabla \cdot (\rho - \rho^v) \nabla H \quad (3.49)$$

and third order effects of the wave operator are neglected

$$\rho^v [(\mathbf{u} - \mathbf{u}^v) \cdot (\mathbf{u} - \mathbf{u}^v) \cdot \nabla H] \quad (3.50)$$

$$+ (\rho - \rho^v) \left[ \frac{\partial(\mathbf{u} - \mathbf{u}^v) \cdot \nabla H}{\partial t} + \mathbf{u}^v \cdot (\mathbf{u} - \mathbf{u}^v) \cdot \nabla H + (\mathbf{u} - \mathbf{u}^v) \cdot (\mathbf{u}^v) \cdot \nabla H \right] \quad (3.51)$$

and fourth order effects of the wave operator are neglected

$$(\rho - \rho^v) [(\mathbf{u} - \mathbf{u}^v) \cdot (\mathbf{u} - \mathbf{u}^v) \cdot \nabla H]. \quad (3.52)$$

Furthermore, first order interaction terms on the right hand side are neglected

$$\nabla \cdot (\boldsymbol{\omega} \times (\mathbf{u} - \mathbf{u}^v)). \quad (3.53)$$

A final remark on the enthalpy: "What is the velocity in the definition of the enthalpy in (2.99)?" The solution variable of a wave equation excites modes that cannot be part of the flow solution. We conclude that this velocity must be the perturbation computed by the wave equation and not the total velocity including the base flow. The wave modes<sup>9</sup> that are excited by the wave operator (3.45) are solutions to this equation

$$\frac{1}{c^2} (\omega^2 - 2\omega \mathbf{k} \cdot \mathbf{u}^v + (\mathbf{k} \cdot \mathbf{u}^v)^2) - k^2 = 0. \quad (3.54)$$

The dispersion relation solves the equation

$$\omega = \frac{2\mathbf{k} \cdot \mathbf{u}^v \pm \sqrt{4(\mathbf{k} \cdot \mathbf{u}^v)^2 - 4((\mathbf{k} \cdot \mathbf{u}^v)^2 - c^2 k^2)}}{2} \quad (3.55)$$

---

<sup>9</sup> Fourier wave number transforms the operators  $\nabla \rightarrow -i\mathbf{k}$  and  $\frac{\partial}{\partial t} \rightarrow i\omega$ .

and describes all solutions on a hyper-surface in 3+1D

$$\omega = \boldsymbol{k} \cdot \boldsymbol{u}^\vee \pm c \frac{\boldsymbol{k} \cdot \boldsymbol{k}}{||\boldsymbol{k}||_2} . \quad (3.56)$$

# 4 Helmholtz decomposition and acoustic analogies

Helmholtz decomposition obtains a vortical base flow satisfying the incompressibility condition. The original version of Helmholtz decomposition assumes an unbounded, simply connected domain, which is of course infeasible for typical engineering applications, like a fan or a duct system. Considering these practical challenges, numerical simulation techniques and the standard approximation methods are developed for finite domains. Without vanishing fields at the boundaries, Helmholtz decomposition causes a non-unique decomposition.

## 4.1 Simply connected domain

A simple example illustrates the topology based non-uniqueness of Helmholtz decomposition. This non-unique component is called harmonic part or potential flow solution, since the field is the solution of Laplace's equation. If additional information about the flow system is given at the boundaries, the harmonic field can be calculated. A velocity field of the form  $\mathbf{u} = (u_0 + \sin(\pi x))\mathbf{e}_x + x\mathbf{e}_y$  is prescribed on the domain  $\Omega = [0, 2]^2$  (see Fig. 4.1).

- The velocity field comes with a vorticity distribution of  $\nabla \times \mathbf{u} = -\mathbf{e}_z$
- and a rate of expansion of  $\nabla \cdot \mathbf{u} = \pi \cos(\pi x)$ .

The point of interest is the decomposition of the velocity field into a compressible and an incompressible field. Both fields are computed by solving a Poisson equation, in 2D. In doing so for the compressible part, the inhomogeneous Neumann problem is solved

$$\nabla \cdot \nabla \phi^* = \nabla \cdot \mathbf{u}, \quad (4.1)$$

with  $\mathbf{n} \cdot \nabla \phi^* = \mathbf{n} \cdot \mathbf{u}$ . The solution  $\mathbf{u}_c^* = \nabla \phi^*$  and the conjugated field  $\mathbf{u} - \mathbf{u}_c^* = \mathbf{u} - \nabla \phi^*$  are  $L^2$ -orthogonal. When the homogeneous Neumann problem is solved

$$\nabla \cdot \nabla \psi = 0, \quad (4.2)$$

with  $\mathbf{n} \cdot \nabla \psi = \mathbf{n} \cdot \mathbf{u}$ , the harmonic solution  $u_\perp = \nabla \psi$  is obtained. The compressible part and its harmonic component is given in Tab. 4.1 and Fig. 4.1. As indicated the compressible part incorporates the harmonic part. Executing the same procedure for the incompressible part  $\mathbf{u}_{ic}^*$ , we decompose the velocity field again and reach the results shown the results are given in Tab. 4.2 and Fig. 4.1. Both decomposition variants extract the same harmonic part, since the boundary conditions dictate the harmonic component as an exterior influence. For these two possible decompositions of one vector field, each one is orthogonal



Table 4.1: Helmholtz decomposition - The compressible part based on the scalar potential.

Scalar potential	Harmonic field (Scalar)
$\phi^* = -\frac{1}{\pi} \cos(\pi x) + u_0 x + b$	$\psi = u_0 x + b$
$\mathbf{u}_c^* = (u_0 + \sin(\pi x))\mathbf{e}_x$	$\mathbf{u}_\perp = u_0 \mathbf{e}_x$

Table 4.2: Helmholtz decomposition - The incompressible part based on the vector potential.

Vector potential	Harmonic field (Vector)
$A_z^* = u_0 y - \frac{1}{2}x^2 + b$	$B_z = u_0 y + b$
$\mathbf{u}_{ic}^* = u_0 \mathbf{e}_x + x \mathbf{e}_y$	$\mathbf{u}_\perp = u_0 \mathbf{e}_x$

to its conjugated field. The question is, whether the separately decomposed fields  $(\mathbf{u}_c^*, \mathbf{u}_{ic}^*)$  are orthogonal or not?  $L^2$ -orthogonality implies that

$$\int_{[0,2]^2} \mathbf{u}_c^* \cdot \mathbf{u}_{ic}^* d\mathbf{x} = \|u_0\|_{L^2} > 0 \quad (4.3)$$

vanishes and  $L^2$ -orthogonality concludes nonorthogonality. As a remedy, we establish a unique decomposition through an additional condition causing a unique boundary.

## 4.2 Helmholtz decomposition

In the next chapters, we concentrate on the computability and uniqueness of Helmholtz's decomposition. By the weak formulation of Helmholtz's decomposition, the existence of strong derivatives of the potentials  $C^2$  reduces to  $C^1$ . This weak formulation is then discretized by the finite element method.

**Theorem 4.2.1** *Every square integrable vector field  $\mathbf{u} \in [L_2(\Omega)]^3$ ,  $C^1$  smooth, on a simply connected, Lipschitz domain  $\Omega \subseteq \mathbb{R}^3$ , has an  $L^2$ -orthogonal decomposition*

$$\mathbf{u} = \mathbf{u}^{ic} + \mathbf{u}^c = \nabla \times \mathbf{A}^{ic} + \nabla \phi^c, \quad (4.4)$$

with the vector potential  $\mathbf{A}^{ic} \in H(\text{curl}, \Omega)$  and the scalar potential  $\phi^c \in H^1(\Omega)$  [147].

The vector potential is unique up to an additive component  $\nabla \times (\mathbf{A}^{ic} + \mathbf{C}) = \nabla \times (\mathbf{A} + \nabla \theta + \mathbf{C})$ , that can be represented by a gradient field of a scalar function  $\theta$  and a constant vector field  $\mathbf{C}$ . Uniqueness of the vector potential can be incorporated by the gauge condition  $\nabla \cdot (\mathbf{A}^{ic} + \mathbf{C}) = 0$ . Especially, the scalar/vector potential Neumann problem is unique up to an additive constant/constant vector field. These issues are treated by mass regularization and adequate function spaces [148]. The  $L^2$ -orthogonality of the decomposed components implies

$$(\mathbf{u}^{ic}, \mathbf{u}^c) = \int_{\Omega} \mathbf{u}^{ic} \cdot \mathbf{u}^c d\mathbf{x} = 0. \quad (4.5)$$

Integration by parts leads to a general orthogonality condition for the boundaries for the scalar potential

$$(\mathbf{u}^{ic}, \mathbf{u}^c) = -(\nabla \cdot \mathbf{u}^{ic}, \phi^c) + \int_{\partial\Omega} \phi^c (\mathbf{u} - \nabla \phi^c) \cdot \mathbf{n} ds = \int_{\partial\Omega} \phi^c (\mathbf{u} - \nabla \phi^c) \cdot \mathbf{n} ds = 0. \quad (4.6)$$

This implies unique boundaries for the scalar potential; either the scalar potential has a homogeneous Dirichlet boundary or the normal component of the velocity is entirely captured by the scalar potential.

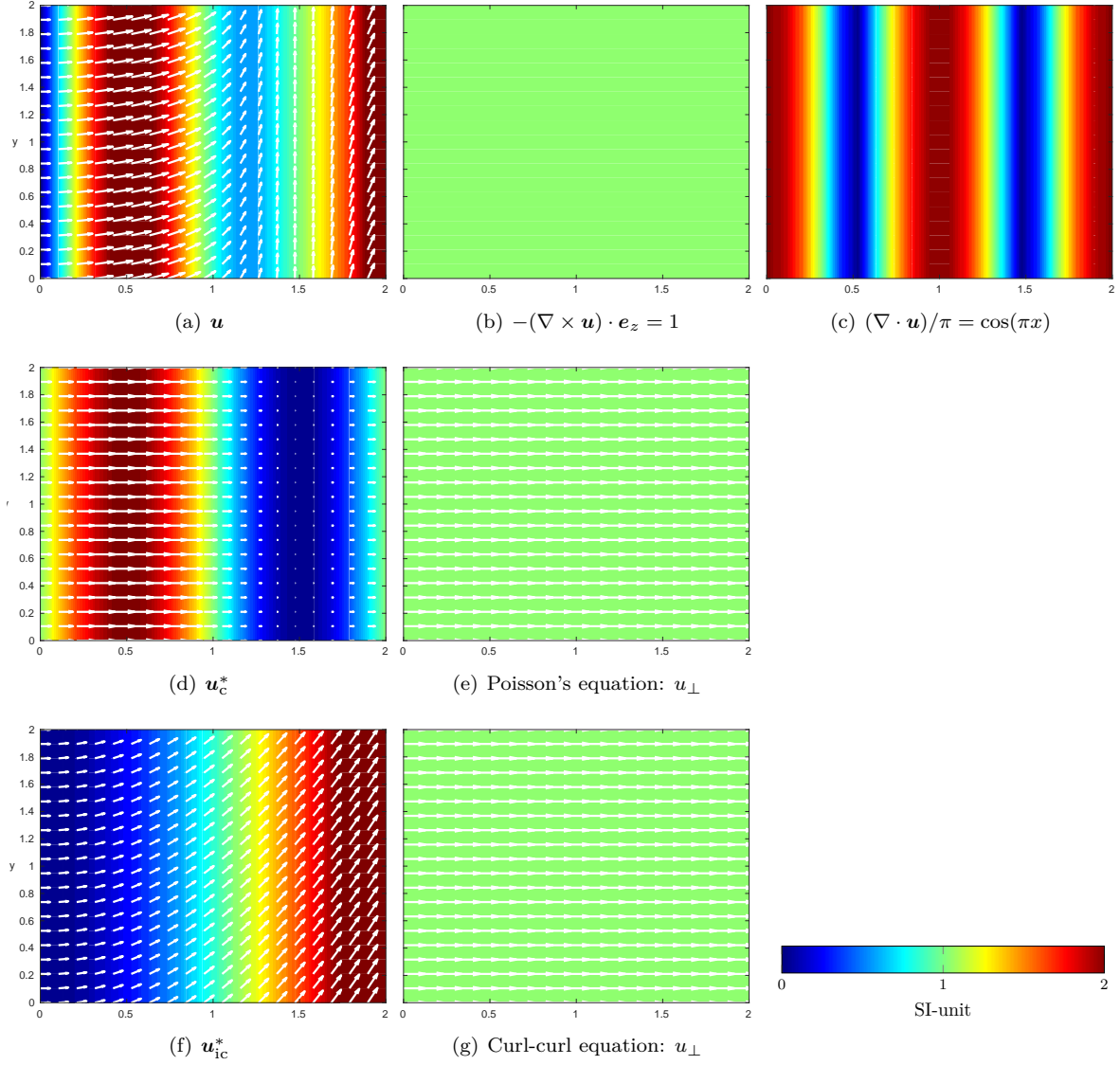


Figure 4.1: This figure illustrates the functions of the simple example. The total velocity field is given in (a), (b) shows the vorticity distribution, (c) the rate of expansion. The figures (d) and (e) show the results of the Poisson's equation, respectively the scalar potential formulation of the Helmholtz decomposition, whereas (f) and (g) show the results for the vortical component and the homogeneous solution of the curl-curl equation.

Applying the same derivation to the vector potential leads to

$$(\mathbf{u}^{\text{ic}}, \mathbf{u}^{\text{c}}) = (\mathbf{A}^{\text{ic}}, \nabla \times \mathbf{u}^{\text{c}}) + \int_{\partial\Omega} \mathbf{A}^{\text{ic}} \cdot (\mathbf{u} - \nabla \times \mathbf{A}^{\text{ic}}) \times \mathbf{n} ds = 0. \quad (4.7)$$

Satisfying a unique boundary for the vector potential is more involved then for the scalar potential. The first possibility is a homogeneous Dirichlet boundary; the second choice is a vector potential, orthogonal to the compressible part of the decomposition  $\mathbf{u}^{\text{c}}$  or  $\mathbf{u}^{\text{c}}|_{\partial\Omega} = \mathbf{0}$ . Boundary treatment is fundamental and can be incorporated in the prescribed function space of the scalar and vector potential. An orthogonal Helmholtz decomposition satisfies (4.6), (4.7) at the boundaries [58]. Depending on the boundaries, it is possible to extract different decompositions that fulfill the orthogonality condition. The conjugated decomposition pair is always a solution of the inverse problem. Each choice of a unique boundary leads to a distinct separation of the harmonic field that represents the exterior properties  $\mathbb{R}^3/\Omega$  of the decomposed vector field  $\mathbf{u}$ .

### 4.3 Scalar potential

In this section, we derive the equation for the scalar potential  $\phi^{*,\text{c}} \in H^1(\Omega)$ , which is associated with the compressible part and the property  $\nabla \times \mathbf{u}^{*,\text{c}} = 0$ . The star denotes the joint function of both, the compressible and the harmonic one.

$$\mathbf{u} = \nabla \times \mathbf{A}^{\text{ic}} + \nabla \phi^{*,\text{c}} \quad (4.8)$$

$$\nabla \phi^{*,\text{c}} = \mathbf{u}^{*,\text{c}} = \mathbf{u}^{\text{c}} + \mathbf{u}^{\text{h}} = \nabla \phi^{\text{c}} + \nabla \phi^{\text{h}} + \mathbf{u}^{\text{holes}} \quad (4.9)$$

A harmonic part  $\mathbf{u}^{\text{h}}$  can be further split into parts accounting for closed boundary curves [149]. Each domain hole, representing solid cutouts, defines a homogeneous Neumann boundary with  $\mathbf{u}^{\text{holes}} \cdot \mathbf{n} = 0$  on the boundary (see Sec. 4.6). The homogeneous Neumann boundary (solid, no penetration, no slip boundaries in continuum theory) is intrinsically satisfied by the finite element formulation. However, a general penetrating wall implies an inhomogeneous Neumann boundary.

By taking the divergence of equation (4.8), we obtain a scalar valued Poisson equation with the dilatation  $\nabla \cdot \mathbf{u}$  as forcing

$$\nabla \cdot \nabla \phi^{*,\text{c}} = \nabla \cdot \mathbf{u}. \quad (4.10)$$

The function space of the scalar potential has to obey (4.6) to enforce an orthogonal decomposition and has to be adjusted for different flow problems.

#### 4.3.1 Weak formulation

Starting from the strong formulation, we derive the weak formulation of the partial differential equations and apply the finite element method. Therefore, we multiply the equation by a test function  $\psi \in H^1(\Omega)$  and integrate over the constitutive domain  $\Omega$

$$\int_{\Omega} \psi (\nabla \cdot \nabla \phi) dx = \int_{\Omega} \psi \nabla \cdot \mathbf{u} dx. \quad (4.11)$$

Partial integration of the volume integral

$$\int_{\Omega} \nabla \psi \cdot \nabla \phi dx - \int_{\Omega} \psi (\nabla \cdot \nabla \phi) dx = \int_{\partial\Omega} \psi (\nabla \phi \cdot \mathbf{n}) ds \quad (4.12)$$

leads to the weak form of the partial differential equation and the requirement on the function space is reduced. The differentiation operator swaps onto the test function and an additional surface integral arises over the boundary  $\partial\Omega$  of the domain  $\Omega$ . This is the final equivalent weak formulation of the partial differential equation

$$\int_{\Omega} \nabla \psi \cdot \nabla \phi \, dx - \int_{\partial\Omega} \psi (\nabla \phi \cdot \mathbf{n} \, ds) = \int_{\Omega} \psi \nabla \cdot \mathbf{u} \, dx. \quad (4.13)$$

The boundary term can be expressed in terms of the derivative with respect to the normal direction or as the normal component of the compressible velocity component

$$\int_{\partial\Omega} \psi (\nabla \phi \cdot \mathbf{n} \, ds) = \int_{\partial\Omega} \psi \frac{\partial \phi}{\partial n} \, ds = \int_{\partial\Omega} \psi (\mathbf{u}^c \cdot \mathbf{n} \, ds). \quad (4.14)$$

Functions  $\phi \in \mathbf{V}$  are in the infinite function space  $\mathbf{V}$

$$\mathbf{V} = \{\phi(x) | \phi(x) \in H^1(\Omega), \phi(x) = \phi_e(x) \text{ on } \Gamma_e\}, \quad (4.15)$$

and the corresponding test function  $\psi \in \mathbf{W}$  is in the space  $\mathbf{W}$

$$\mathbf{W} = \{\psi(x) | \psi(x) \in H^1(\Omega), \psi(x) = 0 \text{ on } \Gamma_e\}. \quad (4.16)$$

$H^1(\Omega)$  denotes the standard Sobolev-space of the domain  $\Omega$ .  $\Gamma_e \subset \partial\Omega$  includes all essential boundaries, also named homogeneous Dirichlet boundaries. The boundary term  $\frac{\partial \phi}{\partial n}$  for each subsurface (wall, free boundary, inlet, outlet, and symmetry) must be modeled in compliance with the flow field. Section 4.3.2 discusses typical flow boundaries. The implemented weak formulation is

$$\int_{\Omega} \nabla \psi \cdot \nabla \phi \, dx - \int_{\partial\Omega} \psi \frac{\partial \phi}{\partial n} \, ds = \int_{\Omega} \psi \nabla \cdot \mathbf{u} \, dx. \quad (4.17)$$

For a Neumann problem  $\Gamma_e = 0$  we get the following bilinear form

$$B(\psi, \phi) = \int_{\Omega} \nabla \psi \cdot \nabla \phi \, dx - \int_{\partial\Omega} \psi \frac{\partial \phi}{\partial n} \, ds = \int_{\Omega} \psi \nabla \cdot \mathbf{u} \, dx. \quad (4.18)$$

The bilinear form  $B(\psi, \phi)$  is not coercive for a constant function  $\theta_c$

$$B(\theta_c, \theta_c) = 0 < c \|\theta_c\|_{H^1}. \quad (4.19)$$

Mass regularization recovers the elliptic property, by introducing a small parameter  $0 < \epsilon_{\text{reg}} \ll 1$ , for the Neumann problem

$$B^\epsilon(\psi, \phi^\epsilon) = \int_{\Omega} (\nabla \psi \cdot \nabla \phi^\epsilon + \epsilon_{\text{reg}} \psi \phi^\epsilon) \, dx - \int_{\partial\Omega} \psi \frac{\partial \phi^\epsilon}{\partial n} \, ds = \int_{\Omega} \psi \nabla \cdot \mathbf{u} \, dx, \quad (4.20)$$

and now the bilinear form is coercive

$$B^\epsilon(\theta_c, \theta_c) \geq c \|\theta_c\|_{H^1}^2. \quad (4.21)$$

Finally, mass regularization converges if  $\phi^\epsilon \rightarrow \phi$  as  $\epsilon_{\text{reg}} \rightarrow 0$ .

$$B^\epsilon(\psi, \phi^\epsilon) - B(\psi, \phi) = B^\epsilon(\psi, \phi^\epsilon - \phi) - \int_{\Omega} \epsilon_{\text{reg}} \psi \phi \, dx = 0 \quad (4.22)$$

Utilizing the Friedrich's-type inequality yields for the coercive functional

$$c_1 \|\phi^\epsilon - \phi\|_{L_2}^2 \leq c \|\phi^\epsilon - \phi\|_{L_2}^2 + c \|\nabla(\phi^\epsilon - \phi)\|_{L_2}^2 = c \|\phi^\epsilon - \phi\|_{H^1}^2 \quad (4.23)$$

$$\leq B^\epsilon(\phi^\epsilon - \phi, \phi^\epsilon - \phi) = \epsilon_{\text{reg}}(\phi, \phi^\epsilon - \phi) \quad (4.24)$$

and by using the Cauchy-Schwartz inequality

$$\epsilon_{\text{reg}}(\phi, \phi^\epsilon - \phi) \leq \epsilon_{\text{reg}} \|\phi\|_{L_2} \|\phi^\epsilon - \phi\|_{L_2} . \quad (4.25)$$

In general

$$c_1 \|\phi^\epsilon - \phi\|_{L_2} \leq \epsilon_{\text{reg}} \|\phi\|_{L_2} \quad (4.26)$$

holds and  $\phi^\epsilon \rightarrow \phi$  converges as  $\epsilon_{\text{reg}} \rightarrow 0$ . To obtain the finite element formulation of (4.20), the continuous domain is discretized by a mesh  $\Omega^h \subset \Omega$  and a function space approximation restricts the infinite function space of the field and the test function by a finite subset  $\mathbf{V}^h \subset \mathbf{V}$ , and  $\mathbf{W}^h \subset \mathbf{W}$ .

### 4.3.2 Boundary conditions

The preceding derivation seeks for flow conforming boundary conditions. Based on the orthogonality condition (4.6), we identify the following boundaries for the scalar Poisson problem:

**Wall** At perfectly smooth, no slip, non-penetrated wall boundaries, the flow velocity in normal direction is equal to the compressible wall penetration movement ( $\mathbf{u} \cdot \mathbf{n} = 0 \Rightarrow \mathbf{u}^{\text{ic}} \cdot \mathbf{n} = -\mathbf{u}^c \cdot \mathbf{n}$ ). Assuming a non-penetrating wall for the incompressible component implies

$$\frac{\partial \phi}{\partial n} = \mathbf{u}^c \cdot \mathbf{n} = 0 . \quad (4.27)$$

The condition represents sound hard wall, if the compressible component is interpreted as acoustics.

**Outlet and Inlet** Since the condition of a velocity inlet is in general nonzero ( $\mathbf{u}^{\text{ic}} \cdot \mathbf{n} \neq 0$ ), the orthogonality condition (4.6) leads to

$$\phi = 0 . \quad (4.28)$$

**Symmetry:** A symmetry condition of the field prevents flux exchange over the boundary  $\mathbf{u} \cdot \mathbf{n} = 0$  and respectively  $\mathbf{u}^{\text{ic}} \cdot \mathbf{n} = 0$ .

$$\frac{\partial \phi}{\partial n} = \mathbf{u}^c \cdot \mathbf{n} = 0 \quad (4.29)$$

In viscous flows, the symmetry condition is equivalent to a slipping wall with zero shear.

**Periodic** Periodic conditions satisfy both Dirichlet and Neumann connections of the corresponding periodic interfaces and they maintain the physical quantity and flux.

**Free field - Asymptotic boundary condition/Infinite Mapping Layer** One possible choice is an asymptotic boundary condition for elliptic partial differential equations [150]

$$\frac{\partial \phi}{\partial n} = -\frac{\phi}{r} . \quad (4.30)$$

This boundary condition treats infinity well for circular surfaces and for known point sources distances  $r$ . Typically, the point source distance is unknown and circular domains are inefficient. Therefore, a general

treatment of infinite domains has been developed, called infinite mapping layer (IML). Appendix A illustrates further details on IML. This layer merges benefits of infinite elements and layer techniques to overcome infinite problem domains. The domain extension towards infinity allows the field quantities to have enough space to decay sufficiently. In contrast to hybrid schemes based on analytic Green's functions, the IML is solution independent. Compared to a hybrid method using BEM at the boundary, the IML conserve sparsity and locality of the numerical system. The method works for both linear and nonlinear systems.

### 4.3.3 Poisson problem – Shortcomings

The formulation of the scalar potential, with its algorithmic simplicity and computational efficiency (compared to the vector potential formulation), has two severe drawbacks.

- The computational domain of the scalar potential should capture compressible effects e.g. acoustics. Acoustic radiation in a free field configuration would reach to infinity and the acoustic variable is decaying with  $O(1/||\mathbf{x}||_2)$ . This slow decay results in an involved boundary for the free field. A possible solution strategy is the IML.
- A second issue arises for non-convex domains with a  $C^0$  smooth boundary, like reentrant corners. For such flow domains, the computation of the scalar potential leads to a singular point in the corner and corrupts the solution. Using FEM, a graded mesh can treat this singularity. However, in most cases these reentrant corners are the main aeroacoustic source regions.

Caused by these two drawbacks, the computationally efficient scalar potential separation is limited and we suggest the computation of the vector potential.

## 4.4 Singularity at reentrant corners

To show the limitations of the scalar potential, the singularities of reentrant corner for the both possible Helmholtz decompositions are analyzed. The key difference is the incompressibility condition for the vector potential that ensures a bounded solution of the derivative.

### 4.4.1 Poisson problem

We derive the order of the singularity, occurring at reentrant corners. The investigation is carried out on a wedge with a wedge angle  $\Theta$  (see Fig. 4.2). At a specific angle ( $\Theta < \pi$ ) the domain is convex and for larger angles than  $\pi$  the domain becomes concave. On both radial domain borders a homogeneous Neumann boundary condition, a sound hard wall, is imposed

$$\nabla\phi(r, \theta)|_{\theta=0} = \nabla\phi(r, \theta)|_{\theta=\Theta} = 0. \quad (4.31)$$

According to the Helmholtz decomposition, a Poisson problem is computed on this wedge domain. The Laplace operator in polar coordinates is written as

$$\Delta\phi(r, \theta) = \frac{1}{r} \frac{\partial}{\partial r} r \frac{\partial \phi}{\partial r} + \frac{1}{r^2} \frac{\partial^2 \phi}{\partial \theta^2} = 0. \quad (4.32)$$

A multiplicative variable decomposition ansatz  $\phi(r, \theta) = R(r)\Psi(\theta)$  separates the variables

$$\alpha^2 = \frac{\frac{1}{r} \frac{\partial}{\partial r} r \frac{\partial R}{\partial r}}{R} = -\frac{\frac{\partial^2 \Psi}{\partial \theta^2}}{\Psi}. \quad (4.33)$$

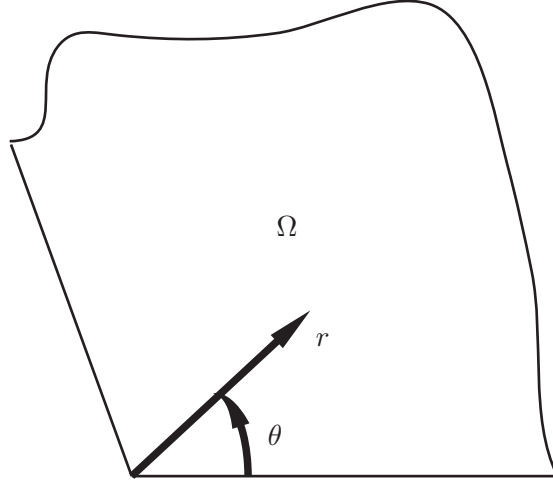


Figure 4.2: A wedge subdomain for the Poisson problem, wedge angle  $\Theta$ .

The separate functions depend exclusively on different variables. Therefore, the conglomerates (4.33) are constant  $\alpha^2$ . The general solution

$$\Psi(\theta) = a \cos(\alpha\theta) + b \sin(\alpha\theta) \quad (4.34)$$

$$R(r) = cr^\alpha + dr^{-\alpha} \quad (4.35)$$

holds for  $\alpha > 0$ . From the second equation, unbounded solutions at  $r \rightarrow 0$  are excluded by choosing  $d = 0$ . A bounded solution at the origin leads to a constant function for  $\alpha = 0$ . The Neumann boundary at  $\theta = 0$  selects  $b = 0$  and the second radial Neumann boundary provides the condition

$$\nabla\phi(r, \theta)|_{\theta=\Theta} = \frac{1}{r} \frac{d\Psi}{d\theta}|_{\theta=\Theta} = -\frac{a\alpha}{r} \sin(\alpha\theta) = 0. \quad (4.36)$$

For all  $\alpha_k = \frac{\pi k}{\Theta}$   $k \in \{1, 2, \dots, n\}$ , the characteristic (4.36) of the boundary value problem is fulfilled. The solution of the wedge is

$$\phi(r, \theta) = \sum_{k=1}^{\infty} A_k r^{\alpha_k} \cos(\alpha_k \theta). \quad (4.37)$$

If the angle of the domain is  $\Theta > \pi$ , the gradient of the leading term  $k = 1$  tends to infinity for  $r \rightarrow 0$  and a singularity occurs at the origin of reentrant corners.

#### 4.4.2 Curl-curl equation

The alternative vector formulation of the Helmholtz decomposition overcomes the reentrant corner singularity. Again, by assuming Coulomb gauge condition  $\nabla \cdot \mathbf{A} = 0$ , a Poisson equation in two dimensional space for the  $z$  component of the vector potential  $A_z$  is solved

$$\Delta A_z = 0. \quad (4.38)$$

However, the boundary conditions are different

$$\nabla \times A_z(r, \theta) \mathbf{e}_z \times \mathbf{n}|_{\theta=0} = \nabla \times A_z(r, \theta) \mathbf{e}_z \times \mathbf{n}|_{\theta=\Theta} = 0. \quad (4.39)$$

Applying the same analysis and ansatz as in the preceding derivation  $d = 0$ ,  $b = 0$ , the second radial Neumann boundary provides a condition for  $a$

$$-\frac{1}{r} \frac{dA_z}{d\theta} \Big|_{\theta=\Theta} = \frac{a\alpha}{r} \sin(\alpha\theta) = 0. \quad (4.40)$$

For all  $\alpha_k = \frac{\pi k}{\Theta}$   $k \in \{1, 2, \dots, n\}$  the characteristic of the boundary value problem is fulfilled. The solution constitutes as

$$A_z(r, \theta) = \sum_{k=1}^{\infty} A_{zk} r^{\alpha_k} \cos(\alpha_k \theta). \quad (4.41)$$

Again, the gradient of the leading term  $k = 1$  tends to infinity for  $r \rightarrow 0$ , when the angle of the domain  $\Theta > \pi$ . A singularity occurs at the origin for  $k = 1$ , but the vector potential obeys divergence freedom. To control divergence for  $k = 1$ , we integrate the normal component of the velocity  $\mathbf{u} \cdot \mathbf{n} = \nabla \times A_z \mathbf{e}_z \cdot \mathbf{n}$  on a closed path  $\Gamma$  (see Fig. 4.3).

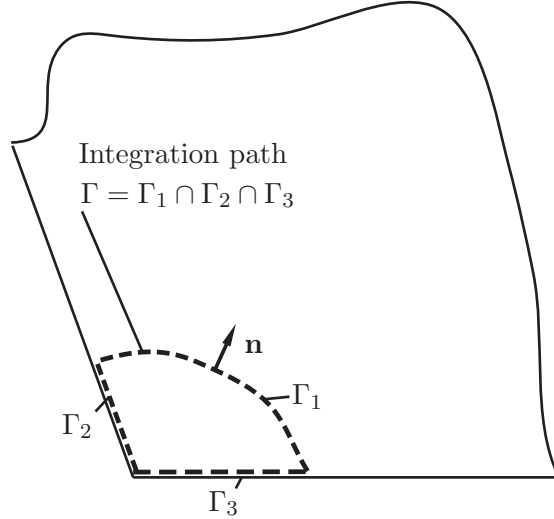


Figure 4.3: Integration path to evaluate global divergence free fields.

The condition for a global divergence free field is

$$\lim_{r \rightarrow 0} \iiint_V \nabla \cdot \mathbf{u} \, dV = \lim_{r \rightarrow 0} \int_{\Gamma} \mathbf{u} \cdot \mathbf{n} \, ds = 0, \quad (4.42)$$

where  $\mathbf{u}$  is a divergence free vector field. Thus, the sum of the integrals over  $\Gamma_2$  and  $\Gamma_3$  is zero, due to a no slip wall boundary. This implies that the integral over  $\Gamma_1$  must vanish for divergence free fields

$$\lim_{r \rightarrow 0} \frac{\pi}{\Theta} A_{z1} r^{\frac{\pi}{\Theta}-1} \int_0^{\Theta} \sin\left(\frac{\pi}{\Theta} \theta\right) d\theta = - \lim_{r \rightarrow 0} A_{z1} r^{\frac{\pi}{\Theta}-1} \left[ \cos\left(\frac{\pi}{\Theta} \theta\right) \right]_0^{\Theta} = \lim_{r \rightarrow 0} A_{z1} r^{\frac{\pi}{\Theta}-1} = 0 \text{ if } A_{z1} = 0, \quad (4.43)$$

hence, the odd  $k = 1$  with  $A_{z1} = 0$ . In particular, all odd  $k$  coefficients  $\alpha_k$  must vanish and no singularity occurs for  $\theta < 2\pi$ . In contrast, all even coefficients are non zero,  $A_{zk} \neq 0$ , and the series of orthogonal functions in  $\theta$  accounts for the wall boundary.



## 4.5 Vector potential

The Helmholtz decomposition, formulated by the vector potential  $\mathbf{A}^{*,ic} \in H(\text{curl}, \Omega)$ , is associated with the incompressible part and the property  $\nabla \cdot \mathbf{u}^{*,ic} = 0$ . A star superscript denotes the joint function of the incompressible and the harmonic part

$$\mathbf{u} = \nabla \times \mathbf{A}^{*,ic} + \nabla \phi^c \quad (4.44)$$

$$\nabla \times \mathbf{A}^{*,ic} = \mathbf{u}^{*,ic} = \mathbf{u}^{ic} + \mathbf{u}^h = \nabla \times \mathbf{A}^{ic} + \nabla \times \mathbf{A}^h + \mathbf{u}^{\text{holes}}. \quad (4.45)$$

As it applies for the scalar potential formulation, the harmonic part accounts for the exterior and interior cutouts [149], with  $\mathbf{u}^{\text{holes}} \times \mathbf{n} = \mathbf{0}$  at a no-slip boundary. The function space of the vector potential enforces an orthogonal and unique decomposition (4.7) and has to be adjusted for different flow problems. By taking the curl of equation (4.44), the curl-curl equation for the vector potential  $\mathbf{A}^{*,ic}$  is obtained

$$\nabla \times \nabla \times \mathbf{A}^{*,ic} = \nabla \times \mathbf{u} = \boldsymbol{\omega}, \quad (4.46)$$

forced by the vorticity  $\boldsymbol{\omega} = \nabla \times \mathbf{u}$ . However, the harmonic component of the vector potential can also be represented by a scalar potential.

### 4.5.1 Weak formulation

From the strong formulation, we derive the weak formulation of the partial differential equations and apply the finite element method. Therefore, a test function  $\mathbf{A}' \in H(\text{curl}, \Omega)$  is multiplied onto the curl-curl equation and the equation is integrated over the domain  $\Omega$

$$\int_{\Omega} \mathbf{A}' \cdot (\nabla \times \nabla \times \mathbf{A}) dx = \int_{\Omega} \mathbf{A}' \cdot \boldsymbol{\omega} dx. \quad (4.47)$$

The next step is indispensable when deriving a weak formulation. Integration by parts reduces the regularity of the function space from  $C^2$  to  $C^1$ . The divergence theorem (Gauss's theorem) is written as

$$\int_{\Omega} \nabla \times \mathbf{F} \cdot \mathbf{G} dx - \int_{\Omega} \mathbf{F} \cdot \nabla \times \mathbf{G} dx = \int_{\partial\Omega} \mathbf{F} \times \mathbf{G} \cdot \mathbf{n} ds, \quad (4.48)$$

and leads to the following equivalent weak formulation of the partial differential equation

$$\int_{\Omega} (\nabla \times \mathbf{A}') \cdot (\nabla \times \mathbf{A}) dx - \int_{\partial\Omega} \mathbf{A}' \times (\nabla \times \mathbf{A}) \cdot \mathbf{n} ds = \int_{\Omega} \mathbf{A}' \cdot \boldsymbol{\omega} dx. \quad (4.49)$$

Gauss's theorem swaps the differentiation operator to the test function (weak derivative); an additional surface integral arises over the domain boundary  $\partial\Omega$ . The Neumann boundary condition enters into the surface integral and the vector identity reformulates the Neumann boundary to the tangential velocity field

$$\mathbf{A}' \times (\nabla \times \mathbf{A}) \cdot \mathbf{n} = \mathbf{A}' \cdot (\nabla \times \mathbf{A}) \times \mathbf{n} = \mathbf{A}' \cdot (\mathbf{u}^{*,ic} \times \mathbf{n}). \quad (4.50)$$

Section 4.5.2 discusses flow conforming inhomogeneous Neumann boundaries and specific model of  $\mathbf{u}^{*,ic}$  at the boundaries. Finally, the weak formulation reads as

$$\int_{\Omega} (\nabla \times \mathbf{A}') \cdot (\nabla \times \mathbf{A}) dx - \int_{\partial\Omega} \mathbf{A}' \cdot (\mathbf{u}^{*,ic} \times \mathbf{n}) ds = \int_{\Omega} \mathbf{A}' \cdot \boldsymbol{\omega} dx. \quad (4.51)$$

The functions  $\mathbf{A} \in \mathbf{V}$  are defined in the infinite function space  $\mathbf{V}$

$$\mathbf{V} = \{\mathbf{A}(x) | \mathbf{A}(x) \in H(\text{curl}, \Omega), \mathbf{A}(x) = \mathbf{A}_e(x) \text{ on } \Gamma_e\}, \quad (4.52)$$

and the corresponding test functions  $\mathbf{A}' \in \mathbf{W}$  are in the space  $\mathbf{W}$

$$\mathbf{W} = \{\mathbf{A}'(x) | \mathbf{A}'(x) \in H(\text{curl}, \Omega), \mathbf{A}'(x) = 0 \text{ on } \Gamma_e\}. \quad (4.53)$$

$H(\text{curl}, \Omega) = \{\mathbf{u} \in [L_2]^3 : \nabla \times \mathbf{u} \in [L_2]^3\}$  denotes the curl-space of the domain  $\Omega$  with the corresponding norm

$$\|\mathbf{u}\|_{H(\text{curl})}^2 = \|\mathbf{u}\|_{L_2}^2 + \|\nabla \times \mathbf{u}\|_{L_2}^2, \quad (4.54)$$

and the essential boundary  $\Gamma_e \subset \partial\Omega$ . Although, the vector potential is in the desired function space, it is non-unique

$$\mathbf{A}^+ = \mathbf{A}^* + \nabla \Pi. \quad (4.55)$$

When the incompressible velocity is computed, the gradient field vanishes

$$\mathbf{u}^{*,\text{ic}} = \nabla \times (\mathbf{A}^{*,\text{ic}} - \nabla \Pi) = \nabla \times \mathbf{A}^{*,\text{ic}}. \quad (4.56)$$

In order to select a unique solution, the vector potential is gauged. The coulomb gauge condition

$$\nabla \cdot \mathbf{A}^{*,\text{ic}} = 0 \quad (4.57)$$

may be incorporated by a Lagrange constraint or mass regularization.

This section further proofs that mass regularization and Coulomb gauging are equivalent in the limit of a vanishing mass regularization parameter. For simplicity homogeneous Neumann boundaries are assumed and a second functional (Lagrange constraint) regularizes the Neumann problem. In doing so, a saddle point problem for  $\mathbf{A} \in H(\text{curl}, \Omega)$  and  $\varphi \in H^1(\Omega)/\mathbb{R}$  is solved

$$\begin{aligned} \int_{\Omega} (\nabla \times \mathbf{A}') \cdot (\nabla \times \mathbf{A}) dx + \int_{\Omega} \mathbf{A}' \cdot \nabla \varphi dx &= \int_{\Omega} \mathbf{A}' \cdot \boldsymbol{\omega} dx & \forall \mathbf{A}' \in H(\text{curl}, \Omega) \\ \int_{\Omega} \mathbf{A} \cdot \nabla \psi dx &= 0 & \forall \psi \in H^1(\Omega)/\mathbb{R}. \end{aligned} \quad (4.58)$$

Mass regularization determines the vector potential  $\mathbf{A}^\epsilon$  uniquely with a small mass parameter  $0 < \epsilon_{\text{reg}} \ll 1$

$$B^\epsilon(\mathbf{A}', \mathbf{A}^\epsilon) = \int_{\Omega} (\nabla \times \mathbf{A}') \cdot (\nabla \times \mathbf{A}^\epsilon) dx + \int_{\Omega} \epsilon_{\text{reg}} \mathbf{A}' \cdot \mathbf{A}^\epsilon dx = \int_{\Omega} \mathbf{A}' \cdot \boldsymbol{\omega} dx, \quad (4.59)$$

with  $\int_{\Omega} \nabla \theta \cdot \boldsymbol{\omega} dx = 0 \quad \forall \theta \in H^1(\Omega)$ . The vorticity is divergence free and cannot be represented as a gradient field. Under this assumption the operator

$$B(\mathbf{A}', \mathbf{A}^\epsilon) = \int_{\Omega} (\nabla \times \mathbf{A}') \cdot (\nabla \times \mathbf{A}^\epsilon) dx = \int_{\Omega} \mathbf{A}' \cdot \boldsymbol{\omega} dx, \quad (4.60)$$

is not coercive for  $\theta \in H^1(\Omega)$

$$B(\nabla \theta, \nabla \theta) = 0 < c \|\nabla \theta\|_{H(\text{curl}, \Omega)}. \quad (4.61)$$

We have to proof that  $\mathbf{A}^\epsilon \rightarrow \mathbf{A}$  converges in the limit  $\epsilon_{\text{reg}} \rightarrow 0$ .

$$B^\epsilon(\mathbf{A}', \mathbf{A}^\epsilon) - B(\mathbf{A}', \mathbf{A}^\epsilon) = B^\epsilon(\mathbf{A}', \mathbf{A}^\epsilon - \mathbf{A}) - \int_{\Omega} \epsilon_{\text{reg}} \mathbf{A}' \cdot \mathbf{A} dx = 0 \quad (4.62)$$

Friedrich's-type inequality estimates the coercive functional

$$c_1 \|\mathbf{A}^\epsilon - \mathbf{A}\|_{L_2}^2 \leq c \|\mathbf{A}^\epsilon - \mathbf{A}\|_{L_2}^2 + c \|\nabla \times (\mathbf{A}^\epsilon - \mathbf{A})\|_{L_2}^2 = c \|\mathbf{A}^\epsilon - \mathbf{A}\|_{H^1}^2 \quad (4.63)$$

$$\leq B^\epsilon(\mathbf{A}^\epsilon - \mathbf{A}, \mathbf{A}^\epsilon - \mathbf{A}) = \epsilon_{\text{reg}}(\mathbf{A}, \mathbf{A}^\epsilon - \mathbf{A}) \quad (4.64)$$

and the Cauchy-Schwartz inequality states the information about the upper limit of the error

$$\epsilon_{\text{reg}}(\mathbf{A}, \mathbf{A}^\epsilon - \mathbf{A}) \leq \epsilon_{\text{reg}} \|\mathbf{A}\|_{L_2} \|\mathbf{A}^\epsilon - \mathbf{A}\|_{L_2}. \quad (4.65)$$

In general,  $\mathbf{A}^\epsilon \rightarrow \mathbf{A}$  converges as  $\epsilon_{\text{reg}} \rightarrow 0$

$$c_1 \|\mathbf{A}^\epsilon - \mathbf{A}\|_{L_2} \leq \epsilon_{\text{reg}} \|\mathbf{A}\|_{L_2}. \quad (4.66)$$

Two further steps are necessary to arrive at the finite element formulation of (4.59). At first, the continuous domain must be discretized by a mesh  $\Omega^h \subset \Omega$ . Secondly, the infinite function space of the field and the test function is restricted to a finite subset  $\mathbf{V}^h \subset \mathbf{V}$ ,  $\mathbf{W}^h \subset \mathbf{W}$ . Nédélec's  $H(\text{curl})$  elements [151] approximate the vector potential of the curl-curl equation

$$\mathbf{A} \approx \mathbf{A}^h = \sum_{e=1}^{m_e} \mathbf{N}_e A_e. \quad (4.67)$$

The edge moments define the degrees of freedom

$$A_e = \int_e \mathbf{A}^h \cdot d\mathbf{s}. \quad (4.68)$$

Inserting the discretization into (4.59) results in the algebraic form of the weak formulation

$$\begin{aligned} & \sum_a \sum_e (A_a \int_\Omega (\nabla \times \mathbf{N}_a) \cdot (\nabla \times \mathbf{N}_e A_e) + \epsilon_{\text{reg}} \mathbf{N}_a \cdot \mathbf{N}_e A_e dx) \\ & - \sum_a \sum_e \left( A_a \int_{\Gamma_{IO}} \mathbf{N}_a \cdot (\mathbf{u} \times \mathbf{n}) d\mathbf{s} - A_a \int_\Omega \mathbf{N}_a \cdot \boldsymbol{\omega} dx \right) = 0. \end{aligned} \quad (4.69)$$

The equation holds for any test coefficient  $A_a$ ; each row in the global system matrix is associated to one specific test function unknown  $A_a$ . All FE basis functions are defined in the discrete function space  $\mathbf{A}^h \in \mathbf{V}^h \subset \mathbf{V}$

$$\mathbf{V}^h = \{\mathbf{A}^h(x) | \mathbf{A}^h(x) \in H(\text{curl}, \Omega), \mathbf{A}^h(x) = \mathbf{A}_e(x) \text{ on } \Gamma_e\}, \quad (4.70)$$

and the corresponding test function is defined in the function space  $\mathbf{A}^h \in \mathbf{W}^h \subset \mathbf{W}$

$$\mathbf{W}^h = \{\mathbf{A}^h(x) | \mathbf{A}^h(x) \in H(\text{curl}, \Omega), \mathbf{A}^h(x) = 0 \text{ on } \Gamma_e\}. \quad (4.71)$$

To sum up, the algebraic weak formulation can be written in standard matrix form

$$\mathbf{K} \tilde{\mathbf{A}} = \mathbf{f}, \quad (4.72)$$

with the element stiffness matrix

$$\mathbf{k}_e = \int_{\Omega_e} ((\nabla \times \mathbf{N}_a) \cdot (\nabla \times \mathbf{N}_e) + \epsilon_{\text{reg}} \mathbf{N}_a \cdot \mathbf{N}_e) dx \quad (4.73)$$

and the element forcing vector

$$\mathbf{f}_e = \int_\Omega \mathbf{N}_a \cdot \boldsymbol{\omega} dx. \quad (4.74)$$

Both are assembled to the global stiffness matrix  $\mathbf{K}$  and the forcing vector  $\mathbf{f}$ . Additional to the forcing term, inhomogeneous Neumann boundaries are discussed in the following section.

### 4.5.2 Boundary conditions

Based on the orthogonality condition (4.7), typical flow boundaries in combination with the curl-curl problem can be identified.

**Wall** For perfectly smooth, no slip, non-penetrating wall boundaries, the overall tangential flow velocity is equal to the wall movement  $\mathbf{u}_{\text{wall}}$  in tangential direction

$$\mathbf{u} \times \mathbf{n} = \mathbf{u}_{\text{wall}} \times \mathbf{n}. \quad (4.75)$$

Rigid walls, with a no-slip condition  $\mathbf{u}_{\text{wall}} = \mathbf{0}$ , enforce a homogeneous Neumann boundary for the vector potential.

**Inlet and Outlet** At the inlet and the outlet the tangential velocity is described by

$$\mathbf{u} \times \mathbf{n} = \mathbf{u}_{\text{inlet/outlet}} \times \mathbf{n}. \quad (4.76)$$

**Symmetry** A symmetry condition on the vector potential field can be imposed by two methods. The first method treats the boundary as a slip wall and imposes the tangential velocity. For this case a Neumann type problem can occur and this is treated by mass regularization. The second method is a real symmetry condition, with a prescribed normal flux  $f_n$

$$f_n = \mathbf{n} \cdot \mathbf{u} = \mathbf{n} \cdot (\nabla \times \mathbf{A}). \quad (4.77)$$

The equivalent problem is to find a function  $\beta$  for which

$$\mathbf{n} \times \mathbf{A} = \beta, \quad (4.78)$$

holds under  $\nabla \cdot \beta = f_n$  [152]. Symmetry states that fluxes over the boundary are zero,  $f_n = 0$ . The trivial choice  $\beta = \mathbf{0}$  leads to

$$\mathbf{n} \times \mathbf{A} = \mathbf{0}. \quad (4.79)$$

**Periodic** Periodic conditions satisfy both Dirichlet and Neumann boundaries of the corresponding periodic interfaces and maintain the physical quantity and flux.

**Free field** If all the compressible physical effects are damped towards the boundaries  $\mathbf{u}^{*,\text{ic}}|_{\partial\Omega} = \mathbf{u}|_{\partial\Omega}$ , then the tangential flow velocities simply describe the exterior. Afterwards, this assumption is used. However, IML is possible.

The tangential velocity component of the total field approximates the free field boundary term. Two facts support this approximation. Firstly, the amplitudes of the acoustic perturbation are very small and if the numerical setup is wave dissipative the waves do not travel until the free boundaries. Secondly, if the numerical setup is not dissipative the prescribed radiation condition at flow boundaries is optimal for normal wave impingement. Consequently, the domains are designed to satisfy normal wave impingement.

### 4.5.3 Boundary term – Transformation

The treatment of the boundary term is difficile and involves the mapping to the integration space (integration coordinates  $\boldsymbol{\xi} = [\xi, \eta, \zeta]^T$ ) and finite element specific operations to obtain the boundary shape functions

$$\int_{\Gamma_{IO}} \mathbf{A}' \cdot (\mathbf{u}^{*,ic} \times \mathbf{n}) d\mathbf{s}. \quad (4.80)$$

Vector space transformations [59, 153] to the integration space involve a covariant transformation of the surface component and a transformation of the integral

$$\int_{\Gamma_{ref}} \mathbf{A}' \cdot \mathbb{J}^{-T} (\mathbf{u}^{*,ic} \times \mathbf{n}) \det \mathbb{J} d\xi d\eta. \quad (4.81)$$

At first, the normal on the surface  $\mathbf{n}$  points outside the connected base volume element. Then, an integration surface element transforms from the "physical" space  $\mathbf{x} = [x, y, z]^T$  to the "integration" space  $\boldsymbol{\xi} = [\xi, \eta, \zeta]^T$  by

$$d\mathbf{s} = \left\| \frac{\partial \mathbf{x}}{\partial \xi} \times \frac{\partial \mathbf{x}}{\partial \eta} \right\|_2 d\xi d\eta \quad (4.82)$$

that includes the definition of determinant in terms of the cross product. Thirdly, the Piola transformation projects the velocity  $(\mathbf{u}^{*,ic} \times \mathbf{n})$  to the parameter space  $\boldsymbol{\xi}$  by the Jacobian  $\mathbb{J}$

$$\mathbb{J} = \begin{pmatrix} \frac{\partial \mathbf{x}}{\partial \xi} & \frac{\partial \mathbf{x}}{\partial \eta} \end{pmatrix}. \quad (4.83)$$

Fourthly, the pseudo inverse of the Jacobian requires the inverse of the symmetric metric tensor  $\bar{\mathfrak{d}}^1$

$$\bar{\mathfrak{d}} = \mathbb{J}^T \mathbb{J}. \quad (4.84)$$

Inserting these four ingredients into the inhomogeneous Neumann boundary yields

$$\int_{\Gamma_{ref}} \mathbf{A}' \cdot \bar{\mathfrak{d}}^{-T} \mathbb{J}^T (\mathbf{u}^{*,ic} \times \mathbf{n}) \left\| \frac{\partial \mathbf{x}}{\partial \xi} \times \frac{\partial \mathbf{x}}{\partial \eta} \right\|_2 d\xi d\eta. \quad (4.85)$$

## 4.6 Helmholtz-Hodge decomposition

Technically, the Helmholtz and the Helmholtz-Hodge decomposition [154] are the same computational algorithms, where the latter aims to decompose the field in three distinctive parts on a manifold. Helmholtz-Hodge theory widens the domain aggregate to manifold and drops the restriction to homologically trivial [59] domains (see Fig. 4.4). Some authors even denote the extension of Helmholtz decomposition from simply connected Lipschitz domains to homologically trivial domains as Helmholtz-Hodge decomposition.

**Theorem 4.6.1** (*Helmholtz-Hodge decomposition [155]*) *A smooth vector field  $\mathbf{u} \in L^2(\Omega)$  on a homologically trivial domain  $\Omega$  can be decomposed in three  $L^2$ -orthogonal velocity field components*

$$\mathbf{u} = \mathbf{u}^{ic} + \mathbf{u}^c + \mathbf{u}^h = \nabla \times \mathbf{A}^{ic} + \nabla \phi^c + \mathbf{u}^h. \quad (4.86)$$

The field  $\mathbf{u}^{ic}$  contains the solenoidal (incompressible) part,  $\mathbf{u}^c$  the irrotational (compressible) part, and  $\mathbf{u}^h$  the harmonic part of the flow velocity. Bachelors [46] describes the motion of a continuum point as

---

<sup>1</sup> The pseudo inverse represents the transformation property described by Monk [59] (Page 216).

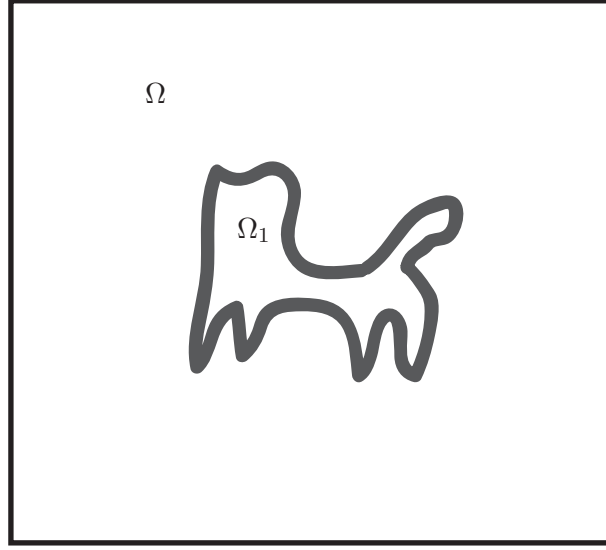


Figure 4.4: Domain  $\Omega$  with cutouts  $\Omega_1$  (e.g. holes).

a combination of three exclusive shapes and motivates the decomposition into three components (see Fig. 2.2).

- (a) An isotropic expansion  $\mathbf{u}^c$  proportional to the volumetric rate of expansion of  $\nabla \cdot \mathbf{u}$ . The field component is described by a scalar potential associated with the compressibility of the fluid.
- (b) Irrotational deformation  $\mathbf{u}^h$  without volume change. Classical potential flow theory describes this velocity component that is divergence-free and curl-free.
- (c) A rigid-body rotation  $\mathbf{u}^{ic}$  at an angular velocity of  $\frac{1}{2}\nabla \times \mathbf{u}$ . Vortical and incompressible flow structures are described by the vorticity and its dynamics.

The harmonic can be interpreted as the exterior properties  $\mathbb{R}^3/\Omega$  of the decomposed vector field  $\mathbf{u}$  [156]. If the decomposition domain is  $\mathbb{R}^3$ , the harmonic part is zero. For  $\Omega$ , the harmonic part can be obtained by the homogeneous solutions of the partial differential equations with the enforced boundaries.

# 5 Aeroacoustic source interpolation

Today, efficient interpolation techniques are especially important when dealing with computational aeroacoustics. Since the beginning of CAA, hybrid methods have been established as the most practical method for fast and accurate aeroacoustic computations at low Mach numbers. The workflow of hybrid aeroacoustics involves three steps (see Fig. 5.1): 1. perform unsteady flow computations on a restricted sub-domain; 2. compute the acoustic sources; 3. simulate the acoustic field. Hybrid aeroacoustic methods seek for robust and flexible procedures that provide a conservative mesh to mesh interpolation of the aeroacoustic sources while high computational efficiency is ensured. For low Mach number applications, a key challenge in CAA is the huge disparity of scales between flow structures and audible acoustic wavelengths. The scaling between the acoustic wavelength  $\lambda$  and the characteristic length  $l_v$  of a vortex is given by

$$\lambda \sim \frac{l_v}{\text{Ma}},$$

where Ma is the Mach number. Utilizing this disparity of scales, aeroacoustic analogies or perturbation techniques separate the flow computation from the acoustic computation (see, e.g., [140,157]). Therefore, the sizes of the two computational grids are in general quite different.

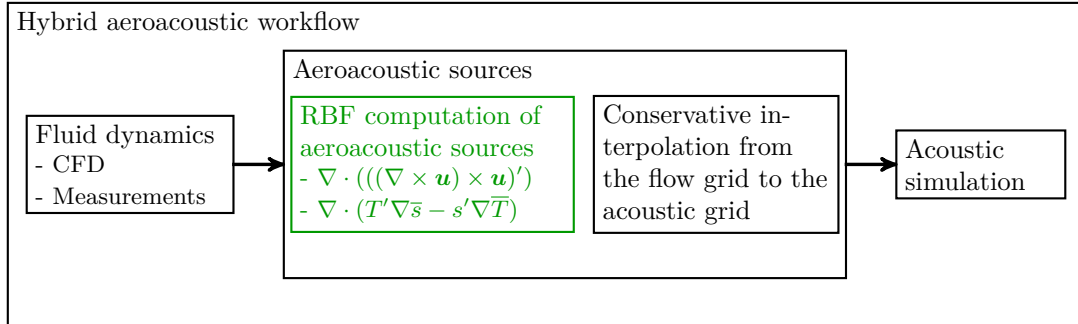


Figure 5.1: The hybrid aeroacoustic workflow consists of three main computational parts, where the presented RBF source term computation is important if the CFD solver provides only primary results, like the pressure  $p$  or the velocity  $\mathbf{u}$ .

For both physical fields, the individual optimal computational grid achieves the highest accuracy and the two grids differ according to the modeling criteria. On the one hand, the flow grid resolves boundary layers and is mostly coarsened towards outflow boundaries to dissipate vortices. On the other hand, the acoustic grid transports waves and therefore needs a uniform grid size all over the computational domain. In order to couple the different meshes, an interpolation scheme is necessary that satisfies the fundamental requirement of hybrid CAA: an accurate data transfer from the flow to the acoustic grid to minimize interpolation errors and conserve the energy. To cope with this task, different interpolation strategies can be applied, starting from low complexity nearest neighbor interpolation to complex source term computation models with volume intersections between the flow and the acoustic grid. The simple nearest neighbor interpolation fails to compute the acoustic sources accurately (see, e.g., [158,159]).

In [158], the aeroacoustic source term is computed by summing the contributions of all flow cells belonging to finite elements that surround an acoustic finite element node. It is assumed that the flow quantities used for the acoustic source term computation are constant over each flow cell. This approach has also been used in [160] for three-dimensional problems, where a grid dependency has been observed, resulting in a too low sound pressure level over the whole frequency spectrum. A fully conservative approach has been used in [161], where the acoustic sources within the finite element formulation are first computed on the fine flow grid. These so-called nodal loads are then interpolated by a conservative scheme to the acoustic grid. This approach is accurate in cases where the flow grid is much finer than the acoustic grid but fails in cases where the flow grid is coarser than the acoustic grid. As a solution to this problem, a cut cell approach has been derived and successfully applied to the aeroacoustic computation of an axial fan [51]. Similar investigations have been performed in [159], where for both the flow and the acoustic field a Finite-Volume scheme has been used. However, most of these methods fail if the CFD simulation only provides primary variables, such as the pressure  $p$  or the velocity  $\mathbf{u}$ , since the aeroacoustic sources are often non-trivial combinations of these primary variables (see Fig. 6.6). Desirably an accurate, flexible, and conservative coupling scheme ensures a rigorous connection between fluid dynamics and acoustics within a hybrid aeroacoustic simulation. The properties of the desired coupling scheme, or interpolation, are summed up as follows:

- An accurate and fast interpolation technique.
- An interpolation technique that handles special grids, e.g. grids to resolve boundary layers.
- A method to compute accurate derivatives of the primary flow variable, such as pressure  $p$ , velocity  $\mathbf{u}$ , density  $\rho$ , temperature  $T$ , and entropy  $s$ .
- A flexible algorithm that can be integrated into a standard product development cycle.
- A flexible algorithm that assembles different hybrid aeroacoustic source terms, e.g. the divergence of the Lamb vector  $\nabla \cdot (((\nabla \times \mathbf{u}) \times \mathbf{u})')$  or the divergence of an entropy source  $\nabla \cdot (T' \nabla \bar{s} - s' \nabla \bar{T})$  [31].
- A conservative algorithm transfers the desired amount of energy, defined by the aeroacoustic sources, from the flow discretization to the mesh of the acoustic simulation [51].

In this paper, we propose to compute the aeroacoustic sources directly from the primary CFD variables by applying an interpolation scheme based on RBFs (Radial Basis Functions) in conjunction with RBF derivatives. We show the ideal setup for the algorithms, the choice of the kernel function and propose a natural neighbors selection based on the connectivity of the flow grid. This patch search technique guarantees the resolution of typical flow structures. The application of local RBFs provides promising capabilities in terms of computational efficiency, known from nearest neighbor algorithms. Furthermore, the computation of RBF derivatives can be carried out elegantly and accurately with a local-global approach.

## 5.1 Interpolation Schemes

In the late 1960's, Hardy developed an approximation and interpolation method for surface fitting problems [162]. Since then, the multiquadric approximation of scattered data

$$\|\mathbf{x} - \mathbf{z}\|_2 \mapsto \Phi(\|\mathbf{x} - \mathbf{z}\|_2) := \sqrt{1 - \|\mathbf{x} - \mathbf{z}\|_2^2} \quad \mathbf{x}, \mathbf{z} \in \mathbb{R}^d \quad (5.1)$$

has been used in geodesy, mapping, signal processing, digital terrain modeling, and hydrology [163]. This function (5.1) is an early representative of RBFs, which are scalar valued multivariant functions  $\mathbb{R}^d \mapsto \mathbb{R}$



that depend on the radial measure  $r$  in terms of the Euclidean norm  $r = \|\mathbf{x} - \mathbf{z}\|_2$  between a scattered data (source) point  $\mathbf{x}$  and the evaluation (target) point  $\mathbf{z}$  (see Fig. 5.2).

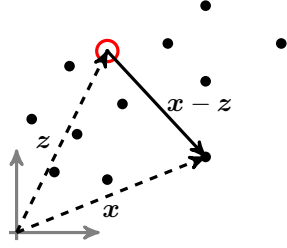


Figure 5.2: Geometric definitions of scattered data  $(\mathbf{x}, \bullet)$  and the target point  $(\mathbf{z}, \odot)$ .

Since then, application-driven development of RBFs has modified function type, shape, and relevant support. The most prominent RBF kernels are the Gaussian, the multiquadric, and the inverse multiquadric [164].

At this point, a clear distinction between local and global methods should be drawn. Global methods, mainly using the Gaussian kernel, are well suited for theoretical analyses since it can be shown that the solution converges to the exact solution under certain conditions [165]. But on the down side, the condition number of the global interpolation matrix tends to infinity. There are some approaches to circumvent this issue [166] using a QR-decomposition or a Taylor-expansion but they are computationally more expensive and less parallelizable than local ones.

With increasing number of ill-placed datapoints in datasets, the demand for RBFs with compact local support [167] increases. Local representations reduce computational time when interpolating data and increase the condition number of each local subproblem. Instead of inverting one ill-conditioned global system matrix, many small well-conditioned stencil-matrices are inverted. Using Wendland's compactly supported RBFs together with a modified Shepard's method as presented in [168], high computational efficiency for large system can be achieved.

An important aspect of this work is the application of RBF interpolation schemes to scattered data distributions with bad quality, such as extremely anisotropic point distribution, e.g. from boundary layer flow. We use a local collocation method that represents the data exactly in the prescribed point. In this sense no algorithmic uncertainty is present at the individual, deterministic, scattered data point. To handle anisotropic point distributions, a special search procedure is used to find the optimal local point distribution for interpolation, which will be presented in Sec. 5.1.3.

### 5.1.1 Radial basis function interpolation

As mentioned above, the main purpose of this method is to interpolate flow results, such as velocity  $\mathbf{u}$  or vorticity  $\boldsymbol{\omega}$ , from a CFD mesh to an acoustic FEM mesh. Since hybrid aeroacoustics deals with a large number of unknowns and unfortunate data distributions, e.g. in boundary layers, a parallelizable algorithm to achieve high computational efficiency is of particular interest.

In this work, the local Wendland kernel  $\Phi$  (5.2) together with a modified Shepard's method was chosen, similar to [168]. This is the most promising approach since it is both fast and capable of handling boundary layer meshes if the chosen kernel is combined with the patch search technique presented in Sec. 5.1.3. The scaled Wendland kernel [168] has the following form:

$$\Phi(\|\mathbf{x} - \mathbf{z}\|_2, \alpha) = \left(1 - \frac{\|\mathbf{x} - \mathbf{z}\|_2}{\alpha}\right), \quad (5.2)$$

where  $\mathbf{x} \in \mathbb{R}^d$  is the location of a scattered data point. For all scattered data points we define the

associated indices  $\omega_s \in 1, 2, \dots, N_s$ , with  $N_s$  as the number of scattered data points, also called *source points*. The point  $\mathbf{z} \in \mathbb{R}^d$  is the point at which the interpolation is evaluated. These points are called *target points* and form a set of target point indices  $\omega_t \in 1, 2, \dots, N_t$ , where  $N_t$  is the number of target points. The parameter  $\alpha$  is responsible for the scaling of the compact support (5.2), which is especially important for bad source point distributions resulting in a high condition number of the interpolation matrices. The parameter  $\alpha$  is chosen to be

$$\alpha \sim r_{\max} = \max_{i \in I_q} \{r_i\}. \quad (5.3)$$

$I_q$  are the indices of the  $N_q$  neighbors of the target point  $\mathbf{z}$  and define the patch set.

**Local interpolation method** Following the approach of Lazzaro [168], two different scattered data patches around the target point are introduced at which the interpolant is evaluated (see Fig. 5.3). The first set is  $X_q = \{\mathbf{x}_i \in \omega_s, i \in I_q\}$ . The second set is  $X_w = \{\mathbf{x}_i \in \omega_s, i \in I_w\}$ , with  $I_w$  as the indices of the  $N_w$  influence points, defines the influence of the different patches. The influence radius  $r_{W_k} = \max_{k \in I_w} \{r_k\}$ , with  $r_k = \|\mathbf{x}_k - \mathbf{z}\|_2$ , is defined to be the maximum distance of a target point in  $X_w$  and  $N_w \subset N_q$ . The interpolant is given by

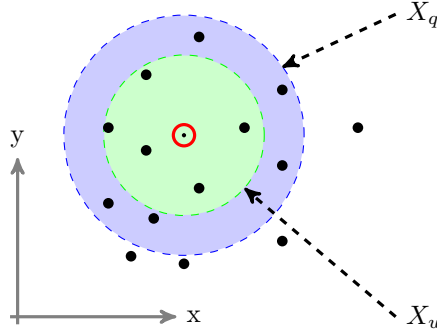


Figure 5.3: Geometric definitions of the two scattered data sets with respect to one target point  $(\mathbf{z}, \odot)$ . The metric of the search algorithm is essential to the shape of the sets.

$$s(\mathbf{z}) = \sum_{k=1}^{N_q} \overline{W}_k(\mathbf{z}) R_k(\mathbf{z}), \quad (5.4)$$

where  $R_k(\mathbf{z})$  defines the local interpolation system and  $\overline{W}_k$  the weight function. The local interpolation system is given by the algebraic system

$$R_k(\mathbf{x}_k) = \sum_{j=1}^{N_q} c_j \Phi(\|\mathbf{x}_j - \mathbf{x}_k\|_2), \quad (5.5)$$

which has to be initially solved for the  $N_q$  temporary (unscaled) interpolation weights  $c_j$ , where  $R_k(\mathbf{x}_k)$  denotes the scattered data (field that is interpolated) at the patch source point  $\mathbf{x}_k$ . The weight function  $\overline{W}_k$  of the modified interpolant  $s(\mathbf{x})$  is chosen to be

$$\overline{W}_k(\mathbf{x}) = \frac{\left( \max\left\{ \frac{(r_{W_k} - r_k)}{r_{W_k} r_k}, 0 \right\} \right)^p}{\sum_{l=1}^{N_q} \left( \max\left\{ \frac{(r_{W_k} - r_l)}{r_{W_k} r_l}, 0 \right\} \right)^p}, \quad (5.6)$$

with the exponent  $p$  as a measure of locality. Since the weights  $\overline{W}_k(\mathbf{x})$  constitute a partition of unity, the following holds,

$$\sum_{k=1}^{N_t} \overline{W}_k(\mathbf{x}) = 1. \quad (5.7)$$

The bigger  $p$ , the more local is the approach, which makes it less accurate but capable of resolving stronger gradients. Then the interpolant  $s(\mathbf{x})$  can be evaluated at every target point  $\mathbf{z}$ . The algorithm of the local RBF interpolation is written in pseudo code (Algo. 1).

---

**Algorithm 1** Local RBF Interpolation

---

```

1:  $s(\mathbf{z}) \leftarrow \text{RBFInterpolation}(\mathbf{x})$ 

2: function RBFINTERPOLATION
3:   for  $k$  in  $\omega_t$  do
4:      $I_q = \text{GetNodeIndicesOfPatch}(k)$   $\triangleright I_q$  holds indices of  $N_q$  source points in patch
5:      $\mathbf{x}_k = \text{GetCoordsOfSrcPointsForTrgPoint}(k)$ 
6:      $\mathbf{R}_k = \text{GetSourceData}(I_q)$   $\triangleright$  get scattered data at patch source point
7:     Solve the  $N_q \times N_q$ -system for the patch coefficients  $\mathbf{c}^k$ , (5.5)
8:      $i_w = I_q[\text{influence-point}]$   $\triangleright$  get index of influence point
9:      $r_{W_k} = \text{GetDistOfPoint}[i_w]$   $\triangleright$  distance between target point and  $i_w$ -th source point
10:    Compute weights for every source point in patch  $k$ :  $\overline{W}_k$ , (5.6)
11:    Compute interpolant  $s(\mathbf{z}_k)$  at target point  $\mathbf{z}_k$ , (5.4)
12:  end for
13: end function

```

---

### 5.1.2 Proof of convergence of the interpolation

As described by Lazzaro in [168], an upper bound for the global approximation error  $E(\mathbf{x})$  reads

$$E(\mathbf{x}) = \|f(\mathbf{x}) - s(\mathbf{x})\| = \left\| \sum_{k=1}^{N_q} \overline{W}_k(\mathbf{x}) f(\mathbf{x}) - \sum_{k=1}^{N_q} \overline{W}_k(\mathbf{x}) R_k(\mathbf{x}) \right\| \leq \sum_{k=1}^{N_q} \overline{W}_k(\mathbf{x}) e_k(\mathbf{x}), \quad (5.8)$$

with  $e_k(\mathbf{x}) = \|f(\mathbf{x}) - R_k(\mathbf{x})\|$  as the approximation error of the interpolant  $R_k(\mathbf{x})$  relative to the local interpolation system. Additionally, Madych has proven in [165] that the following holds if the distance  $h$  between the source points is sufficiently small,

$$e_k(\mathbf{x}) = \|f(\mathbf{x}) - R_k(\mathbf{x})\| \leq C_1 e^{-C_2 \alpha} \|f\|_2, \quad (5.9)$$

where  $C_1, C_2 \in \mathbb{R}^+$  are constants. Thus, for the shape parameter of the Wendland kernel (5.2) with  $\alpha \rightarrow \infty$  the approximation error of the local interpolation system  $e_k(\mathbf{x})$  tends to zero and hence from (5.8) the same is true for the global approximation error  $E(\mathbf{x})$ . Moreover, Madych has shown that  $e_k(\mathbf{x})$  decreases monotonically in the source neighbor spacing.

### 5.1.3 On the optimal choice of neighbors

An important part of the interpolation is the choice of source points  $\mathbf{x}_i$  in the patch  $X_q$  to avoid unphysical artifacts in the interpolated field. This is especially important in boundary layers, where cells or elements are distorted or stretched with high aspect ratios. A common approach to obtain a specific amount of nearest neighbors is to use a kd-tree search, e.g. from CGAL [169] or FLANN [170].

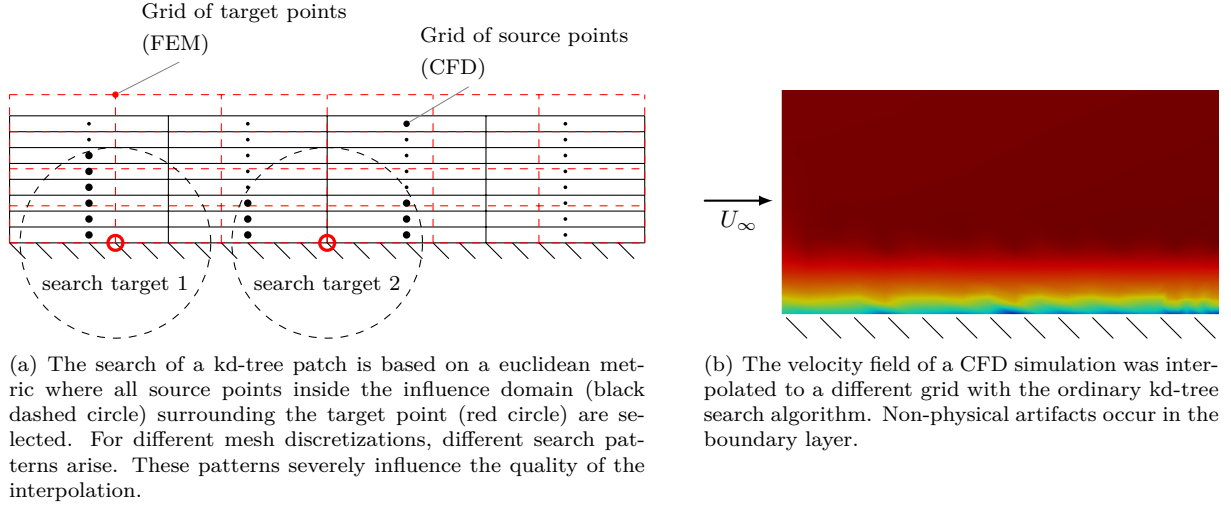


Figure 5.4: kd-tree search and resulting interpolated flow field.

These fast kd-tree algorithms have to be provided with the coordinate of the target point for which the patch is defined and all coordinates of the source points. By doing this, the underlying mesh structure (connectivity) is ignored and the data is represented on discrete scattered points (see Fig. 5.4(a)). Thus, we might miss important information to improve the quality of the interpolation. To understand the shortcoming of this approach, a simple example of a boundary layer flow in a channel is provided, where the cell data from a CFD simulation is interpolated to nodes of a different FEM mesh. The interpolation from a CFD Finite Volume mesh to an FEM mesh is the standard procedure; however, the findings are also true for other mesh types without loss of generality.

The interesting part is the area close to the wall, where a mesh refinement is necessary for the boundary layer to be resolved properly. The resulting patch of elements emerging from a kd-tree search for two example nodes on the boundary layer is shown in Fig. 5.4(a). There, one can see the unfavorable choice of source points (black) for different target points (red circle). As shown in Fig. 5.4(b), this patch choice results in a poor interpolation in streamwise direction, which leads to numerical artifacts. The results become even worse for heavily distorted meshes. Some of the patches only contain vertical neighbors and thus these patches have no connection in stream-wise direction.

However, if we use a connectivity preserving mesh-based neighbor search, the patch looks as displayed in Fig. 5.5(a), which results in an even spatial distribution and good interpolation results (see Fig. 5.5(b)). This modified patch algorithm searches for the next directly connected neighbor elements over the common global nodes. By applying a “layer strategy”, the neighbors of the direct neighbors are also taken into account. This search can be carried out recursively in a layered manner until the preferred number of elements is reached. In the illustrated example, only a one-layer level search was applied.

Another drawback of a coordinate based kd-tree search is the interpolation along slender wing profiles and structures. It is possible that a kd-tree search at the upper side of the wing includes points from the lower side in the patch, which would lead to completely incorrect results. In this case, the modified patch search, based on the connectivity, performs well since elements on the upper side have no direct connection to the elements on the lower side of the slender airfoil.

With the given interpolation formulation it is possible to impose exact boundary conditions, e.g. a no-penetration condition  $\mathbf{u} \cdot \mathbf{n} = 0$ , where the corresponding entries of the interpolant equal is set to zero.

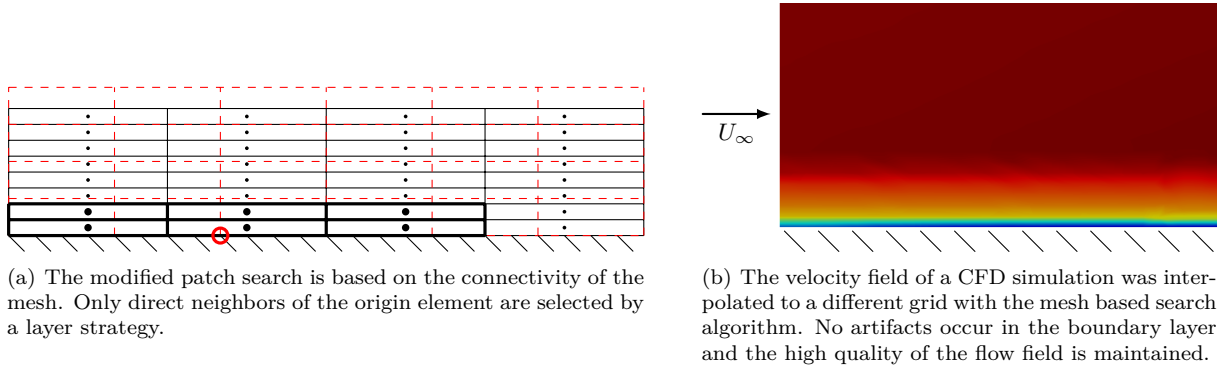


Figure 5.5: Modified patch search and resulting interpolated flow field.

### 5.1.4 Convergence of interpolation

To analyze the convergence of the RBF interpolation and to quantify the more or less heuristic observations of correct choice of patches, we prescribe analytic functions on a unit cube  $\Omega \in [0, 1]^3$  with different node distributions and observe the  $l_2$ -error after interpolating to a different mesh with equidistant node distribution.

The first analytic function

$$f_1(\mathbf{x}) = (x^2 + y^2 + z^2) \sin(10x) \sin(10y) \sin(10z) \quad (5.10)$$

represents the transition of different vortex structures in shear layers (see Fig. 5.6(a)). This smooth function is used to investigate the convergence and accuracy of the RBF interpolation since the majority of pressure fields encountered in low Mach number aeroacoustics are smooth. The second analytic function

$$f_2(\mathbf{x}) = \tanh(20(x + 0.3 \sin(-10y) - 0.3 \sin(-5(z - 0.1)))) \quad (5.11)$$

is a representative of a continuous sinusoidal shock, which is similar to the numerical solution of a shock using a dissipative flow solver [171] (see Fig. 5.7(a)). This function is used to test the capabilities of RBF interpolation to handle strong gradients and sharp transitions.

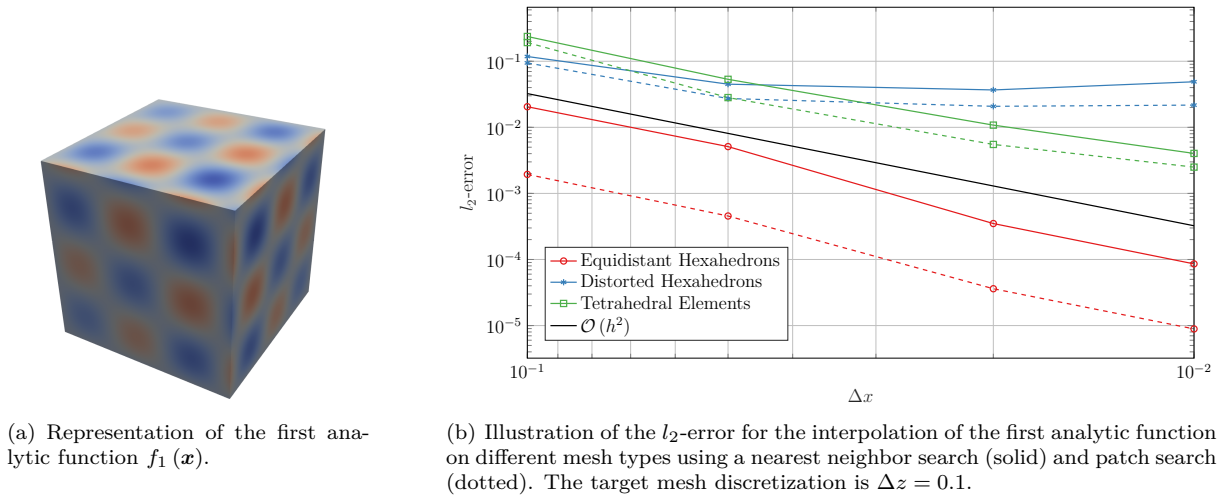


Figure 5.6: Convergence of the interpolation for the first analytic function  $f_1(\mathbf{x})$ .

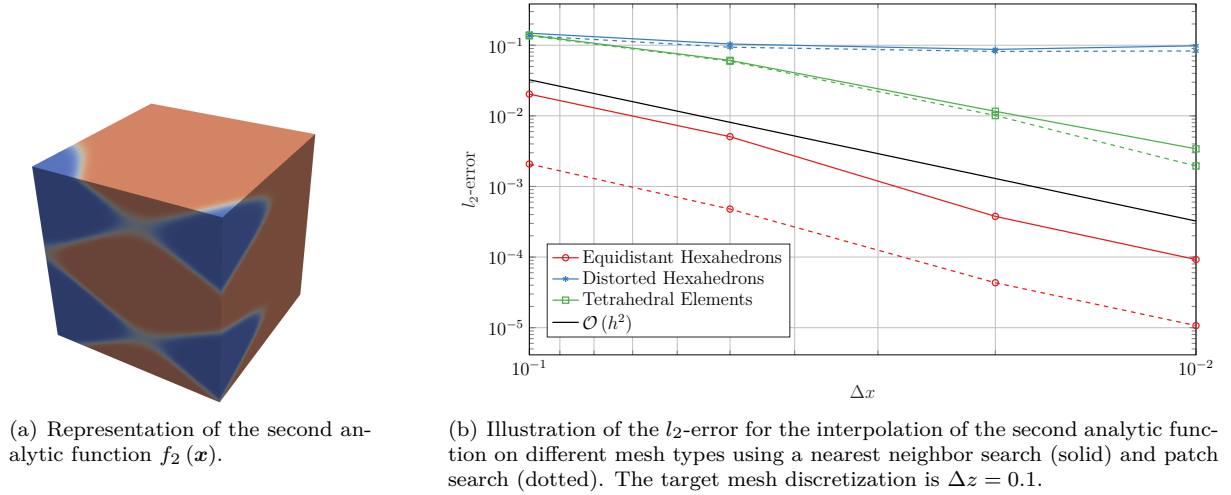


Figure 5.7: Convergence of the interpolation for the second analytic function  $f_2(\mathbf{x})$ .

The unit cube  $\Omega \in [0, 1]^3$  was discretized by equidistant hexahedrons, distorted hexahedrons where the source mesh discretization distance  $\Delta x$  grows exponentially on one side of the unit cube (see Fig. 5.8(a)), and tetrahedron elements. Then the analytic function (nodal values) were interpolated to a different mesh consisting of equidistant hexahedrons with discretization distance  $\Delta z$  using a nearest neighbor search or the modified patch search, respectively.

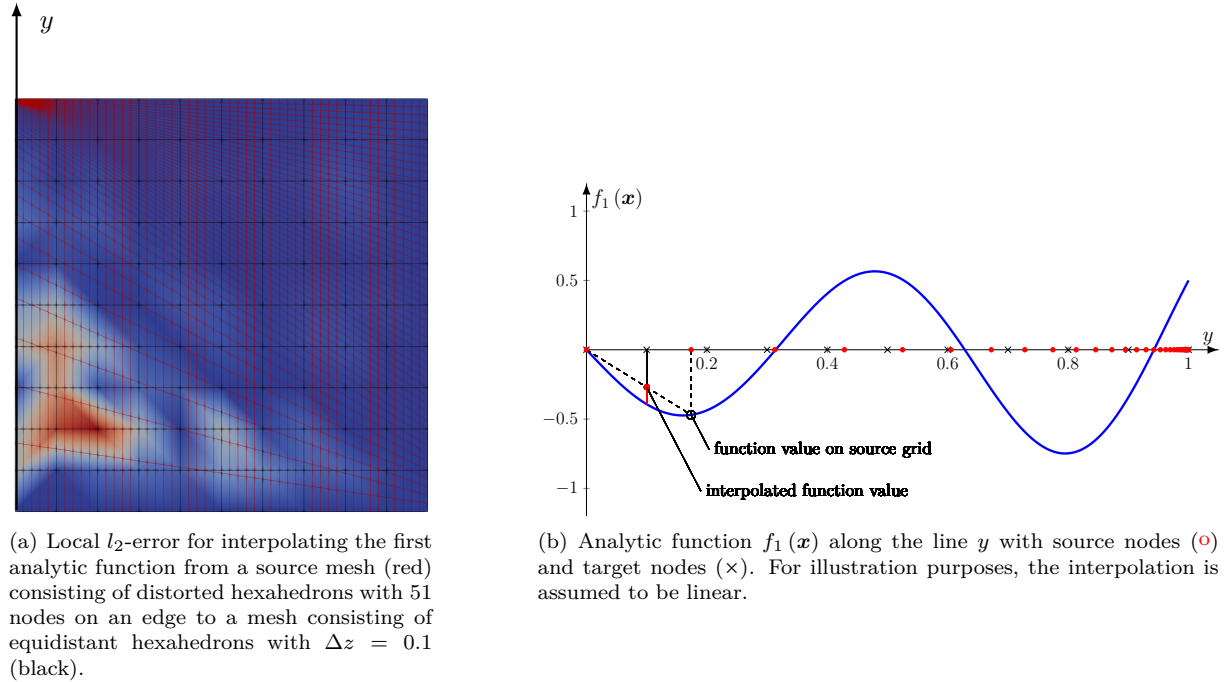


Figure 5.8: Illustration of the development of the  $l_2$ -error for heavily distorted source meshes. As depicted in Subfig. (a), the high errors arise due to the underresolved physical function in the lower left of the computational domain. This phenomenon is illustrated in Subfig. (b).

Figure 5.6(b) and Fig. 5.7(b) show the convergence of the RBF interpolation with respect to the source discretization distance  $\Delta x$  for the first and second analytic function. Obviously, there is an influence resulting from the source data density. The RBF interpolation performs well for both the nearest neighbor search and the modified patch search on all of the different mesh types, except for

distorted hexahedrons. The reasons for this lie in the source node distribution and the form of the function to be interpolated.

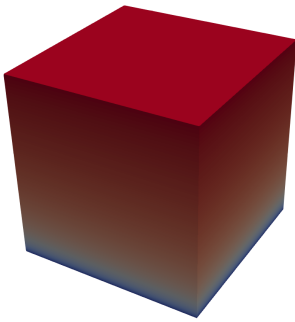
Figure 5.8 illustrates how the  $l_2$ -error develops. As it can be seen from the local  $l_2$ -error in Fig. 5.8(a), the interpolation delivers good results, except in regions where the source discretization becomes too coarse and the distance from the source points in the respective area to the target points becomes too big. Looking at the analytic function that is to be interpolated along the line where the maximum local  $l_2$ -errors occur (see Fig. 5.8(b)), we can see that in order to minimize the  $l_2$ -error while still using a coarse source mesh discretization, the distance between the source and target points needs to be minimal and the gradients between the source points should not vary too much.

In order to further analyze the capability of the RBF interpolation for handling boundary layer data in combination with the different choices of neighbors, we use the function

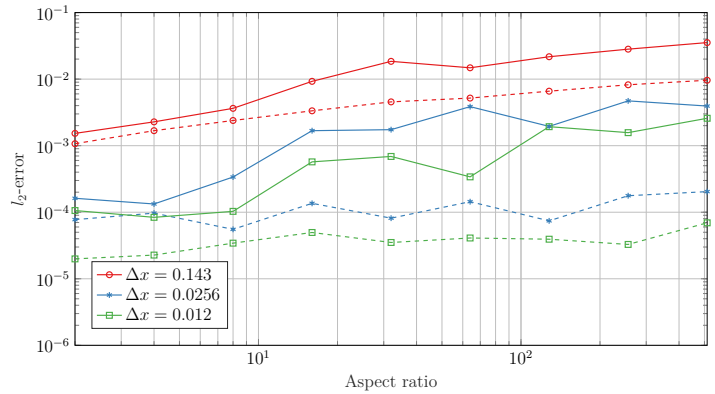
$$f_3(\mathbf{x}) = \frac{10}{4.6151} (\log(y + 10^{-2}) - \log(10^{-2})). \quad (5.12)$$

The analytic function  $f_3(\mathbf{x})$  roughly describes the flow velocity component in inflow direction in a boundary layer (see Fig. 5.9(a)). Here, the wall that is the reason for the boundary layer to develop is located at  $y = 0$ . As mentioned above, a CFD mesh to properly resolve the boundary layer is characterized by cells with a big aspect ratio in the region adjacent to the wall, where the largest gradients occur. For this investigations, a mesh consisting of hexahedrons with different aspect ratios in the range of 2 to 512 for the cells at  $y = 0$  (typical CFD boundary layer mesh [172]) is used. With growing distance  $y$ , the mesh gradually becomes coarser. In order to realize different aspect ratios in the first cell row, the cell height is varied while the number of nodes on the edges stays the same.

As shown in Fig. 5.9(b), the kd-tree based nearest neighbor search interpolation causes increasing errors with increasing aspect ratio. Hence, the interpolation error for large aspect ratios limits the application of the nearest neighbor search. However, the previously described patch search leads to better results at large aspect ratios where it significantly outperforms the kd-tree based nearest neighbor search. Ideally, the  $l_2$ -error is independent of the aspect ratio. One can see that this requirement is approximately met using patch search.



(a) Representation of the third analytic function  $f_3(\mathbf{x})$ .



(b) Illustration of the  $l_2$ -error for the interpolation of the third analytic function on a hexahedron mesh with different source discretizations using a nearest neighbor search (solid) and patch search (dotted). The target mesh discretization is  $\Delta z = 0.1$ .

Figure 5.9: Convergence of the interpolation for the third analytic function  $f_3(\mathbf{x})$  on a mesh to resolve a boundary layer.

## 5.2 Derivatives based on RBFs

Although the procedure to compute derivatives based on RBFs is similar to the RBF interpolation, there is one important difference. For derivatives, there is only one source patch set  $X_q = \{\mathbf{x}_i \in \omega_s, i \in I_q\}$ , with  $I_q$  as the indices of the  $N_q$  neighbors of the target point  $\mathbf{z}$  (see Fig. 5.10).

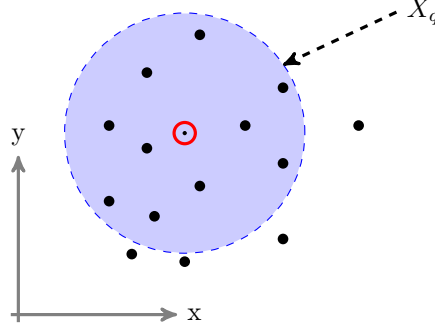


Figure 5.10: Geometric definitions of the scattered data set with respect to one target point  $(\mathbf{z}, \odot)$ . The metric of the search algorithm is essential to the shape of the sets.

Matrix notation demystifies the deduction of the radial basis function derivative of a given function  $s(\mathbf{z})$  at target point  $\mathbf{z}$ . At first, the interpolation weights  $\boldsymbol{\sigma}$  form the interpolant  $s(\mathbf{x})$  are determined by

$$s(\mathbf{x}) = \Phi(\mathbf{x}) \cdot \boldsymbol{\sigma} \quad (5.13)$$

at the values of the discrete datapoints  $\mathbf{x}$ . This system needs to be solved for the weights  $\boldsymbol{\sigma}$ ,

$$\boldsymbol{\sigma} = \Phi^{-1}(\mathbf{x}) \cdot \mathbf{s}. \quad (5.14)$$

Then the differential operator  $\mathcal{L}[\cdot]$  is applied to the interpolant

$$\mathcal{L}[s(\mathbf{z})] = \mathcal{L}[\Phi(\mathbf{z}) \cdot \boldsymbol{\sigma}] \quad (5.15)$$

and the weights from (5.14) are inserted

$$\mathcal{L}[s(\mathbf{z})] = \mathcal{L}[\Phi(\mathbf{z}) \cdot \Phi^{-1}(\mathbf{x}) \cdot \mathbf{s}]. \quad (5.16)$$

Now the fact that  $\boldsymbol{\sigma} = \Phi^{-1}(\mathbf{x}) \cdot \mathbf{s}$  does not depend on  $\mathbf{z}$  is used to pull it out of the operator's range

$$\mathcal{L}[s(\mathbf{z})] = \mathcal{L}[\Phi(\mathbf{z})] \cdot \underbrace{\Phi^{-1}(\mathbf{x}) \cdot \mathbf{s}}_{\boldsymbol{\sigma}}. \quad (5.17)$$

Finally, the derivative is rewrite in a compact form

$$\mathcal{L}[s(\mathbf{z})] = \underbrace{\mathcal{L}[\Phi(\mathbf{z})] \cdot \Phi^{-1}(\mathbf{x})}_{\mathbf{c}(\mathbf{z})} \cdot \mathbf{s}. \quad (5.18)$$

The process from above can now be transformed to a more implementation-friendly form, based on [173], where we first have to apply the spatial derivative operator  $\mathcal{L}$  to the RBF and evaluate it, as



presented in (5.19), where  $\mathbf{x}_k$  and  $\mathbf{x}_l$  are the coordinates of two source points with indices  $k, l \in I_q$ .

$$\mathbf{L}_{\Phi}^k = \mathcal{L}[\Phi(\|\mathbf{z} - \mathbf{x}_k\|_2)] = \sum_{l=1}^{N_q} c_l \Phi(\|\mathbf{x}_l - \mathbf{x}_k\|_2), \quad k = 1, \dots, N_q. \quad (5.19)$$

This system has to be inverted in order to obtain the weights  $c_l$  for the derivatives at the source points  $l \in I_q$ . Then the derivative of the given function  $s(\mathbf{z})$  can be evaluated by

$$\mathcal{L}[s(\mathbf{z})] = \sum_{l=1}^{N_q} c_l s(\mathbf{x}_l) = \sum_{l=1}^{N_q} c_l R_l, \quad (5.20)$$

where  $R_l = s(\mathbf{x}_l) \in \mathbb{R}^{N_q \times 1}$  is the scattered data value of the given function at the source point with index  $l$ .

Algorithm 2 shows how to calculate derivatives of scattered data distributions. Vector-valued datasets can be interpreted as a tuple of scalar components

$$\mathbf{s}(\mathbf{x}) = \begin{pmatrix} s_1(\mathbf{x}) \\ s_2(\mathbf{x}) \\ s_3(\mathbf{x}) \end{pmatrix}. \quad (5.21)$$

Then  $\mathbf{R}_k$  is a matrix  $\mathbb{R}^{N_q \times d}$  with  $d$  as the spatial dimension and evaluating the last expression of Algo. 2 leads to a Jacobian matrix (5.22), where each row  $i$  contains the derivatives of the scattered data vector.

---

**Algorithm 2** Local RBF Derivative

---

```

1:  $s(\mathbf{z}) \leftarrow \text{RBFDerivative}(\mathbf{x})$ 

2: function RBFDIFFERENTIATION
3:   for  $t$  in  $\omega_t$  do
4:      $I_q = \text{GetNodeIndicesOfPatch}(t)$   $\triangleright I_q$  holds indices of the  $N_q$  source points in the patch
5:      $\mathbf{x}_k = \text{GetCoordsOfSrcPointsOfTrgPoint}(t)$ 
6:     for  $k$  in  $I_q$  do
7:        $\mathbf{L}_{\Phi}^k = \text{CalcDerivativesOfRBF}(\mathbf{x}_i)$   $\triangleright \mathcal{L}[\Phi(\|\mathbf{x}_k - \mathbf{x}_i\|_2)] \rightarrow \mathbf{L}_{\Phi}^k \in \mathbb{R}^{N_q \times d}$ 
8:        $\Phi = \text{EvalRBFat}(\mathbf{x}_k, \mathbf{x}_i)$   $\triangleright \Phi \in \mathbb{R}^{N_q \times N_q}$ 
9:        $\mathbf{L}_{\Phi}^k = \Phi \cdot \mathbf{c}(\mathbf{x}_k, \mathbf{z})$   $\triangleright$  Compute the weight for source point  $k$ , (5.19)
10:    end for
11:     $\mathbf{R}_t = \text{GetSourceData}(I_q)$   $\triangleright$  Get the scattered data at patch source point
12:     $\mathbf{S}(\mathbf{z}_t) = \mathbf{c} \cdot \mathbf{R}_t$   $\triangleright$  Derivatives  $s(\mathbf{z}_t)$  at  $\mathbf{z}_t$ , (5.20)
13:  end for
14: end function
```

---

To show how to form the desired differential operator from the spatial differentiation matrix and to outline the workflow, a simple example is presented. Assuming a scattered data vector field  $(s_1, s_2, s_3)^T(\mathbf{z}) \in \mathbb{R}^3$ , then the rows of  $\mathbf{L}_{\Phi}^k$  contain the spatial derivatives of the three-dimensional RBF in the three spatial directions  $\left(\frac{\partial \Phi}{\partial z_1}, \frac{\partial \Phi}{\partial z_2}, \frac{\partial \Phi}{\partial z_3}\right)$ . Additionally, the derivative coefficients  $\mathbf{c}(\mathbf{x}_k, \mathbf{z})$  for source point  $k$  are three-dimensional vectors. The final evaluation  $\mathbf{S}(\mathbf{z}) = \mathbf{c} \cdot \mathbf{R}(\mathbf{z})$  leads to the following  $3 \times 3$  matrix

$$\begin{pmatrix} \frac{\partial s_1}{\partial z_1} & \frac{\partial s_1}{\partial z_2} & \frac{\partial s_1}{\partial z_3} \\ \frac{\partial s_2}{\partial z_1} & \frac{\partial s_2}{\partial z_2} & \frac{\partial s_2}{\partial z_3} \\ \frac{\partial s_3}{\partial z_1} & \frac{\partial s_3}{\partial z_2} & \frac{\partial s_3}{\partial z_3} \end{pmatrix}. \quad (5.22)$$

**Kernel scaling** As mentioned above, the Gaussian kernel is used in a local approach. The local kernel has no numerical stability problem in its basic form and works well on regular grids. But as soon as the mesh becomes distorted (e.g. boundary layer) the results get worse. An improvement can be achieved by scaling the Gaussian ansatz function in the following way,

$$\Phi(\|\mathbf{x} - \mathbf{z}\|_2, \alpha) = e^{\left(\frac{\|\mathbf{x} - \mathbf{z}\|_2}{\alpha}\right)^2}. \quad (5.23)$$

Theoretically, the Gaussian kernel leads to high accuracy (in theory differentiation up to any given order is possible) but the stability problem, similar to the global interpolation method, restricts the maximum flatness  $\alpha$ . Roberts proposed a method using a Taylor's expansion in the flatness parameter  $\alpha$  to circumvent this issue [174]. However, there are optimization strategies [164] to find optimal values of the flatness parameter  $\alpha$ .

It should be emphasized here that the parameter  $\alpha$  is computed differently depending on whether an interpolation or derivation procedure is carried out. An idea to find an optimal shape parameter for the RBF derivative procedure is to derive a relationship (a confident initial guess)

$$\alpha \sim f(r_{12}) \quad (5.24)$$

for the parameter  $\alpha$  with respect to the distance  $r_{12}$  to the next point. The basic approach is to minimize the following objective functional

$$E(\alpha, r_{12}) + \lambda(\kappa(\alpha, r_{12}) - \kappa_{\text{limit}}), \quad (5.25)$$

with the  $L_2$ -error  $E$ , the Lagrange multiplier  $\lambda$ , the condition number  $\kappa$ , and the limit of the condition number  $\kappa_{\text{limit}}$ , where the system becomes sensitive to floating-point round-off errors. The  $L_2$ -error represents the deviation of the basis function from being one (absolutely flat,  $\alpha \rightarrow \infty$ ) on the whole domain. This error measure can simply be obtained by integrating

$$E(\alpha, r_{12}) = \int_{\Omega_{2/3}} |1 - \Phi(\|\mathbf{x} - \mathbf{z}\|_2, \alpha)|^2 d\Omega. \quad (5.26)$$

The challenging task is to find the influence of the shape parameter  $\alpha$  on the condition number of the resulting linear system. In general, the condition number  $\kappa$  of a matrix is defined as the ratio of the largest to the smallest eigenvalue,

$$\kappa(\alpha, r_{12}) = \frac{\sigma_{\max}(\alpha, r_{12})}{\sigma_{\min}(\alpha, r_{12})}. \quad (5.27)$$

Therefore, the smallest eigenvalue must be non-zero in order to stay invertible.

The minimization is trivial since the functional decreases monotonically in  $\alpha$  while a critical condition number  $\kappa_{\text{limit}}$  guarantees the invertibility of the matrix. With this constraint, a confident initial guess  $\alpha_{\text{initial}}$  is

$$\alpha_{\text{initial}} \sim 1/r_{12} \quad (5.28)$$

and from this starting point the shape parameter is iterated to the limit of the matrix invertibility, depending on the inversion algorithm.

As depicted in Fig. 5.11, by increasing the  $\alpha$ -parameter the  $l_2$  error decreases. However, when a certain critical condition number of the interpolation matrix is reached, the inversion suffers from numerical instabilities. The critical  $\alpha$ -parameter is dependent on the RBF kernel, the size of the system matrix, and the function which is to be differentiated. For the example shown in Fig. 5.11 using the Gaussian kernel, the critical  $\alpha$ -parameter is about 2.

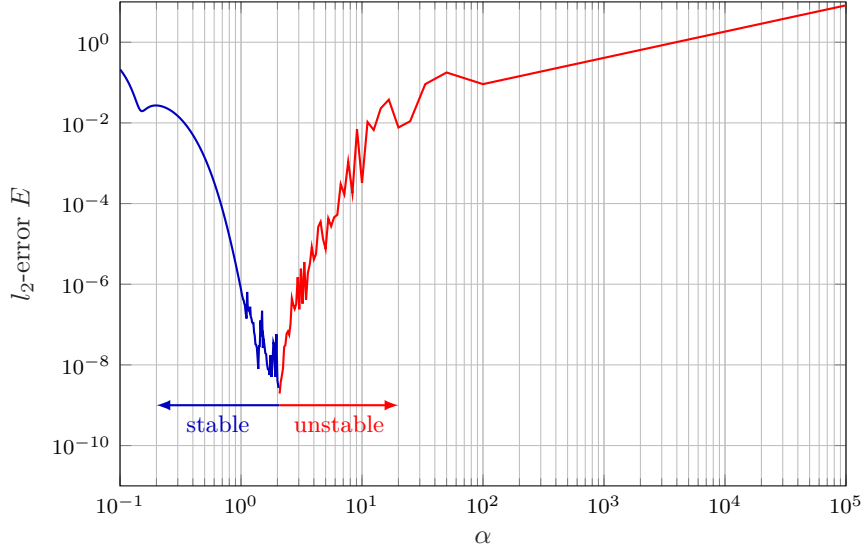


Figure 5.11: Illustration of the  $l_2$ -error for derivatives using the global Gaussian kernel. For this example, the optimal  $\alpha$ -parameter is about 2. For larger  $\alpha$ -parameters, a numerical stability problem occurs during the inversion of the ill-conditioned system matrix.

**Additional notes** During the computation, there is an easy way to assess how accurate the derivative will be. Looking at the last expression of Algorithm 2, where the weight matrix  $\mathbf{c} \in \mathbb{R}^{d \times N_q}$  and the source data matrix  $\mathbf{R} \in \mathbb{R}^{N_q \times d}$  are multiplied, we can state that the row-sum of each row must be zero for an accurate derivative. This can be seen by considering a constant field, where all entries are equal  $R_{ij} = \text{const.}$  and the resulting derivative must be zero (derivative of a constant function)  $S_i(\mathbf{z}) = \sum_{j=0}^{N_q} c_{ij} R_j = 0$ . For non-trivial coefficients, this only holds if the rowsum is zero  $\sum_{j=0}^{N_q} c_{ij} = 0$  for  $i = 1, \dots, d$ . This rowsum condition is used for optimal neighbor consideration.

During investigations, the local Wendland kernel  $\Phi_{2,0} = (1 - \|\mathbf{x} - \mathbf{z}\|_2)^2$  was found to work perfectly for generic test cases with moderately distorted elements. But as soon as the the Wendland kernel was applied to more sophisticated problems (e.g. boundary layers) severe numerical artifacts were observed, especially when computing the divergence. Therefore, a local approach with a Gaussian kernel (5.23) is used, which produces accurate results for a wide range of mesh discrepancies.

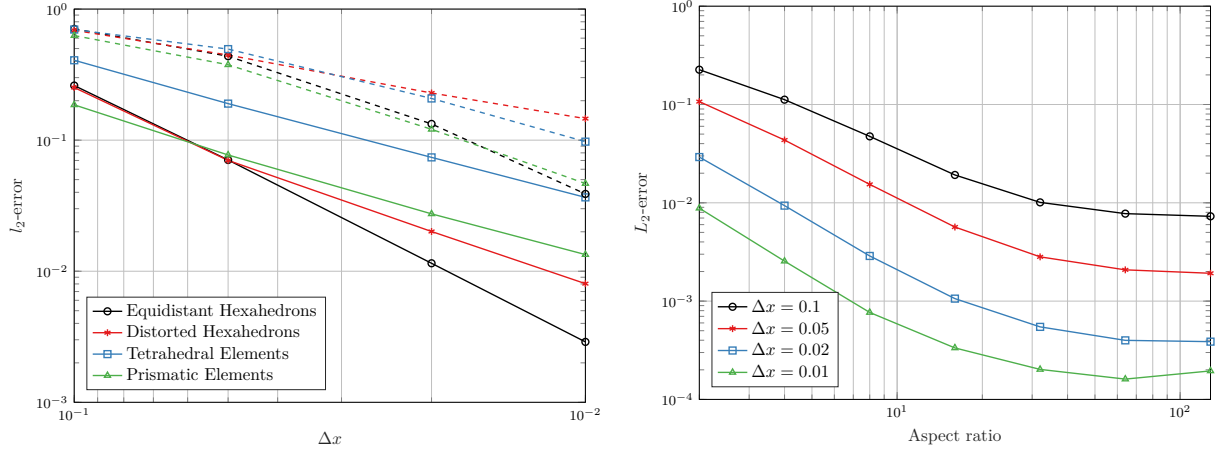
### 5.2.1 Convergence of derivatives

To analyze the convergence and accuracy of the RBF derivatives, the analytic functions (5.10 - 5.12) are again prescribed on a unit cube  $\Omega \in [0, 1]^3$  with different node distributions and observe the  $l_2$ -error after computing the gradient of the field.

Figure 5.12(a) shows the convergence of the RBF derivatives with respect to the characteristic discretization distance  $\Delta x$  for the first and second analytic function. Similar to the RBF interpolation, we find that there is an influence resulting from the data density. Although the RBF derivatives are accurate for both analytic functions, it is obvious that larger gradients (as encountered in the second analytic function) lead to larger deviations.

Additionally, the convergence of the derivatives in boundary layers was analyzed considering the analytic function (5.12). This analytic function was again prescribed on a mesh consisting of hexahedrons with different aspect ratios in the range of 2 to 128 for the cells in the first row.

As shown in Fig. 5.12(b), the  $l_2$ -error decreases with increasing number of nodes in the region where the largest gradients occur (next to the wall). However, since the number of nodes on the edges perpendicular to the wall stays the same while the height of the cells is varied, a point is eventually



(a) Illustration of the  $l_2$ -error for the gradient of the first analytic function (solid) and the second analytic function (dashed) with respect to the mesh discretization. (b) Illustration of the  $l_2$ -error for the gradient of the third analytic function on a hexahedral mesh with respect to the mesh discretization.

Figure 5.12: Convergence of the derivatives for the analytic functions (5.10), (5.11), and (5.12).

reached where the nodes are not distributed well enough over the entire region of the largest gradients. This is the reason for the flattening of the curves for hexahedrons with large aspect ratios.

### 5.3 Application of RBF algorithm

Based on the RBF algorithm, the implemented aeroacoustic source terms are verified (see Tab. 5.1). In the convergence study the numerical source terms were compared to the analytical reference. The

Table 5.1: In CFSDAT (Coupled Field Simulation DATA Transformation is an inhouse data transformation tool.) implemented aeroacoustic source terms, based on RBFs.

Formulation
$\nabla \cdot ((\nabla \times \mathbf{u}) \times \mathbf{u})$
$\nabla \cdot ((\nabla \times \mathbf{u}) \times \mathbf{u}) + \nabla \cdot \nabla \cdot (\frac{1}{2} \mathbf{u} \cdot \mathbf{u})$
$\nabla \cdot \nabla \cdot (\rho \mathbf{u} \mathbf{u})$

reference is an analytic velocity distribution  $\mathbf{u}(\mathbf{x})$  that is similar to vortical structures and isentropic in space

$$\mathbf{u}(\mathbf{x}) = (x^2 + y^2 + z^2) \sin(2\pi x) \sin(2\pi y) \sin(2\pi z) (\mathbf{e}_x + \mathbf{e}_y + \mathbf{e}_z). \quad (5.29)$$

Figure 5.13 shows the analytic function and the convergence of the computed source terms with respect to the number of points per wavelength. The computation involves a second derivative and the source terms converge to the analytic solution.

### 5.4 Conservative Interpolation

After assembling the aeroacoustic sources, a conservative interpolation scheme transforms the total energy from the CFD mesh to the acoustic mesh. Energy conservation is guaranteed by the interpolation algorithm through an integration over the cell volume. A rudimentary approach is to sum up all volume weighted aeroacoustic loads from the CFD centroids whenever the centroid is located inside an acoustic element. Figure 5.14 shows this computational efficient variant based on the cell centroids of the CFD

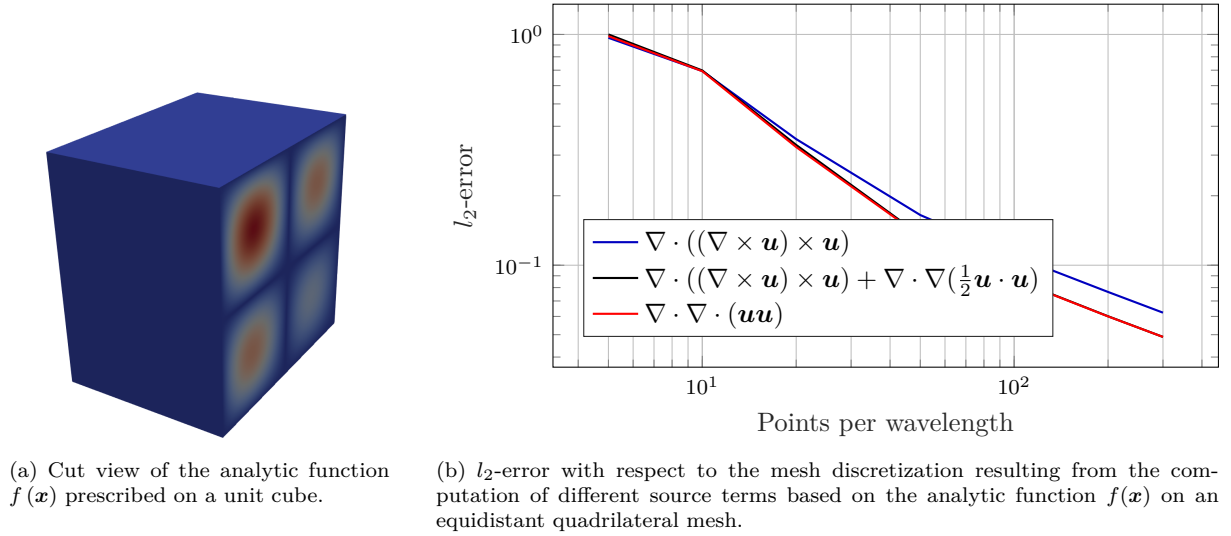


Figure 5.13: Convergence of the aeroacoustic source terms.

grid. However, this approach computes wrong acoustic sources if the acoustic cells are smaller than the flow cells. To avoid this limit, an advanced interpolation algorithm has been proposed in [175] that is

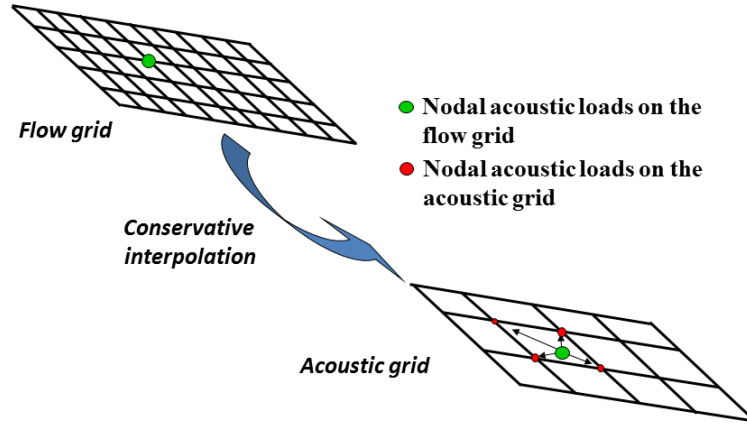


Figure 5.14: Standard approach of the conservative interpolation based on the flow grid cell centroids. Extracted from [175].

based on the intersection of the different acoustic and flow grid. Based on the intersection, the volume integral adds up the contributions to the respective CAA elements (see Fig. 5.15).

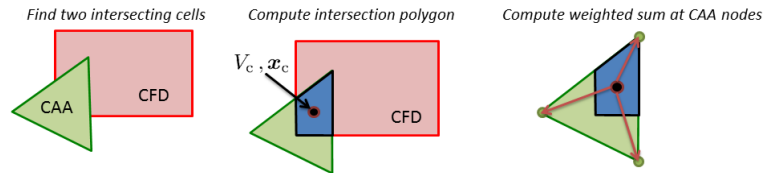


Figure 5.15: Computational steps for the conservative interpolation based on cut-volume-cell approach. Extracted from [175].

The standard conservative interpolation and the cut-volume-cell approach are compared and verified against an analytic function

$$f(\mathbf{x}) = \sin(3\pi x), \quad (5.30)$$

on the domain  $\Omega \in [0, 1]^2$ . Considering the standard approach, energy errors will occur for large mesh ratios  $\Gamma$

$$\Gamma = \frac{N_{\text{CAA}}}{N_{\text{CFD}}}, \quad (5.31)$$

with  $N_{\text{CAA}}$  the number of nodes on the edges of the CAA mesh and  $N_{\text{CFD}}$  the number of nodes on the edges of the CFD mesh per resolved wavelength  $\lambda_a = 2/3m$ , for this example. Figure 5.16 shows how the FE nodal right hand side values develop on the line at  $y = 0.5$ . Along the evaluation line, the number of nodes of the CFD grid are constant for the different evaluations, 101 nodes. In contrast to that, the number of the nodes along the CAA mesh vary according to the mesh ratio. If  $\Gamma < 1$ , the CFD grid is finer than the CAA mesh; for  $\Gamma > 1$ , the CFD grid is coarser than the CAA mesh. The standard interpolation performs satisfactory for low mesh ratios, when the CFD grid is fine. For larger mesh ratios, the standard interpolation exhibits spurious modes and energy is transferred to higher wave length (unphysical). Overall, the cut-volume cell approach has the desired conservative properties for all mesh ratios.

Based on Parseval's theorem, the relative energy content of the real wavelength  $\lambda_a$  is evaluated compared to the total energy by the energy ratio  $e_r$

$$e_r = \frac{\left(\hat{Q}_{\text{RHS}}(\lambda_a)\right)^2}{\sum_{k=1}^N \left(\hat{Q}_{\text{RHS}}(\lambda_k)\right)^2}. \quad (5.32)$$

Here,  $\hat{Q}_{\text{RHS}}$  are the amplitudes of the discrete wave number transformation at the corresponding wavenumber, respectively. Table 5.2 compares the standard conservative integration based on the cell centroids (standard) to the conservative cut-volume-cell interpolation (cut-volume-cell). As expected the more accurate conservative cut-volume-cell interpolation performs superior. However, the computational demand

Table 5.2: Ratio of the energy corresponding to the actual wavelength and the total energy for the standard procedure and the cut volume-cell procedure, respectively.

$\Gamma$	Standard $e_r$	Cut volume-cell $e_r$
0.5	99.59 %	99.34 %
1	99.51 %	99.14 %
2	87.5 %	98.76 %
5	55 %	98.94 %
10	31.23 %	98.96 %
20	15.85 %	99.06 %
30	10.6 %	99.1 %

increases with the number of cell intersections (see Tab. 5.2). Compared to the standard approach, the cut-volume-cell intersection takes about 5 times as long, but overall the computational demand increases linearly.

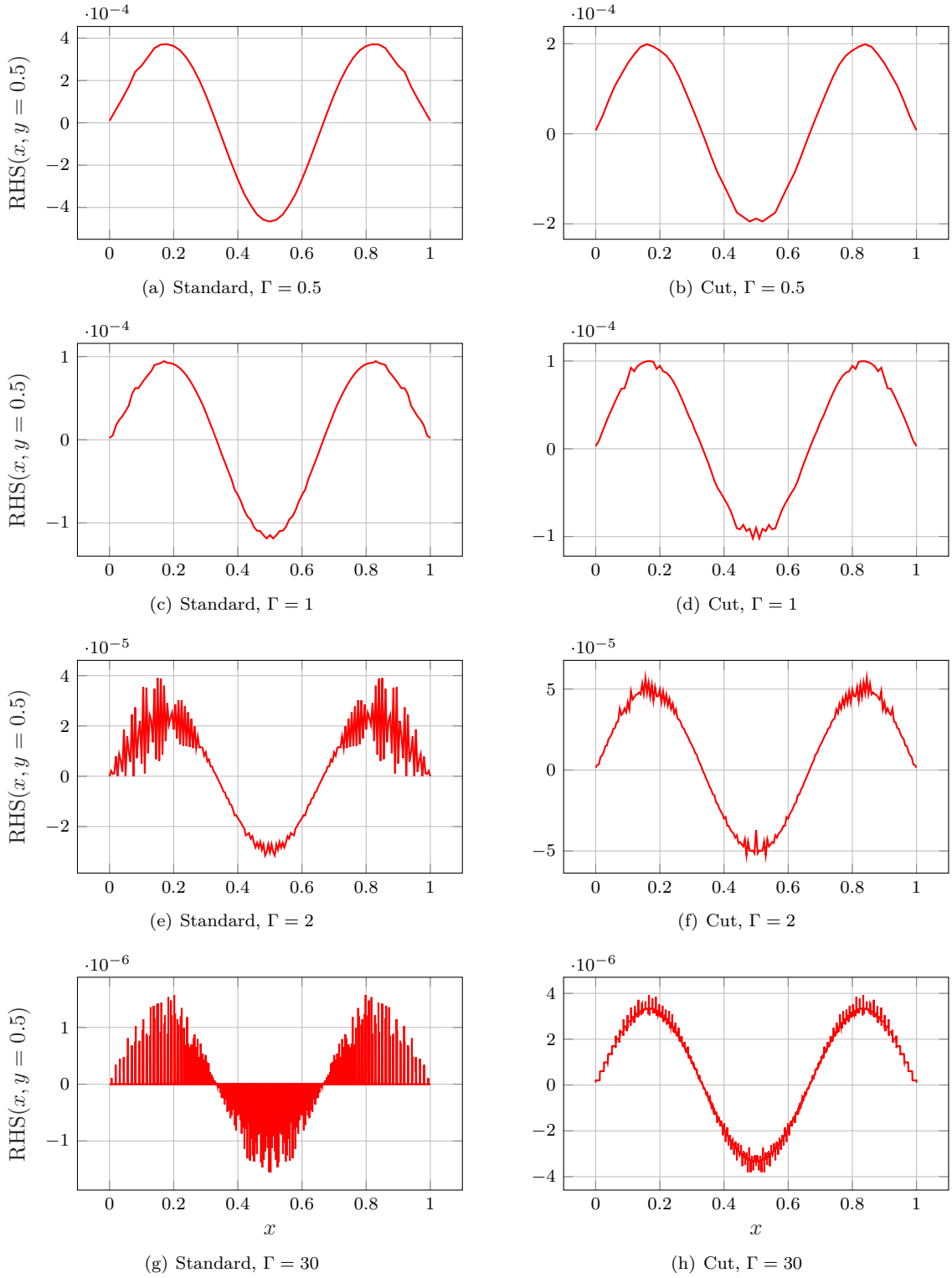


Figure 5.16: FE nodal right hand side values at  $y = 0.5$  with respect to the distance in  $x$ -direction. Number of nodes of the CFD grid on along the line evaluation line is 101; whereas the number of the nodes along the line is based on the mesh ratio  $\Gamma$ .  $\Gamma < 1$ : the CFD grid is finer than the CAA mesh;  $\Gamma > 1$ : the CFD grid is coarser than the CAA mesh. The standard interpolation for different mesh ratios is illustrated in (a, c, e, g) and the cut-volume cell approach is illustrated in (b, d, f, h).

## 6 Validation and Applications

The validation links the missing or contradicting thoughts of readers. In combination with the developed methodology continuously four typical questions arose through review processes. These four misunderstandings are addressed by a separate validation example.

Firstly, the capability of the Helmholtz decomposition is underestimated. Without merit, thoughts spread that the decomposition cannot split colorful, and rich fluid dynamics into vortical and non-vortical components. This misinterpretation is clarified by all four examples in this thesis; the first example, a cylinder in a crossflow, focuses exclusively on the separation. The conclusion reveals that the Helmholtz decomposition extracts the incompressible part of a low Mach number compressible flow simulation.

Secondly, the developed method has no fundamental fluid dynamic justification. Goldstein justifies that the vortical part of Helmholtz decomposition of the compressible flow field is non-radiating. The non-radiating base flow is used to extend the Mach number limitation of hybrid aeroacoustic analogies. Typical hybrid analogies follow a three step approach: the incompressible CFD simulation, the extraction of acoustic sources, and the direct one-way coupling to the acoustic simulation. The incompressible fluid restricts fluid dynamics such that only compact acoustic feedback mechanisms are resolved. If the feedback mechanism is not acoustically compact, the state of the art is a DSC simulation of flow and acoustics. Investigations proved that even a coarser discretization than the one used by the DSC resolves the dominant aeroacoustic feedback. At low Mach numbers, we show that acoustically under-resolved DSC simulations in combination with the Helmholtz decomposition are able to compute the non-radiating base flow. The Mach extended hybrid analogy follows again a three step approach, the compressible CFD simulation in combination with a Helmholtz decomposition, the direct one-way coupling of the non-radiating base flow to the acoustic. This second example "cavity with a lip" validates the workflow in 2D.

Thirdly, turbulent structures are used to doubt the capabilities of the Helmholtz decomposition. Thoughts spread that the decomposition cannot resolve turbulent vortical structures. The third example "cavity with a lip" clarifies the method in 3D.

Fourthly, a disfavor arose with the conceptual extension to larger Mach numbers, well below Mach one. Although, the first three examples are simple, they proof validity of the concept and support application of a Helmholtz decomposition at higher Mach numbers. The last example compares hybrid simulations at higher Mach numbers with DSC data. This comparison emphasizes further investigation of this method.

This hybrid aeroacoustic workflow focuses on the acoustic properties of the simulation task. The aeroacoustic problem is analyzed; significant aeroacoustic sources are detected. Based on this, an acoustic behavior-oriented solution is favored. Impedance boundaries and other experimentally justified acoustic material properties are easily integrated. Furthermore, a fast and optimal numerical scheme, designed for wave equations, computes the acoustic. To conclude, this chapter manifests valid applications of the theory.



## 6.1 Cylinder in a crossflow – 2D

This section is dedicated to show the physical capabilities and mathematical difficulties on the Helmholtz decomposition. Since the Helmholtz decomposition does not compute fluid dynamics, but separates the compressible and vortical effects, it is self-evident that this decomposition can reproduce an incompressible flow. The intention of this case is to show that the Helmholtz decomposition with the exact boundaries is indeed able to recover the incompressible CFD solution. As the Mach number is quite low and no feedback mechanism will occur for the given flow state, the compressible and the incompressible CFD results develop the same flow structures. Therefore, the compressible CFD results are projected to the incompressible function space and finally compare it with the incompressible CFD solution.

Mathematically, the decomposition on a homologically trivial domain (domain with holes) causes a generally non-unique decomposition and an additional harmonic term occurs. This harmonic term is known as the potential flow solution. For the vector potential formulation and the given Neumann boundaries, the potential flow solution is hidden in the vortical component.

Table 6.1: Geometric and flow parameters of the "cylinder in a crossflow".

Parameter	Value	Description
Re	200	Reynolds number
M	0.03	Mach number
$U_\infty$	10 m/s	Free stream velocity
$D = 2a$	0.02 m	Cylinder diameter
St	0.2	Strouhal number

In fluid dynamics the most simplest example of a homologically trivial domain is a cylinder, with radius  $a$ , in a crossflow. The geometrical and fluid dynamic properties are given in Fig. 6.1 and Tab. 6.1. A circular domain surrounds the cylinder. Asymptotic approximation provides the potential flow solution

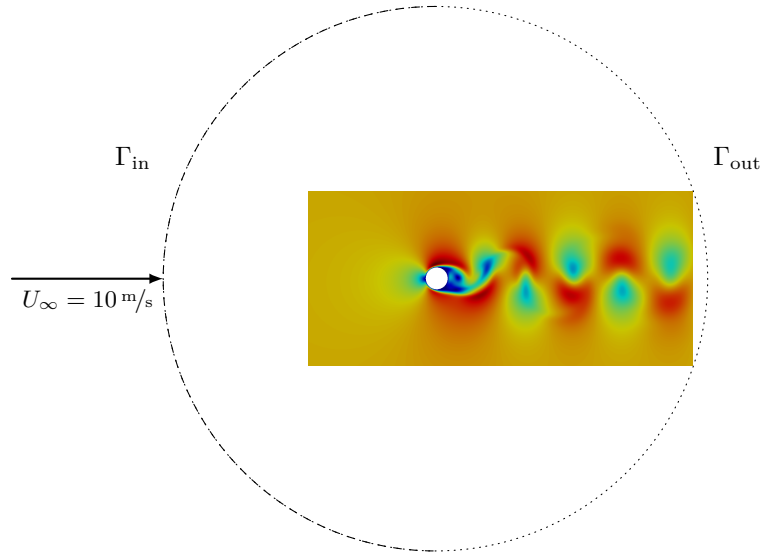


Figure 6.1: Schematic of the geometry and the flow configuration.

of the velocity potential  $\Phi$

$$\Phi = U_\infty \left( 1 - \frac{a^2}{r^2} \right) r \sin \varphi. \quad (6.1)$$

### 6.1.1 Fluid dynamics

Compressible as well as incompressible, viscous flow simulations of the "cylinder in a crossflow" are performed on the circular 2D domain, discretized by a structured grid. The time-step is chosen to resolve the vortices in the wake of the cylinder, known as "Von Karman vortex street", characterized by the Strouhal number. During the compressible simulation the fluid is modeled as an ideal gas. At the cylinder's wall a no-slip and no-penetration condition is enforced. A velocity inlet at  $\Gamma_{\text{in}}$  and a pressure outlet condition at  $\Gamma_{\text{out}}$  complete the setup.

### 6.1.2 Helmholtz decomposition

The "cylinder in a crossflow" involves no aeroacoustic feedback at such a low Mach number and as a consequence the incompressible and the compressible flow structures converge to each other. A decomposition of the compressible velocity field in its compressible component and vortical component should recover the incompressible CFD solution.

Helmholtz decomposition computes the vortical component for a rectangular subdomain of the CFD region. To extract the vortical velocity, we solve the curl-curl equation for the vector potential. The tangential velocity imposes accurate boundaries and mass regularization guarantees solvability of the Neumann problem. Figure 6.2 shows the similarity of the incompressible CFD and incompressible result of the Helmholtz decomposition. The results of the velocity magnitude converged up to a relative  $l_2$ -error of 0.6% between the fields. The remaining error is partly connected to the difference between the compressible and incompressible vorticity field and partly due to the numerical procedures used obtain the incompressible projection.

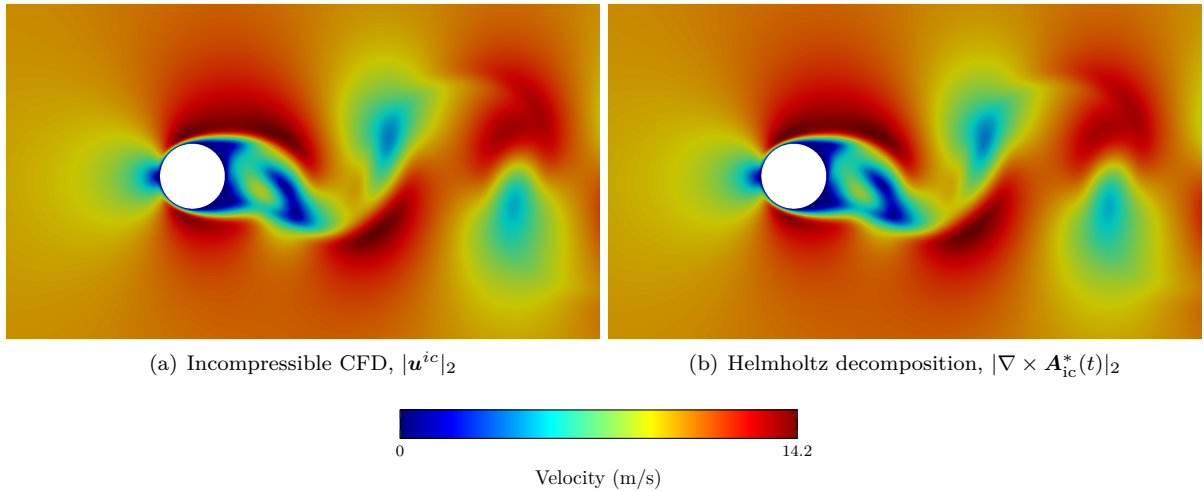


Figure 6.2: Comparison of the incompressible velocity (a) and the incompressible projection of a compressible velocity (b).

For this example the Helmholtz decomposition based on the compressible potential (4.10) was not investigated, as we expect large numerical errors due to a extremely small rate of dilatation at this low Mach number. At this small rate of expansion, the numerical noise of the numerical procedure will be in the order of the rate of dilatation.

### 6.1.3 Conclusions

In this section, the application of the Helmholtz decomposition to a homologically trivial domain was demonstrated. Considering the vorticity distribution and the used Neumann boundaries, the simulation

model suppresses the potential flow solution. The vector potential formulation, being the solution of the inhomogeneous curl-curl equation, gives accurate results compared to the incompressible flow simulation. To conclude, the Helmholtz decomposition extracts vortical components, but strictly relies on the quality of the CFD simulation. Consequently, this decomposition cannot resolve further or finer structures in the velocity field.

## 6.2 Cavity with a lip – 2D

Hybrid analogies follow a three step approach, the incompressible CFD simulation, the direct one-way coupling to the acoustic, and the acoustic simulation. The incompressible fluid restricts fluid dynamics, only compact acoustic feedback mechanisms are resolved. If the feedback mechanism is not acoustically compact, the state of the art simulation approach is a DSC. This investigation aims to prove that even a coarser discretization, than the one used by the DSC, resolves the dominant aeroacoustic feedback. At low Mach numbers, we show that acoustically under-resolved DSC simulations in combination with the Helmholtz decomposition are able to compute the non-radiating base flow. Goldstein labels the vortical part of Helmholtz decomposition of the compressible flow field as non-radiating. The non-radiating base flow is used to extend the Mach number limitation of hybrid aeroacoustic analogies. Similar the previously discussed workflow, the Mach extended hybrid analogy follows again a three step approach, the compressible CFD simulation in combination with a Helmholtz decomposition, the direct one-way coupling of the non-radiating base flow to the acoustic. This hybrid workflow is validated in 2D by the aeroacoustic benchmark case "cavity with a lip" [176]. Figure 6.3 shows the geometrical properties and the flow configuration of the benchmark case, with all spatial dimensions in mm.

A reduced cross-section at the neck of the cavity characterizes a Helmholtz resonator like geometry. Typically, turbulent pressure fluctuations in the boundary layer excite the resonator. The Helmholtz resonance of the cavity is 2150 Hz, but will not be resolved by the URANS flow simulation.

A free-stream of  $U_\infty = 50 \text{ m/s}$  rushes over the plate and develops a boundary layer up to a boundary layer thickness of  $\delta = 10 \text{ mm}$ . For this configuration a first shear layer mode at  $f_{s1} = 1700 \text{ Hz}$  is expected that is well captured by measurements (see Fig. 6.4). Interpretation of the measurements reveal that a duct mode ( $n = 2$ ) occurs in the cavity span at  $f_{sp} = 1360 \text{ Hz}$ , which cannot be resolved by the 2D simulation. The first box mode of the cavity depth, known as  $\lambda/4$ -mode, is at  $f_d = 3000 \text{ Hz}$ . The acoustically under-resolved flow simulation focuses on the frequency range of 1000 Hz – 2000 Hz and especially the resolution of the shear layer mode.

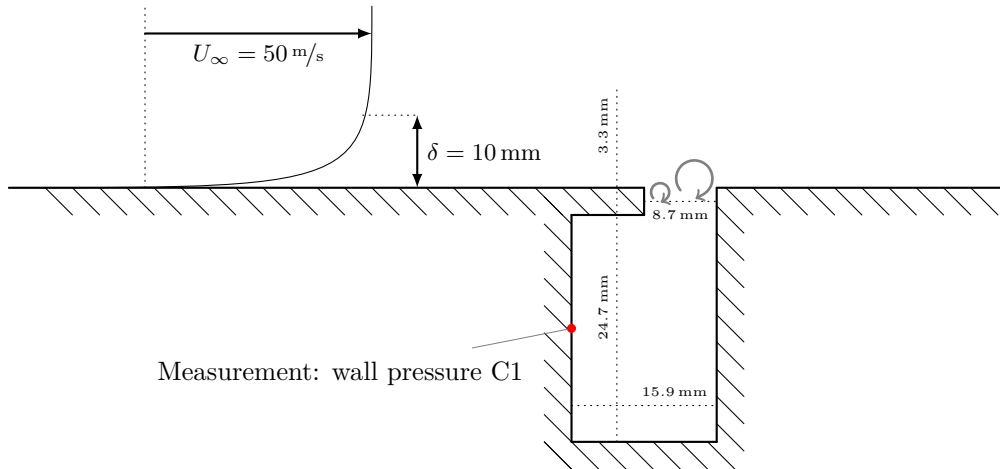


Figure 6.3: The geometry and the flow configuration of the benchmark problem "cavity with a lip".

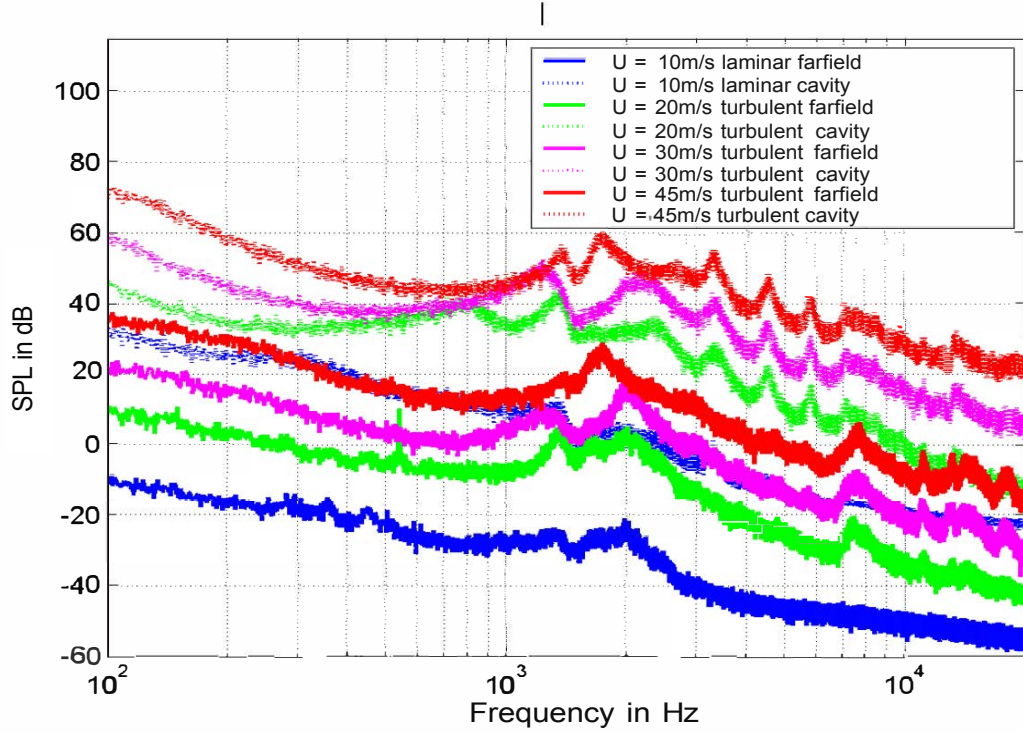


Figure 6.4: Experimental investigation of the cavity with a lip for various boundary layer free stream velocities. The study was conducted at FAU Erlangen during a master thesis. Extracted from [177].

### 6.2.1 Simulation workflow

The workflow is split into three main steps. First, a compressible flow simulation on a reduced domain  $\Omega_F$  is carried out, such that the flow phenomena is captured. The second computation filters the compressible flow data on the flow domain  $\Omega_F$  and extracts the non-radiating base flow in order to construct the vortical source term  $\mathbf{L}$ . Finally, the acoustic propagation is computed on the joint spatial domain  $\Omega_A = \Omega_P \cup \Omega_F$ , both in frequency and time domain (see Fig. 6.5). The perfectly matching layer serves as an accurate free field radiation condition.

### 6.2.2 Fluid dynamics

During this study, compressible as well as incompressible flow simulations of the cavity with a lip are performed on the 2D domain  $\Omega_F$ . Since the expected mode  $f_{s1}$  involves strong aeroacoustic feedback from the compressible part of the solution on the vortical structures, a compressible simulation is indispensable. The unsteady, compressible, and laminar flow simulation is performed with a prescribed velocity profile  $\mathbf{u} = \mathbf{u}_{in}$  at the inlet  $\Gamma_{F1}$ , a no slip and no penetration condition  $\mathbf{u} = \mathbf{0}$  for the wall  $\Gamma_{F2}$ , an enforced reference pressure  $p = p_{ref}$  at the outlet  $\Gamma_{F3}$ , and a symmetry condition  $\mathbf{u} \cdot \mathbf{n} = 0$  at the top  $\Gamma_{F4}$  (see Fig. 6.5).

As known from literature [44], the incompressible simulation misinterprets the physics and predicts a shear layer mode of second type. Figure 6.6 shows the wall pressure level (PL) of the compressible CFD at the measurement point C1. The compressible flow simulation predicts the shear layer mode at 1680 Hz, accurately and measurements confirm the simulation results. A careful reader recognizes ambiguous phenomena in the PL at around 1105 Hz. An acoustic eigenmode analysis detects computational domain resonance  $f_{dom} = 1105$  Hz, the mode of the computational artifacts (see Fig. 6.7). Although performing

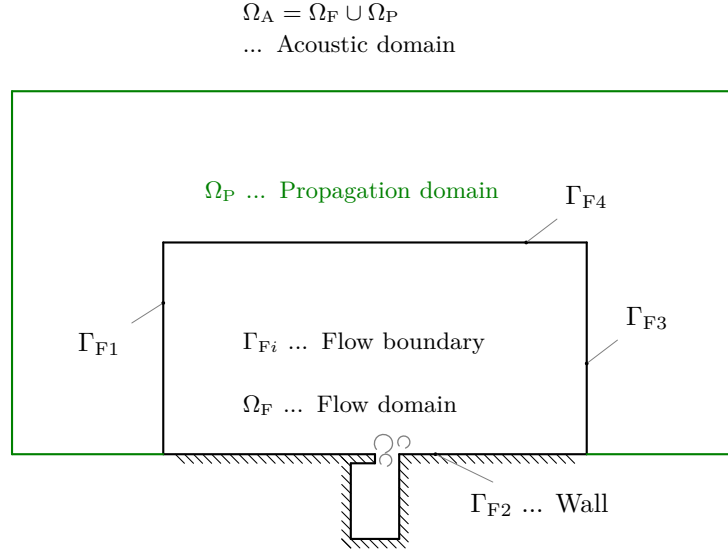


Figure 6.5: Schematic of the computational domain. The flow domain  $\Omega_F$  is a subdomain of the acoustic domain  $\Omega_A$ , which includes the flow domain as its source domain.

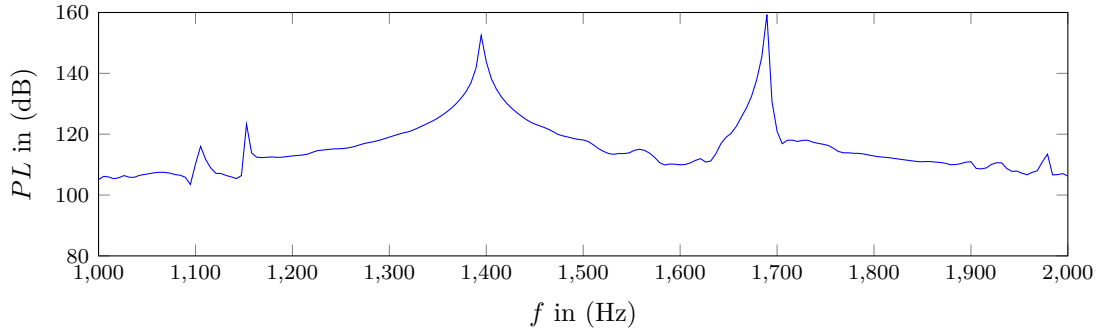


Figure 6.6: The wall pressure level (PL) of the compressible flow simulation at the observation point C1 in the cavity. The 1<sup>st</sup> shear layer mode is located at 1680 Hz and the artificial computational domain resonances are located around 1100 Hz and 1400 Hz. The reference pressure is 20  $\mu$ Pa.

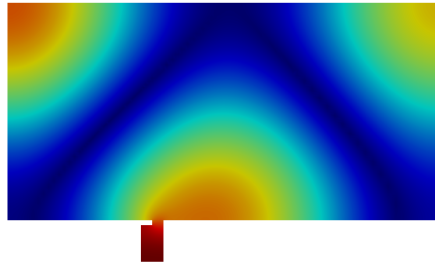


Figure 6.7: Mode of the computational artifacts at 1105 Hz due to the boundary inaccurate treatment during the CFD.

a 2D flow simulation of the cavity, a resonance at 1390 Hz occurs, surprisingly close to the span-wise duct mode of the measurements. A possible explanation is that the computational domain resonance modulates the aeroacoustic source term. This multiplicative combination of flow components generates a beat tone artifact at 1382.5 Hz. The modulation frequency  $f_{\text{mod}}$  is given by

$$f_{\text{mod}} = \frac{f_{s1} + f_{\text{dom}}}{2} = 1382.5 \text{ Hz} . \quad (6.2)$$

At a representative time step, the rate of expansion  $\nabla \cdot \mathbf{u}$  of the compressible flow simulation shows this dominant artificial computational domain resonances at a frequency of 1105 Hz (see Fig. 6.8).

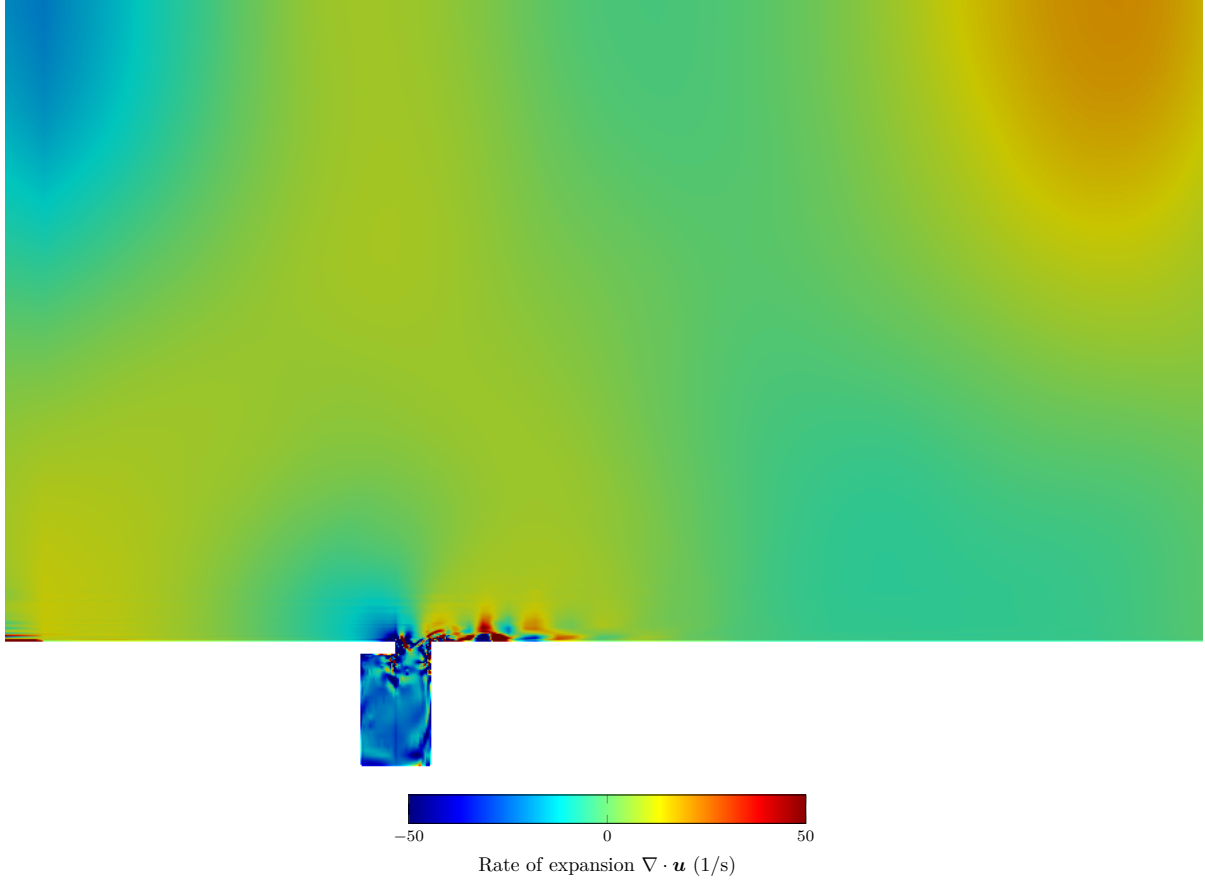


Figure 6.8: The rate of expansion  $\nabla \cdot \mathbf{u}$  of the compressible flow simulation at a representative time step. The figure demonstrates the presence of artificial standing waves due to the boundary conditions of the compressible flow simulation. The figure shows a characteristic time step.

The artificial computational domain resonances emphasize physically correct boundary models. Considering this proprietary flow solver, the free field transmission boundary for vortical and wave structures were limited in the application that resulted in an inaccurate solution.<sup>1</sup> Ordinary CFD boundaries are optimized to propagate vortical structures without reflection. In contrast to that, acoustic radiation conditions are not modeled precisely and as a consequence artificial computational domain resonances superpose the flow field. The common DSC simulation utilizes sponge layer techniques to damp acoustic waves towards the boundaries. However, during ordinary flow simulation, without aeroacoustic feedback, the weak acoustic energy has typically no impact on the flow simulation. Additionally to the lack of boundary models, the used flow solver is second order accurate and the flow stabilizing numerical damping dissipates waves.<sup>2</sup> Consequently, engineers face a relatively high computational burden if they resolve both flow and acoustics with a flow solver. The hybrid aeroacoustic workflow targets the algorithmic challenges. Furthermore, the acoustically inaccurate boundary models during the CFD are corrected by the Helmholtz decomposition.

<sup>1</sup> Although the self-sustained oscillation interact with this boundary reflections, the 3D application shows that the shear layer mode is captured.

<sup>2</sup> Usually before the waves propagate into the far field.

### 6.2.3 Helmholtz decomposition

The Helmholtz decomposition of the flow field extracts the artificial computational domain resonances and the modulation of the aeroacoustic source term due to the boundary condition at  $\Gamma_{F1}$ ,  $\Gamma_{F3}$ ,  $\Gamma_{F4}$ . Physical radiating compressibility is separated from non-radiating base flow components.

Both, the scalar and the vector potential formulation have been implemented applying the finite element method. The simply connected domain  $\Omega_F$ , with its reentrant corners at the orifice of the cavity, causes singularities in the compressible velocity component  $\mathbf{u}^{*,c} = \nabla\phi^{*,c}$  (see Fig. 6.9). In general, this holds for domains, where corners with a corner angle  $\theta > \pi$  exist. The singularities are treatable by a graded mesh. Overall, the  $L^2$ -orthogonality

$$\langle \nabla\phi^{*,c}, \mathbf{u} - \nabla\phi^{*,c} \rangle := \int_{\Omega_F} \phi^{*,c} \cdot (\mathbf{u} - \nabla\phi^{*,c}) dx = 6 \cdot 10^{-4}\% \quad (6.3)$$

of the extracted field component  $\nabla\phi^{*,c}$  to the complementary field  $\mathbf{u} - \nabla\phi^{*,c}$  holds.

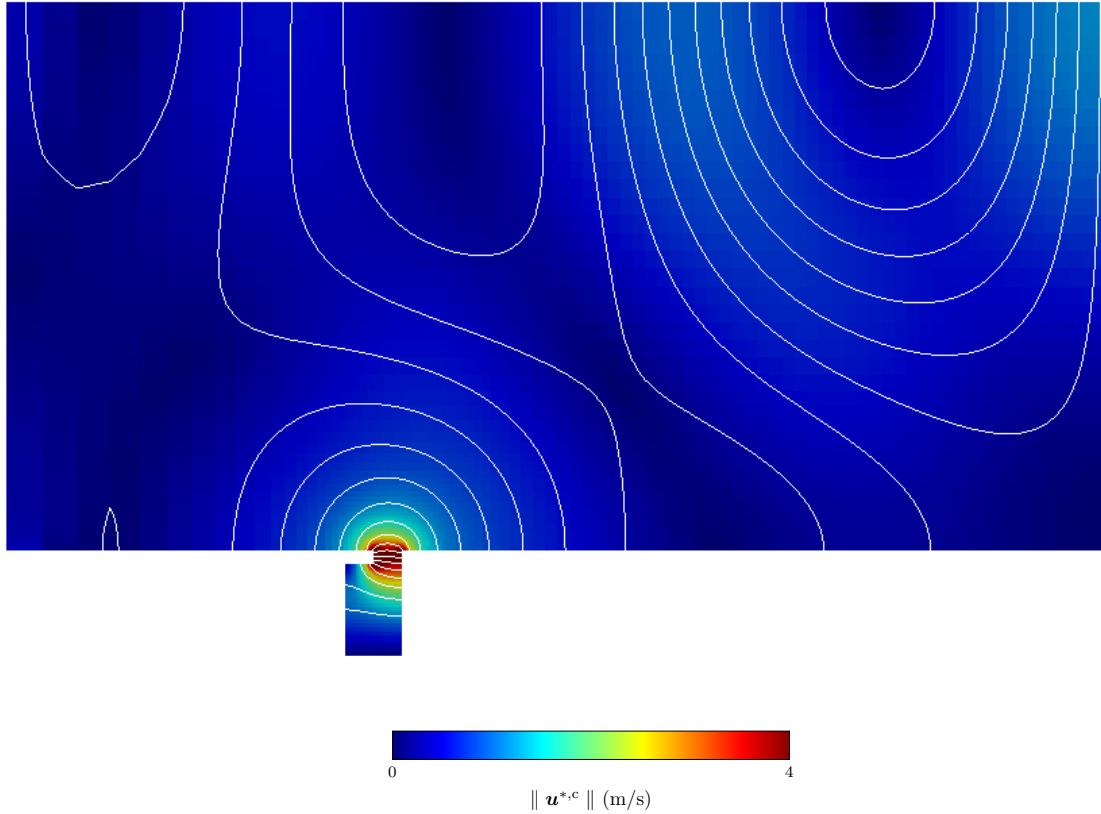


Figure 6.9: The magnitude of the compressible part of the velocity reveals singularities at reentrant corners. As illustrated, the artificial pattern in the domain is captured well. The figure shows a characteristic time step.

Compared to the scalar potential formulation, the vector potential (Fig. 6.10) does not face singularities at the corners. In case of reentrant corners, the vector potential formulation is the method of choice, since no singularities are present and the overall extracted field contains all divergence-free components. The  $L^2$  orthogonality of the extracted field  $\nabla \times \mathbf{A}^{*,ic}$  to the complementary field  $\mathbf{u} - \nabla \times \mathbf{A}^{*,ic}$  holds  $\langle \nabla \times \mathbf{A}^{*,ic}, \mathbf{u} - \nabla \times \mathbf{A}^{*,ic} \rangle = 0.02\%$ .

As the boundaries of both, the scalar and vector potential decompositions, are adjusted to the orthogonality condition at the boundaries (4.6) and (4.7), this adjusted decomposition is able to extract a unique

pair of  $L^2$  orthogonal vector fields  $\langle \nabla \times \mathbf{A}^{*,ic}, \nabla \phi^{*,c} \rangle = 0.03\%$ . The non-radiating field  $\tilde{\mathbf{u}} := \nabla \times \mathbf{A}^{*,ic}$  composes the corrected aeroacoustic source term.

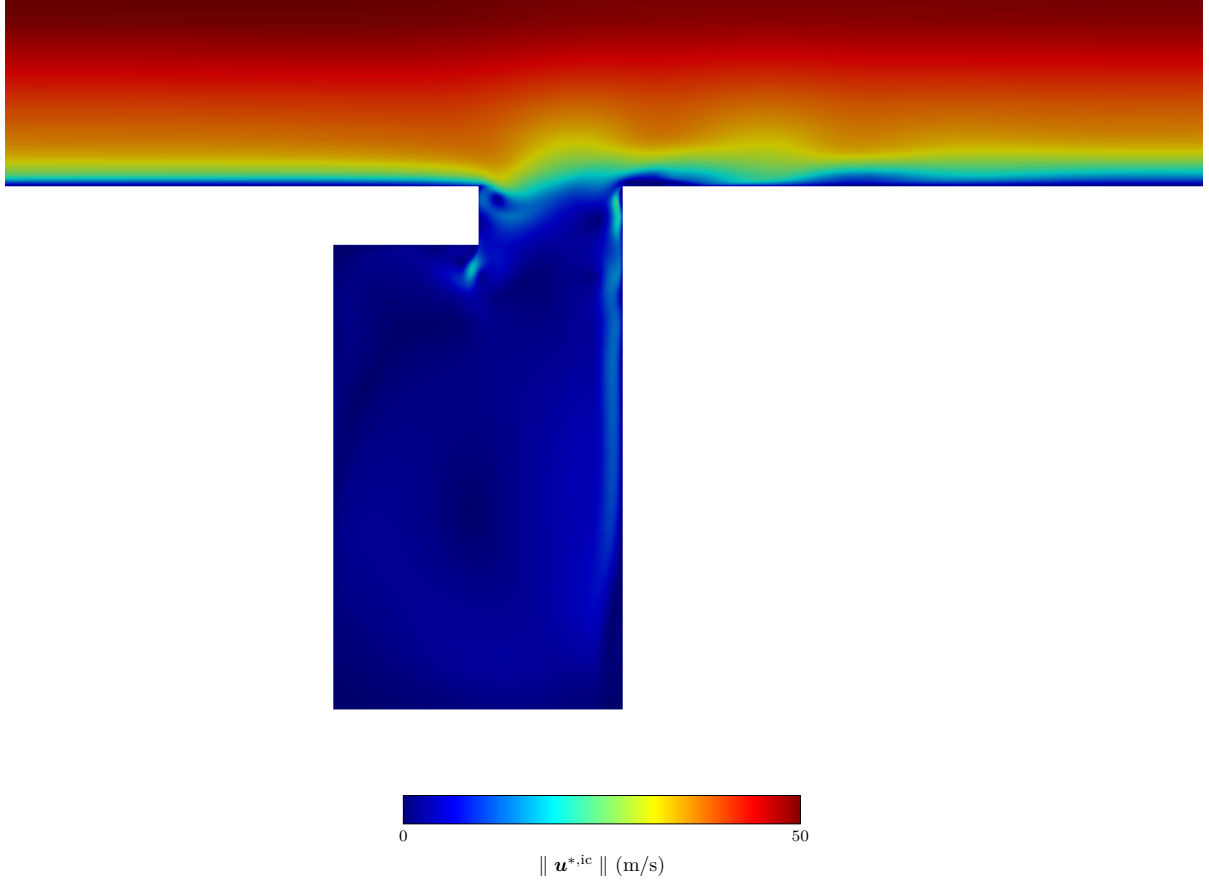


Figure 6.10: The magnitude of the vortical component shows that it captures all vortical flow features of the simulation. The figure shows a characteristic time step.

#### 6.2.4 Acoustic propagation

This method tackles the compressible phenomena inside the domain  $\Omega_F$  by filtering the domain artifacts of the compressible flow field such that the computed sources are not corrupted. The result of the vector potential formulation is used to construct the corrected Lamb vector  $\mathbf{L}(\tilde{\mathbf{u}})$  (Fig. 6.11.a). CFS++ [178] solves the equation of vortex sound (2.102) for the total enthalpy  $H$  in terms of the finite element method. The effectiveness of the filtering technique is investigated based on acoustic propagation in the time and frequency domain, and the simulation results are compared to the measurements inside the cavity as well as outside. In the ideal case, the radiating field in the aeroacoustic source terms are filtered out. Therefore, we compare the acoustic field resulting from the corrected source term and the acoustic field forced by the non-corrected source term. Figure 6.11 illustrates the shape and nature of the Lamb vector for a characteristic time step and surprisingly there is no visible difference in the source term, except its strength. The Lamb vector and the derivatives are computed in the framework of radial basis functions. Doppler's effect is included in the convective wave operator, in upstream direction the wavefronts reduce their wavelength and downstream the distance between the peaks of the wavefronts are enlarged. The finite element domain consists of three discretization independent and non-conforming regions: acoustic source domain, the propagation domain and a PML domain that ensures accurate free field radiation. These domains are connected by non-conforming Nitsche-type Mortar interfaces [179]. The aeroacoustic



sources are prescribed in the source domain. Two different aeroacoustic source variants are investigated, the uncorrected Lamb vector  $\mathbf{L}(\mathbf{u})$  (includes non-radiating and radiating components) and the corrected Lamb vector  $\mathbf{L}(\tilde{\mathbf{u}})$  based on the Helmholtz-Hodge decomposition in the vector potential formulation.

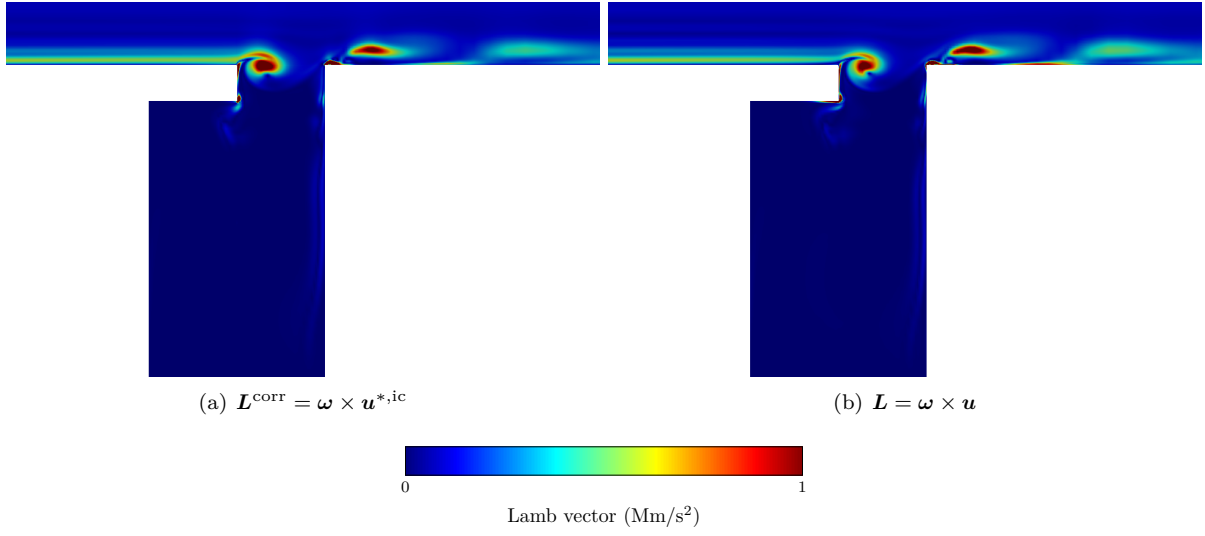


Figure 6.11: Comparison of the Lamb vector for the corrected (a) and the non-corrected (b) calculation. The figure shows a characteristic time step.

Figure 6.12 compares the resulting acoustic field whether for applying the source term correction or not. As expected, the acoustic field of the corrected source term is weaker. The corrected acoustic field represents the acoustics due to the vortical velocity component in the source term.

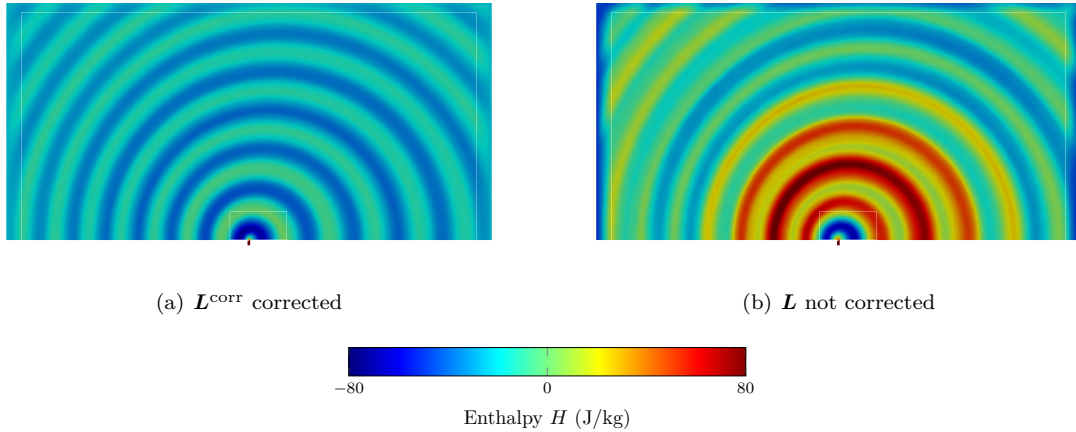


Figure 6.12: Field of the total enthalpy fluctuation  $H$  at a characteristic time. (a) Aeroacoustic sources of the wave equation are corrected. (b) Aeroacoustic sources are not corrected.

Oberai et al. [180] and Kato's approach [181] corrects the 2D SPL values to a representative 3D SPL value, considering a span of the cavity simulation of  $L_s = 1$  m compared to measurements of  $L = 250$  mm. These results meet the expectations for the physical shear layer resonance and the monopole radiation characteristics [182–184]. Equation (2.99) and the ideal gas law relate the specific enthalpy and the sound pressure level in its linearized form  $H/R_s T \ll 1$

$$SPL_{3D} = SPL_{2D} + SPL_C = 20 \log \left( \frac{H}{R_s T p_0} \right) + 20 \log \left( \frac{L}{L_s} \sqrt{\frac{f}{c_0 r}} \right). \quad (6.4)$$

The 3D SPL value are computed at ambient conditions. A comparison of the SPL inside the cavity shows that the non-corrected results are higher. A quantitative analysis is given in Tab. 6.2, where the overall results of the non-corrected acoustic simulation is worse. Speaking of the corrected results, the characteristic frequencies are captured well and the amplitude matches the one of the first shear layer mode. The amplitude of the artificial mode is diminished by the corrected simulation results from 62 dB to 35 dB. The SPL in Fig. 6.13 reveal that the physical shear layer mode is present inside the cavity.

Table 6.2: Comparison of the pressure inside the cavity.

	$f_{s1}/\text{Hz}$	$SPL_{3D}/\text{dB}$	$f_{\text{mod}}/\text{Hz}$	$SPL_{3D}/\text{dB}$
Experiment	1650	60.5	-	-
Simulation $\mathbf{L}(\tilde{\mathbf{u}}) = \boldsymbol{\omega} \times \tilde{\mathbf{u}}$	1660	57	1390	35
Simulation $\mathbf{L}(\mathbf{u}) = \boldsymbol{\omega} \times \mathbf{u}$	1660	77	1390	62

This simulation result coincides with the experiment with respect to the location and the amplitude of the resonance, as well as the derived monopole characteristics. It is self evident that the 2D simulation is not able to compute the span-wise cavity mode.

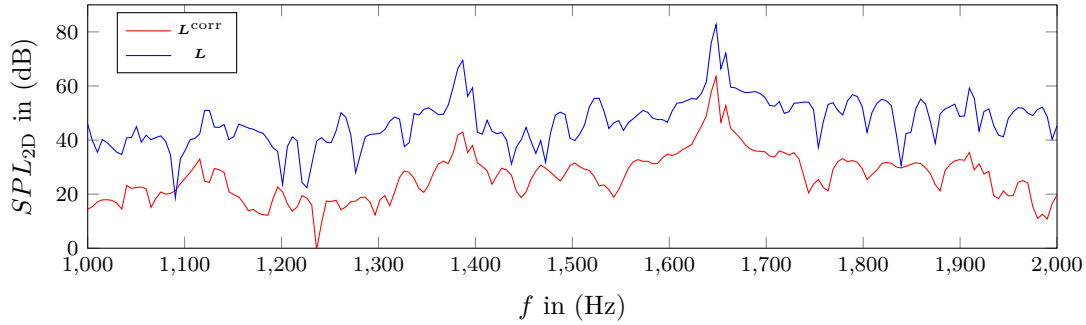


Figure 6.13: Comparison of the sound pressure level inside the cavity. The curves reveal that both physical peaks are present inside the cavity.

The second measurement point, above the cavity, exhibits that results of the corrected Lamb vector formulation coincides with the experiment with respect to the location and the amplitude of the resonances. Table 6.3 quantifies the obtained results in the far-field. Similar to the near-field, the characteristic shear layer mode is captured well. The amplitude of the shear layer mode is slightly overestimated, which can be explained by the higher free stream velocity in the simulation. Like before, the non-corrected

Table 6.3: Comparison of the pressure outside the cavity.

	$f_{s1}/\text{Hz}$	$SPL_{3D}/\text{dB}$	$f_{\text{mod}}/\text{Hz}$	$SPL_{3D}/\text{dB}$
Experiment	1650	30	-	-
Simulation $\mathbf{L}(\tilde{\mathbf{u}}) = \boldsymbol{\omega} \times \tilde{\mathbf{u}}$	1660	32	1390	13
Simulation $\mathbf{L}(\mathbf{u}) = \boldsymbol{\omega} \times \mathbf{u}$	1660	50	1390	39

results are higher and interestingly, the artificial mode at 1390Hz is reduced significantly in the corrected formulation as it is intended by the method. The curve in Fig.6.14 reveals that the shear layer mode is significant outside the cavity.

## 6.2.5 Conclusions

If a compressible flow simulation already contains acoustics (which are solved by the aeroacoustic analogy), the sources of an aeroacoustic analogy have to be filtered such that a non-radiating base flow is obtained to

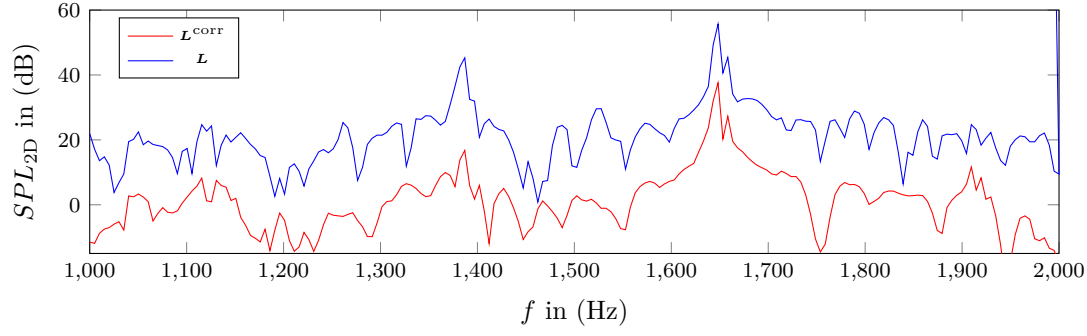


Figure 6.14: Comparison of the sound pressure level outside the cavity. The curve of the corrected Lamb vector formulation reveals that only the shear layer mode is present outside the cavity.

construct the source terms. By applying the Helmholtz decomposition, it is possible to extract the vortical (non-radiating) flow component for arbitrary domains. The method filters domain resonant artifacts, due to the boundaries. However, an accurate treatment of the boundary during CFD simulations is always recommended.

It has to be noted, that for bounded domains and domains with holes, an additional decomposition component arises, which is in the harmonic function space. The additional harmonic term is the solution of the potential flow theory of the geometrical configuration. Since the non-radiating base flow relies on the divergence free formulation, the vector potential equation serves as a valid formulation to extract all divergence-free and non-radiating parts of the flow, whether or not containing harmonic components.

The difference to state of the art hybrid aeroacoustic techniques is that this method handles compressible source data to compute the aeroacoustic source terms. Since the method relies on the extraction of a non-radiating baseflow, as proposed by Goldstein, the application to general aeroacoustic analogies is possible. This means, differently to FW-H that computes the fluctuating pressure, it is possible to compute acoustics applying the method in conjunction with APE-2 or PCWE.

This investigation proved that even a coarser discretization than the one used by the DSC resolves the dominant aeroacoustic feedback. At low Mach numbers, an acoustically under-resolved compressible simulation in combination with the Helmholtz decomposition is able to compute the non-radiating base flow for the Mach number extended hybrid analogy. This Mach extended hybrid analogy follows again a three step approach, the compressible CFD simulation in combination with a Helmholtz decomposition, the direct one-way coupling of the non-radiating base flow to the acoustic. The example "cavity with a lip" validates the workflow in 2D.

## 6.3 Cavity with a lip – 3D

The compressible fluid dynamic equations solve both fields, flow and acoustic fluctuations, in the same calculation. During this simulation we use flow focused numerical schemes, grid, and time step size; acoustics is expected to be dissipated with respect to its propagation. The simulation avoids reflection by a special free field condition<sup>3</sup>. As already discussed, a direct sound computation (DSC) is computationally demanding and needs proper non-reflecting boundary conditions that avoid reflections. In contrast to DSC, the proposed flexible hybrid methodology avoids this error sources, too. This section addresses the underestimated capability of the Helmholtz decomposition to resolve turbulent vortical structures.

### 6.3.1 Fluid dynamics

The executed simulations focus exclusively on compressible flow simulations to get a profound understanding of the example (at ambient conditions  $p = 101325 \text{ Pa}$  and  $T = 300 \text{ K}$ ). Figure 6.15 shows the geometry of the cavity used for the simulations. More details on the flow and geometrical parameters can be found in [88], the values coincide with the ones of Farkas [44]. The grid resolves the viscous sublayer and a convergence was assessed by grid convergence for URANS and LES turbulence models. At the free field boundary non-reflective conditions are set. Throughout the simulations turbulence models, flow velocities, and boundary conditions have been varied and compared. The aim of the CFD study is to identify uncharacterized modes in the pressure spectrum, investigate the three-dimensional Taylor-Görtler vortices from the recirculation, and their role on the shear layer instability.

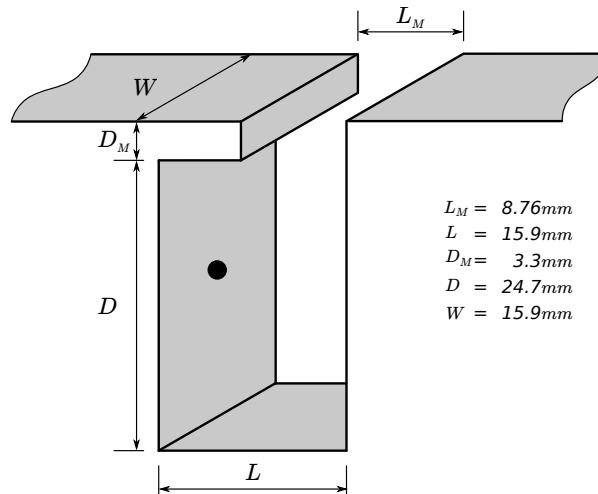


Figure 6.15: Geometrical properties of the cavity with a lip in 3D. The pressure microphone is located in the middle of the front cavity face. Extracted from [88].

### Pressure fluctuations

The computational meshes are analyzed by a general Richardson's interpolation [185, 186] and the best performing meshes, with respect to the mode resolution in the pressure spectrum and the computational efficiency, are selected. The mesh resolves the turbulent boundary layer  $y^+ < 1$ , for both simulations  $k\omega$ -SST (shear stress transport) and SBES (stress blended eddy simulation). Relevant computational settings are given in Tab. 6.4. Further details on the simulation settings, with an in-depth discussion of each choice, are given in [88].

<sup>3</sup> Otherwise, reflections of the boundary conditions could shade physical acoustic waves

Table 6.4: Compressible CFD simulation settings and boundary conditions. Values for  $y^+$  and CFL are maximum values during the convergence study: simulation time  $t = 0.15$  s. [88]

<b>Fluid</b>	Air approximated by perfect gas at $p = 101325$ Pa and $T = 300$ K
<b>Solver</b>	<i>pressure-based</i>
<b>Pressure-velocity coupling</b>	<i>coupled</i>
<b>Gradient</b>	<i>least squares cell based</i>
<b>Pressure</b>	<i>second order</i>
<b>Density</b>	<i>second order upwind</i>
<b>Momentum</b>	<i>second order upwind (<math>k\omega</math>-SST); bounded central differencing (SBES)</i>
<b>Turbulent kinetic energy</b>	<i>second order upwind</i>
<b>Specific dissipation rate</b>	<i>second order upwind</i>
<b>Energy</b>	<i>second order upwind</i>
<b>Transient formulation</b>	<i>second order implicit</i>
<b>Inlet</b>	<i>velocity inlet with <math>p_{gauge} = 101325</math> Pa based on boundary layer simulations and <i>non-reflecting</i></i>
<b>Outlet, Top</b>	<i>pressure outlet with <math>p_{gauge} = 101325</math> Pa; <i>non-reflective and from neighboring cell</i></i>
<b>Front and back (span-wise)</b>	<i>periodic (front – periodic zone; back – shadow zone)</i>
<b>Wall (Cavity and Plate)</b>	<i>wall</i>
<b>Inlet turbulence</b>	turbulent length scale $l_t = 0.4\delta_{inlet}$ low turbulent Intensity $I_t = 0.5\%$
<b><math>y^+</math></b>	$< 1$ plate boundary layer; $< 12$ inside the cavity
<b>CFL-Number</b>	$< 47$ for $\Delta t = 2 \cdot 10^{-5}$ s

Figure 6.16 compares the simulated pressure fluctuations inside the cavity with analytic locations of modes and the measurements of Henderson [176]. Simulations based on the URANS turbulence model calculate the location of the first Rossiter mode (2.162)

$$f_{R_1} = \frac{U_\infty}{L_M} \frac{1 - \alpha}{Ma + \kappa_c^{-1}} = 1733 \text{ Hz} \quad (6.5)$$

and higher harmonics accurately. In (6.5),  $U_\infty$  denotes the free stream velocity,  $L_M$  the length of the cavity mouth, the semi-empirical constant  $\kappa_c = 0.43$  represents the ratio between the vortex convection speed and the flow velocity, and  $\alpha = 0.25$  the time delay between the moment of the vortex impinging on the trailing edge and the emission of the acoustic waves [176]. The brief measurement documentation brought up discussions about the real boundary layer thickness during the experiments. The systematic deviation to the experimental values correlate with the boundary layer thickness and is analyzed in the dedicated paragraph. As expected, no additional modes are triggered by URANS turbulence. Remarkably is the comparable resolution of the Rossiter modes for URANS and LES based simulations. In contrast the URANS based simulations, where only the the first Rossiter mode is resolved, the LES based simulations resolve additionally the Helmholtz resonator mode (2.165)

$$f_H = \frac{c}{2\pi} \sqrt{\frac{\pi R'^2}{V(D_M + \frac{\pi R'}{2})}} = 2149 \text{ Hz} \quad (6.6)$$

and cavity modes, since instantaneous fluctuations are quantified. Equation (6.6) is calculated using the speed of sound  $c = 347.411$  m/s, the total cavity volume  $V$ , the depth of the cavity mouth  $D_M$ , and the equivalent hydraulic radius  $R' = \sqrt{A/\pi}$ , where  $A$  stands for the area of the cavity orifice. The cavity

mode in transversal direction is visible at a frequency of

$$f_{C_y} = \frac{c}{4(D + D_M)} = 3102 \text{ Hz}, \quad (6.7)$$

where  $(D + D_M)$  denotes the total cavity depth. The systematic underestimation of these modes is explained by lower turbulence in the boundary layer compared to the measurements. The flow field shows a two dimensional shear layer structures in the span-wise direction, with small recirculations inside the cavity. The non-reflective boundaries, based on the characteristics of the LEE, absorb acoustics, since no artificial domain resonances have been found in the pressure spectrum.

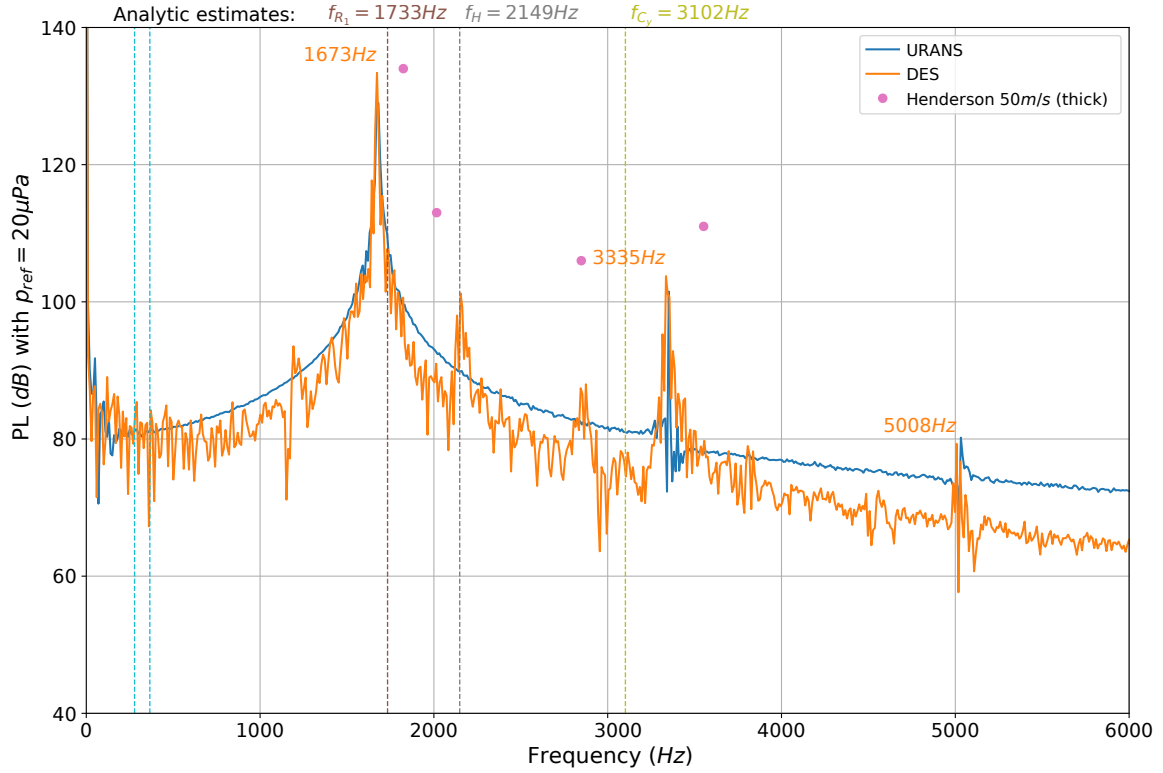


Figure 6.16: URANS and DES pressure fluctuations inside the cavity for  $U_\infty = 50 \text{ m/s}$ . Both simulations are carried out on the same grid. Extracted from [88].

### Velocity variations

The variation of the turbulence model revealed effects of instantaneous fluctuations on the cavity. Sticking to the LES turbulence model, the free stream velocity is varied from  $50 \text{ m/s}$  to  $26.8 \text{ m/s}$ . As described in literature [44], this simulation shows that the first Rossiter modes switches to the second one and beyond this a subharmonic peak occurs at  $800 \text{ Hz}$  (see Fig. 6.17). The analysis of the flow field detects an interesting phenomenon; only every second vortex hits the cavity edge, known as complete clipping, whereas the other partially escapes (see Fig. 2.6). A profound correlation study indicates that strong recirculations below the leading edge separation push the shear layer and produce this different edge interaction. This subsequent different trailing edge interaction causes the subharmonic peak.

### Boundary layer thickness

As previously addressed, the systematic deviation of the resonance frequency compared to the experimental values correlate with the boundary layer thickness. Figure 6.18 illustrates the dependency on the

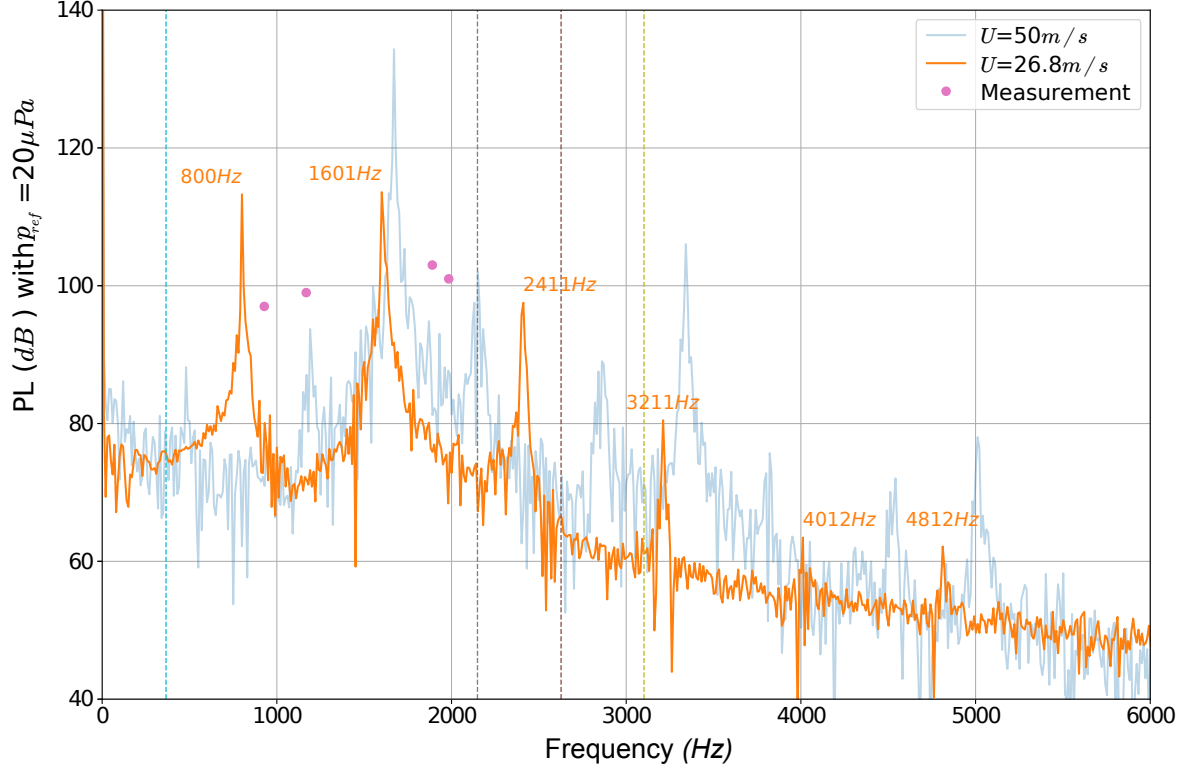


Figure 6.17: DES pressure fluctuations inside the cavity variable flow speeds  $U_\infty = 50 \text{ m/s}$  and  $U_\infty = 26.8 \text{ m/s}$ . The simulations are carried out on the optimal grid (fine) based on the grid convergence study. Extracted from [88].

boundary layer thickness. In general, an increasing boundary layer thickness decreases the pressure level inside the cavity and the mode frequency of the Rossiter mode. For decreasing boundary layer thickness, the energy concentrates at the Rossiter mode and fewer side peaks occur. The LES based simulation results in a 3 dB higher pressure level and a weaker dependency on the boundary layer variations for the frequency. A lower pressure level for  $k\omega$ -SST complies with under-resolved turbulent structures and coincides with [187]. It is curious that at  $\delta = 8 \text{ mm}$  mode switching occurs, which has been investigated by Henderson [176] and causes a small reduction of the amplitude.<sup>4</sup>

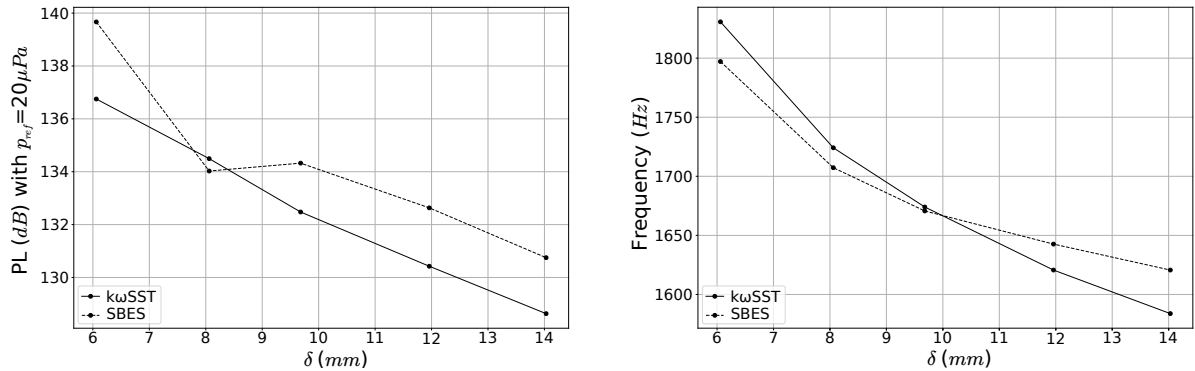


Figure 6.18: Variation of the pressure level (right) and resonance frequency (left) at  $U_\infty = 50 \text{ m/s}$  depending on the boundary layer thickness. Extracted from [88].

<sup>4</sup> "One additional consideration should be made when directly comparing numerical results to experimental results. When multiple tones occur in the spectrum, the preferred or dominant mode often changes randomly. This can result in a change of 3 dB or more in the peak sound pressure levels." [176]

## Vertical ejection

The most remarkable result is the vertical ejection of every second vortex and the amplification of subharmonics by a decreasing time step. Figure 6.19 shows the pressure fluctuations for the different time step sizes at  $U_\infty = 50 \text{ m/s}$ . Similarly to reduced velocities, the edge-interaction transits the flow to a somewhat odd behavior with an increasing recirculation strength. An instantaneous variability below the shear layer distorts the convection of the vortices inside the shear layer. As a consequence, consecutive vortex trailing edge interactions deviate from each other in the range of complete clipping to complete escape.

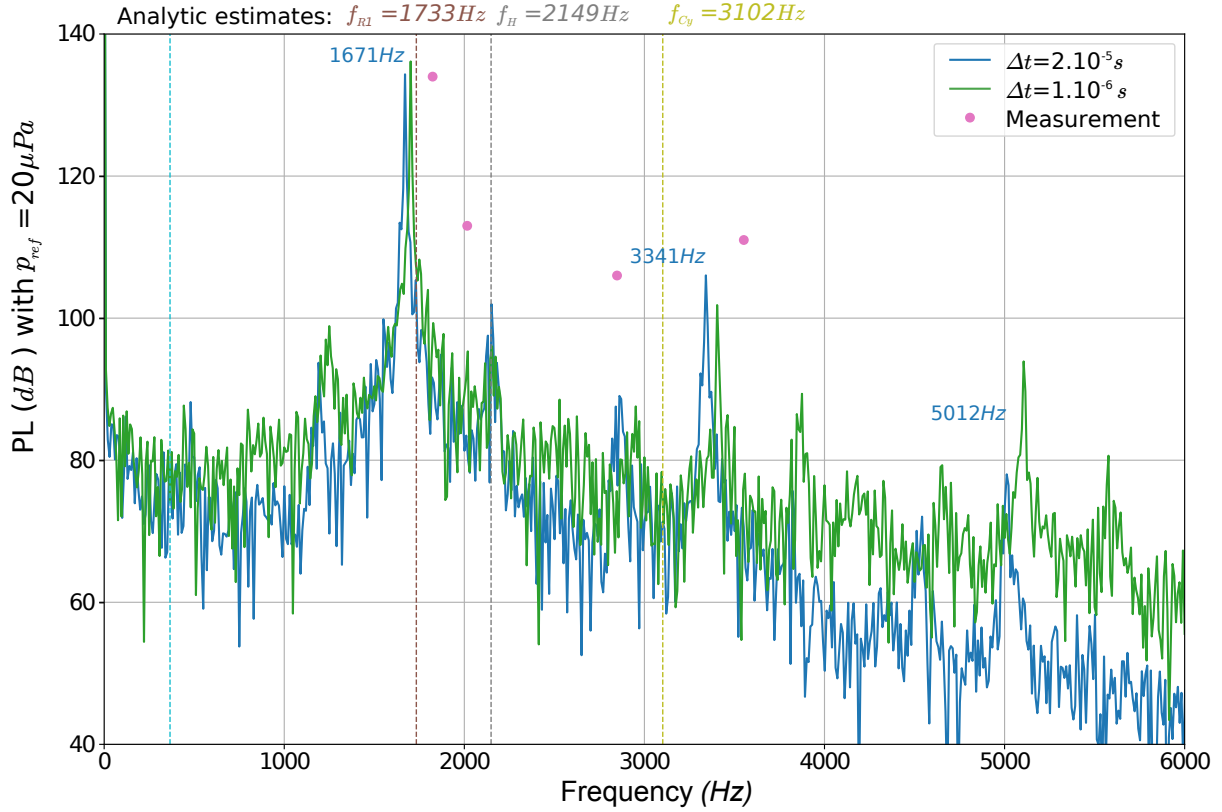


Figure 6.19: Variation of the pressure level at  $U_\infty = 50 \text{ m/s}$  depending on the time step size. The simulations are carried out on the optimal grid (fine) based on the grid convergence study. Extracted from [88].

## Detected modes

Table 6.5 links the modes of Henderson's experiments [176] to the URANS and LES simulations. In contrast to Henderson's measurements in a channel, the present simulation considers free radiation and therefore no duct modes should occur in the simulation results. However, improper radiation boundaries excite a channel like mode. All present subharmonics are subject of further investigations to clarify their causal physical origin. Rossiter's and Helmholtz's resonance are captured well and investigated by a parameter study. The higher harmonics of the Rossiter mode are present as well as the higher harmonics of the cavities' depth mode. Two further modes are unlabeled.



Table 6.5: Comparison of the pressure modes of the different simulations at  $U_\infty = 50 \text{ m/s}$  and  $\delta = 10 \text{ mm}$  to Henderson’s experiments [176]. Mode labels with a  $\square^*$  denote a proposed mechanism.

Henderson		URANS		LES $\Delta t = 20\mu s$		LES $\Delta t = 1\mu s$		Expected mode
$f$ (Hz)	$PL$ (dB)	$f$ (Hz)	$PL$ (dB)	$f$ (Hz)	$PL$ (dB)	$f$ (Hz)	$PL$ (dB)	
380	102.5	—	—	480	88.2	442	87.7	Artificial domain resonance
930	103	—	—	—	—	798	87.1	Shear layer-edge interaction
1340	107	—	—	1190	93.7	1250	98.9	3D effects*
1824	134	1673	131.2	1671	134.3	1702	136.1	First Rossiter mode $f_{R_1}$
2016	113	—	—	2152	102	2154	96.2	Helmholtz resonance $f_H$
2848	106	—	—	2861	89	2952	87.6	First Cavity depth mode $f_{C_y}$
3552	111	3355	99.7	3341	106	3404	101.8	First higher Harmonic $f_{R_1}$
—	—	—	—	3822	75.7	3875	89.4	unknown
—	—	—	—	4543	72	4654	79.3	First harmonic of $f_H$
—	—	5028	75.8	5012	78	5106	93.9	Second higher Harmonic of $f_{R_1}$
—	—	—	—	5502	58.3	5577	80.6	Second Cavity depth mode $f_{C_y}$

### 6.3.2 Helmholtz decomposition

The Helmholtz decomposition of the flow field extracts the artificial computational domain resonances and the modulation of the aeroacoustic source term due to the boundary condition at  $\Gamma_{F1}$ ,  $\Gamma_{F3}$ ,  $\Gamma_{F4}$ . Physical radiating compressibility is separated from non-radiating base flow components. Due to the known drawbacks of the scalar potential formulation, we apply the vector potential formulation with inhomogeneous Neumann boundaries. Figure 6.20 shows the decomposition (vector potential formulation) of a flow simulation with an URANS turbulence model as well as a flow simulation with a SBES turbulence model. The turbulent vortical structures are separated and clearly captured. Additionally to the URANS flow simulation, the SBES turbulence based flow simulations models instantaneous turbulent structures. These turbulent structures are separated by the Helmholtz decomposition.

Figure 6.21 shows the decomposition based on the vector potential for the total domain. Differently to the Poisson equation, the vector potential behaves optimal at reentrant corners. However for large computational domains, solving the curl-curl equation is computational demanding. Another possibility under investigation is the direct extraction of compressible parts during the CFD simulation by solving a Poisson problem.

#### Direct extraction of compressible parts during CFD

The CFD simulation solves generic transport equations and Poisson’s equations. Additionally to the conservation laws, the parallel computation of scalar transport equations is efficient

$$\frac{\partial \rho \phi}{\partial t} + \nabla \cdot (\rho \mathbf{u} \phi - \nabla \phi) = S_\phi, \quad (6.8)$$

where  $\phi$  denotes the scalar function and  $S_\phi$  the source term. Neglecting the convective and unsteady term, Helmholtz decomposition can be directly treated as scalar Poisson’s equation

$$-\nabla \cdot \nabla \phi = S_\phi. \quad (6.9)$$

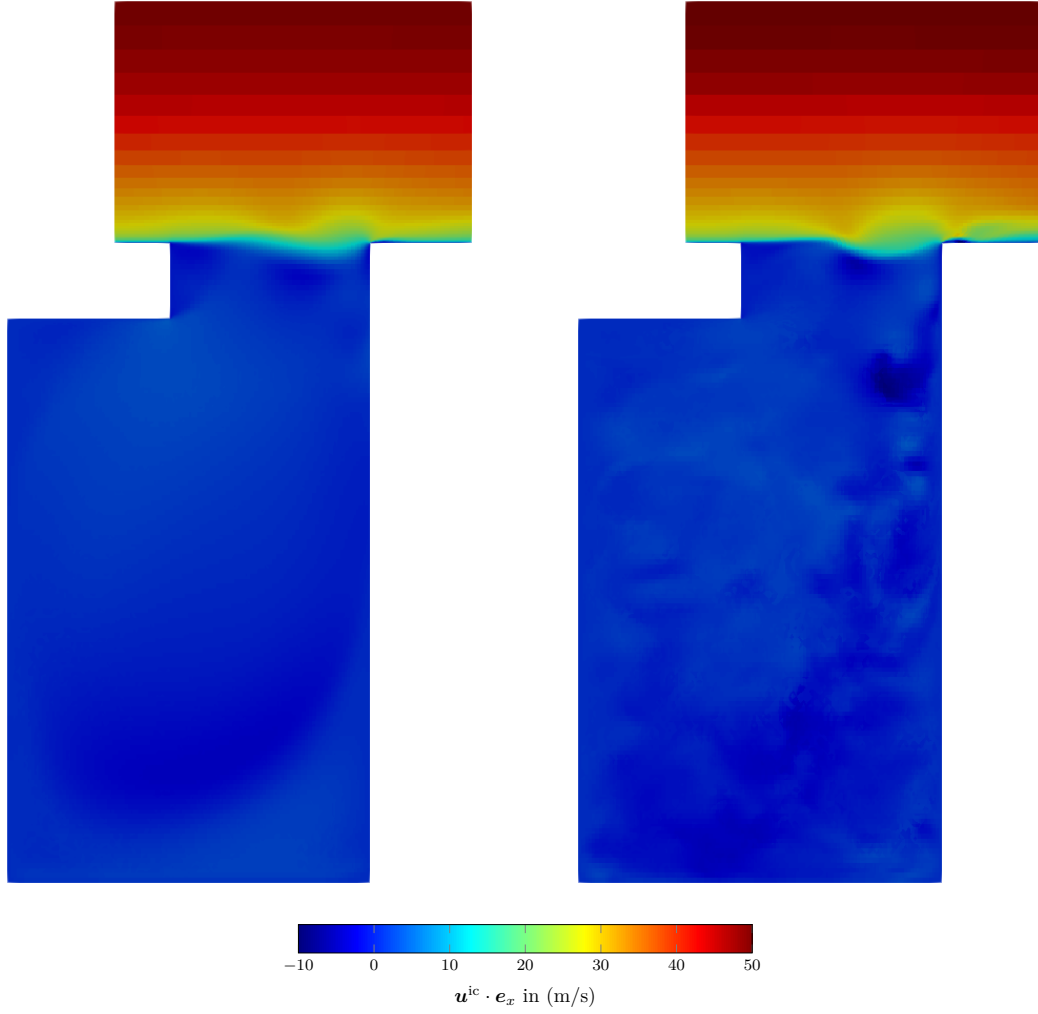


Figure 6.20: Helmholtz decomposition of an URANS simulation (left) and a SBES simulation (right).

The unknown source term  $S_\phi$  is determined through a reformulation of the continuity equation (2.12)

$$\frac{1}{\rho} \frac{d\rho}{dt} + \nabla \cdot \mathbf{u} = 0. \quad (6.10)$$

The Helmholtz decomposition (2.73) is inserted into the divergence of the velocity. Based on the properties of the vector potential  $\mathbf{A}$ , the vector potential term is null and only the scalar potential  $\phi$  remains in the equation

$$-\nabla \cdot \nabla \phi = \frac{1}{\rho} \frac{d\rho}{dt} = -\nabla \cdot \mathbf{u}. \quad (6.11)$$

By comparing the source terms of the reformulated continuity equation with the reduced scalar Poisson equation (6.9), two variants of the source term are available. The first is the relative variation of the density along a streamline, the second variant depends solely on the velocity

$$S_\phi = \frac{1}{\rho} \frac{d\rho}{dt} = -\nabla \cdot \mathbf{u}. \quad (6.12)$$

Although it is not correct, the free field boundary conditions are modeled by a homogeneous Dirichlet boundary and the wall boundaries are a homogeneous Neumann boundary. Further improvement of this free field boundary condition can be applied by the IML, which is not implemented in the CFD solver.

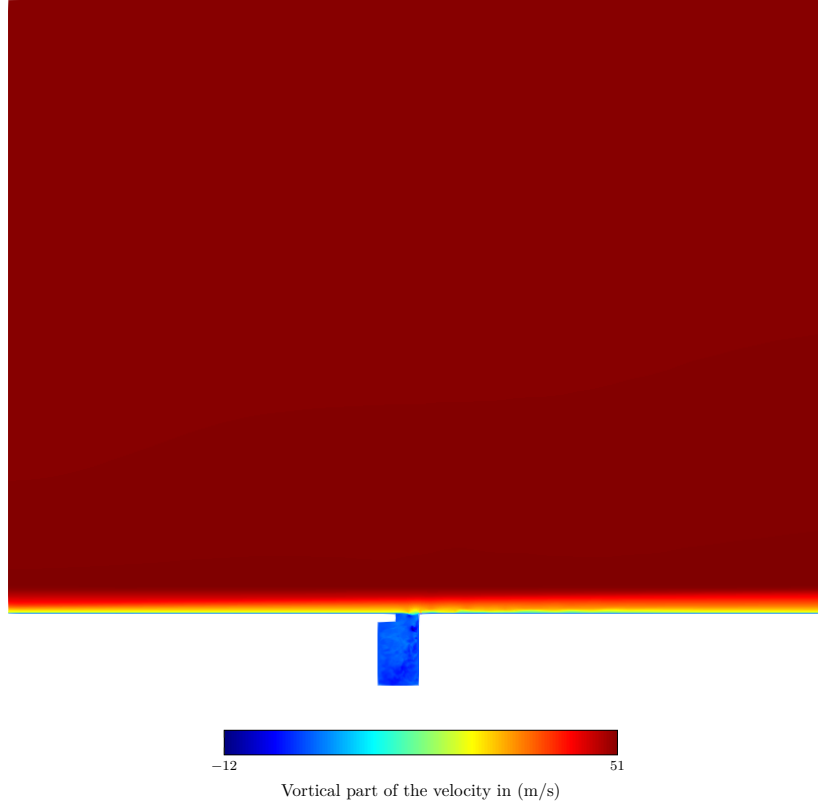


Figure 6.21: Vortical velocity component after the Helmholtz decomposition with the curl-curl equation. X-component of the velocity field.

Figure 6.22 shows the result of this computation. As one can clearly see, the scalar potential extracts the

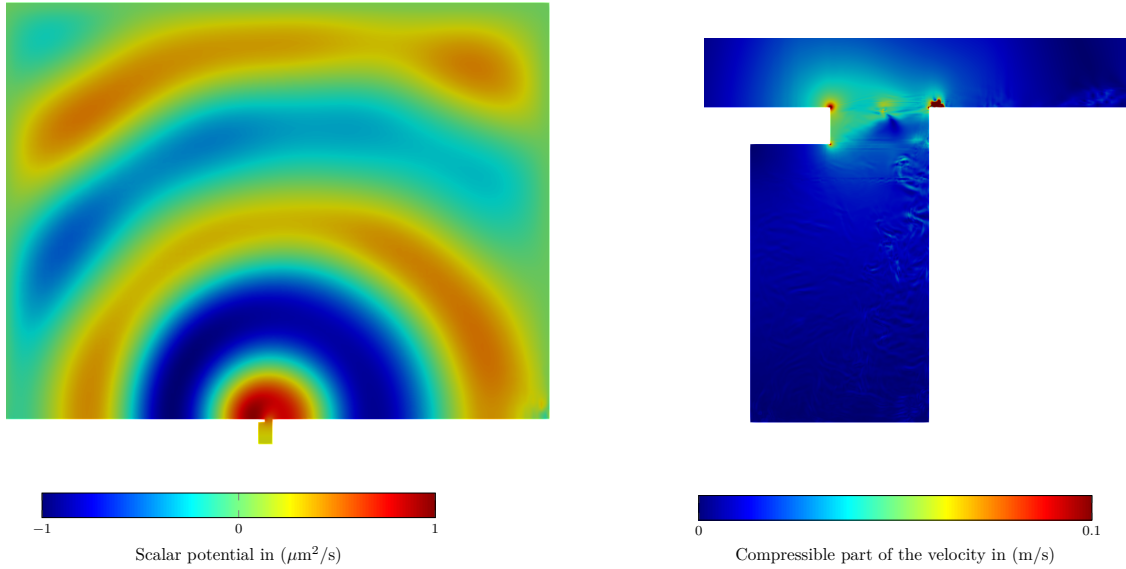


Figure 6.22: Direct execution of the decomposition during the CFD simulation provides the scalar potential (left). Similar to the previous investigations in 2D, the derivative of the scalar potential, compressible part of the velocity field, tends to infinity near reentrant corners (right).

compressible components of the fluid that converge to the acoustic quantities in the far-field. Upstream amplification is captured by the direct simulation of flow and acoustic, but the wrong free field radiation

condition, approximated by a homogeneous Dirichlet boundary, "squeezes" the acoustic field unnaturally. Furthermore, as already indicated in the 2D simulation of the cavity, the computation of the compressible part of the velocity field results in an unbounded solution at reentrant corners.

### 6.3.3 Mapping 3D to 2D

Simulation models aim to reduce computational complexity, while maintaining generality of the results. In order to reduce the computational domain from three dimensions to two, we analyze the correlation of the aeroacoustic source terms  $q_a = \nabla \cdot \nabla \cdot \mathbb{T}$  at the distinct first Rossiter mode. The strongest sources emerge

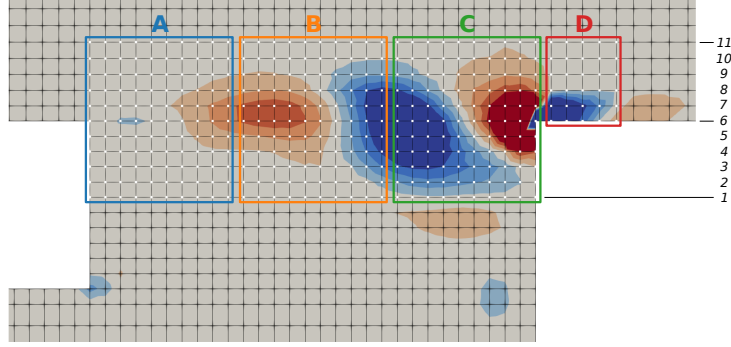


Figure 6.23: Investigated domain of the span-wise correlation study, separated into four areas of shear layer growth. The contours illustrate the sources of Lighthill's aeroacoustic wave equation. Extracted from [88].

inside and above the orifice. Around this region, the span-wise correlation judges the coherence of the radiating structures. If the sources are coherent, a reduction to two dimensions is possible. Additionally, this reduction mapping can be used to detect 3D effects in the flow domain (e.g. the assumed mode mechanism at 1200 Hz). Figure 6.23 depicts the selected region of investigation around the neck of the cavity and its segmentation into four sections that coincide with three areas of shear layer growth A-C [128] and the post-edge interaction zone D. This distinction and the division into line locations above, at the orifice, and inside the neck allows a unique identification of three dimensional regions.

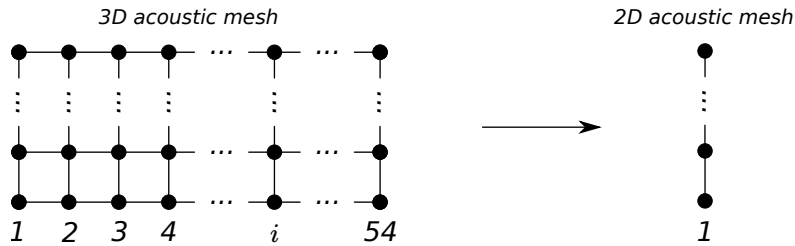


Figure 6.24: Mapping schematic of the uniform, span-wise spaced 3D acoustic mesh to the 2D acoustic mesh. Extracted from [88].

For the purpose of the coherence study, we used 54 equidistant acoustic source term probes  $q_{a,i}$  in the span-wise direction in the region near the cavity mouth, where the dominant sources occur (see Fig.6.23). After defining a reference probe  $q_{a,\text{ref}}$  at the middle of the cavity's span, the coherence

$$\gamma_i^2(f) = \frac{|G_{q_{a,\text{ref}}q_{a,i}}(f)|^2}{G_{q_{a,\text{ref}}q_{a,\text{ref}}}(f) \cdot G_{q_{a,i}q_{a,i}}(f)}, \quad 0 \leq \gamma_i^2(f) \leq 1 \quad (6.13)$$

was calculated with regard to all other 53 probes. In (6.13)  $G_{q_{a,\text{ref}}q_{a,i}}(f)$  denotes the cross spectral density between reference probe and probe  $i$ , whereas  $G_{q_{a,\text{ref}}q_{a,\text{ref}}}(f)$  and  $G_{q_{a,i}q_{a,i}}(f)$  denote the power spectral

densities of both probes,  $q_{a,\text{ref}}$  and  $q_{a,i}$ .

Figure 6.25 presents the span-wise coherence for line 11, 6, and 1 at the dominant Rossiter frequency. Aeroacoustic sources cohere well on the lines 11 and 6 for all segments A-D. This indicates two dimensional aeroacoustic structures inside and above the shear layer. Being inside the neck of the cavity, the coherence of the flow structure increases towards the trailing edge. At the trailing edge, where the dominant shear layer tones are generated, the flow is again nearly two dimensional and we conclude that a reduction is possible. The incoherent structures below the leading edge separation of the boundary layer proof evidence of three dimensional recirculations tuning the shear layer instability to some extent.

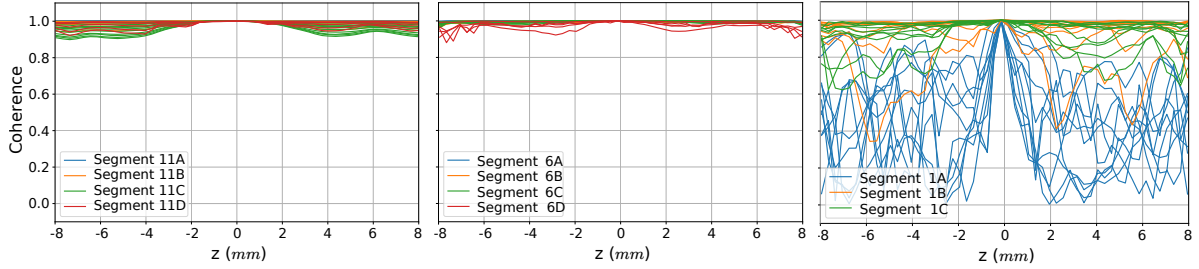


Figure 6.25: Span-wise coherence at 1671 Hz of different segments on different lines for the mesh cluster 11 (left), 6 (middle) and 1 (right). Extracted from [88].

The high correlation between the sources justifies the reduction to two dimensions by a span-wise average over the aeroacoustic source terms. The aeroacoustic sources are mapped from an uniform distributed span-wise mesh to a 2D coordinate (see Fig. 6.24). For uniform spaced meshes the mean value is simply computed by the span-wise average. The domain reduction to the mean quantity  $\bar{q}$  follows

$$\bar{q} = \frac{1}{N} \sum_{i=1}^N q_i.$$

This span-wise averaged aeroacoustic sources are now used to compute the sound propagation in 2D.

### 6.3.4 Acoustics

The acoustic simulation is performed by applying FEM to the vortex sound equation in 2D (see (3.45)). The simulation parameters are summarized in Tab. 6.6. Conceptually, the acoustic simulation setup coincides with the previous example (see Sec. 6.2). The Lamb vector  $\mathbf{L}$  of the compressible CFD

Table 6.6: Simulation setup of the FE program CFS++ that is used to compute the wave propagation.

<b>Fluid</b>	Air, perfect gas at $p = 101325$ Pa and $T = 300$ K
<b>Wall</b>	sound hard
<b>Non-conforming Grid</b>	<i>Nitsche</i> -Type Mortar interface ( <i>nitscheFactor</i> = 100)
<b>PML</b>	<i>inverseDist</i> with <i>dampFactor</i> = 1
<b>Acoustic wave</b>	Vortex sound equation
<b>Time stepping</b>	<i>Hilbert-Hughes-Taylor</i> with <i>timeStepAlpha</i> = -0.3
<b>Solver</b>	<i>pardiso</i>

simulation is compared to the corrected Lamb vector  $\mathbf{L}^{\text{corr}}$ . Based on the Helmholtz decomposition that was performed directly in the CFD (scalar potential formulation), the corrected Lamb vector is computed

by

$$\mathbf{L}^{\text{corr}} = \boldsymbol{\omega} \times (\mathbf{u} - \nabla\phi). \quad (6.14)$$

As illustrated in the previous investigation, using the scalar potential formulation is not optimal (e.g. corner singularities). Nevertheless, this decomposition is performed along with the CFD simulation that leads to a low computational cost for large simulation models.

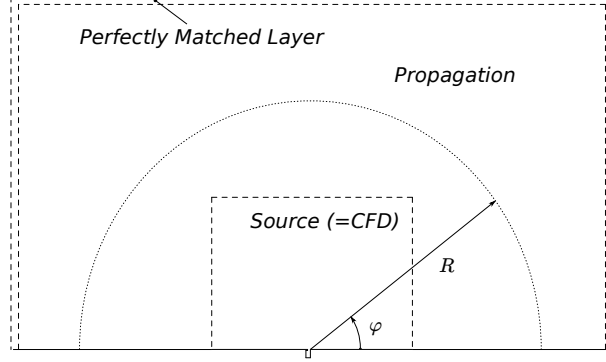


Figure 6.26: Simulation domain of the FE simulation, source domain followed by a propagation domain and a PML. The domains are connected by Nitsche-Type Mortar interfaces.

Figure 6.26 shows the simulation domain of the FE simulation, a source domain is followed by a propagation domain and a PML. The separated sub-domains are connected by Nitsche-Type Mortar interfaces. At an radius  $R = 0.775$  m, a microphone array detects the radiation pattern of the acoustic propagation, which is expected to amplify radiation in upstream direction and will be of monopole characteristics. At this low Mach number, the convective mean flow effects are very small. Figure 6.27

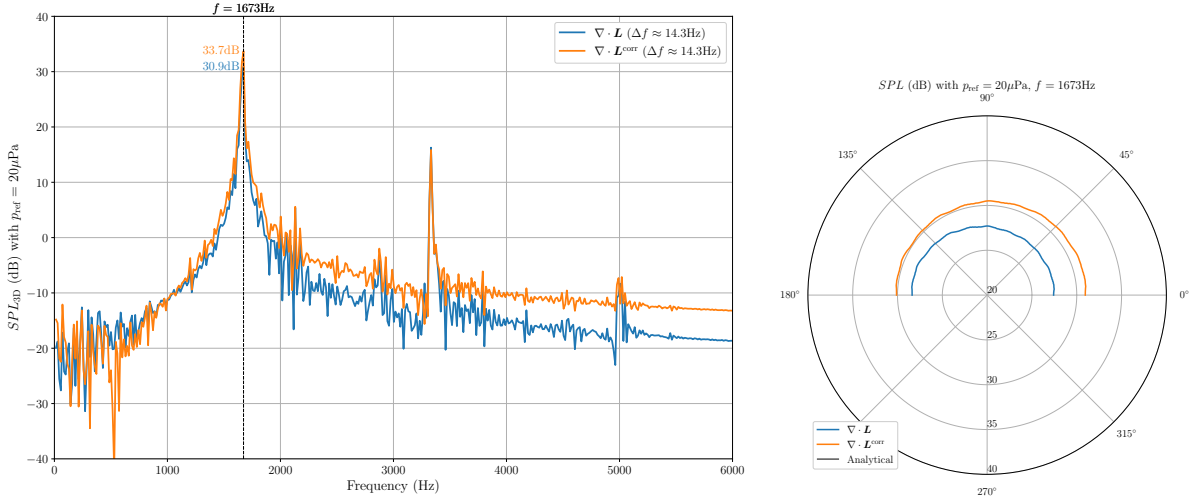


Figure 6.27: Uncorrected source term computed with constant density and SBES turbulence model and the corrected source term are compared at the microphone position of  $\varphi = 90^\circ$  on the evaluation circle (left) and the radiation pattern at the first shear layer mode (right).

depicts the radiation pattern of the cavity at the 1<sup>st</sup> shear layer mode. As detected in previous studies, the radiation pattern is a monopole, slightly directed to the upstream direction. The sound pressure level in 2D is corrected according to (6.4) to 3D values. Since the free field radiation condition of the CFD simulation fulfills radiation during the flow simulation, no reduction on the SPL is visible in the spectrum, comparing the corrected,  $\nabla \cdot \mathbf{L}^{\text{corr}}$ , and the non-corrected source term,  $\nabla \cdot \mathbf{L}$ , (see Fig. 6.27). Figure 6.27 shows the SPL as a function of the frequency of the microphone at  $\varphi = 90^\circ$  on the evaluation

circle. The amplitude of the corrected and the non-corrected SPL at the 1<sup>st</sup> shear layer mode is close to the experimental result of 30 dB (this was measured at a slightly lower free stream velocity).

All higher harmonics are captured and the Helmholtz frequency as well as the depth mode of the cavity. Additionally, the mode at 1200 Hz is not present in the sound spectrum, hence a 3D effect must be the origin. The SPL of the microphone inside the cavity shows good agreement with the measurements [177].

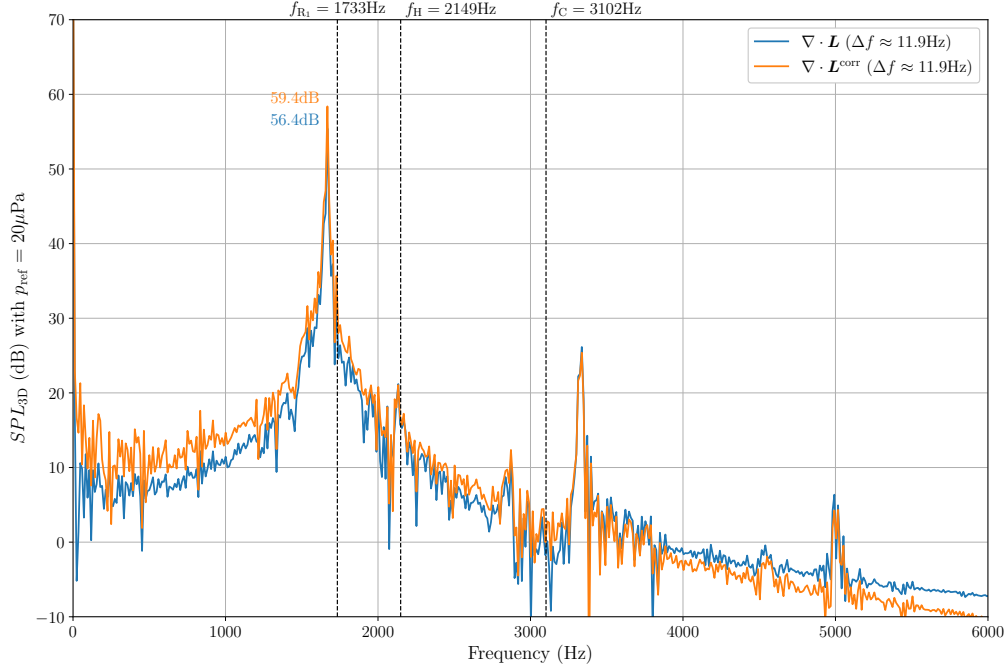


Figure 6.28: Uncorrected source term computed with constant density and SBES turbulence model and the corrected source term are compared at the microphone position inside the cavity.

The SPL of the corrected simulation at the first shear layer mode is 59.4 dB compared to the measurement 60.5 dB.

### 6.3.5 Discussion of the deviation

Overall, it is possible that the corner singularities pollute the computation and increase the radiated sound slightly. A possible alternative would be a direct extraction of incompressible parts during CFD. Similar to the scalar Poisson's equation, the curl-curl problem can be transformed into a vector Poisson equation for Coulomb gauging (just on a convex domain)

$$\nabla \times \nabla \times \mathbf{A}^{*,\text{ic}} = \nabla \nabla \cdot \mathbf{A}^{*,\text{ic}} - \Delta \mathbf{A}^{*,\text{ic}} = -\Delta \mathbf{A}^{*,\text{ic}} = \nabla \times \mathbf{u} = \boldsymbol{\omega}. \quad (6.15)$$

The three unknown source terms of the three Poisson's equations are the components of the vorticity. However, the complex boundary terms of each vector potential equation depend on the three computational variables and therefore require a general CFD solver having the necessary boundary conditions.

## 6.4 Cavity 2M4 and 2M8

The application of the Helmholtz decomposition to a DSC of a flow past a cavity demonstrates the workflow for a higher Mach number. An extensive numerical investigation of this problem was performed by Colonius [188]. The cavity case 2M4 and 2M8, both exciting the shear layer mode, are investigated (see Fig. 6.29). The Blasius boundary layer prescribes the velocity field at the inlet, with a free stream

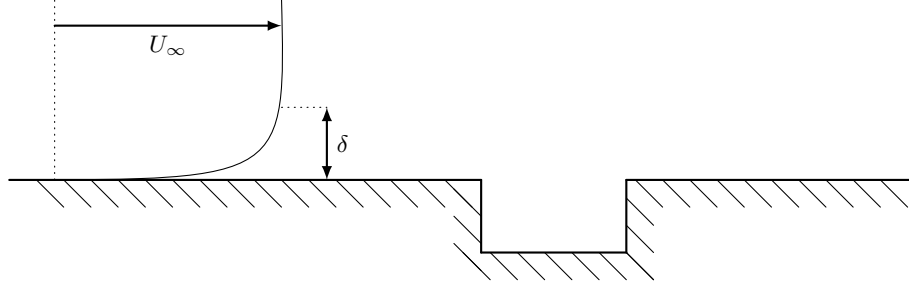


Figure 6.29: Schematic of the cavities geometry and the flow conditions. The cavity has a length to depth ratio of two.

velocity ensuring  $Ma = 0.4$  and  $Ma = 0.8$  respectively. For both cases, the Reynolds number of  $Re_\delta = 56.8$  describes the viscous flow configuration and  $L/\delta = 52.8$  the geometrical property relative to the boundary layer thickness. All dimensionless numbers are computed with  $D = 2.54$  mm and result in the following physical quantities for the wave equation (see Tab. 6.7). For compressible flows, this cavity involves a

Table 6.7: Geometric and flow parameters of the cavity 2M4 and 2M8.

Parameter	Value 2M4	Value 2M8	Description
$Re_\delta$	56.8	56.8	Reynolds number
$Ma$	0.4	0.8	Mach number
$U_\infty$	136 m/s	272 m/s	Free stream velocity
$D$	2.54 mm	2.54 mm	Cavity depth
$L$	5.08 mm	5.08 mm	Cavity length
$\delta$	0.0962 mm	0.0962 mm	Boundary layer thickness

shear layer instability, a typical fluid dynamic-acoustic resonance. This resonance is characterized by distinctive processes over one limit cycle. The vortical structure in the shear layer impinges the trailing edge of the cavity. During the slash on the edge, flow energy propels acoustic radiation. Acoustic waves travel upstream and hit the cavity's leading edge and trigger a vortical instability in the shear layer. The shear layer instability and its process has been described by Rossiter [96]. He developed a semi-empirical formula to predict resonance frequency measurements. The modified Rossiter formula [189] is

$$St_m = \frac{m - \alpha}{Ma \sqrt{1 + \frac{\kappa - 1}{2} Ma^2 + \frac{1}{\kappa_c}}} . \quad (6.16)$$

For this cavity  $L/D = 2$ , the parameters are specified by  $m \in \mathbb{N}^+$ ,  $\alpha = 0.25$ ,  $\kappa_c = 0.57$ , the specific heat ratio  $\kappa = 1.4$ , and the Mach number  $Ma$  [96].

The main purpose of the simulation is to convince skeptical readers that the method is valid at higher Mach numbers. The herein presented hybrid aeroacoustic workflow is compared to a DSC simulation. Since the direct simulation resolves the acoustic field, the validity of two essential ingredients can be assessed: the decomposition itself and the whole hybrid aeroacoustic workflow. At first, the Helmholtz decomposition must be capable of extracting the compressible velocity components of the direct simula-



tion. In the far-field, this compressible part converges to the acoustic part of the DSC simulation. If this is the case, the remaining component is the vortical flow part. Secondly, the proposed hybrid aeroacoustic procedure is applied. The acoustic propagation simulation recalculates a acoustic field and will be judged by the DSC far-field.

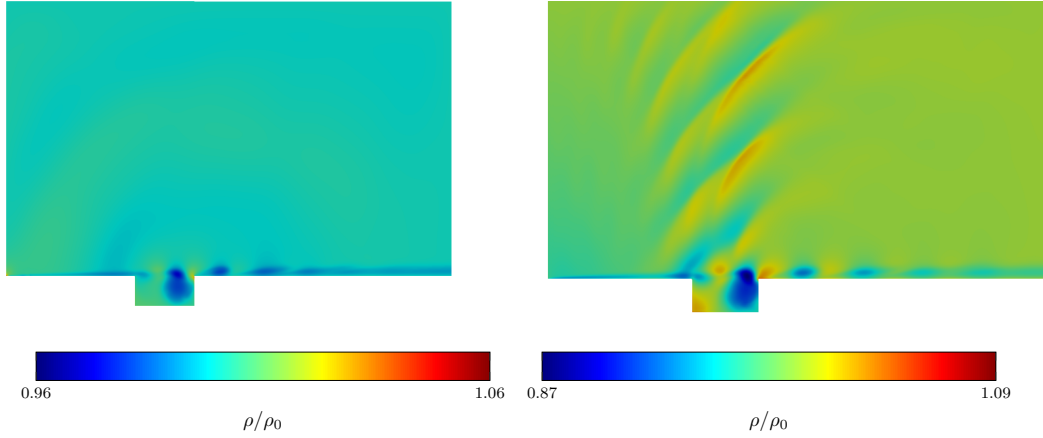


Figure 6.30: The relative density of the flow field displays compressible flow structures and the resulting acoustic wave propagation in the flow domain. 2M4 (left) and 2M8 (right).

Before the hybrid method is analyzed, the accurate DSC simulation are discussed. Thanks to the developers of the FLEXI solver [190] and Thomas Kuhn, Universität Stuttgart Institut für Aerodynamik und Gasdynamik, who provided the DSC simulation for this investigation. This DSC simulation is computed by a higher order discontinuous Galerkin scheme in space and time in non-dimensional form. The non-dimensional time step  $\Delta\tau$  corresponds to a physical time step size of  $\Delta\tau D/U_\infty = t = 0.9337 \mu\text{s}$  (2M4) and  $\Delta\tau D/U_\infty = t = 0.46685 \mu\text{s}$  (2M8). Both, vortical structures and acoustic waves are resolved in the DSC data. The density field and the velocity field indicate the presence of a shear layer mode (see Fig. 6.30 and Fig. 6.31). Weak relative density variations are present inside the cavity; the density variations convect downstream the cavity. Radial density variations outside the cavity indicate acoustic propagation. The acoustic waves originate at the cavity's trailing edge. Typical cavity tone effects such as the Doppler's shift and upstream amplification of the acoustic wave are captured by the DSC for both cases.

A whip shaped shear layer of the velocity field proofs the presence of a shear layer mode. A typical side effect of this shear layer mode is the secondary vortex in the rear half of the cavity. Compared to the fluid dynamic velocity field, the acoustic velocity is of orders of magnitude smaller. This first validation shows how the weak acoustic velocity component is extracted by using Helmholtz decomposition.

#### 6.4.1 Helmholtz decomposition

Helmholtz decomposition of the flow field into compressible and vortical structures requires either the computation of the rate of expansion or the vorticity of the velocity field. The rate of expansion (see Fig. 6.32) is a measure of the compressibility of the flow field. Compressibility is highly connected to wave structures and density variations. A careful reader detects line artifacts in Fig. 6.32; these line artifacts indicate borders between the discontinuous elements and are due to the discontinuous velocity field. In the left corner of the domain, the prescribed incompressible Blasius boundary layer adapts its velocity profile to the compressible fluid and low Reynolds number assumption  $\text{Re}_x \gg 1$ , with respect to the developing length, might be violated. The very steep velocity gradient at the inlet leads to unsatisfying divergence of the numerical flow field. A grid study of the radial basis function derivatives showed that

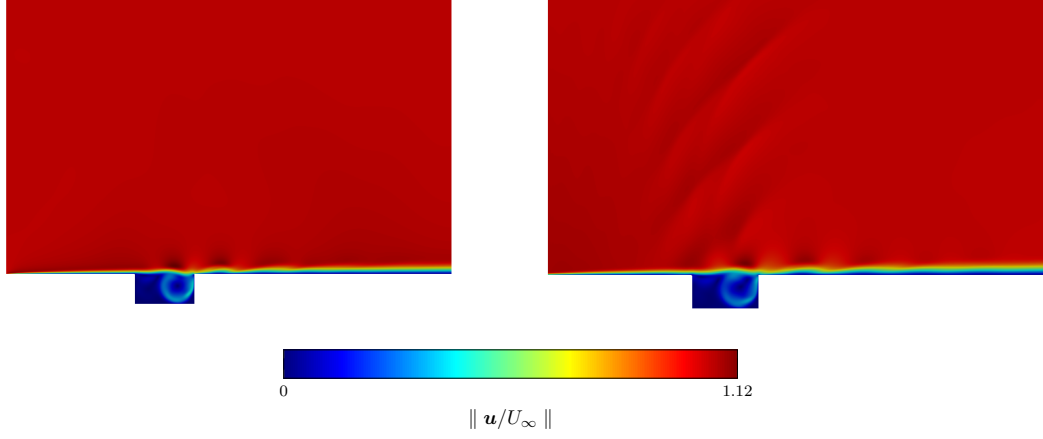


Figure 6.31: The magnitude of the flow velocity indicates the presence of the shear layer mode. 2M4 (left) and 2M8 (right).

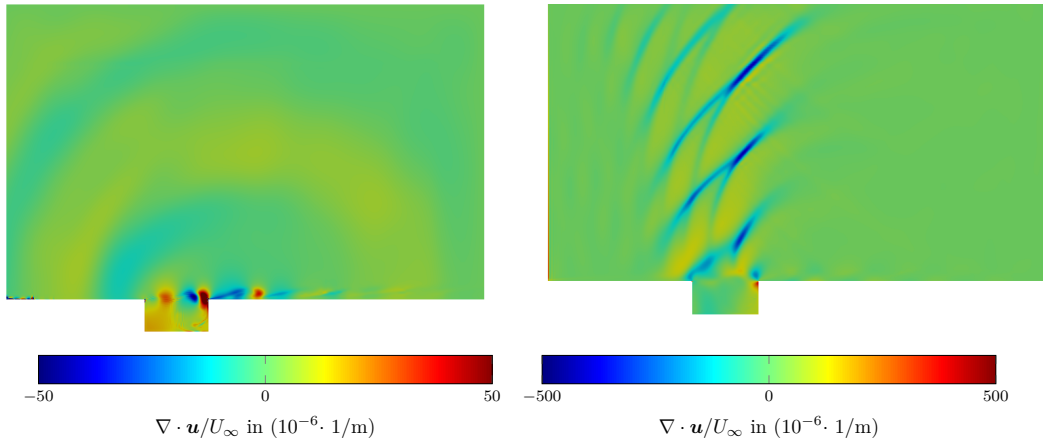


Figure 6.32: Rate of expansion of the velocity field. 2M4 (left) and 2M8 (right).

the origin of the checkerboard pattern is partly due to the weak approximation of the divergence by the direct numerical simulation. However, the direct Helmholtz decomposition of the compressible part with the rate of expansion is not possible on a non-convex domain. The computation of the scalar potential results in a singular behavior for reentrant corners. However, Helmholtz decomposition based on the vorticity works for reentrant corners.

Figure 2.7 shows the vorticity of the shear layer mode [91]. The distinctive shear layer separates the weak, and stationary secondary vortex inside the cavity, as well as the free stream outside the cavity. The curl-curl equation of the vector potential is used to obtain the vortical velocity component of the Helmholtz decomposition. Referring to the first validation, the compressible flow field is obtained indirectly by subtracting the vortical velocity component from the total velocity field of the DSC. In these cases, the Mach numbers are 0.4 and 0.8; significant compressible flow structures are expected around the cavity orifice as well as propagating waves in the decomposed velocity field.

The curl-curl equation with the vorticity as source term computes the vector potential  $\mathbf{A}^{*,v}$ . Radial basis function derivatives derive the local vorticity. Afterwards, the local vorticity is integrated conservatively to finalize the correct finite element loads. At all boundaries, the tangential component of the velocity field is introduced as a Neumann boundary. Mass regularization guarantees a unique solution of the Neumann curl-curl problem; the system of equations is solvable. Having the solution of the vector potential, the incompressible (vortical) velocity component is obtained by  $\mathbf{u}^v = \nabla \times \mathbf{A}^{*,v}$ . Figure 6.34

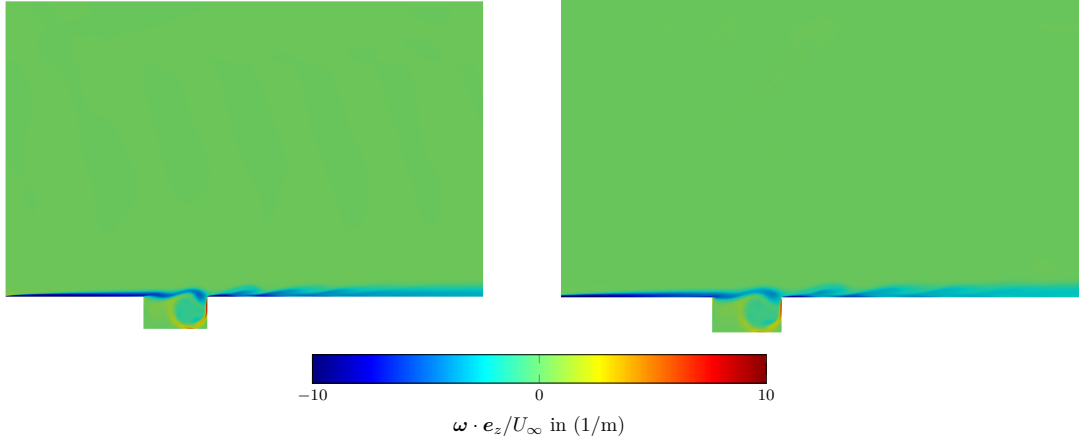


Figure 6.33: Vorticity of the cavity configuration in the shear layer mode. 2M4 (right) and 2M8 (left).

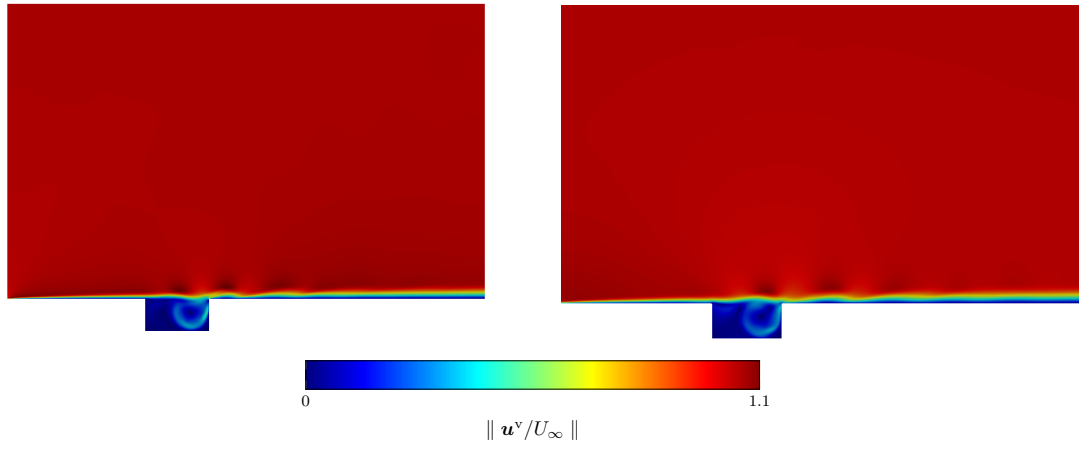


Figure 6.34: Incompressible velocity component of the Helmholtz decomposition. 2M4 (left) and 2M8 (right).

illustrates the vortical velocity component. A comparison to the flow field reveals that vortical structures dominate the flow.

The complementary field  $\mathbf{u} - \nabla \times \mathbf{A}^{*,v}$  represents the compressible part of the DSC (see Fig. 6.35). An analysis of the compressible structures shows radiating waves and strong compressible circular shaped structures convecting through the cavity orifice analog to the DSC density field. From the compressible component, an upstream amplification of the compressible waves is detected. As expected, the compressible velocity is about two orders of magnitude lower than the total velocity. The simulation shows the extraction of the weak acoustic velocity component using Helmholtz decomposition. In the next validation step, the effect of the hybrid workflow on the acoustic radiation, based on filtered aeroacoustic sources, is evaluated.

#### 6.4.2 Aeroacoustic simulation

The aeroacoustic propagation simulation recalculates the total stagnating enthalpy  $H$  based on the equation of vortex sound (2.102). This equation is solved in terms of the FEM by the in-house solver CFS++ [178]. The non-radiating base flow  $\mathbf{u}^v$  is used to construct the corrected Lamb vector. Finally, the acoustic field is judged by the DSC far-field.

The wave equation is discretized in space by the finite element method and in time by a Newmark time integration scheme. Doppler's effect is included in the convective wave operator. Non-conforming Nitsche-

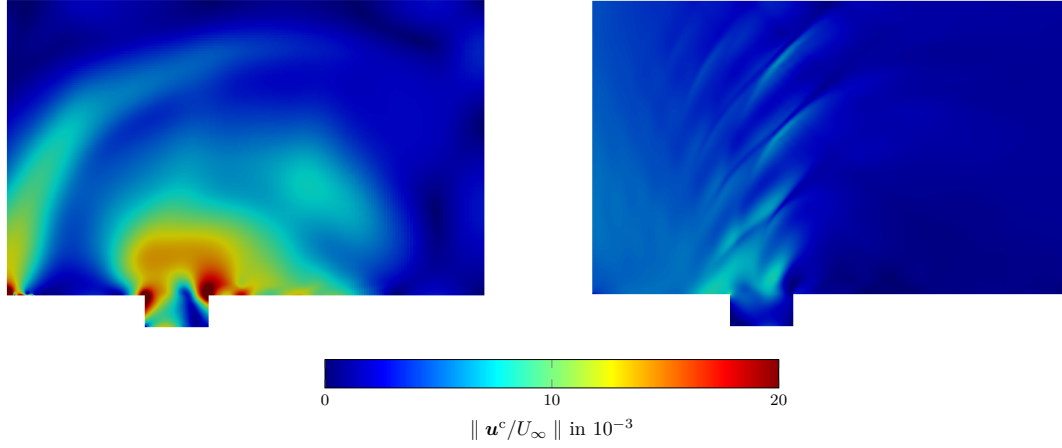


Figure 6.35: Compressible velocity component of the Helmholtz decomposition. 2M4 (left) and 2M8 (right).

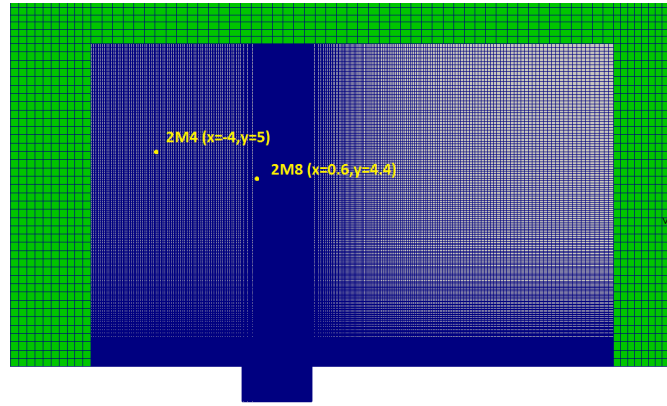


Figure 6.36: Non-conforming interfaces are used to lower the number of elements.

type Mortar interfaces connect the finite element domain that consists of three independent discretizations and non-conforming regions [179] (see Fig. 6.36). The divergence of the Lamb vector, which is computed by radial basis functions and the non-radiating base flow  $\mathbf{u}^v$  and forms the aeroacoustic sources, is prescribed on the source domain. A propagation domain is enclosed between the source domain and the outer PML. The PML ensures accurate free field radiation for low Mach number of the convective wave equation. At higher Mach numbers,  $M = 0.8$  reflections occur at the interface from the propagation region to the PML that emphasizes a further development of the PML. Currently, the PML is just implemented for the standard wave equation without mean flow.

Figure 6.37 shows the acoustic field of the simulation. The acoustic field represents the acoustics due to the vortical velocity component. The comparison to the direct numerical simulation leads to satisfying results for the acoustic field. Upstream amplification and downstream attenuation is captured. The convection of the acoustic waves is computed correctly for the given Mach number. Equation (2.99) in the far-field approximation [146],  $H = p/\rho_0$ , and the ideal gas law for the perturbation serve an approximate relation between the specific enthalpy fluctuation and the relative density fluctuation

$$\mathrm{d}H/c^2 = \frac{\mathrm{d}\rho}{\rho_0}. \quad (6.17)$$

Table 6.8 compares the density variations. The density fluctuations of the DSC simulation and the density variations of the acoustic propagation simulation show similar results in direction of propagation.

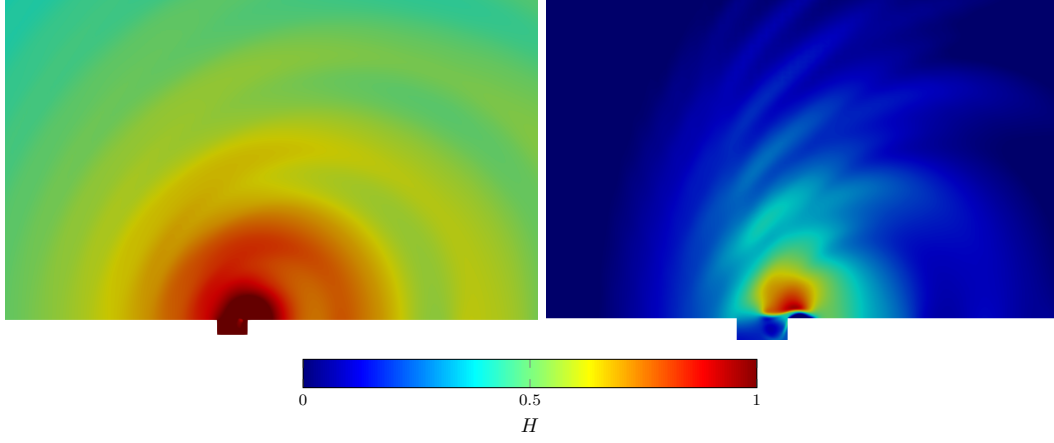


Figure 6.37: Characteristic snapshot of the acoustic propagation. 2M4 (left) and 2M8 (right).

Table 6.9 shows the dominant shear layer mode and the first secondary mode for the considered simulation setups. The deviations of the predicted shear layer frequency, compared to the experiments and the semi-

Table 6.8: Comparison of the acoustic density fluctuations outside the cavity (the location is depicted in Fig. 6.36).

Acoustic	$d\rho/\rho_0$	$dH$	$d\rho/\rho_0$
DSC 2M4	0.0035	-	0.0035
Hybrid 2M4	-	0.0218	0.003488
DSC 2M8	0.0345	-	0.0345
Hybrid 2M8	-	0.0402	0.0256

empirical modified Rossiter formula, are in the range of Colonius [73] meticulous cavity study. Figure 6.38 shows the Fourier modes ( $St_1$ ,  $St_2$ ) of the acoustic radiation for Mach 0.8 using the vortex sound equation. The radiation characteristics of both the dominant first and the secondary Rossiter mode are examined.

Table 6.9: Comparison of the shear layer frequency of 2M4 and 2M8. The dominant Rossiter mode is depicted and the subdominant Rossiter mode is written in brackets.

	$St_1$ 2M4	( $St_2$ 2M4)	( $St_1$ 2M8)	$St_2$ 2M8
Experiments [93]	-	0.91	-	0.69
Analytic (6.16)	0.35	0.81	0.29	0.67
Simulation [73]	0.48	0.78	0.34	0.63
DSC	0.471	(0.76)	(0.34)	0.645
Hybrid	0.47	0.76	0.342	0.645

Starting with the dominant mode, strong vertical wave amplification is present, very similar to the overall radiation character. The secondary mode has a lower oscillation frequency and a more spread radiation pattern. Most important, the radiation pattern of different acoustic meshes is compared to the reference solution, the DSC. For Mach 0.4, the radiation pattern converges to the DSC as the simulation mesh is refined. The shape and the magnitude agree with the direct simulation. However for the Mach 0.8 case, the strong radiation lobes in vertical direction are underestimated. With increasing mesh refinement, the parasitic side lobes are reduced and the nature of the main lobe is formed. If further linear and non-linear terms are included in the wave operator, these difference can be reduced to a minimum. By using the instantaneous flow field in the convective wave operator, second order and third order effects are investigated. This preliminary study examines the effects of a nonlinear wave equation. Replacing

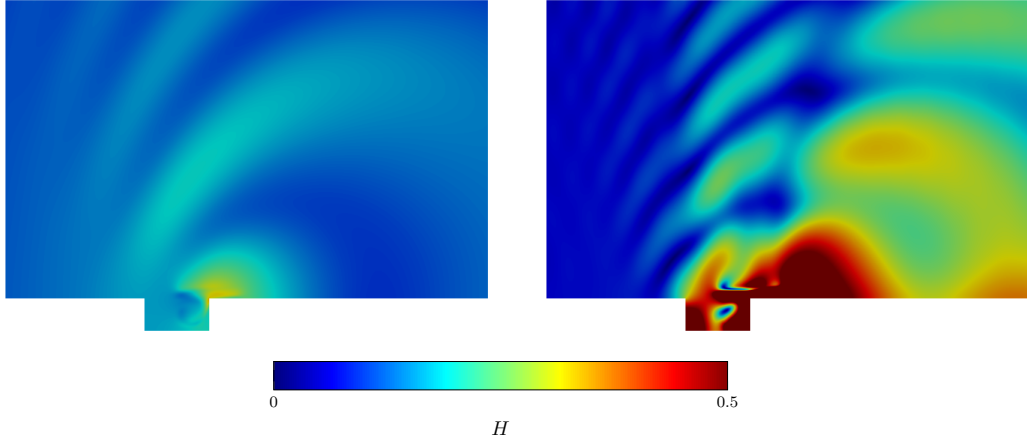


Figure 6.38: Fourier modes of the 2M8 cavity. First Rossiter mode (left) and second Rossiter mode (right).

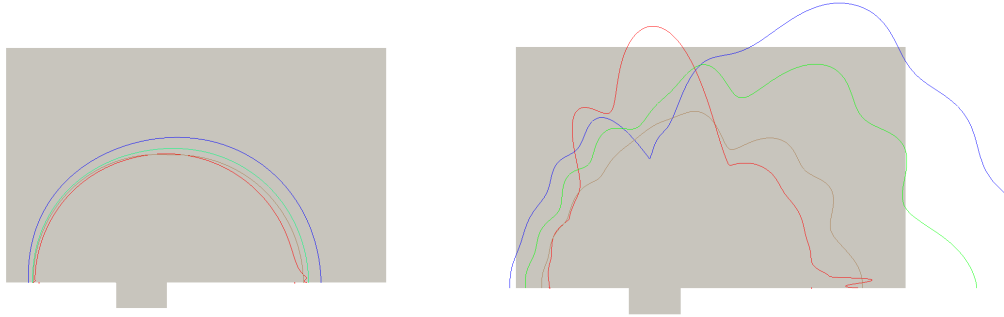


Figure 6.39: Radiation pattern at the dominant Rossiter mode. 2M4 (right) and 2M8 (left). The different meshes of the acoustic mesh study, coarse (blue), middle (green), and fine (brown), are compared to the reference solution (red).

the vortical velocity in the wave operator by the instantaneous flow field, the operator writes as

$$\frac{d}{dt} = \frac{\partial}{\partial t} + \mathbf{u}^v \cdot \nabla \quad \rightarrow \quad \frac{d}{dt} = \frac{\partial}{\partial t} + \mathbf{u} \cdot \nabla. \quad (6.18)$$

This change causes nonlinear interactions in the wave operator. Second order acoustic velocity effects of the wave operator that are included are summarized by

$$\rho_0 \left[ \frac{\partial(\mathbf{u} - \mathbf{u}^v) \cdot \nabla H}{\partial t} + \mathbf{u}^v \cdot (\mathbf{u} - \mathbf{u}^v) \cdot \nabla H + (\mathbf{u} - \mathbf{u}^v) \cdot (\mathbf{u}^v) \cdot \nabla H \right] \quad (6.19)$$

and third order acoustic velocity effects of the wave operator are included by

$$\rho_0 [(\mathbf{u} - \mathbf{u}^v) \cdot (\mathbf{u} - \mathbf{u}^v) \cdot \nabla H]. \quad (6.20)$$

To incorporate these interaction terms into the wave equation, they must be expressed in terms of the enthalpy or additional equations arise to compute the acoustic quantities. Figure 6.40 shows the nonlinear effects for the cavity 2M8. Compared to the linear computation (see Fig. 6.37), the results of the extended equation illustrate that including further nonlinear effects may lead to a general wave equation,

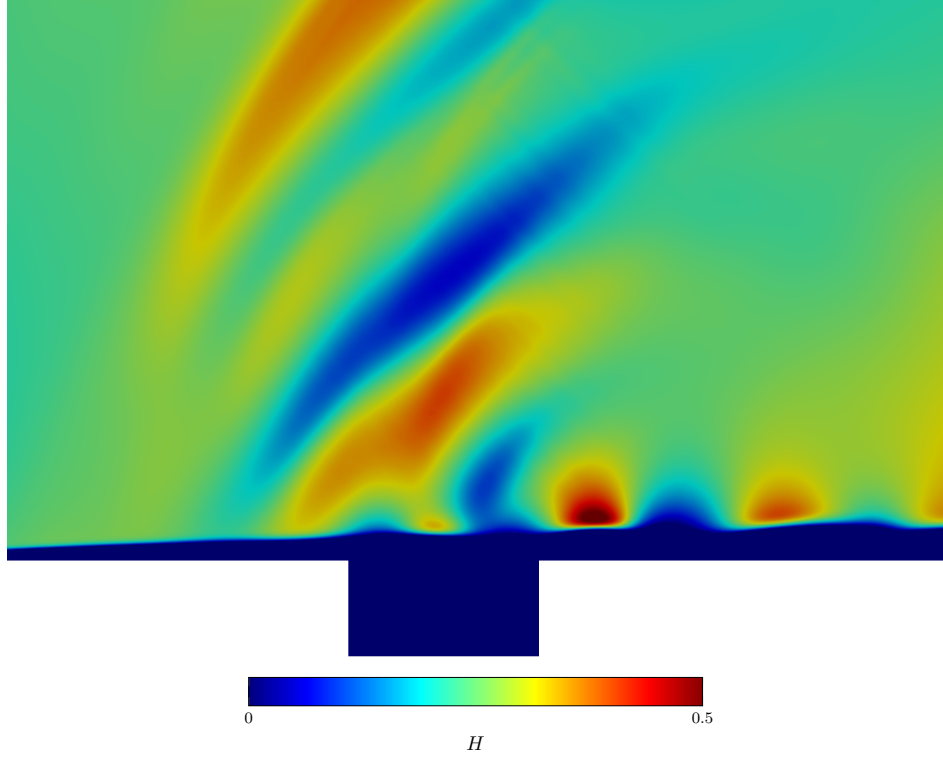


Figure 6.40: Simulation including nonlinear compressible velocity interactions, 2M8 cavity.

propagating acoustics at higher Mach numbers. Furthermore, the first order vorticity interaction term

$$\nabla \cdot (\boldsymbol{\omega} \times (\mathbf{u} - \mathbf{u}^v)), \quad (6.21)$$

must be modeled within the wave equation, to follow the proposed concept of Chap. 3.

### 6.4.3 Conclusions

Based on the DSC data the validity of two essential ingredients is analyzed: the Helmholtz decomposition itself and the whole hybrid aeroacoustic workflow. At first, the Helmholtz decomposition extracts the compressible velocity components and the vortical component of the DSC velocity. Secondly, the proposed hybrid aeroacoustic procedure computes vortex sound that is justified by the DSC far-field. The hybrid aeroacoustic workflow is enhanced through the computation of the aeroacoustic sources. As proposed by Goldstein, aeroacoustic sources are based on the non-radiating base flow. It is possible to extract the vortical (non-radiating) flow component for non-convex domains with the help of a Helmholtz decomposition. The acoustic field, based on hybrid aeroacoustics and the vortex sound, converges to the acoustic mode of the DSC in the far-field for Mach 0.4. For Mach 0.8, the strong radiation lobes in vertical direction are underestimated, since only linear wave propagation is considered in this study. Although, we are far beyond the limits of the equation of vortex sound and the hybrid methodology, the results are promising for further studies. This satisfactory match validates the workflow for vorticity dominated aeroacoustic method. However, further investigations on the relevant terms of the wave operator have to be done in the future.

## 7 Summary and Conclusions

Direct sound computation resolves flow and acoustics at all Mach numbers, but for practical applications, this is infeasible, even though great advances have been made in direct computation of aerodynamic sound. Furthermore, open issues of proprietary CFD, e.g. radiation conditions and acoustic active materials, severely diminishes the applicability in product development. Acoustic analogies based on incompressible flow simulations overcome these open issues, except the aeroacoustic feedback. To incorporate aeroacoustic feedback, the presented hybrid aeroacoustic method relies on a compressible flow simulation. Since the beginning of computational aeroacoustics (CAA), hybrid methodologies have been established as the most practical methods for aeroacoustic computations (see Fig. 7.1). Especially in low Mach number aeroacoustics, the well known disparity of length scales makes it possible to apply well suited simulation models using different meshes for flow and acoustics, which leads to a very efficient computational procedure. However, the procedure is generally not limited to low Mach numbers. The workflow of these aeroacoustic approaches is based on three steps: 1. perform unsteady flow computations on a restricted sub-domain; 2. compute the acoustic sources; 3. simulate the acoustic field. Hybrid aeroacoustic methods seek for robust and flexible procedures that provide a conservative mesh to mesh interpolation of the aeroacoustic sources while high computational efficiency is ensured. We realized this source term computations by radial basis function interpolation in combination with a volume cut-cell approach.

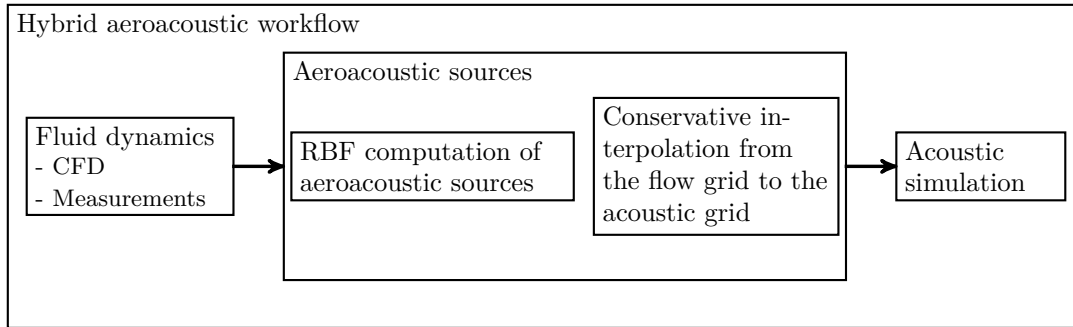


Figure 7.1: The hybrid aeroacoustic workflow consists of three main computational parts.

A general aeroacoustic analogy assumes a causal forward coupling of the forcing (obtained by an in-dependent flow simulation) on fluctuating quantities, e.g. the fluctuating pressure  $p'$  that approaches the acoustic pressure  $p^a$  at large distances from the turbulent region. Thereby, a general acoustic analogy composes a hyperbolic left hand side defined by a wave operator and a generic right hand side **RHS**( $\star$ )

$$\square p' = \mathbf{RHS}(p, \mathbf{u}, \rho, \dots). \quad (7.1)$$

As already illustrated, the separation of the flow and acoustic quantities is of major importance. The acoustic quantities are modeled by the wave equation. A preceding compressible flow simulation computes fluid dynamic structures, including aeroacoustic feedback. Based on these compressible simulations a



vortical projection of the flow variables is used as the consistent source term and base flow for the linear or non-linear wave operator.

The herein presented Helmholtz decomposition obtains a vortical base flow satisfying the incompressibility condition. In contrast to the original version of Helmholtz decomposition, which assumes an unbounded, simply connected domain, we introduced consistent boundary conditions for the Helmholtz decomposition in order to be applicable for engineering applications. Considering these practical challenges, numerical simulation techniques and the standard approximation methods are developed for finite domains, without vanishing flow fields at the boundaries. This causes a non-unique Helmholtz decomposition up to the influence of the exterior of the simulation domain. We show that the scalar potential formulation of Helmholtz decomposition fails for reentrant corners (often these reentrant corners are regions of edge-tone and therefore relevant for the acoustic simulation), but the vector potential formulation based on the curl-curl equation succeeds in decomposing the velocity field, even for high Mach numbers and highly turbulent structures. The crucial difference between the scalar and the vector potential is the incompressibility condition of the vector potential that ensures a bounded solution of the derivative at reentrant corners (s-regularity). Additionally, we investigated the possibility of decomposing the field directly during the CFD simulation by solving a Poisson equation in each time-step during the CFD computation.

Furthermore, we have to note that this hybrid aeroacoustic workflow focus on the acoustic properties of the problem, an acoustic behavior-oriented solution. The aeroacoustic problem is analyzed, significant aeroacoustic sources are detected, and acoustic absorbing materials and boundaries are modeled precisely. Impedance boundaries and experimentally justified acoustic material properties can be integrated.

## 7.1 Application

The presented numerical simulation method, based on compressible flow data, is applied to different aeroacoustic examples. With the proposed workflow we are capable of combining the properties of a fully resolved compressible flow simulation (including feedback from acoustics to flow structures) and the desirable advantage of a separated acoustic simulation. In this sense, we extend the hybrid approach from underlying incompressible flow simulations to compressible flow simulations using Helmholtz projection to obtain a vortical base flow to apply the established hybrid method. The application of this hybrid method seems to be unconventional and fluid dynamically not rigorous, but with the correct wave operator the equation is conforming the conservation equations.

The validation linked the missing or contradicting thoughts of readers and we addressed all four confusions by a separate validation example.

- *First, the capability of the Helmholtz decomposition is underestimated.* Without merit, thoughts spread that the decomposition cannot split colorful, and rich fluid dynamics into vortical and non-vortical components. This misinterpretation is clarified by all four applications in this thesis; the first example, cylinder in a crossflow, focuses exclusively on the separation. The conclusion reveals that the Helmholtz decomposition extracts the incompressible part of a low Mach number compressible flow simulation. Both, the incompressible and vortical (Helmholtz decomposition) solution coincide.

We demonstrated the application of the Helmholtz decomposition to a homologically trivial domain. The special use of Neumann boundaries suppresses the potential flow solution. The vector potential formulation, as the solution of the inhomogenous curl-curl equation, gives accurate results compared to the incompressible flow simulation. We conclude that the Helmholtz decomposition

extracts vortical components, but relies on the quality of the CFD simulation. Consequently, this decomposition cannot resolve further or finer structures in the velocity field.

- *Second, the developed method has a fundamental fluid dynamic justification.* Goldstein justifies that the vortical part of Helmholtz decomposition of the compressible flow field is non-radiating. The non-radiating base flow is used to extend the Mach number limitation of hybrid aeroacoustic analogies. Typical hybrid analogies follow a three step approach: the incompressible CFD simulation, the extraction of acoustic sources, and the direct one-way coupling to the acoustic simulation. The incompressible fluid restricts fluid dynamics that only compact acoustic feedback mechanisms are resolved. If the feedback mechanism is not acoustically compact, the state of the art is a DSC simulation of flow and acoustics. Investigations proved that even a coarser discretization than used by the DSC resolves the dominant aeroacoustic feedback. At low Mach numbers, we show that acoustically under-resolved DSC simulations in combination with the Helmholtz decomposition are able to compute the non-radiating base flow. The Mach extended hybrid analogy follows again a three step approach, the compressible CFD simulation in combination with a Helmholtz decomposition, the direct one-way coupling of the non-radiating base flow to the acoustic. This second example "cavity with a lip" validates the workflow in 2D.

If a compressible flow simulation already contains acoustics (which are solved by the aeroacoustic analogy), the sources of an aeroacoustic analogy have to be filtered such that a non-radiating base flow is obtained to construct the source terms. We show, that with the help of a Helmholtz decomposition, it is possible to extract the vortical (non-radiating) flow component for arbitrary domains. The method filters domain resonant artifacts, due to the boundaries. However, an accurate treatment of the boundary during CFD simulations is always recommended.

It has to be noted, that for bounded domains and domains with holes, an additional decomposition component arises, which is in the harmonic function space. The additional harmonic term is the solution of the potential flow theory of the geometrical configuration. As we rely on the divergence free formulation, the equation to obtain the vector potential serves as a valid formulation to extract all divergence-free and non-radiating parts of the flow, whether or not containing harmonic components.

- *Third, turbulent structures are used to doubt the capabilities of the Helmholtz decomposition.* Thoughts spread that the decomposition cannot resolve turbulent vortical structures. The third example "cavity with a lip" clarifies the method in 3D. Further investigation on the example including experimental validation is planned for the future.
- *Fourth, a profound disfavor arose with the conceptual extension to larger Mach numbers, well below Mach one.* Although, the first three examples are simple, they proof validity of the concept and support application of a Helmholtz decomposition at higher Mach numbers. The last example compares hybrid simulations at higher Mach numbers with DSC data.

Based on the DSC data, we analyzed the validity of two essential ingredients: the Helmholtz decomposition itself and the whole hybrid aeroacoustic workflow. First, the Helmholtz decomposition extracts the compressible velocity components and the vortical component of the DSC velocity. Second, the proposed hybrid aeroacoustic procedure computes vortex sound that is justified by the DSC far-field. The hybrid aeroacoustic workflow is enhanced through the computation of the aeroacoustic sources. As prosed by Goldstein, aeroacoustic sources are based on the non-radiating base flow. We show, with the help of a Helmholtz decomposition that it is possible to extract the vortical (non-radiating) flow component for non-convex domains. The acoustic field, based on hybrid aeroacoustis and the vortex sound, converges to the acoustic mode of the DSC in the far-field

for Mach 0.4. For Mach 0.8, the strong radiation lobes in vertical direction are underestimated, since only linear wave propagation is considered in this study. Although, we are far beyond the limits of the equation of vortex sound and the hybrid methodology the results are promising for further studies. This satisfactory match validates the workflow for vorticity dominated aeroacoustic method. However, further investigations on the relevant terms of the wave operator have to be done in the future. This comparison emphasizes further investigation of the method.

## 7.2 Properties of the extended hybrid workflow

The Mach number extended hybrid workflow advertises its application through the following properties, including the most important computational benefits.

### Subsonic Flows

The splitting into compressible and vortical components has no Mach number restriction. However, for large Mach numbers the interpretation of the components is difficult and for very low Mach numbers the compressible component can be overwhelmed with numerical errors. In general, the proposed workflow is only restricted to the resolution of the relevant effects by the wave operator (could be a Mach number constraint).

### Domain requirement

With respect to engineering applications, no domain assumptions are made during the derivation. The workflow is applicable for confined and unbounded domains with appropriate boundary conditions during the CFD simulation. The limiting factor is the computational capability of the cluster. In some cases, a homologically trivial domain can result in additional harmonic component during the decomposition. Usually, the domain extension can be reduced through this method just to the region of sound generation.

### Incompressible projection

The vortical component of the Helmholtz decomposition fulfills the incompressible equations (see Sec. 2.5.3). However, this incompressible solution branch is not necessarily the solution of incompressible CFD.

### Noise generation mechanism

The separation leads to a detailed investigation of different source mechanisms and interactions as well as the energy transfer between the components can be analyzed. A exact determination of the source area can confine the source domain and reduce the computational effort. Additionally, the combination of the aeroacoustic source and correct wave equation allows the reduction of the overall computational workload (similar to the coupling strategy in multi-physical simulations). Similar to the wave number decomposition, Helmholtz decomposition can be used as an adequate post-processing method to extract the compressible phenomena, which correspond to acoustic fluctuations in the far-field.

### Focus on acoustics

The hybrid workflow centers on an acoustic behavior-oriented solution. Significant aeroacoustic sources are detected and acoustic active materials and boundaries are modeled precisely, e.g.: impedance boundaries and experimentally justified acoustic material properties are easily integrated. This is beneficial, since the absorbers are acoustically modeled and not fluid dynamically resolved, up to very small scales.

### **Far-field extrapolation**

With the Helmholtz decomposition, a combination of a CFD source simulation and a separate propagation simulation through a transformation layer is possible [30].

The Mach number extended hybrid workflow is limited by the following effects.

### **Interaction directly**

The resolution of the interactions between the fluid perturbations is limited if the CFD simulation neglects them. In order to predict acoustics accurately, the most dominant acoustic source mechanism must be resolved.

### **Interpretation of compressible part**

The Helmholtz decomposition of the compressible velocity field into compressible and vortical component suffers from a clear physical interpretation of the compressible part for higher Mach numbers. There is no simple selection of the acoustic component of a direct sound computation. Partly this task can be achieved by a wave number decomposition of the compressible part.

### **Decomposition errors**

At low Mach numbers the divergence of the flow field is so small that it could be dominated by non-negligible numerical errors. Therefore, the vorticity based decomposition equation is preferred at low Mach number, beside the other optimal properties.

### **Computational time**

Focusing just on the feedback region of the domain, the computational workload of the method compared to a direct sound computation is reduced drastically. However, compared to the ordinary hybrid method the computational workload is higher due to the additional Helmholtz decomposition.

## **7.3 Further investigations**

Throughout this work, several interesting aspects are not addressed and could be subject to further investigations. First of all, the integration of the decomposition into a CFD simulation tool would be computationally efficient. This parallel computation of the vortical projection would result in a severe reduction in the overall computational time. Instead of implementing the Poisson problem or the curl-curl problem directly in the elliptic formulation, divergence correction techniques could be used [191,192].

A second route is the incorporation of linear interactions and non-linear terms into the aeroacoustic wave equation. These additional effects will account for scattering and refraction by the instantaneous vortical flow field as well as density variations. Based on this formulation, the distinctive terms can be quantified systematically and can be neglected if certain conditions are fulfilled.

# A Infinite mapping layer

Based on the drawbacks of other unbounded domain methods, the infinite domain method encounters some major advantages. Most importantly, the restriction to special geometries (ballooning, asymptotic boundaries, analytic-FEM, Green's function - FEM, conformal mapping techniques) is avoided. The method is motivated by the Cartesian coordinate mapping and represents the Laplace operator on an infinite domain. In contrast to infinite elements, the mapping layer is discretized radially by several layers of finite elements and ordinary basis functions constitute the elements in the IML. Differently to hybrid schemes which are based on analytic Green's functions, the infinite mapping layer is solution independent. Compared to a hybrid method using BEM at the boundary IML conserves sparsity and locality of the numerical system. The method is applicable for both, linear and nonlinear, equations.

## A.1 Mapping Layer Formulation

IML formulation maps an infinite computation domain to finite domain (see Fig. A.1). A compressed domain is then discretized by ordinary finite elements. The derivatives and operators are adapted to the mapping and used consistently to constitute the finite element formulation in the layer. All finite elements use ordinary basis functions to approximate the continuous solution. These difficulties of the unbounded mapping are avoided by placing the quadrature points inside the elements.

A general Poisson's problem in the space  $\mathbb{R}^n$  with  $n$  dimensions and the forcing function  $f$  in unbounded domains with a bounded solution at  $\|\mathbf{x}\|_2 \rightarrow \infty$  is written as

$$\nabla \cdot \nabla \phi(\mathbf{x}) = f \quad (1.1)$$

$$\phi(\mathbf{x}) \rightarrow 0 \quad \|\mathbf{x}\|_2 \rightarrow \infty, \quad (1.2)$$

where  $\|\mathbf{x}\|$  is the Euclidean norm of  $\mathbf{x}$ . The fundamental solution (Green's function) of the Laplace operator writes as

$$G(\mathbf{x}) = \begin{cases} \frac{1}{2\pi} \ln(\|\mathbf{x}\|_2) & n = 2 \\ -\frac{1}{\eta_n \|\mathbf{x}\|_2^{n-2}} & n > 2, \end{cases} \quad (1.3)$$

where  $\eta_n$  is the surface of the unit ball with respect to  $\mathbb{R}^n$ . The decay of a solution  $u(\mathbf{x})$  based on an arbitrary source can be estimated in the limit  $\|\mathbf{x}\|_2 \rightarrow \infty$  as

$$u(\mathbf{x}) = \begin{cases} C_2 \ln(\|\mathbf{x}\|_2) & n = 2 \\ \frac{C_n}{\|\mathbf{x}\|_2^{n-2}} & n > 2. \end{cases} \quad (1.4)$$

Knowing the behavior of the solution allows to design mapping functions with reasonable approximation of the infinite domain. The mapping must be bijective and  $C^2$  smooth, since the formulation requires the first and the second derivative of the mapping. A slightly different formulation can be obtained where only

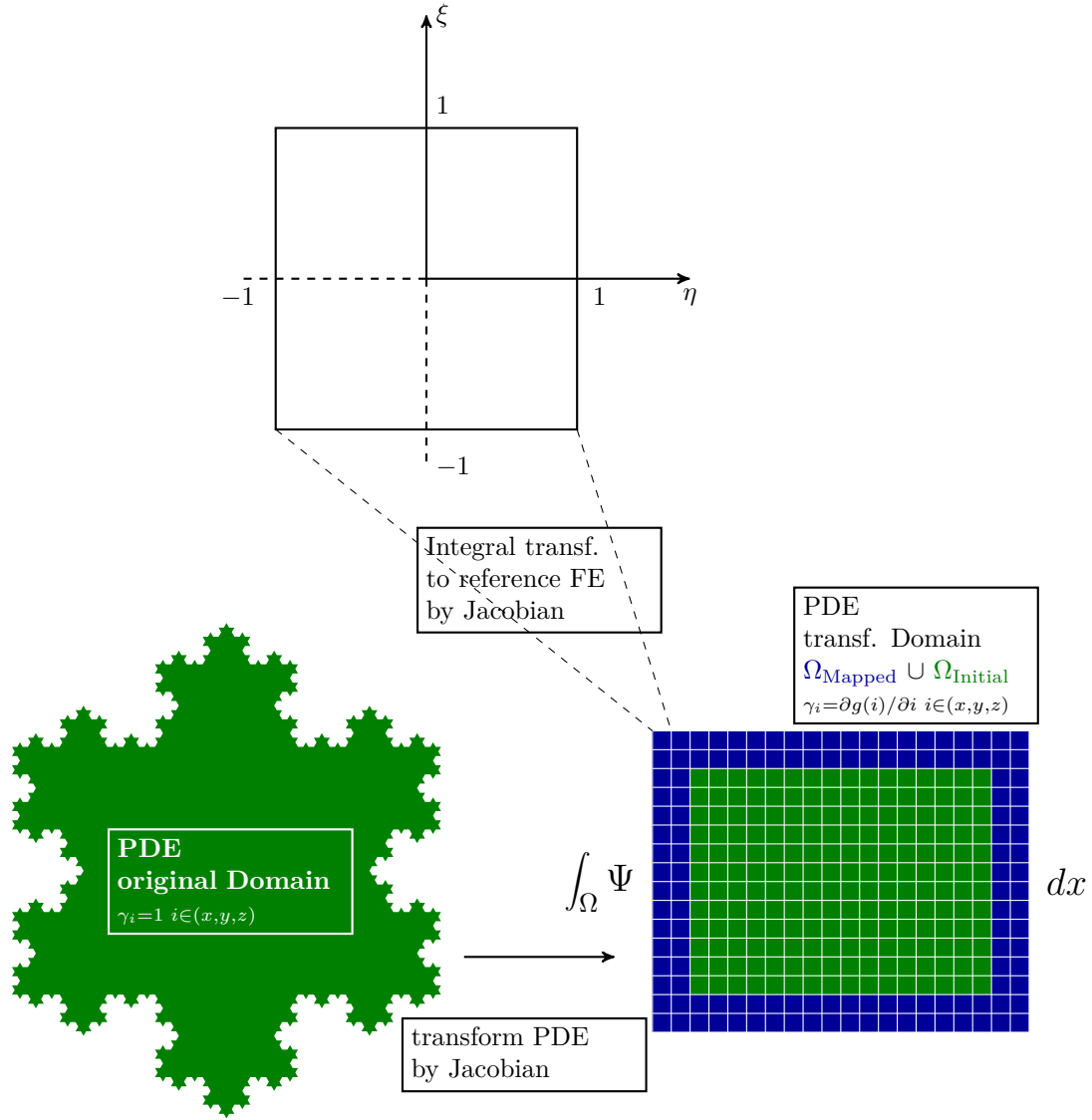


Figure A.1: The transformation of the PDE of an infinite domain to a finite domain and the derivation of the weak form and its connection to the isoparametric representation.

the first derivative is required and additionally the inverse of the Jacobian. The ideas and requirements of the mapping are summarized in Fig. A.2. In general, the mapping function maps an unbounded spatial coordinate  $[x_{i0}(= 0), \infty)$  to a standard interval  $[0, 1)$ . Four different mapping functions are presented. The rational map was found [193] to work well for a number of examples. In general, a mapping can be tuned to be the exact inverse mapping of the solution, such that the solution behaves linearly in the mapping layer. However, the tuning requires information about the analytic solution or an optimization procedure. The exponential map used by [193] shows one major drawback: it distributes the points of numeric evaluation oddly and as a result large errors occur. Additionally to the exponential map, an arctan function is proposed. Furthermore, the behavior and the difference to the rational function is investigated in details. Table A.1 summarizes the mapping functions, the inverse mapping and derivatives. The mapping functions are extended over the entire domain by the composition

$$g(x_i) = \begin{cases} f(x_i) & x_i \in \Omega_{\text{Mapped}} \\ x_i & x_i \in \Omega_{\text{Initial}} \end{cases} \quad (1.5)$$

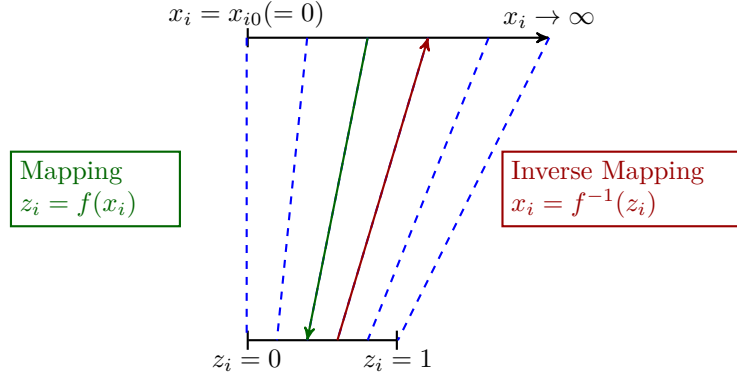


Figure A.2: The mapping transformation and the geometric variables illustrate the truncation of a domain with respect to an orthogonal set of geometric variables.

In the infinite zone, the infinite mapping is active and in the non-mapped region the relation is identical to the coordinate. Based on the mapped analytic solution, the mapping layer behavior is estimated for the three mapping functions with  $\kappa = 1$ ,  $L = 1$  (see Fig. A.3). The exact mapping transforms the

Table A.1: The three different mapping functions under investigation.

Name	Mapping $z_i = f(x_i)$	Inverse $x_i = f^{-1}(z_i)$	Derivative $\frac{\partial z_i(x_i)}{\partial x_i}$
Exponential	$L(1 - \exp^{-x_i/\kappa})$	$-\kappa \log(1 - \frac{z_i}{L})$	$\frac{L}{\kappa} \exp^{-x_i/\kappa}$
Tangent	$\frac{2L}{\pi} \arctan \frac{x_i}{\kappa}$	$\kappa \tan(\frac{\pi z_i}{2L})$	$\frac{2L}{\kappa \pi} \frac{1}{(x_i/\kappa)^2 + 1}$
Rational	$\frac{x_i L}{x_i + \kappa}$	$\kappa \frac{z_i/L}{1 - (z_i/L)}$	$\frac{L\kappa}{(x_i + \kappa)^2}$

solution to a straight line in the mapping layer; the exact mapping is the rational mapping with  $\kappa = 4$ ,  $L = 1$ . Relaxing the optimal condition  $\kappa = 1$ ,  $L = 1$ , the rational mapping gains curvature in the layer and behaves similar as the tangent mapping. At the outer boundary, the tangent function is steeper with slightly higher curvature. The overall behavior of the rational and tangent map is supporting their accuracy compared to the exponential map, with a steep inclination towards virtual infinity.

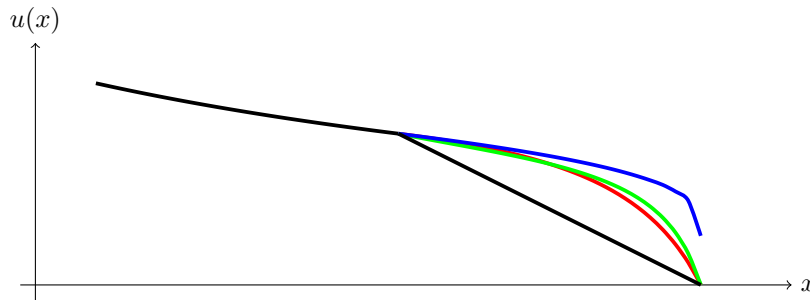


Figure A.3: The solution, Green's function, is mapped analytically to the infinite mapping layer to determine the behavior of the mapped solution. The analytic solution mapped by its inverse, rational mapping  $\kappa = 4$ ,  $L = 1$  (black); mapped by the rational mapping  $\kappa = 1$ ,  $L = 1$  (red); mapped by the tangent mapping  $\kappa = 1$ ,  $L = 1$  (green); mapped by the exponential mapping  $\kappa = 1$ ,  $L = 1$  (blue).

## A.2 Finite Element Implementation

An analytic mapping truncates the infinite domain to a finite domain. The core derivation of the IML introduces the finite element formulation. Basis functions of the IML elements are in the space  $\mathbf{V}$

$$\mathbf{V} = \{\phi(x) | \phi(x) \in H^1(\Omega), \phi(x) = \phi_e(x) \text{ on } \Gamma_e\}, \quad (1.6)$$

and the corresponding test functions are in the space  $\mathbf{W}$

$$\mathbf{W} = \{\psi(x) | \psi(x) \in H^1(\Omega), \psi(x) = 0 \text{ on } \Gamma_e\}. \quad (1.7)$$

$H^1(\Omega)$  denotes the standard Sobolev-space. Based on the definition of the function spaces we derive the weak formulation for an ordinary Poisson equation.

## A.3 Laplace Operator

Considering a Poisson problem in Cartesian coordinates (1.1) we derive the weak finite element formulation and apply the IML technique. In the case of an isotropic material parameter, this equation represent the electrostatic field. In unmapped coordinates, the gradient operator is defined as

$$\nabla_{\mathbf{x}} = \left( \frac{\partial}{\partial x_1}, \frac{\partial}{\partial x_2}, \frac{\partial}{\partial x_3} \right)^T. \quad (1.8)$$

The transformed operator  $\nabla_{\mathbf{z}}$  in Cartesian coordinates writes as

$$\nabla_{\mathbf{x}} = \mathbb{J} \nabla_{\mathbf{z}} = \left( \frac{\partial z_1}{\partial x_1} \frac{\partial}{\partial z_1}, \frac{\partial z_2}{\partial x_2} \frac{\partial}{\partial z_2}, \frac{\partial z_2}{\partial x_2} \frac{\partial}{\partial z_3} \right)^T. \quad (1.9)$$

Based on the transformation with the Jacobian  $\mathbb{J}$ , we derive the Poisson's equation in the coordinate system  $z_i$ . According to FEM the mapped Poisson's equation is integrated over the domain and the weak form of the IML is obtained.

$$\int_{\Omega_z} \nabla_{\mathbf{z}}(\psi) \mathbb{J} \cdot \mathbb{J} \nabla_{\mathbf{z}}(\phi) dz + \int_{\Omega_z} \psi (\nabla_{\mathbf{z}} \cdot \mathbb{J}) \cdot \mathbb{J} \nabla_{\mathbf{z}}(\phi) dz = \int_{\Omega_z} \psi f dz \quad (1.10)$$

If  $\mathbb{J}$  is symmetric, the bilinear form is symmetric; and for Cartesian coordinates  $\mathbb{J}$  is diagonal. The profound application of the IML to water waves is given in [52].



# Bibliography

- [1] V. P. Sergienko and S. N. Bukharov. *Noise and Vibration in Friction Systems*. Springer Series in Materials Science. Springer International Publishing, 2014.
- [2] T. Ifukube. *Sound-Based Assistive Technology: Support to Hearing, Speaking and Seeing*. Springer International Publishing, 2017.
- [3] Zeller P. (Hrsg.). *Handbuch Fahrzeugakustik*. Vieweg+Teubner Verlag, 2012.
- [4] A. Fuchs, E. Nijman, and H. H. Pribsch. *Automotive NVH Technology*. SpringerBriefs in Applied Sciences and Technology. Springer International Publishing, 2015.
- [5] M. Pflüger, F. Brandl, U. Bernhard, and K. Feitzelmayer. *Fahrzeugakustik*. Der Fahrzeugantrieb. Springer Vienna, 2010.
- [6] M. J. Lighthill. On sound generated aerodynamically I. General theory. *Proceedings of the Royal Society of London*, 211:564–587, 1951.
- [7] M. J. Lighthill. On sound generated aerodynamically II. Turbulence as a source of sound. *Proceedings of the Royal Society of London*, 222:1–32, 1953.
- [8] N. Curle. The Influence of Solid Boundaries upon Aerodynamic Sound. *Proceedings of the Royal Society of London A: Mathematical, Physical and Engineering Sciences*, 231(1187):505–514, 1955.
- [9] J. E. Ffowcs Williams and D. L. Hawkings. Sound Generation by turbulence and surface in arbitrary motion. *Philosophical Transactions of the Royal Society of London, Series A, Mathematical and Physical Sciences*, 264:321–342, 1969.
- [10] W. R. Morgan. The Kirchhoff Formula Extended to a Moving Surface. *Philosophical Magazine*, 9:141–161, 1930.
- [11] H. S. Ribner. Aerodynamic Sound from Fluid Dilatations - A Theory of the Sound from Jets and Other Flows. Technical report, Institute for Aerospace Studies, University of Toronto, 1962.
- [12] A. Powell. Theory of Vortex Sound. *J. Acoust. Soc. Am.*, 36:177 – 196, 1964.
- [13] M. S. Howe. Contributions to the theory of aerodynamic sound, with application to excess jet noise and the theory of the flute. *Journal of Fluid Mechanics*, 71(04):625–673, 1975.
- [14] W. Möhring. On vortex sound at low Mach number. *Journal of Fluid Mechanics*, 85(04):685–691, 1978.
- [15] P. E. Doak. Fluctuating total enthalpy as a generalized acoustic field. *Acoustical Physics*, 41:677–685, September 1995.

- [16] M. E. Goldstein. A generalized acoustic analogy. *Journal of Fluid Mechanics*, 488:315–333, 2003.
- [17] J. B. Freund, S. K. Lele, and P. Moin. Numerical simulation of a Mach 1.92 turbulent jet and its sound field. *AIAA journal*, 38(11):2023–2031, 2000.
- [18] E. Fares, B. Duda, and M. R. Khorrami. Airframe Noise Prediction of a Full Aircraft in Model and Full Scale Using a Lattice Boltzmann Approach. In *22nd AIAA/CEAS Aeroacoustics Conference*, page 2707, 2016.
- [19] L. Sanders, E. Manoha, M. Murayama, Y. Yokokawa, K. Yamamoto, and T. Hirai. Lattice-Boltzmann Flow Simulation of a Two-Wheel Landing Gear. In *22nd AIAA/CEAS Aeroacoustics Conference*, page 2767, 2016.
- [20] R. Brionnaud, G. Trapani, M. C. Modena, and D. M. Holman. Direct Noise Computation with a Lattice-Boltzmann Method and Application to Industrial Test Cases. In *22nd AIAA/CEAS Aeroacoustics Conference*, page 2969, 2016.
- [21] J. B. Freund. Noise sources in a low-Reynolds-number turbulent jet at Mach 0.9. *Journal of Fluid Mechanics*, 438:277–305, 2001.
- [22] M. E. Goldstein. On identifying the true sources of aerodynamic sound. *Journal of Fluid Mechanics*, 526:337–347, 2005.
- [23] C. Tam and Z. Dong. Radiation and outflow boundary conditions for direct computation of acoustic and flow disturbances in a nonuniform mean flow. *Journal of Computational Acoustics*, 4(02):175–201, 1996.
- [24] C. Tam, L. Auriault, and F. Cambuli. Perfectly matched layer as an absorbing boundary condition for the linearized Euler equations in open and ducted domains. *Journal of Computational Physics*, 144(1):213–234, 1998.
- [25] K. W. Thompson. Time dependent boundary conditions for hyperbolic systems. *Journal of computational physics*, 68(1):1–24, 1987.
- [26] K. W. Thompson. Time-dependent boundary conditions for hyperbolic systems, II. *Journal of Computational Physics*, 89(2):439–461, 1990.
- [27] J. B. Freund. Proposed inflow/outflow boundary condition for direct computation of aerodynamic sound. *AIAA journal*, 35(4):740–742, 1997.
- [28] C. Bailly and D. Juve. Numerical solution of acoustic propagation problems using linearized Euler equations. *AIAA journal*, 38(1):22–29, 2000.
- [29] C. Bogey, C. Bailly, and D. Juvé. Computation of flow noise using source terms in linearized Euler’s equations. *AIAA journal*, 40(2):235–243, 2002.
- [30] W. De Roeck, G. Rubio, M. Baelmans, and W. Desmet. Toward accurate hybrid prediction techniques for cavity flow noise applications. *International journal for numerical methods in fluids*, 61(12):1363–1387, 2009.
- [31] R. Ewert and W. Schröder. Acoustic perturbation equations based on flow decomposition via source filtering. *Journal of Computational Physics*, 188(2):365–398, 2003.
- [32] J. C. Hardin and D. S. Pope. An acoustic/viscous splitting technique for computational aeroacoustics. *Theoretical and Computational Fluid Dynamics*, 6(5-6):323–340, 1994.

- [33] W. Z. Shen, J. N-oacute, R. S-oacute, and R. S-oacute. Comment on the aeroacoustic formulation of Hardin and Pope. *AIAA journal*, 37(1):141–143, 1999.
- [34] W. Z. Shen and J. N. Sørensen. Aeroacoustic modelling of low-speed flows. *Theoretical and Computational Fluid Dynamics*, 13(4):271–289, 1999.
- [35] S. A. Slimon, M. C. Soteriou, and D. W. Davis. Computational aeroacoustics simulations using the expansion about incompressible flow approach. *AIAA journal*, 37(4):409–416, 1999.
- [36] J. Seo and Y. J. Moon. Perturbed compressible equations for aeroacoustic noise prediction at low mach numbers. *AIAA journal*, 43(8):1716–1724, 2005.
- [37] Y. Bae and Y. J. Moon. Computation of phonation aeroacoustics by an INS/PCE splitting method. *Computers & Fluids*, 37(10):1332–1343, 2008.
- [38] J. H. Seo and Y. J. Moon. Linearized perturbed compressible equations for low Mach number aeroacoustics. *Journal of Computational Physics*, 218(2):702–719, 2006.
- [39] A. Hüppe, J. Grabinger, M. Kaltenbacher, A. Reppenhagen, G. Dutzler, and W. Kühnel. A Non-Conforming Finite Element Method for Computational Aeroacoustics in Rotating Systems. In *20th AIAA/CEAS Aeroacoustics Conference*, page 2739, 2014.
- [40] C.-D. Munz, M. Dumbser, and M. Zucchini. The multiple pressure variables method for fluid dynamics and aeroacoustics at low Mach numbers. *Numerical methods for hyperbolic and kinetic problems*, 7:335–359, 2003.
- [41] S. Roller, T. Schwartzkopff, R. Fortenbach, M. Dumbser, and C.-D. Munz. Calculation of low Mach number acoustics: a comparison of MPV, EIF and linearized Euler equations. *ESAIM: Mathematical Modelling and Numerical Analysis*, 39(3):561–576, 2005.
- [42] C.-D. Munz, M. Dumbser, and S. Roller. Linearized acoustic perturbation equations for low Mach number flow with variable density and temperature. *Journal of Computational Physics*, 224(1):352–364, 2007.
- [43] W. De Roeck and W. Desmet. Accurate CAA-Simulations using a Low-Mach Aerodynamic/Acoustic Splitting Technique. In *15th AIAA/CEAS Aeroacoustics Conference (30th AIAA Aeroacoustics Conference)*, page 3230, 2009.
- [44] B. Farkas and G. Paál. Numerical Study on the Flow over a Simplified Vehicle Door Gap-an Old Benchmark Problem Is Revisited. *Periodica Polytechnica. Civil Engineering*, 59(3):337, 2015.
- [45] E. Feireisl, T.G. Karper, and M. Pokorný. *Mathematical Theory of Compressible Viscous Fluids: Analysis and Numerics*. Advances in Mathematical Fluid Mechanics. Springer International Publishing, 2016.
- [46] G. K. Batchelor. *An Introduction to Fluid Dynamics*. Cambridge Mathematical Library. Cambridge University Press, 2000.
- [47] H. Altenbach. *Kontinuumsmechanik: Einführung in die materialunabhängigen und materialabhängigen Gleichungen*. Springer Berlin Heidelberg, 2015.
- [48] A. N. Kolmogorov. The local structure of turbulence in incompressible viscous fluid for very large reynolds numbers. In *Dokl. Akad. Nauk SSSR*, volume 30, pages 299–303, 1941.

- [49] F. Durst. *Grundlagen der Strömungsmechanik—Eine Einführung in die Theorie der Strömungen und Fluide*. Berlin: Springer, 2006.
- [50] M. S. Howe. *Acoustics of fluid-structure interactions*. Cambridge university press, 1998.
- [51] M. Kaltenbacher. *Computational Acoustics*. CISM International Centre for Mechanical Sciences. Springer International Publishing, 2017.
- [52] F. Toth, S. Schoder, and M. Kaltenbacher. An infinite mapping layer for deep water waves. *PAMM*, 17(1):689–690, 2017.
- [53] H. von Helmholtz. LXIII. On Integrals of the hydrodynamical equations, which express vortex-motion. *The London, Edinburgh, and Dublin Philosophical Magazine and Journal of Science*, 33(226):485–512, 1867.
- [54] H. Lamb. *Hydrodynamics*. Cambridge university press, 1932.
- [55] D. J. Griffiths. Electrodynamics. *Introduction to Electrodynamics, 3rd ed., Prentice Hall, Upper Saddle River, New Jersey*, pages 301–306, 1999.
- [56] G. B. Arfken and H. J. Weber. *Mathematical methods for physicists international student edition*. Academic press, 2005.
- [57] P. G. Saffman. *Vortex dynamics*. Cambridge university press, 1992.
- [58] H. Bhatia, G. Norgard, V. Pascucci, and P. Bremer. The helmholtz-hodge decomposition—a survey. *IEEE Transactions on visualization and computer graphics*, 19(8):1386–1404, 2013.
- [59] P. Monk. *Finite Element Methods for Maxwell’s Equations*. Numerical Mathematics and Scientific Computation. Clarendon Press, 2003.
- [60] T. H. Zheng, S. K. Tang, and W. Z. Shen. Simulation of vortex sound using the viscous/acoustic splitting approach. *Canadian Society for Mechanical Engineering. Transactions*, 35(1):39–56, 2011.
- [61] P. Martínez-Lera, C. Schram, H. Bériot, and R. Hallez. An approach to aerodynamic sound prediction based on incompressible-flow pressure. *Journal of Sound and Vibration*, 333(1):132–143, 2014.
- [62] F. Farassat. *Introduction to generalized functions with applications in aerodynamics and aeroacoustics*. NASA-TP-3428, 1996.
- [63] F. Farassat. Acoustic radiation from rotating blades—the Kirchhoff method in aeroacoustics. *Journal of sound and vibration*, 239(4):785–800, 2001.
- [64] W. Mohring. A well posed acoustic analogy based on a moving acoustic medium. *arXiv preprint arXiv:1009.3766*, 2010.
- [65] W. Möhring, E.-A. Müller, and F. Obermeier. Problems in flow acoustics. *Reviews of modern physics*, 55(3):707, 1983.
- [66] X. Gloerfelt, C. Bailly, and D. Juvé. Direct computation of the noise radiated by a subsonic cavity flow and application of integral methods. *Journal of Sound and Vibration*, 266(1):119–146, 2003.
- [67] R. D. Sandberg, N. D. Sandham, and P. F. Joseph. Direct numerical simulations of trailing-edge noise generated by boundary-layer instabilities. *Journal of sound and vibration*, 304(3):677–690, 2007.

- [68] D. Flad H. Frank, M. Werner and C.-D. Munz. Direct Aeroacoustic Simulation of Feedback Mechanisms. In *DLES10 Limassol Cyprus*, 2015.
- [69] S. Succi. *The Lattice Boltzmann Equation: For Fluid Dynamics and Beyond*. Numerical Mathematics and Scientific Computation. Clarendon Press, 2001.
- [70] T. Krüger, H. Kusumaatmaja, A. Kuzmin, O. Shardt, G. Silva, and E.M. Vigen. *The Lattice Boltzmann Method: Principles and Practice*. Graduate Texts in Physics. Springer International Publishing, 2016.
- [71] Y. B. Bao and J. Meskas. Lattice boltzmann method for fluid simulations. *Department of Mathematics, Courant Institute of Mathematical Sciences, New York University*, 2011.
- [72] D. Givoli. *Numerical methods for problems in infinite domains*, volume 33. Elsevier, 2013.
- [73] T. Colonius. Modeling artificial boundary conditions for compressible flow. *Annu. Rev. Fluid Mech.*, 36:315–345, 2004.
- [74] C. Tam and L. Auriault. Time-domain impedance boundary conditions for computational aeroacoustics. *AIAA journal*, 34(5):917–923, 1996.
- [75] Y. Ozyoruk, V. Ahuja, and L. Long. Time domain simulations of radiation from ducted fans with liners. In *7th AIAA/CEAS Aeroacoustics Conference and Exhibit*, page 2171, 2001.
- [76] Q. Zhang and D. J. Bodony. Impedance prediction of three-dimensional honeycomb liners with laminar/turbulent boundary layers using DNS. In *19th AIAA/CEAS Aeroacoustics Conference*, page 2268, 2013.
- [77] S. Sinayoko, A. Agarwal, and Z. Hu. Flow decomposition and aerodynamic sound generation. *Journal of Fluid Mechanics*, 668:335–350, 2011.
- [78] S. Klainerman and A. Majda. Singular limits of quasilinear hyperbolic systems with large parameters and the incompressible limit of compressible fluids. *Communications on pure and applied Mathematics*, 34(4):481–524, 1981.
- [79] M. E. Rose. Compact finite difference schemes for the Euler and Navier-Stokes equations. *Journal of Computational Physics*, 49(3):420–442, 1983.
- [80] W. C. Meecham and G. W. Ford. Acoustic radiation from isotropic turbulence. *The Journal of the Acoustical Society of America*, 30(4):318–322, 1958.
- [81] M. Kaltenbacher. Skript zur Vorlesung Strömungsakustik. *Technische Universität Wien*, 2015.
- [82] B. Chu and L. S. G. Kovásznyay. Non-linear interactions in a viscous heat-conducting compressible gas. *Journal of Fluid Mechanics*, 3(05):494–514, 1958.
- [83] C. Henke. Separation of acoustic waves in isentropic flow perturbations. *Annals of Physics*, 355:70–86, 2015.
- [84] P. Martínez-Lera and C. Schram. Correction techniques for the truncation of the source field in acoustic analogies. *The Journal of the Acoustical Society of America*, 124(6):3421–3429, 2008.
- [85] D. G. Crighton. Computational aeroacoustics for low Mach number flows. In *Computational aeroacoustics*, pages 50–68. Springer, 1993.

- [86] R. R. Mankbadi, M. E. Hayder, and L. A. Povinelli. Structure of supersonic jet flow and its radiated sound. *AIAA journal*, 32(5):897–906, 1994.
- [87] R. Ewert. *A hybrid computational aeroacoustics method to simulate airframe noise*. Shaker Verlag, 2003.
- [88] I. Lazarov. *Strömungsakustische Simulation einer tiefen Kavität, Diplomarbeit*. TU Wien, 2018.
- [89] X. Gloerfelt. Cavity noise. *VKI lecture series*, 3, 2009.
- [90] K. Karamcheti. *Sound radiation from surface cutouts in high speed flow*. PhD thesis, California Institute of Technology, 1956.
- [91] C. W. Rowley, T. Colonius, and A. J. Basu. On self-sustained oscillations in two-dimensional compressible flow over rectangular cavities. *Journal of Fluid Mechanics*, 455:315–346, 2002.
- [92] A. Roshko. Some measurements of flow in a rectangular cutout. Technical report, CALIFORNIA INST OF TECH PASADENA, 1955.
- [93] K. Karamcheti. *Acoustic radiation from two-dimensional rectangular cutouts in aerodynamic surfaces*. NACA, Tech. Note 3487, 1955.
- [94] H. E. Plumblee, J. S. Gibson, and L. W. Lassiter. *A theoretical and experimental investigation of the acoustic response of cavities in an aerodynamic flow*. DTIC Document, 1962.
- [95] S. A. Elder, F. M. Farabee, and F. C. DeMetz. *Mechanisms of flow-excited cavity tones at low Mach number*. The Journal of the Acoustical Society of America, Vol. 72, Issue 2, p. 532–549, 1982.
- [96] J. E. Rossiter. Wind tunnel experiments on the flow over rectangular cavities at subsonic and transonic speeds. Technical report, Ministry of Aviation; Royal Aircraft Establishment; RAE Farnborough, 1964.
- [97] D. Rockwell and E. Naudascher. Self-sustaining oscillations of flow past cavities. *Journal of Fluids Engineering*, 100(2):152–165, 1978.
- [98] D. Rockwell and E. Naudasher. *Self-sustained oscillations of impinging free shear layer*. Annual Review of Fluid Mechanics, Vol. 11, p. 67–94, 1979.
- [99] D. Rockwell and E. Naudasher. *Review – Self-sustaining Oscillations of Flow Past Cavities*. Journal of Fluids Engineering, Vol. 100, p. 152–165, 1978.
- [100] M. Gharib and A. Roshko. The effect of flow oscillations on cavity drag. *Journal of Fluid Mechanics*, 177:501–530, 1987.
- [101] P. J. W. Block. *Noise response of cavities of varying dimensions at subsonic speeds*. NASA TN D-8351, 1976.
- [102] L. Chatellier, J. Laumonier, and Y. Gervais. Theoretical and experimental investigations of low Mach number turbulent cavity flows. *Experiments in fluids*, 36(5):728–740, 2004.
- [103] V. Sarohia. *Experimental and analytical investigation of oscillations in flows over cavities*. PhD thesis, California Institute of Technology, 1975.
- [104] K. K. Ahuja and J. Mendoza. *Effects of Cavity Dimensions, Boundary Layer, and Temperature on Cavity Noise With Emphasis on Benchmark Data to Validate Computational Aeroacoustic Codes*. NASA, 1995.

- [105] P. T. Nagy, A. Hüppe, M. Kaltenbacher, and G. Paál. Acoustic source term formulations in the cavity tone. *Journal of Computational & Applied Mechanics*, 11(2), 2016.
- [106] M. D. Dahl. *Third computational aeroacoustics (CAA) workshop on benchmark problems*. NASA/CP-2000-209790, 2000.
- [107] T. M. Faure, P. Adrianos, F. Lusseyran, and L. Pastur. Visualizations of the flow inside an open cavity at medium range Reynolds numbers. *Experiments in Fluids*, 42(2):169–184, 2007.
- [108] Y. J. Moon, S. R. Koh, Y. Cho, and J. M. Chung. Aeroacoustic computations of the unsteady flows over a rectangular cavity with a lip. In *Third Computational Aeroacoustics(CAA) Workshop on Benchmark Problems*, volume 1, 2000.
- [109] K. Chang, G. Constantinescu, and S. Park. Analysis of the flow and mass transfer processes for the incompressible flow past an open cavity with a laminar and a fully turbulent incoming boundary layer. *Journal of Fluid Mechanics*, 561:113–145, 2006.
- [110] J. C. Hardin and D. S. Pope. Sound generation by flow over a two-dimensional cavity. *AIAA journal*, 33(3):407–412, 1995.
- [111] M. S. Howe. Mechanism of sound generation by low Mach number flow over a wall cavity. *Journal of sound and vibration*, 273(1):103–123, 2004.
- [112] D. Rockwell and C. Knisely. *Vortex-edge interaction: Mechanisms for generating low frequency components*. The Physics of Fluids, Vol. 23(2), p. 239–240, 1980.
- [113] D. Tonon, A. Hirschberg, J. Golliard, and S. Ziada. Aeroacoustics of pipe systems with closed branches. *International Journal of Aeroacoustics*, 10(2-3):201–275, 2011.
- [114] J. Laufer and P. Monkewitz. *On turbulent jet flow in a new perspective*. AIAA Paper 80-0962, 1980.
- [115] M. A. Kegerise. *An experimental investigation of flow-induced cavity oscillations*, Ph.D. thesis. Syracuse University, 1999.
- [116] V. Sarohia. *Experimental oscillations in flows over shallow cavities*. AIAA Journal, Vol 15(7), p. 987–991, 1977.
- [117] S. A. Elder. Forced oscillations of a separated shear layer with application to cavity flow-tone effects. *The Journal of the Acoustical Society of America*, 67(3):774–781, 1980.
- [118] A. F. Charwat, J.N. Roos, F. C. Dewey, and J. A. Hitz. *An investigation of separated flows. Part 1. The pressure field*. Journal of Aerospace Sciences, Vol. 28, p. 457–470, 1961.
- [119] H. Schlichting and K. Gersten. *Grenzschicht-Theorie*. Springer-Verlag, 2006.
- [120] M. Weitz. *Numerical Investigation of the Resonance Behavior of Flow-Excited Helmholtz Resonators*, Bachelor Thesis. TU Wien, 2017.
- [121] H. E. Plumblee, J. S. Gibson, and L. W. Lassiter. A theoretical and experimental investigation of the acoustic response of cavities in an aerodynamic flow. 1962.
- [122] Sengpiel Audio Web Page. *Rechner-Raummoden*. Alexander Sengpiel, (cited on: 30.12.2017).
- [123] H. Kook and L. Mongeau. Analysis of the periodic pressure fluctuations induced by flow over a cavity. *Journal of Sound and Vibration*, 251(5):823–846, 2002.

- [124] S. Schimmelpfennig. *Aeroakustik von Karosseriespalten*. Verlag Dr. Hut, 2016.
- [125] R. Lerch, G.M. Sessler, and D. Wolf. *Technische Akustik: Grundlagen und Anwendungen*. Springer, 2009.
- [126] E. Skudrzyk. *Die Grundlagen der Akustik*. Springer, 1954.
- [127] L. F. East. *Aerodynamically induced resonance in rectangular cavities*. Journal of Sound and Vibration, Vol. 3, Issue 3, p. 277–287, 1966.
- [128] X. Gloerfelt, C. Bogey, and C. Bailly. *Numerical evidence of mode switching in the flow-induced oscillations by a cavity*. International Journal of Aeroacoustics, Vol. 2(2), p. 99–124, 2003.
- [129] C. K. W. Tam and P. J. W. Block. *On the tones and pressure oscillations induced by flow over rectangular cavities*. Journal of Fluid Mechanics, 1978.
- [130] H. Illy. *Contrôle de l'écoulement au dessus d'une cavité en régime transsonique, Ph.D. thesis*. Ecole Centrale de Lyon, 2005.
- [131] X. Gloerfelt. *Aeroacoustic computations of high-Reynolds number cavity flows on staggered grids*. AIAA Paper 2006-2433, 2006. 12th AIAA/CEAS AeroAcoustics Conference, 8-10 May, Cambridge, Massachusetts.
- [132] S. Albensoeder and H. C. Kuhlmann. *Nonlinear three dimensional flow in the lid driven square cavity*. Journal of Fluid Mechanics, Vol. 569, p. 465–480, 2006.
- [133] G. B. Ashcroft, K. Takeda, and X. Zhang. *A numerical investigation of the noise radiated by a turbulent flow over a cavity*. Journal of Sound and Vibration, vol. 265(1), p. 43–60, 2003, 2003.
- [134] D. G. Crighton. Acoustics as a branch of fluid mechanics. *Journal of Fluid Mechanics*, 106:261–298, 1981.
- [135] C. Bailly and G. Comte-Bellot. *Turbulence*. Springer, 2015.
- [136] F. Jenko. *An introduction to turbulence*. Ecole de Physique de Houches, (cited on: 22.05.2018).
- [137] W. Bechara, C. Bailly, P. Lafon, and S. M. Candel. Stochastic approach to noise modeling for free turbulent flows. *AIAA journal*, 32(3):455–463, 1994.
- [138] J. M. Seiner, D. K. McLaughlin, and C. Liu. Supersonic jet noise generated by large scale instabilities. 1982.
- [139] J. M. Seiner and M. K. Ponton. Aeroacoustic data for high Reynolds number supersonic axisymmetric jets. 1985.
- [140] D. G. Crighton. Computational aeroacoustics for low Mach number flows. In *Computational aeroacoustics*, pages 50–68. Springer, 1993.
- [141] O. M. Phillips. On the generation of sound by supersonic turbulent shear layers. *Journal of Fluid Mechanics*, 9(1):1–28, 1960.
- [142] G. M. Lilley. *On the noise from jets*. AGARD-CP-131, 1974.
- [143] M. E. Goldstein. Aeroacoustics. *New York, McGraw-Hill International Book Co., 1976. 305 p., 1976.*



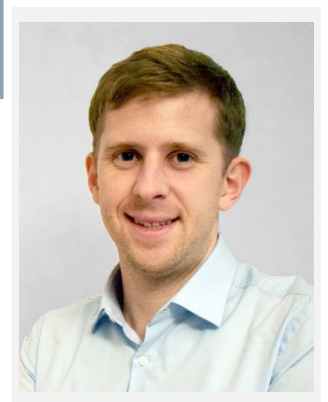
- [144] M. Kaltenbacher, A. Hüppe, A. Reppenhagen, F. Zenger, and S. Becker. Computational Aeroacoustics for Rotating Systems. In *22nd AIAA/CEAS Aeroacoustics Conference*, page 3025, 2016.
- [145] P. J. Schmid. Dynamic mode decomposition of numerical and experimental data. *Journal of fluid mechanics*, 656:5–28, 2010.
- [146] M. S. Howe. *Theory of vortex sound*, volume 33. Cambridge University Press, 2003.
- [147] S. Zaglmayr. *High order finite element methods for electromagnetic field computation*, Universität Linz. PhD thesis, Dissertation, 2006.
- [148] S. Reitzinger and J. Schöberl. An algebraic multigrid method for finite element discretizations with edge elements. *Numerical linear algebra with applications*, 9(3):223–238, 2002.
- [149] G. Schwarz. *Hodge Decomposition - A Method for Solving Boundary Value Problems*. Lecture Notes in Mathematics. Springer Berlin Heidelberg, 2006.
- [150] Q. Chen, A. Konrad, and P. P. Biringer. An integrodifferential finite element-Green’s function method for the solution of unbounded eddy current problems. *IEEE Transactions on Magnetics*, 29(2):1874–1877, 1993.
- [151] J.-C. Nédélec. Mixed finite elements in R 3. *Numerische Mathematik*, 35(3):315–341, 1980.
- [152] A. Kost. *Numerische Methoden in der Berechnung elektromagnetischer Felder*. Springer-Lehrbuch. Springer Berlin Heidelberg, 2013.
- [153] P. J. Matuszyk and L. F. Demkowicz. Parametric finite elements, exact sequences and perfectly matched layers. *Computational Mechanics*, 51(1):35–45, 2013.
- [154] W. V. D. Hodge. *The theory and applications of harmonic integrals*. CUP Archive, 1989.
- [155] S. K. Harouna and V. Perrier. Helmholtz-Hodge Decomposition on  $[0, 1]$  d by Divergence-Free and Curl-Free Wavelets. *Curves and Surfaces*, 6920:311–329, 2010.
- [156] H. Bhatia, V. Pascucci, and P. Bremer. The natural Helmholtz-Hodge decomposition for open-boundary flow analysis. *IEEE transactions on visualization and computer graphics*, 20(11):1566–1578, 2014.
- [157] C. Wagner, T. Hüttl, and P. Sagaut, editors. *Large-Eddy Simulation for Acoustics*. Cambridge University Press, 2007.
- [158] S. Caro, Y. Detandt, J. Manera, F. Mendonca, and R. Toppinga. Validation of a New Hybrid CAA Strategy and Application to the Noise Generated by a Flap in a Simplified HVAC Duc. In *15th AIAA/CEAS Aeroacoustics Conference*, AIAA 2009-3352, 2009.
- [159] T. Schröder, P. Silkeit, and O. Estorff. Influence of source term interpolation on hybrid computational aeroacoustics in finite volumes. In *InterNoise 2016*, pages 1598–1608, 2016.
- [160] M. Piellard and C. Bailly. A hybrid method for computational aeroacoustic applied to internal flows. In *NAG-DAGA International Conference on Acoustics*, NAGDAGA2009/369, 2009.
- [161] M. Kaltenbacher, M. Escobar, I. Ali, and S. Becker. Numerical Simulation of Flow-Induced Noise Using LES/SAS and Lighthill’s Acoustics Analogy. *International Journal for Numerical Methods in Fluids*, 63(9):1103–1122, 2010.

- [162] R. L. Hardy. Multiquadric equations of topography and other irregular surfaces. *Journal of geophysical research*, 76(8):1905–1915, 1971.
- [163] R. L. Hardy. Theory and applications of the multiquadric-biharmonic method 20 years of discovery 1968–1988. *Computers & Mathematics with Applications*, 19(8-9):163–208, 1990.
- [164] M. Mongillo. Choosing Basis Functions and Shape Parameters for Radial Basis Function Methods. Available from: [www.siam.org/students/siuro/vol4/S01084.pdf](http://www.siam.org/students/siuro/vol4/S01084.pdf), 2011.
- [165] W. R. Madych. Miscellaneous Error Bounds for Multiquadratic and Related Interpolants. *Computers Math. Applic.*, 24(12):121–138, 1992.
- [166] B. Fornberg, E. Larsson, and N. Flyer. Stable computations with gaussian radial basis functions. *SIAM Journal*, pages 869–892, 2011.
- [167] H. Wendland. Piecewise polynomial, positive definite and compactly supported radial functions of minimal degree. *Advances in computational Mathematics*, 4(1):389–396, 1995.
- [168] D. Lazzaro and L. Montefusco. Radial basis functions for the multivariate interpolation of large scattered data sets. *Journal of Computational and Applied Mathematics* 140, pages 521–536, 2002.
- [169] The CGAL Project. *CGAL User and Reference Manual*. CGAL Editorial Board, 4.10 edition, 2017.
- [170] M. Muja and D. G. Lowe. *FLANN: Fast library for approximate nearest neighbor*. M. Muja, 1.8.4 edition, 2013.
- [171] F. Alauzet. A parallel matrix-free conservative solution interpolation on unstructured tetrahedral meshes. *Computer Methods in Applied Mechanics and Engineering*, 299:116–142, 2016.
- [172] M. Casey and T. Wintergerste. *Best Practice Guidelines: ERCOFTAC Special Interest Group on “Quality and Trust in Industrial CFD”*. ERCOFTAC, 2000.
- [173] E. Larsson, E. Lehto, A. Heryudono, and B. Fornberg. Stable computation of differentiation matrices and scattered node stencils based on Gaussian radial basis functions. *SIAM Journal on Scientific Computing*, 35(4):A2096–A2119, 2013.
- [174] J. L. Roberts. A method for calculating meshless finite difference weights. *International journal for numerical methods in engineering*, 74(2):321–336, 2008.
- [175] M. Kaltenbacher, A. Hüppe, A. Reppenhagen, F. Zenger, and S. Becker. Computational aeroacoustics for rotating systems with application to an axial fan. *AIAA journal*, pages 3831–3838, 2017.
- [176] B. Henderson. Automobile Noise Involving Feedback- Sound Generation by Low Speed Cavity Flows. *Third Computational Aerocompressibles(CAA) Workshop on Benchmark Problems*, 1, 2000.
- [177] T. Seitz. Experimentelle Untersuchungen der Schallabstrahlung bei der Überströmung einer Kavität. Master’s thesis, FAU Erlangen, Germany, 2005.
- [178] M. Kaltenbacher. *Numerical Simulation of Mechatronic Sensors and Actuators: Finite Elements for Computational Multiphysics*. Springer Berlin Heidelberg, 2015.
- [179] M. Kaltenbacher, A. Hüppe, J. Grabinger, and B. Wohlmuth. Modeling and Finite Element Formulation for Acoustic Problems Including Rotating Domains. *AIAA Journal*, 2016.

- [180] A. Oberai, F. Roknaldin, and T. Hughes. Trailing edge noise due to turbulent flows, 02-002. *Boston University*, 2002.
- [181] C. Kato, A. Iida, Y. Takano, H. Fujita, and M. Ikegawa. Numerical prediction of aerodynamic noise radiated from low mach number turbulent wake. In *31st Aerospace Sciences Meeting*, page 145, 1993.
- [182] Y. J. Moon. Aerocompressible computations of the unsteady flows over a rectangular cavity with a lip. In *Third Computational Aerocompressibles(CAA) Workshop on Benchmark Problems*, 2000.
- [183] Y. J. Moon. Aeroacoustic tonal noise prediction of open cavity flows involving feedback. *Computational mechanics*, 31(359), 2000.
- [184] X. Zhang G. B. Ashcroft, K. Takeda. Computations of self-induced oscillatory flow in an automobile door cavity. In *Third Computational Aerocompressibles(CAA) Workshop on Benchmark Problems*, 2000.
- [185] P. J. Roache. *Verification and validation in computational science and engineering*. Hermosa, 1998.
- [186] L. F. Richardson and J. A. Gaunt. Viii. the deferred approach to the limit. *Phil. Trans. R. Soc. Lond. A*, 226(636-646):299–361, 1927.
- [187] W. H. Lin and R. H. Loh. *Numerical Solutions to the Fourth and Second Computational Aeroacoustics (CAA) Workshop Benchmark Problems*.  
In: "Fourth Computational Aeroacoustics (CAA) Workshop on Benchmark Problems". NASA, vol. CP 2004-212954, Cleveland, Ohio, Oct. 2003.
- [188] T. Colonius, A. J. Basu, and C. W. Rowley. Numerical investigation of the flow past a cavity. *positions*, 23:24, 1999.
- [189] H. H. Heller and D. B. Bliss. Flow-induced pressure fluctuations in cavities and concepts for their suppression. *Aeroacoustics: STOL Noise; Airframe and Airfoil Noise*, 45:281–296, 1976.
- [190] F. Hindenlang, G. J. Gassner, C. Altmann, A. Beck, M. Staudenmaier, and C.-D. Munz. Explicit discontinuous Galerkin methods for unsteady problems. *Computers & Fluids*, 61:86–93, 2012.
- [191] C.-D. Munz, P. Omnes, R. Schneider, E. Sonnendrücker, and U. Voss. Divergence correction techniques for maxwell solvers based on a hyperbolic model. *Journal of Computational Physics*, 161(2):484–511, 2000.
- [192] A. Dedner, F. Kemm, D. Kröner, C.-D. Munz, T. Schnitzer, and M. Wesenberg. Hyperbolic divergence cleaning for the mhd equations. *Journal of Computational Physics*, 175(2):645–673, 2002.
- [193] G. Grosch, I. Doxiadis, B. Lang, R. J. Schweyen, and F. Kaudewitz. A one-step method for RHO+ cRNA/RHO<sup>-</sup> DNA hybridization in mapping of the mitochondrial genome of *saccharomyces cervisiae*. In *Mitochondria 1977: Genetics and Biogenesis of Mitochondria: Proceedings of a Colloquium Held at Schliersee, Germany, August 1977*, page 425. Walter de Gruyter, 1977.



## Stefan Schoder



Staatsbürgerschaft Österreich  
Geburtsdatum 27.03.1989  
Adresse Schubertplatz 4, 3361 Aschbach  
Telefon +43 650 999 2489  
E-Mail [schoder.jstefan@gmx.at](mailto:schoder.jstefan@gmx.at)

### Bildung

- 06/2015 – 12/2018 **Doktorat der technischen Wissenschaften** an der TU Wien,  
Thesis: „Aeroacoustic Analogies based on Compressible Flow Data“
- 09/2009 – 02/2015 **Studium: Wirtschaftsingenieurwesen - Maschinenbau** an der TU Wien,  
Masterthesis: „CFD-Simulation of a high head Francis turbine and comparison with experimental data“  
Bachelorthesis: „Tooth contact analysis of TGB“
- 09/2003 – 06/2008 **Matura** an der HTL 2 in Linz für Mechatronik  
Ausbildungsschwerpunkt Automatisierung und Robotik

### Berufserfahrung

- seit 06/2015 **Technische Universität Wien, Wien**  
Wissenschaftlicher Mitarbeiter
- Aeroakustik/Vibroakustik und stochastische Simulationstechnologie (Human Phonation, Vehicle Design, CompressorSound, Strömungsakustik)
  - Finite Elemente Methode - Coupled Field Simulation (CFS++)
  - Projekt Manager CFS-DAT (C++ Projekt)
  - Robust Design, Optimierung
  - Betreuung von Bachelor- und Masterarbeiten sowie Führung des Aeroakustik Teams
- seit 04/2016 **Tax@Home, Wien**  
Entrepreneur
- Strategische Entwicklung und Führung in der Startup Phase
  - Produktentwicklung (Android, iOS, Web, Python)
  - Digitaler Innovationsprozess (Künstliche Intelligenz und Deep Learning)
  - Kommunikation und Branding
- vor 06/2015 **Technische Universität Wien, Wien**  
Studentenjob
- CFD-Simulation einer Francis Turbine (Energietechnik Institut)
  - Antriebskonzepte in der Luftfahrt – Hubschraubergetriebe (Maschinenelemente Institut)
  - Tutor der Lehrveranstaltungen CAD und Mechanik
- vor 06/2015 **voestalpine AG, Linz**  
Konstruktion und Berechnung
- Festigkeitsberechnung und Konstruktion von Maschinen und Anlagenkomponenten des Stahlwerkes Linz (CAE, Ansys)
  - Material Modellierung und Crash Simulation (LS-DYNA, Matlab, CAE)

### Persönliche Fähigkeiten und Kompetenzen

---

Sprachen	<b>Deutsch</b> Muttersprache <b>Englisch</b> verhandlungssicher <b>Dänisch</b> Grundkenntnisse
Kenntnisse	<ul style="list-style-type: none"><li>• Programmieren, Datenanalyse, Künstliche Intelligenz und Maschinelles Lernen</li><li>• Office, Projektmanagement und Analysetools</li><li>• Simulation, Optimierung, FE-Tools: Abaqus, Hyperworks und CFD-Tools: Fluent, CFX, OpenFoam, MKS-Tool: Simpack</li></ul>
Kompetenzen	<ul style="list-style-type: none"><li>• Sehr gutes technisches und wirtschaftliches Verständnis, erworben durch die Schwerpunkte des Studiums wie Strategie, Risikomanagement, Mechanik, Mathematik, Thermodynamik und Regelungstechnik</li><li>• Fundierte Kenntnisse in der Simulation, erworben durch Fortbildungen und Berufserfahrung</li><li>• Führung von Mitarbeitern und Projektmanagement von Spitzenforschung im Bereich der Methodenentwicklung und Anwendung an konkrete Aufgabenstellungen</li></ul>

### Auslandserfahrung

---

2012 – 2016	<b>Diverse Austauschprogramme</b> der TU Wien, CISM Udine 2016, IST Lissabon 2014, TU München 2014 und 2013, TU Delft 2012
08/2012 – 01/2013	<b>Erasmus: Wirtschaftsingenieurwesen - Maschinenbau</b> an der DTU Denmark

### Referenzen

---

TU Wien	<b>TU Wien</b> , Getreidemarkt 9, 1060 Wien Prof. Manfred Kaltenbacher, Mechanik und Mechatronik T +43158801 - 325 410 • E <a href="mailto:manfred.kaltenbacher@tuwien.ac.at">manfred.kaltenbacher@tuwien.ac.at</a>
voestalpine	<b>voestalpine Stahl GmbH</b> , voestalpine-Str. 3, 4020 Linz Reinhold Lauß, B4I T - • E <a href="mailto:reinhold.lauss@voestalpine.com">reinhold.lauss@voestalpine.com</a>

Aschbach, September 2018

*Stefan J. Schoder*

### Publikationen

---

- Konferenzbeiträge
- Schoder, Stefan, and Manfred Kaltenbacher. *Interpolation Technique for Computational Aeroacoustics and Vibroacoustics*. DAGA, 2018.
- Schoder, Stefan, and Manfred Kaltenbacher. "Aeroacoustic source term filtering based on Helmholtz decomposition." *23rd AIAA/CEAS Aeroacoustics Conference*. 2017.
- Schoder, Stefan, Florian Toth, and Manfred Kaltenbacher. "Hybrid computational aeroacoustics based on compressible flow data at low Mach numbers." *PAMM* 17.1 (2017): 687-688.
- Kaltenbacher, Manfred, and Stefan Schoder. *Computational Aeroacoustics Based on a Helmholtz-Hodge Decomposition*. No. 2018-01-1493. SAE Technical Paper, 2018.
- Toth, Florian, Stefan Schoder, and Manfred Kaltenbacher. "An infinite mapping layer for deep water waves." *PAMM* 17.1 (2017): 689-690.
- Lenarcic, M., et al. "Numerical investigation of a high head Francis turbine under steady operating conditions using foam-extend." *Journal of Physics: Conference Series*. Vol. 579. No. 1. IOP Publishing, 2015.